# Building and operating a quantum node of a microwave network

Théau Peronnin


Numéro National de Thèse : 2020LYSEN025

**THESE de DOCTORAT DE L'UNIVERSITE DE LYON**
opérée par
**l'Ecole Normale Supérieure de Lyon**

**Ecole Doctorale** N° 52
**Physique et Astrophysique de Lyon**

**Discipline** : Physique

Soutenue publiquement le 16/06/2020, par :
**Théau PERONNIN**

---

# Building and operating a quantum node of a microwave network

Construction et operation d'un nœud quantique d'un réseau microonde

---

Devant le jury composé de :

| | | |
|---|---|---|
| Estève, Daniel | directeur de recherche, CEA | Rapporteur |
| Buisson, Olivier | directeur de recherche, CNRS | Rapporteur |
| Milman, Perola | directrice de recherche, CNRS | Examinatrice |
| Carpentier, David | directeur de recherche, CNRS | Examinateur |
| | | |
| Huard, Benjamin | professeur, ENS de Lyon | Directeur de thèse |

## ABSTRACT

After years of academic development, the circuit quantum electrodynamics is entering the age of applications. This thesis was realized in this context of creating tools to bridge the gap between an astounding academic quantum system, superconducting circuits, and a grand goal, the universal quantum computer. A likely blueprint for quantum processors consists in the assembly of a large number of elementary modules arranged in a network.

In this experimental thesis, a possible node for such a network, the *quantum node*, was developed and fabricated using state-of-the-art techniques for 2D superconducting microwave circuits. This node was first used to implement a novel sequential readout method for a superconducting qubit. This experiment, first proposed in 2013 by Sete *et al.*, potentially allows for faster, more accurate read out of superconducting qubits. The read out of qubits is one of the several bottlenecks limiting the development of fault-tolerant superconducting quantum computers, which made this project both useful as a demonstration of the quantum node and for applications. This novel readout method achieves readout performances close to state-of-the-art of superconducting qubit readout even though the chip was not optimized for that purpose.

During this work, we also contributed to two other experiments engineering quantum measurement and dissipation with superconducting circuits.

First, a dedicated circuit was developed to demonstrate a new form of quantum measurement: the multiplexed photon number measurement. In that experiment led by A. Essig and Q. Ficheux, a superconducting transmon quantum bit is read out at multiple frequencies simultaneously to extract more than one bit of information about the number of photons contained in a microwave resonator coupled to that quantum bit.

Second, we contributed to the experimental demonstration of the exponential suppression of bit-flips in a qubit encoded in a Schrödinger Cat state of a microwave mode. This experiment led by R. Lescanne and Z. Leghtas, demonstrates the improvement by a factor 300 of the lifetime of a qubit thanks to the autonomous error correction realized through the engineering of the dissipation of a microwave mode.

## RÉSUMÉ

Après des années de développement académique, l'électrodynamique quantique en circuit entre dans l'ère des applications. Cette thèse a été réalisée dans une volonté de créer des outils pour faire le lien entre une curiosité académique quantique, les circuits supraconducteurs, et un objectif majeur, l'ordinateur quantique universel. Une architecture vraisemblable de processeur quantique consiste à connecter en réseau un grand nombre de modules élémentaires.

Lors de cette thèse expérimentale, le noeud d'un tel réseau, le *quantum node*, a été développé et fabriqué grâce aux techniques de l'état de l'art des circuits imprimés quantiques microonde. Ce circuit a été utilisé pour réaliser pour la première fois une méthode de lecture séquentielle d'un qubit supraconducteur. Cette méthode, proposée en 2013 par Sete *et al.*, permettrait une lecture plus rapide et plus précise des qubits supraconducteurs. La lecture des qubits est l'un des obstacles majeurs limitant le développement d'ordinateurs quantiques universels sans erreur, ce qui rend ce projet autant intéressant pour sa mise en oeuvre inédite du quantum node que pour ses applications. Cette nouvelle méthode de lecture atteint des performances proches de l'état de l'art alors même que le circuit n'était pas optimisé pour cette fin.

Lors de cette thèse, nous avons aussi contribué à deux autres expériences d'optique quantique microonde, détaillées ici.

Un circuit dédié a été développé pour démontrer une nouvelle forme de mesure quantique: la mesure multiplexée du nombre de photons. Dans cette expérience, menée par A. Essig et Q. Ficheux, un qubit supraconducteur est lu simultanément à plusieurs fréquences pour extraire plus d'un bit d'information à la fois à propos du nombre de photons contenus dans un résonateur microonde couplé à un qubit.

Enfin, nous avons contribué à la démonstration expérimentale de la suppression exponentielle des bit-flips dans un qubit encodé dans un état de chat de Schrödinger d'un mode microonde. Cette expérience, menée par R. Lescanne et Z. Leghtas, démontre une augmentation par un facteur 300 du temps de vie du qubit grâce à la correction d'erreur quantique autonome réalisée grâce à l'ingénierie de la dissipation d'un mode microonde.

# ACKNOWLEDGMENTS AND PERSONAL REMARKS

> Que m'importent les fleurs et les arbres, et le feu et la pierre, si je suis sans amour et sans foyer ! Il faut être deux - ou, du moins, hélas ! il faut avoir été deux - pour comprendre un ciel bleu, pour nommer une aurore ! Les choses infinies comme le ciel, la forêt et la lumière ne trouvent leur nom que dans un coeur aimant. Et le souffle des plaines, dans sa douceur et dans sa palpitation, est d'abord l'écho d'un soupir attendri.
>
> G. Bachelard

Ce manuscrit présente très succinctement ce que mon travail de doctorant propose à la communauté scientifique, et il me semble indispensable de reconnaître aussi brièvement ce que ce travail, ainsi que ceux qui l'ont accompagné, m'ont apporté personnellement. Car comme l'illustrent l'hommage répété à G. Bachelard en épigraphe, la quête de la science est pour moi bien plus qu'une quête de savoir : elle façonne l'imaginaire et, ainsi, construit l'homme.

Quelle chance pour un passionné de physique que de faire son entrée dans le monde académique à une époque où il est possible de jouer avec les lois les plus étranges et fondamentales de notre monde ! Bien loin de la simple expérience de pensée, l'état de l'art actuel m'a permis lors de ces travaux de doctorat de me livrer à un véritable corps-à-corps avec la physique quantique. Sans donner tort à R. Feynman, si je n'ai pas compris l'essence de la réalité qu'elle dépeint, j'ai au moins acquis la certitude qu'elle ne nous a pas tout dit. Il ne fait aujourd'hui aucun doute que je consacrerai une grande partie de ma vie à chercher à la dompter, à l'asservir pour les besoins de la technologie, avec la conviction personnelle que c'est le meilleur chemin vers la compréhension de ses rouages cachés (évidemment non locaux). Vous l'aurez compris, mon doctorat m'a avant tout fait découvrir mon amour pour l'exotisme élémentaire de la mécanique quantique.

Et comme dans toute histoire d'amour, j'ai alterné des périodes d'euphorie et d'autres d'immense solitude. Bon nombre avant moi ont vécu une aventure doctorale similaire. Et ce que le diplôme auquel je prétends aujourd'hui sanctionne, c'est avant tout d'avoir su naviguer en solitaire dans les eaux tumultueuses des expériences non concluantes et des biais de confirmation sans perdre son cap. Je me suis découvert une créativité scientifique dont je ne rougis pas mais aussi une incapacité maladive à m'atteler aux

tâches qui ne m'inspirent pas. Et, s'il m'est arrivé par moment de me perdre dans des nuages, esseulé, à la recherche d'une nouvelle épiphanie éphémère, incapable de faire le deuil d'un éclair de génie anachronique, c'est grâce à Toi que j'en sors grandi, que je ne retiens de cette aventure uniquement ces innombrables moments de pure joie, scientifique et humaine. C'est grâce à Toi que je suis fier d'avoir accompli la mission qui m'avait été confiée : developper un circuit quantique capable de capturer, manipuler et relâcher un paquet d'onde microonde dans le domaine quantique; que je suis particulièrement fier de l'avoir utilisé pour réaliser une expérience que j'ai intégralement conçu : la lecture séquentielle d'un qubit; que je tire ma plus grande fierté de savoir que je laisse à mes successeurs une plateforme performante avec laquelle ils produiront sans doute de nombreux résultats scientifiques, ainsi que des techniques de fabrication et de conception de circuits quantiques qui leur permettront à leur tour de laisser libre cours à leur imagination.

Toi, tu es tous ceux qui m'ont fait tel que je suis aujourd'hui, qui ont fait naître en moi le désir de comprendre et que je me dois de remercier ici.

Je pense en particulier à mes professeurs, de sciences mais pas uniquement, dont V. Lemoro, S. Benlhajlahsen, C. Botet, C. Debernardi, C. Lafitte, E. Goldsztejn. Je remercie aussi chaudement les trois jeunes chercheurs, N. Chevalier, C. Ravat et G. Toombes qui m'ont fait découvrir la physique expérimentale et l'art de joute verbale scientifique dans le cadre de l'International Young Physicists Tournament, ainsi que mes professeurs de l'école Polytechnique et en particulier D. Suchet avec qui nous avons remporté l'International Physicists Tournament en 2014. Je salue aussi S. Hudlet qui m'a en premier initié à la physique quantique et à G. Bachelard.

Je suis encore aujourd'hui particulièrement ému par la chaleureuse place que l'équipe du Quantum Electronics Group m'a faite à mon arrivée dans le groupe en 2015 pour mon stage de M1, puis à nouveau en 2016 pour mon stage de M2 suivi par ma thèse. Par Seb., Nath., Dani., Quentin, dont je serais toujours le 'stagiaire de troisième' : le cadet a qui l'on inculque les rudiments du métier. Quelle chance que de faire mes débuts entouré par des aînés que j'admire et avec qui le temps passe si vite ! Je pense aussi à Zaki et Raph, restés à Paris, qui ont commencé en même temps que moi au-sein du groupe et m'ont pris sous leur aile pour mes premières mesures quantiques et avec qui je continue de débuter, dans l'entrepreneuriat cette fois-ci. Je remercie les équipes du LPA et de l'ENS de Lyon, qui nous ont accueillis très chaleureusement, en particulier Fatiha et Thierry.

Ma plus grande dette est envers Benjamin Huard, qui m'a encadré lors de ce doctorat. Benjamin m'a offert, dès mon premier jour de stage et jusqu'à la fin de ma laborieuse rédaction, une confiance infaillible et une constante bienveillance qui, sans l'ombre d'un doute, ont été le terreau de mon épanouissement. Scientifiquement, Benjamin m'a inculqué les nombreux pans de la physique nécessaires à notre domaine, de la nanofabrication à la théorie de la mesure. J'ai été vraiment impressionné par sa disponibilité et sa capacité à se plonger instantanément dans le problème qu'on lui présente, que ce soit un bug de lithographie électronique ou un obscure plot sans axe... Sa force pédagogique sait trouver dans les idées farfelues que je rapportais de week-end, le détail qui m'échappait et ainsi affuter, semaine après semaine, ma comprehension de la

physique. Humainement, Benjamin a été de très loin le meilleur exemple de leadership de ma scolarité, au grand dam des officiers de Polytechnique ! Il a toujours su entretenir dans le groupe ce subtil équilibre entre rigueur scientifique et légèreté bienveillante. Il ne passe jamais avant ses étudiants et inculque ainsi une humilité qui appelle à l'excellence. Benjamin a été, lors de ces 5 dernières années, le tuteur idéal pour la jeune pousse que j'étais, et je lui en suis éternellement reconnaissant.

Je me réjouis de voir me succéder dans le groupe une génération de physiciens toujours plus malins et à l'esprit toujours plus vif : Jérémy, Antoine, Réouven, Rémy, Daniel et Audrey. Ils font vivre et développent la culture de ce groupe qui m'a été si chère.

Enfin je remercie profondément mes proches qui m'ont construit et continuent à me soutenir dans mes aventures scientifiques : mes parents, mon frère et ma soeur, mes quatre amis, et ma tendre et chère fiancée, qui a supporté la distance et m'a soutenu inlassablement.

*Merci.*

I thank D. Esteve, O. Buisson, P. Milman and D. Carpentier,
for accepting to be members of my thesis jury.

# CONTENTS

# 1 INTRODUCTION

> Le temps n'a qu'une réalité, celle de l'instant. Autrement dit, le temps est une réalité resserée sur l'instant et suspendue entre deux néants
>
> G. Bachelard

After years of academic development, the circuit quantum electrodynamics ([1]) is entering the age of applications ([2]). This thesis was realized in this context of creating tools to bridge the gap between an astounding academic quantum system, superconducting circuits, and a grand goal, the universal quantum computer. A likely blueprint for quantum processors consists in the assembly of a large number of elementary modules arranged in a network ([3]). At the beginning of this PhD work, our group had realized a proof of principle of a node, the *quantum node* (see chapter 3), of such a network with a 3D cavity connected to the network via a nonlinear coupling element, the Josephson Ring Modulator (JRM) ([4–6]). This preliminary work lead to the conclusion that reaching the right amount of nonlinearity required to realize this device on chip using a superconducting coplanar waveguide architecture ([6]) (a description of the nonlinear elements in superconducting circuits can be found in chapter 2). A large part of the PhD work consisted in developing the design and fabrication techniques for 2D superconducting microwave circuits since our group had little prior knowledge of them. Using a wealth of published results on these techniques ([7]), we determined the simplest yet optimal state-of-the-art fabrication techniques for those circuits. Nanofabrication is close to black magic and heavily depends on the equipement and the particular cleanroom facilities ([8–10]). Over the course of this development suited to our equipment in consortium Salle Blanche Paris Centre, which took about a year, several key fabrication tricks were invented and allowed us to maximize yield and quality. At the end of the development, the superconducting circuits we could fabricate were close to state-of-the-art despite limited fabrication resources. Up to the day of this writing, the design and fabrication know-how generated during the first year of my PhD work has been broadly used in the group and beyond at Ecole Normale Supérieure Paris and Ecole Normale Supérieure de Lyon for several projects.

The quantum node is composed of two resonators that are connected via a JRM. One resonator, the buffer, is strongly coupled to the external network via a transmission line. It acts as the interface between the transmission line and the rest of the device. The other resonator, the memory, is a high Q resonator whose purpose is to store

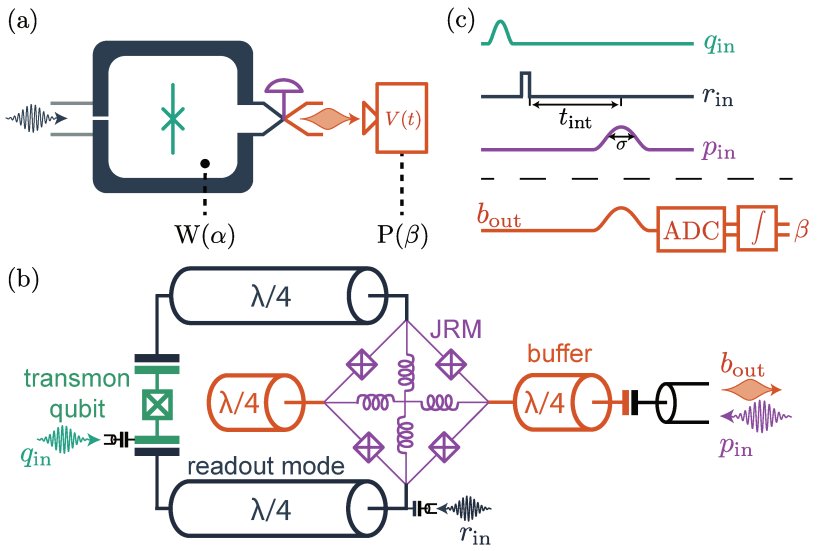


Figure 1.1: (a) The readout resonator (dark gray) is first prepared in a coherent state to probe a transmon qubit. Owing to the dispersive interaction between them, the resonator and the qubit evolve unitarily during a time $t_{\text{int}}$. The readout mode is then upconverted and released into an output line (via purple valve). The complex amplitude $\beta$ of the released mode is encoded in the recorded output voltage $V(t)$. Both the Wigner function $W(\alpha)$ of the readout mode and the probability distribution $P(\beta)$ can be measured. (b) Scheme of the device. The readout mode is a $\lambda/2$ coplanar waveguide resonator (dark gray) that is capacitively coupled to a transmon qubit (green). The readout resonator is coupled to another $\lambda/2$ resonator (buffer in orange) by a Josephson Ring Modulator (JRM in purple). The readout resonator is driven by $r_{\text{in}}$, the transmon (green) by $q_{\text{in}}$, the buffer resonator (orange) outputs in $b_{\text{out}}$, and the JRM is pumped at amplitude $p_{\text{in}}$ by the buffer input. (c) Pulse sequence of the qubit measurement (top) and the released field measurement scheme (bottom).

and perform unitary operations on a quantum state. The JRM can be pumped in order to convert photons between buffer and memory modes or to generate two mode squeezing between them ([5]). A detailed description of the quantum node is provided in chapter 3. In the shape of the proof-of-principle quantum node from 2014 ([4]), the type of operations that could be realized on the memory state were strongly limited. During this PhD work, the memory state was coupled to a transmon qubit (see chapter 2 for introduction to transmon qubits), equipped with a readout resonator, such that many nonlinear operations and measurements could be operated on the memory mode.

In its current form the quantum node promises to implement many functions and quantum protocols for quantum computing, sensing and communication. During the development of the device, I came up with a novel experiment proposal, which ended up being the cornerstone of my PhD work. It consists in a new method to read out the state of a superconducting qubit that alleviates several issues of conventional superconducting qubit readout.

SEQUENTIAL READOUT OF A SUPERCONDUCTING QUBIT We later found out that it was a slight deviation from what Sete *et al.* proposed in 2013 ([11]) but never experimentally realized. The read out of qubits is one of the several bottlenecks

limiting the development of fault-tolerant superconducting quantum computers, which made this project both useful as a demonstration of the quantum node and for applications. In particular, the new readout potentially allows for faster, more accurate read out of superconducting quantum bits. This novel readout method achieves readout performances close to state-of-the-art of superconducting qubit readout ([12, 13]) even though the chip was not optimized for that purpose. A copy of the corresponding preprint is provided in chapter 4.

Beyond its technological relevance, this experiment serves a purpose for basic science. It indeed offers a textbook illustration of the quantum measurement process by separating in time and space the three steps of the measurement process: the deterministic preparation of the quantum probe, its entanglement with the system undergoing measurement, and the projective and destructive measurement of the probe.

One of the important byproduct of this work lead to the development and improvement of quantum state tomography methods for stationary and itinerant microwave wave packets (see appendix a for an introduction to quantum tomography in microwave modes).

With the same device, I also conducted a preliminary work aiming at greatly improving the measurement efficiency of a microwave mode. For the last decade, parametric amplifiers have enabled the detection of microwave modes with near quantum limit efficiencies ([14]). However the need for circulators or other microwave components between the quantum system and the amplifier diminishes the efficiency considerably. Getting the amplifying nonlinear element as close as possible to the mode of interest ([15, 16]) is thus a logical next step in order to improve efficiency. Leveraging the amplifying properties of the Josephson Ring Modulator non linearity, I demonstrated that measurement efficiencies as large as 80 % could be obtained on the memory state. This preliminary work is not included in this manuscript as it is still under development. Were these promising results confirmed, they would pave the way for novel remote state preparation experiments, a possible way towards quantum state teleportation and thus modular architecture for quantum computers.

Finally, I showed that this preliminary work provides a path to demonstrating a prediction from A. Kronwald *et al* ([17]). It should be possible to generate a *stationary* state of light that is squeezed by more than 6 dB. This experiment is undergoing in our group at the time of this writing.

MULTIPLEXED PHOTON NUMBER MEASUREMENT Using the design and fabrication techniques I developed for the quantum node, I could design and fabricate a device that implements a new form of quantum measurement: the multiplexed photon number measurement. In that experiment, a superconducting transmon quantum bit is read out at multiple frequencies simultaneously to extract more than one bit of information about the number of photons contained in a microwave resonator coupled to that quantum bit. This experiment was realized by my coworkers A. Essig and Q. Ficheux. I designed and fabricated the coplanar waveguide superconducting circuit, and contributed to the calibration of the first versions of the device until it reached sufficient performances to meet the requirement of the experiment. This novel experiment

illustrates the seemingly counter-intuitive fact that a two level system can be used to extract simultaneously more than one bit of information. A copy of the corresponding preprint is provided in chapter 5.

QUANTUM ERROR CORRECTION The final published work to which I contributed during this thesis was the exponential suppression of bit-flips in a qubit encoded in a Schrödinger Cat state of a microwave mode. The major bottleneck of quantum computing consits in the limited coherence time of qubits. It came as a surprise in 1996 ([18]) that one could correct for any errors happening to qubits despite their large Hilbert space compared to classical bits. It can even be done autonomously by channeling the entropy increase of a qubit to external degrees of freedom. Several strategies exist to perform this autonomous error correction. Some, as in the surface code ([19]), consist in using registers of physical (imperfect) qubits to generate a collective protected 2 level quantum system. Others, proposed by our colleagues M. Mirrahimi and Z. Leghtas and pioneered at Yale ([20]), consist in isolating two states in the large Hilbert space of a microwave cavity. One choice is to engineer the dissipation to stabilize a qubit formed by two Schrödinger cat states $|\alpha\rangle \pm |-\alpha\rangle$. Our experiment was conducted by my coworkers R. Lescanne and Z. Leghtas. My contribution to this ground-breaking experiment was mainly on the design and fabrication of the circuit. With the experiment, we could demonstrate an improvement by a factor 300 of the lifetime of the qubit. A copy of the corresponding preprint is provided in chapter 6.

This experiment is now the foundation of my next project, the start-up company Alice&Bob that I am currently co-founding with R. Lescanne. Our company aims at developing universal fault-tolerant quantum computers using Schrödinger Cat quantum bits.

Finally, I initiated the invention with B. Huard, Q. Ficheux and S. Jezouin, of a new autonomous scheme to stabilize the parity of the number of photons stored in a microwave resonator. This scheme aims at reducing the phase-flip error rate in a quantum bit encoded with Schrödinger cat states in order to provide a simplified quantum error correction scheme. This on-going experiment is not explained in this manuscript as it will be soon patented.

This manuscript is organized as follows. The first part is a toolbox intended to help the reader with the various concepts that are now standard in circuit quantum electrodynamics. Chapter 2 details how to quantize a superconducting circuit and how the transmon qubit and the JRM operate. Chapter 3 is an in-depth description of the quantum node.

The second part of the manuscript gathers the publications and preprints to which I contributed significantly over the course of this PhD work.

Part I

# TOOLBOX FOR CIRCUIT QED

# 2

# SUPERCONDUCTING CIRCUIT QUANTUM ELECTRODYNAMICS

Nous comprenons la nature en lui resistant.

G. Bachelard

The goal of this section is to provide a brief introduction to circuit quantum electrodynamics. We present the tools required to engineer these circuits and achieve certain desired properties. We illustrate them by studying two elementary circuits used in this thesis: the transmon qubit and the Josephson Ring Modulator (JRM). We then detail how to design, control and exploit those properties to realize experiments on interacting multipartite systems. Finally we discuss how to handle losses in open quantum systems and the coupling to a transmission line.

## 2.1 SUPERCONDUCTING MICROWAVE CIRCUITS

Light has always been a central piece of mankind evolution, whether it is as a means of understanding our world from to the essence of matter to distant black-holes, or as a tool keeping us warm around the fire-pit and transmitting petabytes of data in optical fibers. In recent years, advances in manipulating light at the individual photon level through cavity quantum electrodynamics (CQED) has enabled for groundbreaking experiments ([21, 22]). These experiments not only revealed the elementary interaction between light and matter and the peculiar rules of quantum systems, but they also allowed us to envision a new kind of machine exploiting the exotic features of quantum mechanics. This progress was further accelerated with the invention of the first superconducting quantum bit (qubit) ([23]) on chip in the late 90's and circuit quantum electrodynamics (cQED). In cQED, microwave light at angular frequency $\omega$ is confined in a superconducting circuit printed on a silicon or sapphire chip and operates at cryogenic temperatures $T$ of about 10 mK such that $k_B T \ll \hbar\omega$. These macroscopic systems can behave quantum mechanically and be designed almost at will. Those properties make them a weapon-of-choice to further use light to sneak peek at nature's clockwork and build machines that exploit some of nature's most exotic tricks.

A good metric to grasp the rapid developments made by cQED is the coherence time of superconducting qubits, the characteristic time after which quantum features of the

qubit are lost to the environment. They increased by nearly 6 orders of magnitude from the 1999 Cooper-pair box ([23]) to the 2018 fluxonium by L. Nguyen *et at* ([24]). These increased coherence times combined with the improvement of control and coupling of qubits enable nearly $10^4$ gates to be performed before an error occurs. These advances make superconducting circuits one of the leading platforms to implement universal quantum computing. In this thesis, we built a cQED device that we used to realize two experiments: a sequential measurement of a transmon qubit and the remote state preparation of a flying wavepacket, bearing in mind the long term goal to use it to build a network of microwave quantum nodes.

### 2.1.1 *Microwave resonators*

The historical idea behind CQED is that traveling light cannot interact strongly with a local system such as an atom as it flies by too rapidly. But light contained in a stationary mode, for example bouncing back and forth between two mirrors of a Fabry-Perot cavity, can interact much more strongly with an atom lying inside the cavity. An illustrative way to view this is to consider that for a cavity of quality factor Q, photons inside that cavity bounce on average Q times, thus interact Q times with an atom inside the cavity. This problem comes from the small natural coupling of atom to light and is alleviated in engineered system such as superconducting circuits, quantum dots and spins in solid state systems.

In this work we manipulate microwave light whose frequency is in the GHz range. The equivalent of the Fabry-Perot cavity is the 3D microwave cavity: a box made of ideally lossless conducting walls. This impose boundary conditions for the Maxwell's equations inside of the cavity as described by the London model of superconductivity. The tangent component of the electric field and the normal component of the magnetic field relative to the surface must be null on the inner surfaces of the cavity. For a rectangular cavity of dimensions $d_x$, $d_y$ and $d_z$, the resonant frequencies of the $\mathrm{TE}_{mnl}$ and the $\mathrm{TM}_{mnl}$ modes are ([1])

$$f_{mnl} = \frac{c}{2}\sqrt{\left(\frac{m}{d_x}\right)^2 + \left(\frac{n}{d_y}\right)^2 + \left(\frac{l}{d_z}\right)^2} \tag{2.1}$$

where $m$,$n$ and $l$ correspond to the number of maxima of amplitude either for the electric field (TE modes) or magnetic field (TM modes) along the $x$,$y$ and $z$ directions. A rectangular cavity can also be seen as a finite length rectangular waveguide. The approach to microwave resonators that we present here aims at emphasizing that microwave resonators can always be seen as segments of a waveguide delimited by impedance ruptures. This perspective is useful to understand the so called *post cavity* also largely used in microwave cQED ([25]) because they can be made with a high quality factor. The latter is equivalent to a coaxial waveguide shorted at one end and open at the other. Hence, the wavelength $\lambda$ of the first resonant mode of a cylindrical post cavity is equal to $4l$, with $l$ the length of the post as displayed in Fig. 2.1.

I

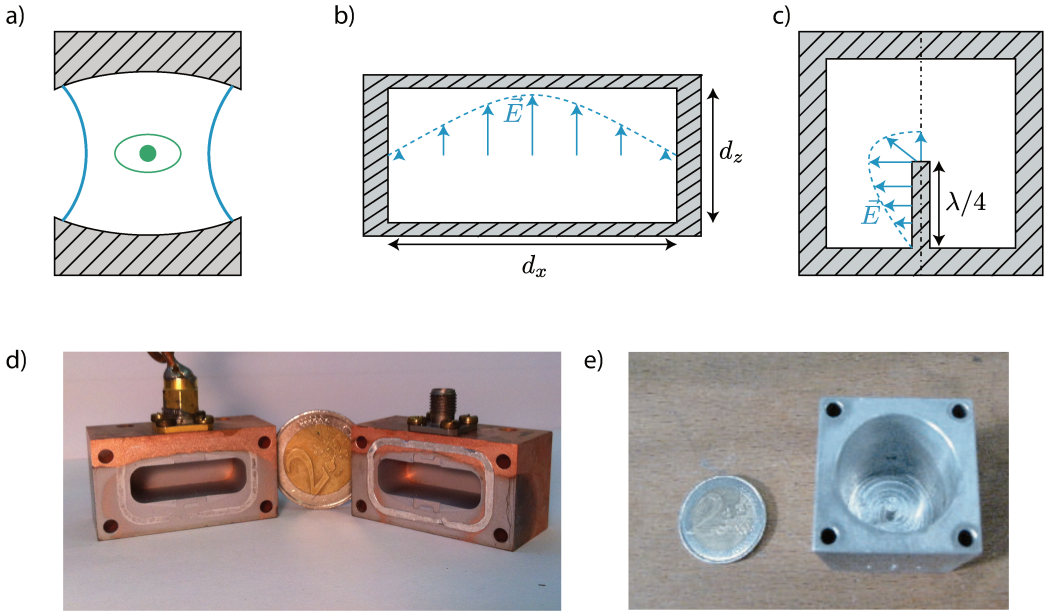


Figure 2.1: a) Scheme of a CQED experiment ([26]) where a Fabry-Perot cavity confines light in a standing wave, whose contour is depicted in blue, to increase the interaction with a flying Rydberg atom (in green). b) Lateral cut of a rectangular microwave cavity. The profile of the electric field of the $TE_{110}$ mode is depicted in blue. c) Lateral cut of a cylindrical post microwave cavity. The profile of the electric of the $\lambda/4$ mode is depicted in blue. d) Picture of an open rectangular cavity in copper plated with lead made in this thesis. The frequency of its $TE_{110}$ mode is $f_{110} \simeq 8$ GHz. e) Top view of a high Q cylindrical post microwave cavity in aluminium made in this thesis. The quality factor of the $\lambda/4$ mode is $Q = 6 \times 10^6$.

3D microwave cavities are easy to design individually and have great quality factors, but they tend to be very cumbersome when assembling multiple devices together. One can get around this limitation by using 2D microwave resonators instead. The coplanar waveguide (CPW) architecture allows one to confine charges and currents in a 2D plane. CPW is made by a central strip of conductor separated from a ground plane by a gap on each side. The conductors and ground planes are deposited on a silicon or sapphire substrate, chosen for their small loss factor $\tan\delta$ ([27]). The substrate contains most of the electric field due to its large electric permittivity $\epsilon_r \simeq 10$. CPW can be modeled in a simple transmission line model, with the impedance defined by the transverse dimensions of the central conductor and gap. The transmission line model explains how CPW can constitute a waveguide. Hence impedance ruptures along the line can define a standing wave, either $\lambda/2$ or $\lambda/4$ resonators depending on the boundary conditions imposed by the impedance ruptures at both ends ([1]). Fig. 2.2 summarizes this analogy. Provided that the substrate height is large compared to the gap width (such that there is no edge effect) the effective electric permittivity of the CPW is $\epsilon_{\text{eff}} = (1 + \epsilon_r)/2$. Hence the frequency of the resonator $f$ is given by $f = \frac{2c}{\lambda\sqrt{\epsilon_{\text{eff}}}}$. There is no simple

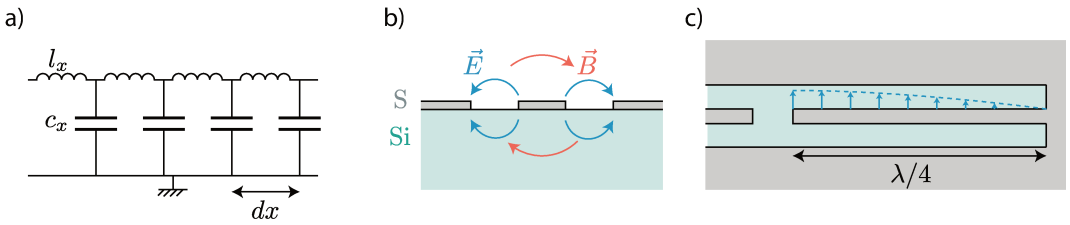


Figure 2.2: a) Transmission line model where each small length $dx$ of the transmission line is modeled by an inductor $l_x$ and a capacitor $c_x$. The impedance of this transmission line is thus $Z = \sqrt{\frac{l_x}{c_x}}$. b) Side view of a CPW transmission line with the electric field in blue and the magnetic field in red. A superconducting layer denoted as S is deposited on top of an insulating substrate (here Si). c) Top view of a CPW $\lambda/4$ resonator with the electric field profile in blue.

expression for the impedance of CPW transmission line but many numerical tools can be used (such as microwave101).

We can map our distributed model of those resonators, either 3D or 2D, onto the simple lumped LC resonator. In an LC oscillator the energy goes back and forth from the inductor to the capacitor, similarly to the classical pendulum where the energy switches from kinetic to potential. Owing to this analogy, we will arbitrarily treat in the following the energy in the inductor as kinetic and the energy in the capacitor as potential. The time dependent energy for each of these element is defined from the current and voltage

$$E(t) = \int_{-\infty}^{t} dt' V(t') I(t'). \tag{2.2}$$

We also define the flux $\Phi$ in the inductor and the charge $Q$ of the capacitor from this

$$\Phi(t) = \int_{-\infty}^{t} dt' V(t') \mathcal{Q}(t) = \int_{-\infty}^{t} dt' I(t'). \tag{2.3}$$

The Lagrangian of the LC oscillator hence reads

$$\mathcal{L} = \frac{Q^2}{2C} - \frac{\Phi^2}{2L}, \tag{2.4}$$

which leads to the Hamiltonian

$$H = Q\dot{\Phi} - \mathcal{L} = \frac{Q^2}{2C} + \frac{\Phi^2}{2L} \tag{2.5}$$

as expected for an electrical LC circuit. This is analogous to a mechanical oscillator of mass $m = C$ and frequency $\omega = \frac{1}{\sqrt{LC}}$.

We can now consider the circuit in the quantum formalism by treating the two variables $\Phi$ and $Q$ as quantum operators ([28]). We will omit all hats in the following. They obey the commutation relation $[\Phi, Q] = i\hbar$. The Hamiltonian can hence be diagonalized

$$H = \hbar\omega(a^\dagger a + \frac{1}{2}) \tag{2.6}$$

where $a$ is defined as

$$\begin{cases} a &= \frac{1}{\sqrt{2\hbar\omega L}}\Phi + \frac{i}{\sqrt{2\hbar\omega C}}Q \\ a^\dagger &= \frac{1}{\sqrt{2\hbar\omega L}}\Phi - \frac{i}{\sqrt{2\hbar\omega C}}Q \\ \left[a, a^\dagger\right] &= 1 \end{cases} \tag{2.7}$$

The operator $a$ is the annihilation operator and we also define the photon number operator $N = a^\dagger a$ that counts the number of photons in the system (see [29] for more details). The eigenvalues of the photon number operator are integers thus leading to equally spaced energy levels (Fig 2.3b) ).

Symmetrically, we can rewrite the charge and flux operator as a function of the annihilation operator

$$\begin{cases} \Phi &= \Phi_{\text{zpf}}(a + a^\dagger) \\ Q &= -iQ_{\text{zpf}}(a - a^\dagger) \end{cases}, \tag{2.8}$$

where the zero-point fluctuation flux and charge can be written as a function of the impedance $Z = \sqrt{\frac{L}{C}}$

$$\begin{cases} \Phi_{\text{zpf}} &= \sqrt{\frac{\hbar Z}{2}} \\ Q_{\text{zpf}} &= \sqrt{\frac{\hbar}{2Z}} \end{cases}. \tag{2.9}$$

It is also useful to define the reduced flux $\varphi = \Phi/\varphi_0$ and the reduced charge $n = Q/(2e)$ where $e$ is the charge of the electron, $\varphi_0 = \hbar/2e$ is the superconducting magnetic flux quantum. Hence $n$ corresponds to the number of excess Cooper pairs on one side of the capacitor and $\varphi$ is the gauge invariant phase of the inductor. The Hamiltonian now reads

$$H = 4E_C n^2 + \frac{1}{2}E_L\varphi^2 \tag{2.10}$$

where $E_C = e^2/(2C)$ is the energy required to add one electron on one side of the capacitor and $E_L = \varphi_0^2/L$ is the inductive energy. We remark that $\omega = \sqrt{8E_L E_C}/\hbar$ and $[\varphi, n] = i$. We can also define the zero-point fluctuation of $n$ and $\varphi$

$$\begin{cases} \varphi_{\text{zpf}} &= \left(\frac{2E_C}{E_L}\right)^{1/4} \\ n_{\text{zpf}} &= \left(\frac{E_L}{32E_C}\right)^{1/4} \end{cases} \tag{2.11}$$

### 2.1.2 *Transmon qubit*

Controlling a microwave resonator with commercially available microwave sources and detectors limits the accessible states to coherent states. To prepare other states, we need a non linear element: the Josephson junction. Josephson junctions are central to superconducting circuits because they are lossless non linear elements. They obey the Josephson equations

$$I = I_0 \sin(\varphi), V = \frac{\hbar}{2e}\dot{\varphi}, \tag{2.12}$$

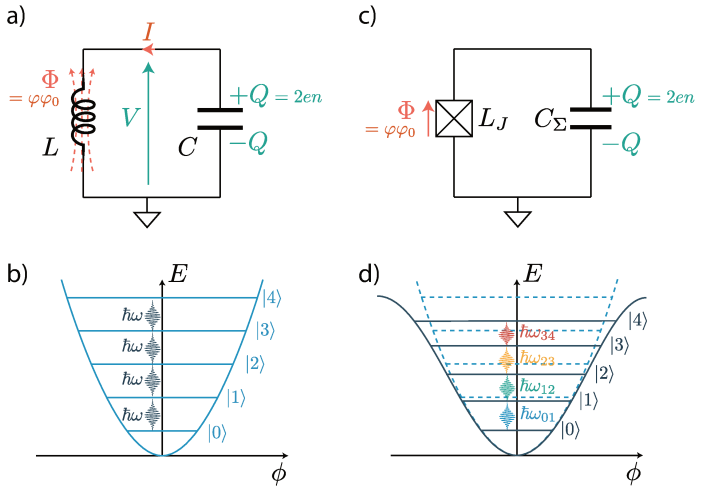


Figure 2.3: a) Scheme of an LC oscillator. During an oscillating cycle the energy of the oscillator goes from being stored as flux in the inductor to being stored as charge difference across the capacitor. b) Energy spectrum of an LC harmonic oscillator. The energy levels are equally spaced by $\hbar\omega$. c) Scheme of a Cooper pair box oscillator. The Josephson junction is substituted to the inductor of an LC oscillator, and corresponds to the equivalent inductance $L_J$. d) Energy spectrum of a non-linear oscillator where the inductor was replaced by a Josephson junction. The cosine energy potential of the junction induces an increasing drift from the quadratic potential of the harmonic oscillator (in dashed blue). Its energy levels are no longer equally spaced.

where $I_0$ is the critical current of the junction. This characteristic current can be obtained from the Ambegaokar-Baratoff relation ([30]) $I_0 R = \frac{\pi\Delta}{2e}$ where $R$ is the electrical resistance of the junction in the normal state and $\Delta$ the superconducting gap. Empirically $R$ can be estimated from the easily accessible room temperature resistance of the junction $R_{\text{rt}} \simeq 1.1R$.

Replacing the inductor of the LC oscillator by a Josephson junction leads to the modified Hamiltonian

$$H = 4E_C n^2 - E_J \cos(\varphi) \tag{2.13}$$

where $E_J = I_0\varphi_0 \equiv \varphi_0^2/L_J$ defines the equivalent inductor $L_j$ and $E_C = e^2/(2C_\Sigma)$. We took into account the self-capacitance of the junction $C_s$ that modifies the total capacitance of the system $C_\Sigma = C_s + C$.

The Josephson junction can effectively be made tunable by replacing it by a SQUID: a loop of two Josephson junctions biased by an external reduced flux $\varphi_{ext}$. In the case of two identical junctions, the Hamiltonian of a symmetric SQUID is simply $H_{\text{SQUID}} = -E_{J_{\text{SQUID}}} \cos\varphi_{ext} \cos\varphi$, thus equivalent to a single junction of tunable inductance $L_J = L_{\text{SQUID}}/\cos\varphi_{ext}$. In recent years, more elaborated local Josephson circuits have been introduced, among which the *SNAIL* ([31]) which can be seen as a SQUID where one junction has been replaced by a chain of junctions. Under certain condition, it can behave as a 3-wave-mixing dipole element at first order in $\varphi$: $H_{\text{SNAIL}} \simeq E_{3wm}\varphi^3$.

It is also informative to consider the charge state of the Josephson junction $\{|n\rangle, n \in \mathbb{Z}\}$ in order to rewrite the Josephson energy (see [32] for demonstration)

$$-E_J \cos(\varphi) = -\frac{E_J}{2} \sum_n \left( |n+1\rangle\langle n| + |n\rangle\langle n+1| \right). \tag{2.14}$$

Here it is clear that $E_J$ correspond to the tunneling energy of a Cooper pair.

We are describing here the general case of the Cooper-pair box. But its behavior, in particular its sensitivity to charge and flux noise, strongly depends on the ratio $E_J/E_C$. During the last decade the superconducting circuit community has demonstrated that it is much easier to mitigate flux noise than charge noise and hence has converged on the so called *transmon* regime ([33]) where $E_J \geq 40E_C$. To reach this regime, it is common to reduce $E_C$ by using a large shunting capacitor $C$. In this regime, the Josephson energy induces a potential that confines $\varphi$ in the potential well (Fig. 2.3), centered in 0.

Developing the Hamiltonian to the $2^{\text{nd}}$ order in $\varphi$ around 0 yields the Hamiltonian of a harmonic oscillator $H = 4E_C n^2 + \frac{1}{2}E_J\varphi^2$ up to a constant offset $-E_J$ that we will omit in the following. Fig. 2.3c) illustrate this analogy. We want to treat this nonlinear system as a deviation from its linear counterpart. To do so, we rearrange the Hamiltonian

$$H = \underbrace{4E_C n^2 - \frac{E_J}{2}\varphi^2}_{\text{harmonic part}} \quad \underbrace{-E_J\left(\cos(\varphi) + \frac{\varphi^2}{2} - 1\right)}_{\text{anharmonic perturbation}} \tag{2.15}$$

This system has non equally spaced energy levels and provided that the decoherence rate are small enough compared to this energy variation, it allows one to address selectively each of those transitions. Moreover one can build a two-level system (qubit) by restraining one-self to the first two levels of the energy ladder. More precisely, developing the Hamiltonian up to the $4^{\text{th}}$ order in $\varphi$ and using the same notation as for LC oscillator (while substituting $L_J$ to $L$) we obtain

$$H = \hbar\omega a^\dagger a - \hbar\frac{\alpha}{2} a^\dagger a^\dagger a a \tag{2.16}$$

where the anharmonicity $\alpha = \omega_{01} - \omega_{12} = E_C/\hbar$. This anharmonicity quantifies by how much the transition frequency is reduced as we climb the energy ladder of the transmon. Hence the anharmonicity of a transmon can not be made arbitrarily large and is usually in the range $100 - 300$ MHz.

Fig. 2.4 displays several examples of superconducting circuits made during this thesis. We provide here the reader with some orders of magnitude. The dimension of the chips used in this thesis are $8.12 \times 8.67 \times 0.29$ mm$^3$. They are made of silicon of resistivity $\rho > 10$ k$\Omega$.cm and held in a PCB and cooled in a BlueFors dilution refrigerator to 25 mK. Junctions of transmons have inductances of the order of 10 nH corresponding to a room temperature resistance of 10 k$\Omega$, a junction size of $100 \times 200$ nm and anharmonicity of $100 - 160$ MHz. Qubit and resonator frequencies range from 3 to 12 GHz. Josephson junctions of weakly anharmonic systems, such as the Josephson Ring modulator (see below) have inductances of 100 pH. Unless specified otherwise, resonators and transmission lines have an impedance of 50 $\Omega$. This impedance corresponds to a gap /

core conductor width of 50 / 84 $\mu$m for on chip lines and resonators, and 200 / 300 $\mu$m for ports and PCB lines.

### 2.1.3 *Josephson Ring Modulator and Josephson Parametric Converter*

Josephson junctions are used in a large variety of circuits. We present here one of them: the Josephson Ring Modulator (JRM) ([34]). With the transmon qubit, they are the 2 non-linear elements that we use in this work. The JRM can be used for a wide range of purposes, such as a quantum-limited amplifier ([35, 36]), a new kind of multi-qubits device called the Trimon ([37]) or a parametric coupler ([38]). Our group studied this device in depth ([5, 6]) and we present here only a brief introduction to its behavior in order to arm the reader with sufficient knowledge to understand the usage of the JRM that we did in this work.

The JRM is made of a ring of 4 identical Josephson junctions with inductance $L_J$ and, in this work, will always be shunted by 4 linear inductors $L$. Here, we show how, thanks to its symmetry, the Hamiltonian of this device can be written in a compact form using 3 eigenmodes. In a second time, the JRM will be connected to 4 LC circuits respecting the symmetry of those eigenmodes to form the Josephson Parametric Converter (JPC).

The circuit Hamiltonian reads

$$\begin{aligned} H_{\text{ring}} &= -E_J\left(\cos\varphi_a + \cos\varphi_b + \cos\varphi_c + \cos\varphi_d\right) \\ &\quad + \tfrac{E_L}{2}\left(\varphi_\alpha^2 + \varphi_\beta^2 + \varphi_\gamma^2 + \varphi_\delta^2\right) \end{aligned} \tag{2.17}$$

with notations analogous to previous ones, see Fig. 2.5.

We remark that the current across the inductances is $\varphi_0\varphi/L$. Hence, using the conservation law of the current at the central node of the circuit leads to

$$\varphi_\alpha + \varphi_\beta + \varphi_\gamma + \varphi_\delta = 0 \tag{2.18}$$

and following Faraday's law in each sub-loop

$$\begin{cases} \varphi_a + \varphi_\alpha - \varphi_\delta &= \frac{\varphi_{ext}}{4} + 2n_a\pi \\ \varphi_b + \varphi_\beta - \varphi_\alpha &= \frac{\varphi_{ext}}{4} + 2n_b\pi \\ \varphi_c + \varphi_\gamma - \varphi_\beta &= \frac{\varphi_{ext}}{4} + 2n_c\pi \\ \varphi_d + \varphi_\delta - \varphi_\gamma &= \frac{\varphi_{ext}}{4} + 2n_d\pi \end{cases}, \tag{2.19}$$

where $\varphi_{ext}$ is the reduced flux across the whole device and $n_i$ is the number of flux quanta in each sub loop.

While $4E_J\cos\frac{\varphi_{ext}}{4} > -E_L$ the system remains in a symmetric configuration where the fluxes across each sub loop are identical (see [5] for details). The other case is out of the scope of this thesis despite being of interest for the rich Hamiltonian it produces.

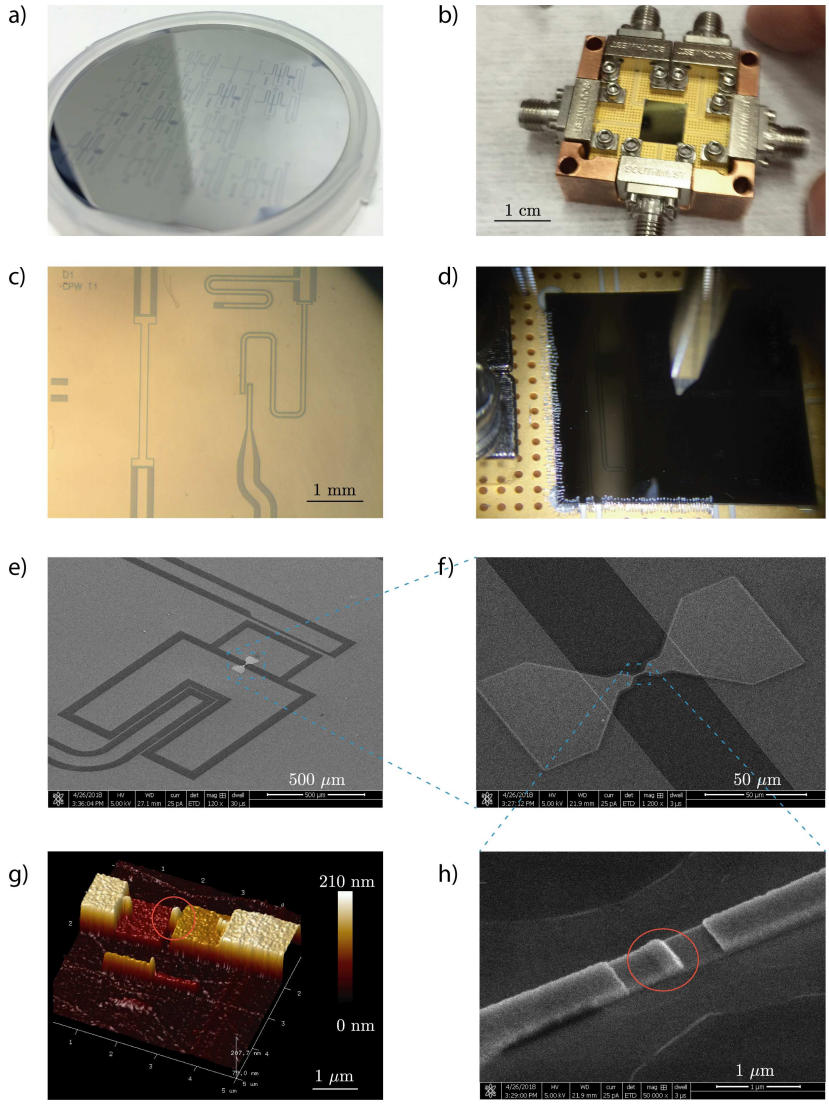


Figure 2.4: a) Photograph of a 2" silicon wafer sputtered with niobium featuring 18 chips optically lithographed and awaiting to be diced. b) Photograph of a niobium on silicon chip mounted on a PCB. The PCB is equipped with SMA to CPW Southwest launcher for further wiring. It is held in a copper sample holder. c) Photograph of a niobium on silicon chip with two CPW $\lambda/2$ resonators used for calibration of simulations. On the left side, a 10 GHz resonator is connected to 2 ports for transmission measurements. On the right side, a 7 GHz resonator is also connected for transmission measurements. The top port also features a stub filter. d) Photograph of a chip being wirebonded to the PCB. Aluminium wirebonds ensure electrical conduction between the chip and the PCB. e), f) and h) e-beam images of a transmon qubit in niobium on silicon. The 2 large pads on e) dominate the capacitance of the transmon. It is connected on both sides to CPW resonators. The larger pad on the right side is used to ensure sufficient coupling to the resonator. The whiter element in the middle is the Al/AlOx/Al Josephson junction, enlarged in f) and h). h) shows the Josephson junction (circled in red). The silicon lighter part is due to ion milling prior to the Al deposition and is delimited by a small resist left-over (also visible in the top and bottom of g). g) Atomic force microscope image of a 10 nH Josephson junction used for another transmon. The junction is circled in red. The bottom island is an artefact of the modified Dolan bridge geometry developed in this thesis.

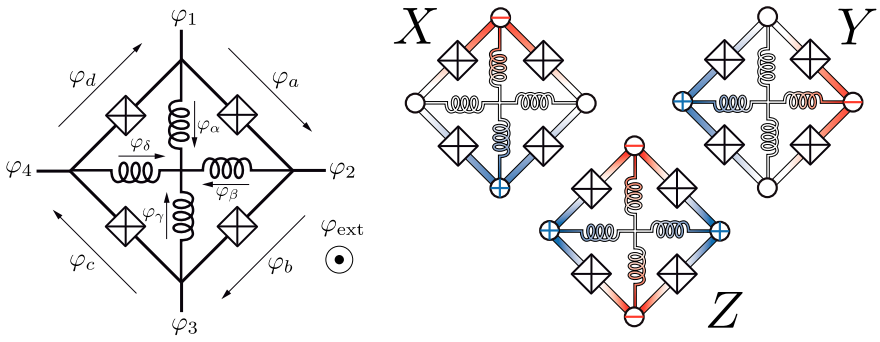


Figure 2.5: Scheme of the shunted Josephson Ring Modulator (JRM) made of 4 identical Josephson junctions shunted by 4 linear inductors. The ring symmetry induces 3 eigenmodes displayed on the left (fig. reproduced from [5]).

We introduce the following notations (see Fig. 2.5)

$$\begin{cases} \varphi_X &= \varphi_3 - \varphi_1 \\ \varphi_Y &= \varphi_4 - \varphi_2 \\ \varphi_Z &= \frac{1}{2}\left(\varphi_2 + \varphi_4 - \varphi_3 - \varphi_1\right) \end{cases}, \tag{2.20}$$

which leads to write the system's Hamiltonian in the compact way

$$\begin{aligned} H_{\text{ring}} &= -4E_J \cos\tfrac{\varphi_{ext}}{4} \cos\tfrac{\varphi_X}{2} \cos\tfrac{\varphi_Y}{2} \cos\varphi_Z \\ &\quad -4E_J \sin\tfrac{\varphi_{ext}}{4} \sin\tfrac{\varphi_X}{2} \sin\tfrac{\varphi_Y}{2} \sin\varphi_Z \\ &\quad +\tfrac{1}{4}E_L\left(\varphi_X^2 + \varphi_Y^2 + 2\varphi_Z^2\right) \end{aligned} . \tag{2.21}$$

Developing this Hamiltonian to the second order in $\varphi_X$, $\varphi_Y$ and $\varphi_Z$ leads to

$$\begin{aligned} H_{\text{ring}} &= -4E_J \cos\tfrac{\varphi_{ext}}{4} \\ &\quad +\tfrac{1}{2}\left(\tfrac{E_L}{2} + E_J \cos\tfrac{\varphi_{ext}}{4}\right)\left(\varphi_X^2 + \varphi_Y^2\right) \\ &\quad +\tfrac{1}{2}\left(E_L + 4E_J \cos\tfrac{\varphi_{ext}}{4}\right)\varphi_Z^2 \\ &\quad -E_J \sin\left(\tfrac{\varphi_{ext}}{4}\right)\varphi_X\varphi_Y\varphi_Z \\ &\quad +O(|\varphi|^4). \end{aligned} \tag{2.22}$$

The first term is a flux dependent energy offset. The second and third term are flux dependent inductances for each eigenmode and the last one is a three-wave-mixing term. For each eigenmode, the JRM is equivalent to the following inductance

$$\begin{cases} L_{X,Y} &= \frac{\varphi_0^2}{\frac{E_L}{2} + E_J \cos\frac{\varphi_{ext}}{4}} \\ L_Z &= \frac{\varphi_0^2}{E_L + 4E_J \cos\frac{\varphi_{ext}}{4}} \end{cases} . \tag{2.23}$$

The symmetry breaking corresponds to $L_Z < 0$ in this expression.

To exploit the JRM, we combine it with LC oscillators, connected according to the ring symmetry as displayed in Fig 2.6. The whole device constitutes the JPC. We accept that the eigenmodes of the JRM, which can be seen as eigenmodes of the equivalent

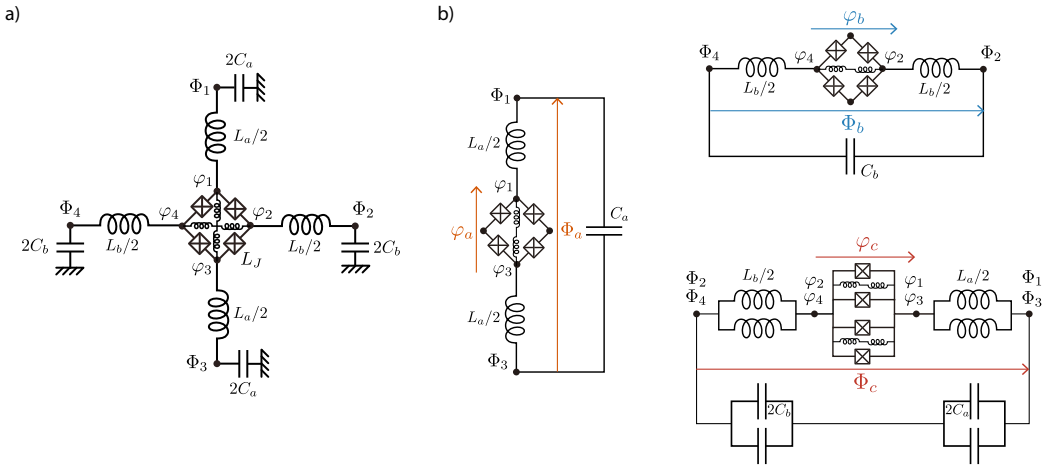


Figure 2.6: a) Equivalent electrical circuit of the JPC. The 4 added LC resonators respect the axial and central symmetries of the JRM eigenmodes. b) Equivalent circuit for each eigenmode of the JPC. In each of those equivalent circuits, the JRM can be replaced by the flux dependent equivalent inductor as defined previously to retrieve the frequency of the mode (fig. reproduced from [5]).

inductance matrix of the JRM, enforce the same geometry for the JPC's eigenmodes. We label a, b and c the modes of the JPC corresponding to the JRM modes X, Y and Z respectively.

The total inductance of each of mode is

$$\begin{cases} L_a^{tot}(\varphi_{ext}) &= L_a + L_X(\varphi_{ext}) \\ L_b^{tot}(\varphi_{ext}) &= L_b + L_Y(\varphi_{ext}) \\ L_c^{tot}(\varphi_{ext}) &= \frac{L_a+L_b}{4} + L_Z(\varphi_{ext}) \end{cases} \tag{2.24}$$

which leads to the frequencies, in the limit $L_i \gg L_{X,Y,Z}$,

$$\omega_i(\varphi_{ext}) = \frac{1}{\sqrt{L_i^{tot}(\varphi_{ext})C_i}} \approx \omega_i^0(1 - \frac{1}{2}\xi_i^{tot}(\varphi_{ext})) \tag{2.25}$$

with $i \in \{a, b, c\}$, $C_c = \frac{4C_aC_b}{C_a+C_b}$, $\omega_i^0 = \frac{1}{\sqrt{L_iC_i}}$ and the participation ratios defined as

$$\begin{cases} \xi_a^{tot}(\varphi_{ext}) &\equiv \frac{\varphi_0\varphi_a}{\Phi_a} = \frac{L_X(\varphi_{ext})}{L_a^{tot}(\varphi_{ext})} \\ \xi_b^{tot}(\varphi_{ext}) &\equiv \frac{\varphi_0\varphi_b}{\Phi_b} = \frac{L_Y(\varphi_{ext})}{L_b^{tot}(\varphi_{ext})} \\ \xi_c^{tot}(\varphi_{ext}) &\equiv \frac{\varphi_0\varphi_c}{\Phi_c} = \frac{L_Z(\varphi_{ext})}{L_c^{tot}(\varphi_{ext})} \end{cases} \tag{2.26}$$

The participation ratio of a mode $i$ should be understood as the ratio of the inductive energy contained in the JRM over the total inductive energy of the mode. It characterizes how the non-linearity of the JRM influences each mode of the device.

Similarly to the harmonic oscillator, we define the annihilation operators

$$\begin{cases} \Phi_a &= \sqrt{\frac{\hbar Z_a}{2}}(a+a^\dagger) \\ \Phi_b &= \sqrt{\frac{\hbar Z_b}{2}}(b+b^\dagger) \\ \Phi_c &= \sqrt{\frac{\hbar Z_c}{2}}(c+c^\dagger) \end{cases} . \tag{2.27}$$

with the mode impedances $Z_i = \sqrt{L_i^{tot}/C_i}$.

Developing the Hamiltonian to the 4$^{\text{th}}$ order leads to the total Hamiltonian

$$\begin{aligned} H_{\text{JPC}}(\varphi_{ext}) &= \textstyle\sum_{\lambda\in\{a,b,c\}} \hbar\omega_\lambda(\varphi_{ext})\lambda^\dagger\lambda \\ &\quad +\hbar g \sin\left(\tfrac{\varphi_{ext}}{4}\right) \textstyle\prod_{\lambda\in\{a,b,c\}}(\lambda+\lambda^\dagger) \\ &\quad +\hbar \cos\left(\tfrac{\varphi_{ext}}{4}\right) \textstyle\sum_{\lambda,\nu\in\{a,b,c\}} \frac{K_{\lambda\nu}}{2}\lambda^\dagger\lambda\nu^\dagger\nu. \end{aligned} \tag{2.28}$$

where the first line contains the flux dependent frequencies, the second line is the 3 wave-mixing term and the third line is the self and cross Kerr term (power dependent frequency shift). The value of the Kerr terms $K_{ij}$ can be found in [5] and

$$g = \frac{1}{2}\sqrt{\frac{\xi_a\xi_b\xi_c\omega_a\omega_b\omega_c}{2E_{JRM}/\hbar}} \tag{2.29}$$

where $E_{JRM} = \varphi_0^2\frac{L_J^2}{L_X L_Y L_Z}$.

It is important to remark that the external flux $\varphi_{ext}$ controls this Hamiltonian and can be set by an external flux bias. For example $\varphi_{ext} = 0$ cancels the 3-wave-mixing while maximizing the Kerr terms whereas $\varphi_{ext} = 2\pi$ cancels the Kerr terms while maximizing the 3-wave-mixing. In the experiment conducted in this thesis, we will extensively use the 3-wave-mixing while avoiding Kerr distortion thus working near $\varphi_{ext} = 2\pi$. Furthermore, one can see that the 3-wave-mixing depends on the participation ratio of each mode and we will exploit that later on. Fig. 2.7 displays examples of JRM made during this thesis. The JRMs mostly used in this thesis have linear shunt inductances and their Josephson junctions are estimated to have $L_J \simeq 0.1$ nH while the shunting inductances are $L \simeq 30$ nH.

## 2.2 INTERACTING NONLINEAR CIRCUITS

The approach we used to determine the Hamiltonian of the JPC exploited the ring symmetry of the device and is not general in the sense that it does not cover the case of a ring with asymetric junctions nor the case of sub-loop dependent flux bias. A recent method (open source QuCAT python library [39]) enables Hamiltonian design of Josephson circuit from a symbolic definition of the device. This method consists in numerically diagonalizing the Hamiltonian, finding its minimum and then developing it around that minimum to retrieve the interaction Hamiltonian. As this method is posterior to the design of the chip used in this work and does not yet take into account the superconducting loops, we will not detail it. Instead we present here a standard

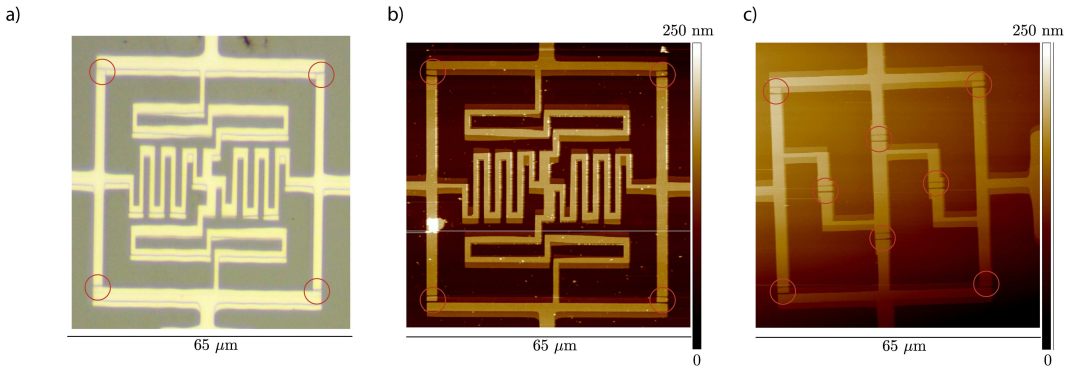


Figure 2.7: a) Microscope image of the JRM made in Al/AlOx/Al on silicon used in this thesis. The Josephson junctions are circled in red. b) AFM topography of the same JRM highlighting the junctions and the three heights due to the two steps of aluminium angle evaporation in the fabrication process. c) AFM topography of a JRM where the shunting inductances were replaced by large Josephson junctions in order to make the JRM smaller with less parasitic inductances. This design was abandoned as the shunting junctions induced unwanted non-linearity. One could reduce this effect by using a chain of larger junctions but this option was not investigated here.

perturbation approach called the Black Box Quantization (BBQ) that is particularly useful to understand the transmon to resonator coupling and how harmonic resonators can inherit part of the anharmonicity of a Josephson junction when placed in its vicinity. We will conclude by looking into Hamiltonian engineering through the application of microwave drives and exemplify it with two use-cases of the JPC.

### 2.2.1 *Black box quantization and driven hamiltonian*

The BBQ was developed at Yale by Nigg *et al.* ([40]) and further generalized ([41], [42]) to treat the case of complex environments. This method is a perturbative approach that considers the system of $M$ LC resonators in series coupled to a Josephson junction. Bare in mind that the LC elements do not necessarily correspond to any physical element but rather are such that their eigenmodes correspond to those of the actual system in which the Josephson junction is replaced by a linear inductor accordingly. This method can include the losses of each mode by adding resistors.

The method consists in doing a Foster decomposition of the environment seen by the non-linear part of the junction. Hence we start by including the capacitance and the equivalent inductance of the junction in the environment. Then we proceed with the Foster decomposition of the impedance of that total environment

$$Z(\omega) = \sum_{p=1}^{M} (j\omega C_p + \frac{1}{j\omega L_p} + \frac{1}{R_p})^{-1} \tag{2.30}$$

which leads to the following Hamiltonian, when neglecting the losses,

$$H_{\text{linear}} = \sum_{p=1}^{M} \hbar\omega_p a_p^\dagger a_p \tag{2.31}$$

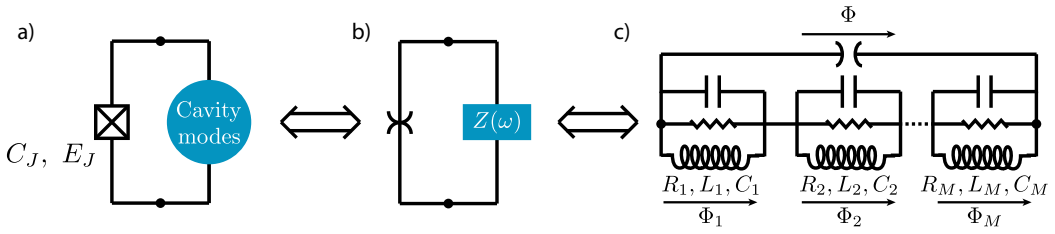


Figure 2.8: a) Scheme of a Josephson junction coupled to a set of harmonic oscillators. b) The Josephson junction is stripped of its linear part and represented by a spider element. The capacitance and the inductance of the junction are included in the set of resonators, treated here as a total impedance $Z(\omega)$. c) The total impedance is then replaced by its pole decomposition $Z(\omega) = \sum_{p=1}^{M}(j\omega C_p + \frac{1}{j\omega L_p} + \frac{1}{R_p})^{-1}$.

with notation analogous to the LC oscillator case. This description provides the flux across the non linear part of the junction $\Phi = \sum_{p=1}^{M} \Phi_p$ which in turn can be reinjected into the non-linear part of the Hamiltonian 2.15. We assume here that we are in the weak coupling regime meaning that the coupling rate to the non-linearity is small compared to the mode frequencies, such that we can apply the Rotating Wave Approximation (RWA) in order to neglect the non-resonant terms of the Hamiltonian. Hence the Hamiltonian of the junction (developed at the $4^{\text{th}}$ order) leads to

$$H_{4^{\text{th}}\text{order}} = \sum_p \hbar\Delta_p N_p + \frac{1}{2}\sum_{p,p'} \hbar\chi_{pp'} N_p N_{p'} \tag{2.32}$$

with, as before, $N_p = a_p^\dagger a_p$. And the expressions of the Lamb-shift $\Delta_p$, the self-Kerr $\chi_{pp}$ and the cross-Kerr $\chi_{pp'}$ read

$$\begin{cases} \hbar\Delta_p &= -\frac{e^2}{2L_J}\left(Z_p \sum_{p'} Z_{p'} - \frac{Z_p^2}{2}\right) \\ \hbar\chi_{pp} &= -\frac{C_\Sigma}{L_J} E_C Z_p^2 \\ \chi_{pp'} &= -2\sqrt{\chi_{pp}\chi_{p'p'}} \end{cases} \tag{2.33}$$

where $C_\Sigma$ is the capacitance of the transmon. Finally the quality factor of the mode p is given by the zeros of the admittance following

$$Q_p = \frac{\omega_p \text{Im } Y'(\omega_p)}{2\text{Re } Y(\omega_p)}. \tag{2.34}$$

This perturbative approach shows several important results. First, the Lamb-sift means that the introduction of the non-linearity induces a frequency shift for each mode due to the presence of all the others. Then this coupling induces a spread of losses over all modes. In a way, equation 2.34 can be seen as each mode driving all others at its resonant frequency and hence inheriting their loss channels.

Another point of view on the BBQ perturbation method, useful for numerical simulation, consists in solving the linear part of the problem to retrieve the eigenmodes of the device. Then the flux across the junction can be decomposed as before on this basis with $\Phi = \sum_{p=1}^{M} \varphi_{\text{zpf},p}(a_p + a_p^\dagger)$. Every quantity we want to compute can then be obtained from the list $\{\varphi_{\text{zpf},p}\}$.

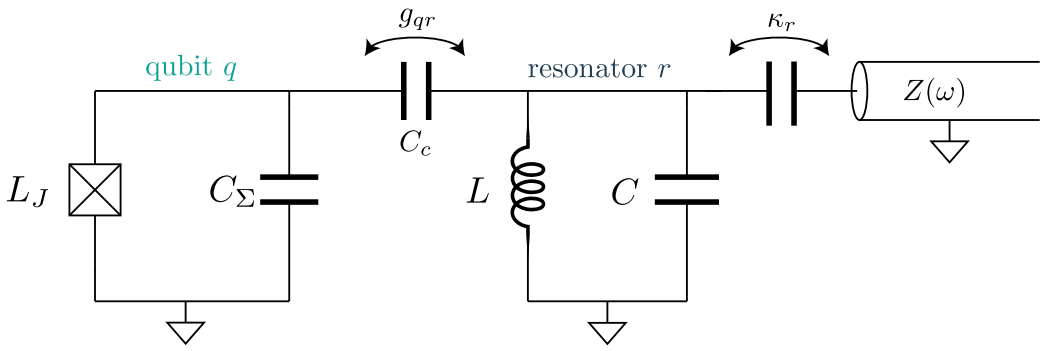


Figure 2.9: Schematic of a transmon qubit ($q$) capacitively coupled to a harmonic resonator ($r$) at a rate $g$. The resonator is itself coupled to a transmission line at a rate $\kappa_r$. In the dispersive regime ($\Delta \gg g_{qr}$) the coupling slightly modifies each mode as described by the BBQ formalism.

$$H_{\text{junction}} = E_J \left( -\sum_p \frac{\varphi_{\text{zpf},p}^2}{2} N_p + \sum_{p,p'} \frac{\varphi_{\text{zpf},p}^2 \varphi_{\text{zpf},p'}^2}{48} N_p N_{p'} \right). \tag{2.35}$$

Hence, one can access the $\varphi_{\text{zpf},p}$ by monitoring the ratio of inductive energy stored in the junction versus the total inductive energy of that mode. In particular, $\varphi_{\text{zpf},p}$ for the weakly anharmonic modes can be numerically estimated by

$$\omega_p = \omega_p^0 \left( 1 - \frac{1}{2} \frac{E_J}{\hbar \omega_p^0} \varphi_{\text{zpf},p}^2 \right). \tag{2.36}$$

In the general case of weakly anharmonic resonators, where the Hamiltonian $H = f(\varphi_{\text{zpf},p}(a_p^\dagger + a_p))$, with $f$ a non linear function, the $\varphi_{\text{zpf},p}$ parameters are obtained by identification of terms in the Taylor expansion of $H$.

This can be applied to estimate the participation ratios defined for each mode of the JPC by noticing that, for example in mode $a$,

$$\omega_a = \omega_a^0 \left( 1 - \frac{1}{2} \frac{E_{L_X}}{\hbar \omega_a^0} \varphi_{\text{zpf},a}^2 \right) = \omega_a^0 \left( 1 - \frac{1}{2} \xi_a^{tot}(\varphi_{ext}) \right) \tag{2.37}$$

thus numerical simulations of the JPC will treat each equivalent circuit of Fig. 2.6 by replacing the JRM by an equivalent inductance and estimate the zero-point fluctuations by computing the frequency shift induced by a small change of this equivalent inductance.

### 2.2.2 *Dispersive coupling of a resonator to a transmon qubit*

We treat here the instructive case of the transmon qubit capacitively coupled to a harmonic LC resonator as depicted in Fig. 2.9. These results will be extensively used throughout this thesis. An in depth study of the transmon coupled to a harmonic resonator was previously done in our group and can be found in [32].

We limit ourselves to the dispersive regime where the coupling rate $g_{rc}$ between the transmon and the resonator is small compared to their frequency detuning $\Delta$. In that case, we can apply the BBQ method to derive the system's Hamiltonian (again developed to the $4^{\text{th}}$ order)

$$H = \hbar\omega_q q^\dagger q + \hbar\omega_r r^\dagger r - \hbar\chi_{qr} q^\dagger q r^\dagger r - \hbar\frac{\alpha}{2} q^{\dagger 2} q^2 + \hbar\frac{K}{2} r^{\dagger 2} r^2 \tag{2.38}$$

where, assuming $C \gg C_c$,

$$\begin{cases} \omega_1 &= \sqrt{8E_J E_{C_\Sigma}}/\hbar \\ \omega_2 &= \frac{1}{\sqrt{LC}} \\ \Delta &= \omega_2 - \omega_1 \\ g_{qr} &= \frac{C_c}{2\sqrt{C(C_\Sigma + C_c)}}\sqrt{\omega_q \omega_r} \\ \omega_q &\simeq \omega_1 - \frac{g_{qr}^2}{\Delta} \\ \omega_r &\simeq \omega_2 + \frac{g_{qr}^2}{\Delta} \end{cases} \tag{2.39}$$

The first two frequencies correspond to the bare frequencies of the transmon and the resonator. In the dispersive regime, the coupling induces a small frequency renormalization described by the latter two. Also,

$$\begin{cases} \alpha &= -\chi_{qq}/\hbar = E_{C_\Sigma}/\hbar & \text{(qubit anharmonicity)} \\ \chi &= -\chi_{qr}/\hbar = \alpha\left(\frac{g_{qr}}{\Delta}\right)^2 & \text{(dispersive shift)} \\ K/2 &= \chi_{rr}/\hbar = -\frac{\chi^2}{\alpha} & \text{(cavity self-Kerr)} \end{cases} \tag{2.40}$$

It is also worthwhile to consider the loss channel induced in the transmon by the resonator coupling to the line, called the Purcell effect ([43])

$$\gamma_{1,Purcell} = \frac{\mathrm{Re}(Y(\omega_q))}{C_\Sigma + C_c} \simeq \kappa_r \frac{g^2}{\Delta^2} \tag{2.41}$$

even though the approximation of the right hand side has been proven to be coarse ([41]). As this decay arises from a leakage of the transmon through the resonator at the transmon frequency, it is possible to strongly mitigate it by filtering the qubit frequency on the resonator port, thus allowing to increase greatly $g$ and $\kappa_r$ without affecting the transmon's lifetime ([12]). In the case of a Purcell filter centered at the resonator's frequency and of quality factor $Q_F$, the Purcell decay rate becomes ([44])

$$\gamma_{1,Purcell-filtered} \simeq \kappa_r \left(\frac{g^2}{\Delta^2}\right)\left(\frac{\omega_q}{2Q_F\Delta}\right). \tag{2.42}$$

To provide the reader with order of magnitudes, in this thesis we used $\Delta \approx 1$ - $-$ 3 GHz, $\alpha \simeq 100$ MHz, $g_{qr} \approx 150$ MHz, $Z_r \simeq 50\ \Omega$, $L_J \simeq 10$ nH, $C_\Sigma \simeq 1$ pF, $\chi = 0.5$ $-$ 2 MHz and $K \simeq 10$ kHz.

Since we only consider the first two levels of the transmon, it is convenient to rewrite the Hamiltonian with the transmon treated as a qubit. To do so, we introduce the Pauli matrix $\sigma_z = \begin{pmatrix} 1 & 0 \\ 0 & -1 \end{pmatrix}$ in the $\{|e\rangle, |g\rangle\}$. Thus

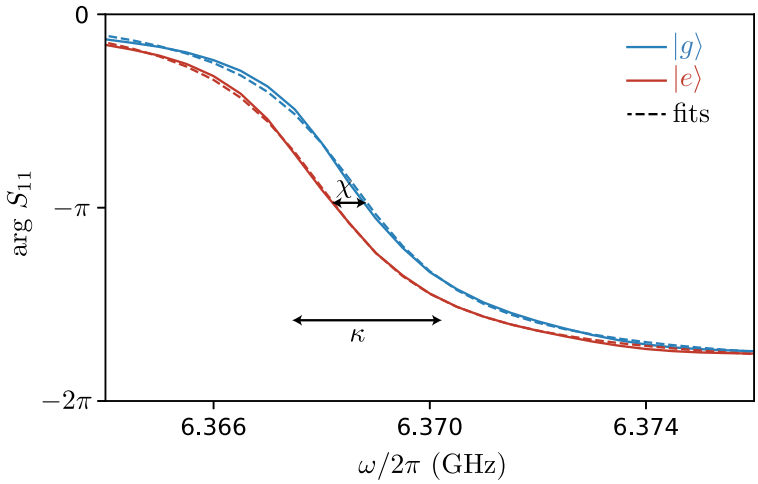


Figure 2.10: Solid lines: Argument of the measured reflection coefficient of the resonator dispersively coupled to a transmon in blue when the qubit is in the ground state and in red for the excited state. Dashed lines: fits using Eq.2.55, with color matching the fitted curve. We obtain $\chi = 0.6$ MHz and $\kappa = 3.3$ MHz. At the average resonance frequency the argument of $S_{11}$ depends on the state of the qubit, hence, measuring the response of the cavity leads to a measurement of the qubit's state.

$$H = \hbar\omega_r r^\dagger r + \hbar\omega_q \frac{\sigma_z}{2} - \hbar\chi \frac{\sigma_z}{2} r^\dagger r. \tag{2.43}$$

From this writing, it appears clearly that the frequency of the resonator is shifted by $+/-\frac{\chi}{2}$ depending on the state of the qubit. Symmetrically, the frequency of the qubit depends on the number of photons in the resonator. The first phenomenon is wildly used as a mean for quantum non-demolition readout of a transmon qubit by a resonator. Indeed, probing the frequency of the resonator leads to quantum non-demolition measurement of the qubit state as shown in Fig. 2.10. This effect is at the core of the experiment of sequential measurement of a transmon reported in this thesis. On the other hand, we will use the transmon to count photons in a resonator in the remote state preparation experiment.

### 2.2.3 *Pumped JPC*

To fully exploit the Hamiltonians created by the previous non-linear elements, it is common to apply a stiff pump in order to promote certain terms of those Hamiltonian. In particular, we treat here two cases used in this thesis exploiting the 3-wave mixing Hamiltonian of the JPC : the conversion and the phase preserving amplification.

In both cases we apply a pump driving off-resonantly the Z mode of the JRM, for the first case at a frequency $\omega_p = |\omega_b - \omega_a|$ and in the second case at a frequency $\omega_p = \omega_a + \omega_b$ as displayed in Fig. 2.11. We remind the 3-wave-mixing Hamiltonian

$$H_{3\text{wm}} = \hbar g(a^\dagger + a)(b^\dagger + b)(c^\dagger + c) \tag{2.44}$$

and we replace $c$ by the off-resonant stiff pump $p$ at a frequency $\omega_p$ treated here as a classical drive, i.e. a complex variable. In the RWA, the only remaining term is

$$\begin{cases} H_\Delta &= \hbar g p a b^\dagger + \text{h.c.} \quad \text{if } \omega_p = |\omega_b - \omega_a| \\ H_\Sigma &= \hbar g p^* a b + \text{h.c.} \quad \text{if } \omega_p = \omega_b + \omega_a \end{cases} . \tag{2.45}$$

The first one correspond to frequency conversion and is used as a tunable coupler ([38]). A photon of the pump is used to provide/retrieve the missing/excess energy to convert a photon of mode $a$ into one of mode $b$. Whereas the second correspond to parametric down conversion, which can be used for phase preserving quantum limited amplification ([45]) or for EPR state generation ([38]). There, a photon of the pump is split into a pair of photons, one in mode $a$ and one in mode $b$.

It is useful to introduce the cooperativity

$$C = \left| \frac{2gp}{\sqrt{\kappa_a \kappa_b}} \right|^2 \tag{2.46}$$

where $\kappa_a$ and $\kappa_b$ are the couplings of mode $a$ and $b$ to the environment. The cooperativity can be seen as the squared ratio of the rate of interaction versus the geometrical average rate of decay. It comes in handy when computing the gain of phase preserving amplification ([5]). We reproduce here the gain $G$ of an JPC used as a quantum limited phase preserving amplifier

$$\sqrt{G} = \frac{1 + C}{1 - C} \tag{2.47}$$

which shows that the gain diverges when the parametric down conversion exactly compensate for losses and this formula breaks down afterward as the system has no stationary state (negative loss rate).

Similarly, one can show that the conversion case corresponds to overcoupled oscillators, in the limit that will be of interest to us $\kappa_b \ll \kappa_a$, boils down to $C > \frac{\kappa_a}{4\kappa_b}$ i.e. $16|gp|^2 > \kappa_a^2$.

In this thesis the pumps will be treated as stiff classical drives as they are largely ($> 1$ GHz) detuned from any resonant mode and hence replenish at a rate much greater than the interaction rate $g$, i.e. the autocorrelation time of the pump is much smaller than $1/g$. Interestingly, as the best of the author's knowledge, the resonant case where the frequency of the oscillators is such that one of the frequency matching is achieved (e.g. $\omega_c = |\omega_a - \omega_b|$) has not been studied yet. It would be interesting to investigate whether there is an optimal detuning such that the pump can still be considered stiff while minimizing the detuning in order to reduced the necessary driving strength.

Substituting some terms of Hamiltonian by a classical stiff pump is a technique widely used throughout cQED. It is valuable to note that it is mainly used with a single Josephson junction as a source of non linearity. An example of choice are the

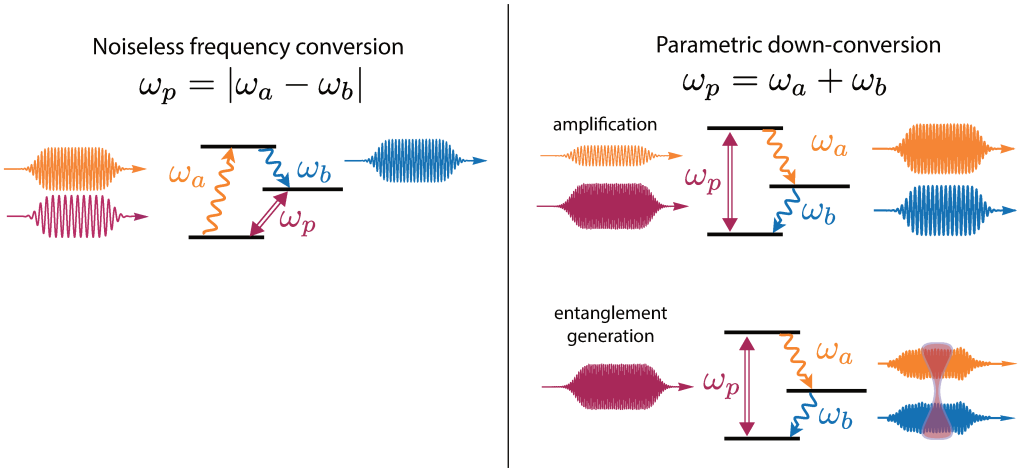


Figure 2.11: Energy ladders illustrating frequency matching condition for the conversion case $\omega_p = |\omega_b - \omega_a|$ and the amplification/EPR case $\omega_p = \omega_a + \omega_b$.

longitudinal coupling engineering experiments ([46, 47]). In those experiments they needed to engineer a coupling Hamiltonian in the form $H = g_l(r + r^\dagger)\frac{\sigma_z}{2}$. One way to explain their experiments is to go back to the developed interaction Hamiltonian of the Josephson junction in the case of a transmon qubit capacitively coupled to a resonator mode $r$, without applying the RWA, (for simplicity of notation, we omit the zpf index to $\varphi_{\text{zpf}}$)

$$H_{\text{int}} = \frac{E_J}{2}\left((\varphi_q(q+q^\dagger) + \varphi_r(r+r^\dagger))^2 - \frac{1}{12}(\varphi_q(q+q^\dagger) + \varphi_r(r+r^\dagger))^4\right) \tag{2.48}$$

where, if we were to apply the RWA, the first term would lead to frequency shift (due to the linear inductor equivalent of the junction) and the second term would lead to the cross-Kerr interaction term, but in no way, without further modification would a third order interaction term arise from this Hamiltonian. Lets now consider a local stiff drive $p$, inducing a flux across the junction such that the total flux across the junction is $\Phi = \varphi_q(q+q^\dagger) + \varphi_r(r+r^\dagger) + \varphi_p(p+p^*)$. Then setting the frequency of this drive to be $\omega_p = \omega_r$ induces the following interaction Hamiltonian, in the RWA, where we omit the expected terms for the resonator, the qubit and their interaction,

$$\begin{aligned} 2H_{\text{int}}/E_J &= \varphi_r\varphi_p p^* r + \text{h.c.} - \tfrac{1}{12}(\varphi_r\varphi_p\varphi_q^2 q^\dagger q p^* r + \varphi_r^2\varphi_p^2 p^{*2} r^2 + \text{h.c.} \\ &\quad + \varphi_r^2\varphi_p^2 p^* p r^\dagger r + \varphi_q^2\varphi_p^2 p^* p q^\dagger q) \end{aligned} \tag{2.49}$$

The first term is a drive by the pump of the resonator through the junction, the second one is the desired interaction and the third one is a squeezing term. The fourth and fifth terms are cross-Kerr terms with the pump. Since the pump is assumed to be stiff, those terms correspond to frequency shifts that can be accounted for and are not limitations of the process.

Since $\varphi_q \gg \varphi_r, \varphi_p$ we can neglect the squeezing and the cross-Kerr pump-resonator. Thus we obtain the desired interaction with a rate $|g_l| = E_J\varphi_r\varphi_p\varphi_q^2|p|/24$ provided that we cancel out the displacement induced by the first term by driving the resonator through another port to compensate and track the qubit frequency accordingly. Bare

in mind that, even though the strength and the phase of the interaction is controlled by the pump $p$, it cannot be made arbitrarily large because of the ionization of the transmon ([48–50]). Nevertheless, this method allows for a wide range of Hamiltonian to be engineered, the main challenge being to achieve sufficient participation ratios such that a reasonable pump strength is required to achieve the desired coupling rate.

Finally, using a single Josephson junction has the limitation that since its Taylor expansion contains possible combinations at all even orders, it always includes Kerr terms. Those can be detrimental to some experiments. This, among other reasons, led us (see Chap. 6) to design a new non-linear device, so called the ATS, to achieve a non-linear interaction in the form $\sin \sum_\lambda \varphi_\lambda(\lambda + \lambda^\dagger)$ which in turn provided the 1 to 2 photons exchange between two resonators: $H_{\text{int}} = g_{2ph} a b^{\dagger 2} + \text{h.c.}$ required to stabilize cat states. Contributing to the design of this experiment was a by-product of this thesis.

## 2.3 OPEN SYSTEMS

This thesis focuses on controlling itinerant and stationary photons, converting one into the other and investigating the measurement it produces when the itinerant photon is lost to the environment. We present here a brief introduction to the input-output formalism that models these systems.

### 2.3.1 *Input output formalism*

We recall that the dynamics of open quantum systems is governed by the Lindblad master equation. For a quantum system of Hamiltonian $H$ and density matrix $\rho_t$, it reads

$$\frac{d\rho_t}{dt} = -\frac{i}{\hbar}[H, \rho_t] + \sum_k \mathcal{D}_k(\rho_t)dt \tag{2.50}$$

with $\mathcal{D}_k$ the decoherence super-operator for the loss channel $k$. If we introduce the jump operator $L_k$ associated with this loss channel, then $\mathcal{D}_k(\rho_t) = L_k \rho_t L_k^\dagger - \frac{1}{2}\rho_t L_k^\dagger L_k - \frac{1}{2} L_k^\dagger L_k \rho_t$.

Several hypotheses are required to use Lindblad formalism ([29]) but mainly the environment must be Markovian, meaning that no information that leaked out of the system can reenter it. In our case, the connexion with the environment is either through internal losses, assumed to be Markovian, and through transmission lines assumed to be ideal and reflectionless thus also Markovian.

Two cases are of interest to us: a resonator coupled to a zero-temperature transmission line and an imperfect qubit coupled to a thermal bath.

We first consider the case of the resonator coupled to a zero-temperature transmission line at a rate $\kappa$ and coupled to an unmonitored loss channel (internal losses) at a

rate $\kappa_i$. We define the jump operator associated: $L = \sqrt{\kappa}a$ and $L_i = \sqrt{\kappa_i}a$. Using the input-output relation

$$\sqrt{\kappa}a = a_{\text{in}} + a_{\text{out}} \tag{2.51}$$

in Eq. (2.50), in the Heisenberg frame, we obtain

$$\dot{a} = \frac{i}{\hbar}[H, a] - \frac{\kappa + \kappa_i}{2}a + \sqrt{\kappa}a_{\text{in}} + \sqrt{\kappa_i}a_{\text{in},i}. \tag{2.52}$$

Finally, to characterize the coupling rates of a resonator it is often easy to do so by monitoring its reflection coefficient as a fonction of the frequency. Driving a resonator at a frequency $\omega_d$ can be described by the term

$$H_d = \hbar(A_d(t)e^{-i\omega_d t}a^\dagger + \text{h.c.}) \tag{2.53}$$

where $A_d$ represent the amplitude of the drive. Currently commercially available microwave sources produce coherent states (after being attenuated by 40 dB at in a cold bath), thus the stationary state of a harmonic resonator of frequency $\omega_r$ driven by a microwave source at a frequency $\omega$ is a coherent state of complex field amplitude $\alpha(t)$ given by

$$\dot{\alpha}(t) = -i\omega_r\alpha(t) - \frac{\kappa + \kappa_i}{2}\alpha(t) + \sqrt{\kappa}\alpha_{\text{in}} \tag{2.54}$$

Thus the expected reflection coefficient (see [1]) $S_{11} = \alpha_{\text{out}}/\alpha_{\text{in}}$ reads (see Fig 2.12a),

$$S_{11} = \frac{\kappa - \kappa_i + 2i(\omega - \omega_r)}{\kappa + \kappa_i - 2i(\omega - \omega_r)}, \tag{2.55}$$

which in turn defines the quality factor of the resonator $Q = \omega_r/(\kappa + \kappa_i)$. We will call a resonator overcoupled to the transmission line if $\kappa \gg \kappa_i$. The current state-of-the-art for Q factor of high-Q resonators at the single photon level is $10^{10}$ for the $\text{TE}_{011}$ mode of cylindrical 3D aluminum cavity ([51]) and $10^6$ for CPW resonator ([52]) in sputtered TiN. In our work, high-Q will refer to niobium CPW resonator of Q factor of the order of $10^5$, while Purcell limited resonators will have coupling rate in the range $1 - 20 \times 2\pi$ MHz.

### 2.3.2 *Coupled oscillators*

It will be of practical use for us to consider the case of cascaded resonators (see Fig 2.12b) to describe the case of two resonators coupled through the parametric noiseless frequency conversion of the JRM. In particular, we study here the case where one resonator mode $m$ is high-Q and loses photon at a rate $\kappa_m$. This mode is coupled through the JRM at a rate $|gp|$ to an overcoupled mode $a$, which is in turn coupled to a transmission line at a rate $\kappa_a$. One can show (see [5] for details) that the reflection coefficient on the port of mode $a$ is

$$S_{11} = -\frac{(\kappa_a - \gamma_{io}^m + 2i(\omega - \omega_a))}{(\kappa_a + \gamma_{io}^m - 2i(\omega - \omega_a))}\frac{(\gamma_{io}^m - \kappa_m + 2i(\omega - \omega_a))}{(\gamma_{io}^m + \kappa_m - 2i(\omega - \omega_a))} \tag{2.56}$$

where the conversion pump is applied at a frequency $\omega_p = |\omega_a - \omega_m|$, and the effective coupling rate of the mode $m$ to the transmission line $\gamma_{io}^m$ is given by

$$\gamma_{io}^m = \frac{\kappa_a}{2}\left(1 - \sqrt{1 - 16\frac{|gp|^2}{\kappa_a^2}}\right). \tag{2.57}$$

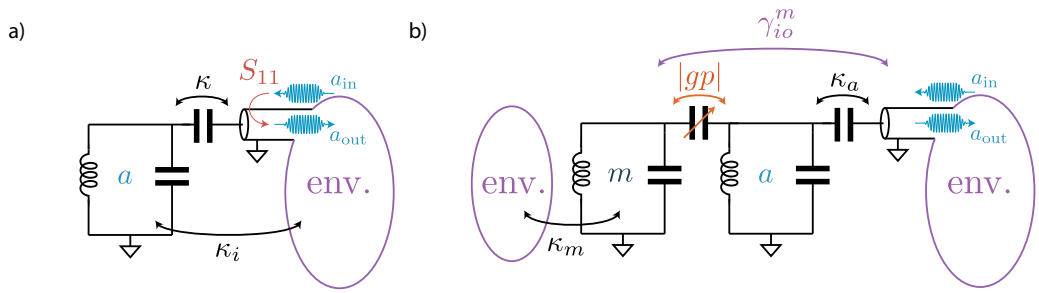


Figure 2.12: a) Harmonic resonator $a$ coupled to a transmission line at a rate $\kappa$ and suffering internal losses at a rate $\kappa_i$. The ratio $\kappa/\kappa_i$ and the quality factor $Q = \omega_r/(\kappa + \kappa_i)$ govern the reflection coefficient $S_{11}$. b) Schematic of two cascaded resonators: a resonator mode $a$ coupled to the transmission line at a rate $\kappa_a$ and whose internal losses are negligible, and high-Q resonator mode $m$ of internal loss rate $\kappa_m$. We use this representation to depict the case of two resonators coupled through a JRM pumped in frequency conversion, thus we denote the coupling rate between them as $|gp|$. The coupling of mode $a$ both to the transmission line and the resonator mode $m$ leads to an effective coupling of the mode $m$ to the transmission line at a rate $\gamma_{io}^m$.

This reflection coefficient is identical to the case of two resonators of identical resonant frequencies (the JRM provides the frequency matching). The resonator mode $a$ sees two effective coupling ports, the transmission line which drives it at a rate $\kappa_a$ and the coupling to the mode $m$ that acts as an effective loss channel for mode $a$ at a rate $\gamma_{io}^m$. Symmetrically the mode $m$ is coupled to the driving port at an effective rate $\gamma_{io}^m$ and has its own loss channel coupled at a rate $\kappa_m$.

Interestingly, $\gamma_{io}^m$ can take complex values iff. $4|gp| > \kappa_a$. This case, called the over-coupled regime (because it is completely analogous to classical coupled oscillators at resonance) leads to a frequency splitting

$$\delta\omega = \text{Im}\frac{\gamma_{io}^m}{2} \overset{\text{overcoupling}}{=} \frac{\kappa_a}{4}\sqrt{16\frac{|gp|^2}{\kappa_a^2} - 1} \tag{2.58}$$

such that $\omega_m \to \omega_m \pm \delta\omega$ and $\omega_a \to \omega_a \pm \delta\omega$, i.e. both modes are hybridized into a symmetric mode $h_+$ and an antisymmetric mode $h_-$, (in the limit $4|gp| \gg \kappa_a$)

$$\begin{cases} a & \to & (h_+ e^{i\pi\delta\omega t} + h_- e^{-i\pi\delta\omega t})/\sqrt{2} \\ m & \to & (h_+ e^{i\pi\delta\omega t} - h_- e^{-i\pi\delta\omega t})/\sqrt{2} \end{cases} \tag{2.59}$$

However the maximum decay rate to the transmission line of a state initially loaded in the memory is limited by $\kappa_a/2$. One way to understand this is to consider the limit $4|gp| \gg \kappa_a$, in which case a photon initially loaded in the memory is now split among the symmetric and antisymmetric hybrid modes. This superposition leads to beating (at a frequency $\delta\omega$) such that the photon spends half of its time in the mode $m$ and the other half in the mode $a$, thus only decaying at rate $\kappa_a/2$ into the transmission line.

We should already remark that there is a work around. Indeed, in this limit, after an interaction time $\delta t = \frac{1}{4\delta\omega}$ the states initially loaded in the mode $m$ and in the mode $a$ have been swapped. Hence by turning on the conversion of the JRM only for that duration, it is possible to extract a state from the mode $m$ arbitrarily fast, but it is only possible to transfert to the transmission line at a rate $\kappa_a$ (instantaneous swap followed by a decay rate $\kappa_a$).

Finally there is an interesting phenomenon happening in the limit $\kappa_a \gg 4|gp|$. In this limit we have

$$\gamma_{io}^{m} \simeq \frac{4|gp|^2}{\kappa_a} \tag{2.60}$$

thus the effective coupling of mode $m$ to the transmission line reduces as the coupling of mode $a$ to the line increases. This counter-intuitive result can be viewed as a Zeno blockade ([53, 54]) of the Hamiltonian conversion between the two modes due to the measurement channel arising from the decay rate of mode $a$. It also possible to kill the coupling between the two modes or kill the coupling to the transmission line by dynamical decoupling of the modes ([55]).

### 2.3.3 *Loss channels of a qubit*

In this thesis we will also need to describe the loss channels associated with a transmon qubit coupled to a thermal bath. We denote three jump operators

- $L_1 = \sqrt{\Gamma_\downarrow}\sigma_-$ for relaxation
- $L_2 = \sqrt{\Gamma_\uparrow}\sigma_+$ for excitation
- $L_3 = \sqrt{\frac{\Gamma_\varphi}{2}}\sigma_z$ for pure dephasing

Those jump operators correspond to the loss of information into the environment and thus a reduction of the off-diagonal terms of the density matrix, i.e. decoherence. The first two correspond to environment measuring that the qubit lost (resp. gained) an excitation, whereas the third one corresponds to the environment inducing a frequency shift of the transmon. They can be measured independently. The characteristic time to reach thermal equilibrium is $T_1 = \frac{1}{\Gamma_\downarrow+\Gamma_\uparrow}$ and the equilibrium population of the qubit is $p_{th} = \frac{\Gamma_\uparrow}{\Gamma_\downarrow+\Gamma_\uparrow}$. The characteristic time of decay of off-diagonal terms of the density matrix can be accessed by a Ramsey interference experiment measuring $T_2 = \frac{1}{\frac{\Gamma_\downarrow+\Gamma_\uparrow}{2}+\Gamma_\varphi}$.

In our experiment the energy decay rate is due to coupling to a bath through impurities and imperfections of the fabrication which are at a temperature barely higher than the refrigerator, leading to $p_{th} < 10^{-2}$. Our fabrication technique for CPW transmon qubit gives $T_1 = 5 - 10$ $\mu$s and $T_2 \simeq 2T_1$, i.e. $\Gamma_\varphi \ll \Gamma_\downarrow,\ \Gamma_\uparrow$.

# 3

# THE QUANTUM NODE

> Le paradis, à n'en pas douter, n'est qu'une immense bibliothèque.
>
> G. Bachelard

After several decades of improvement of quantum technologies, controlling individual quantum systems is now standard over a wide range of physical system. This improvement allowed us to realize what used to be thought experiments a century ago and greatly improved our understanding of elementary quantum mechanics. The 2012 Nobel prize awarded to D. Wineland for the control of single ions and S. Haroche for the development of CQED underline this great achievement. The new frontier of quantum mechanics lies in many body physics. Numerous groups explore this path whether it is to improve our understanding of complex quantum systems, the emergence of classical realism, or build complex quantum mechanical machines that leverage the rich mathematical tools that underpins the quantum realm.

In this chapter, we will present the platform we developed aiming at building a quantum network of microwave modes: the *quantum node*. We justify the design choices and the iteration process as we believe it holds valuable lessons for future experiments. This leads us to expose the main features of our fully functional Quantum Node.

## 3.1 MODEL AND CONSTRAINTS OF THE QUANTUM NODE

In the last decade, superconducting microwave circuits have become a platform of choice to study quantum mechanics thanks to their ease of design and their ease of control. It led to the rise of standard tools and circuits used in the domain. In particular, transmon qubits (see Chapter 2) and weakly anharmonic microwave resonators have become standards of the domain for the last decade because of their reliability and their good coherence to gate time ratio. Consequently in our general goal to develop a quantum network we aimed at building a versatile platform that can both be thought of as a building block for a network of weakly anharmonic microwave resonators controlled and measured by transmon qubits, and as a network of transmon qubits dynamically coupled through microwave resonators (Fig. 3.1). Either way, it requires to couple a transmon to a resonator and be able to transfert on demand the state of the resonator into a communication bus.

More importantly developing such a platform allowed us to implement a novel sequential quantum non-demolition qubit read-out initially proposed by Sete *et al.* in 2013 ([11], see Chapter 4) that we implemented while setting up the quantum node.

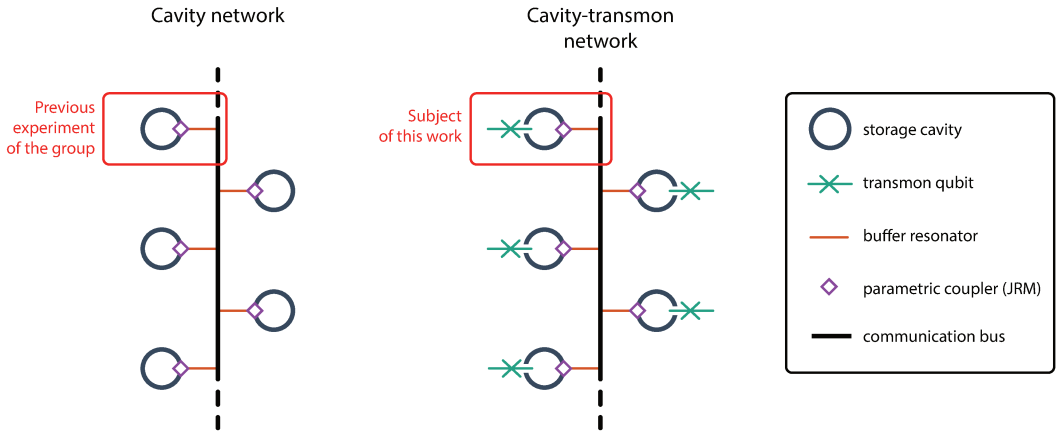


Figure 3.1: Illustration of the longterm goal foreseen for the Quantum Node as building block of a network. On the left, the previous version of our node only featuring a microwave resonator memory and a JRM, limiting the possible operations to gaussian ones on the microwave fields. On the right, our improved version adding a transmon qubit coupled to the memory. It can either be thought of as network microwave resonators controlled and measured by transmon qubits or as a network of transmon qubits dynamically coupled through a network of microwave resonators.

To build the quantum node, we leveraged and combined the extensive knowledge acquired previously in our group on the transmon qubit during P. Campagne-Ibracq's thesis ([56]) and on the JRM during E. Flurin's thesis ([5]). In Fig. 3.2 we illustrate how we assemble both in a single device. The JRM is used as a parametric coupler between a high Q memory resonator mode $\hat{m}$ of angular frequency $\omega_m$, and a buffer resonator mode $\hat{a}$ of angular frequency $\omega_a$ coupled to a transmission line. As seen in Chapter 2, the JRM provides us with a three-wave mixing Hamiltonian when operated at a flux bias $\varphi_{\text{ext}} = 2\pi\ \varphi_0$ with $\varphi_0$ the flux quantum. Hence we assume that we are able to cancel out all even order coupling term generated by the JRM. In particular, we exclude the self-Kerr and cross-Kerr terms that would be induced by the JRM from our Hamiltonian description of the device. Hence the Hamiltonian of the interaction due to the JRM is

$$H_{\text{JRM}} = g(a + a^\dagger)(m + m^\dagger)(p + p^*) \tag{3.1}$$

Two terms (and their hermitian conjugates) can be made resonant in this Hamiltonian by matching the pump frequency to either $\omega_p = |\omega_a - \omega_m|$ or $\omega_p = \omega_a + \omega_m$. In the first case, the Rotating Wave Approximation (RWA) leads to the parametric

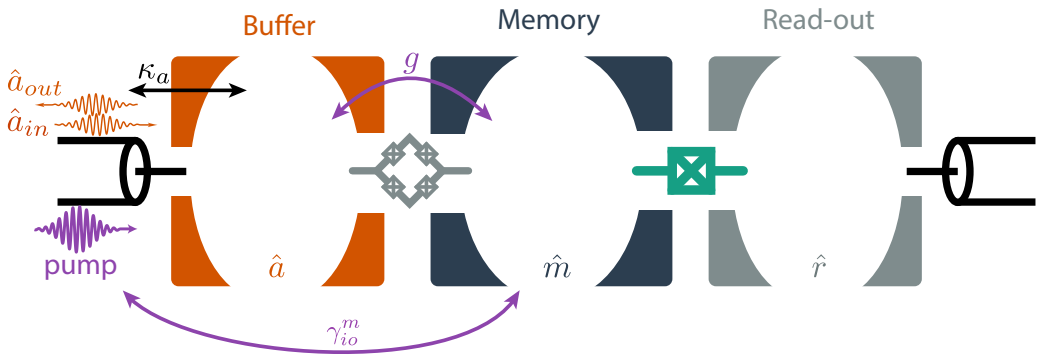


Figure 3.2: Scheme of the complete Quantum Node. The buffer resonator in orange is well coupled to the transmission line with a coupling rate $\kappa_a$. The buffer resonator is parametrically coupled to the high Q memory resonator in dark blue through the JRM. When a pump is applied at the difference between frequencies of the memory and the buffer $\omega_p = \omega_a - \omega_m$, leads to an effective coupling of the memory to the transmission line at a rate $\gamma_{io}^m$. The transmon qubit in green is coupled both to the memory and to a dedicated readout resonator in grey. The latter is coupled to another transmission line for the readout operations.

conversion Hamiltonian $H_{\text{JRM}} = gpam^\dagger + h.c.$. This coupling mechanism is used to perform a controlled catch or release of a wavepacket from the bus into the memory as detailed in subsection 3.2. Whereas the second case leads to the parametric amplification Hamiltonian $H_{\text{JRM}} = gp^*am + h.c.$ and can be used for EPR state generation ([38]) or for built-in amplification ([5]).

The energy decay rate of the memory is denoted $\kappa_m = \frac{1}{T_m}$ and the coupling rate of the buffer to the transmission line is $\kappa_a$. We neglect the internal losses $\kappa_{ai}$ of the buffer as $\kappa_a \gg \kappa_{ai}$ by design. The parametric coupling is controlled by a stiff pump amplitude $p$ treated here as a classical parameter. We will not consider the mode off-resonantly driven by the pump in our Hamiltonian description of the system.

The memory is coupled to a transmon qubit $\hat{q}$ of angular frequency $\omega_q$ in the dispersive regime ([57]) with a dispersive shift $\chi$. The ground state of the transmon is referred to as $|g\rangle$ and its excited state as $|e\rangle$. The anharmonicity of the transmon is denoted $\alpha$ and unless specified otherwise, the transmon will be considered as a 2-level system. We denote $T_1$ and $T_2$ the characteristic energy decay time and coherence time of the qubit. The qubit is also coupled to a dedicated read-out resonator mode $\hat{r}$ of angular frequency $\omega_{ro}$ with a dispersive shift $\chi_{ro}$. The read-out is coupled to a transmission line at a rate $\kappa_{ro}$.

Owing to its coupling to the qubit, the memory is subject to the self-Kerr which is an unwanted feature. Indeed, in both experiment the memory should be as linear as possible. In the sequential read-out experiment the memory self-Kerr limits the maximum number of photon used fo the read-out. In the remote state preparation, it limits the fidelity of arbitrary state preparation. Using black box quantization (see

Chapter 2), one can derive those terms from the participation ratio of the Josephson junction of the transmon in the memory. The latter read

$$H_{JJ} = E_J \cos\left(\varphi_{\text{zpf}_q}(q+q^\dagger) + \varphi_{\text{zpf}_m}(m+m^\dagger) + \varphi_{\text{zpf}_r}(r+r^\dagger)\right) \tag{3.2}$$

We do not discuss the non-linearity of the read-out mode $\hat{r}$ here as it will only impact us as a limitation on the read-out parameters. Nor will we discuss the memory - read-out cross-Kerr as it will be irrelevant in our experiments. The self-Kerr induced in the memory by the transmon is mainly governed by the 4th order development of the cosine leading to non-rotating term of the form $\varphi^4_{\text{zpf}_m} m^{\dagger 2} m^2$. As we will see in our experiment, we need to take into account the correction made by the non-rotating 6th order term of the form $\varphi^4_{\text{zpf}_m}\varphi^2_{\text{zpf}_q} m^{\dagger 2} m^2 q^\dagger q$. We will denote $K_g$ (respect. $K_e$) the memory effective self-Kerr rates when the qubit is in its ground state (respect. excited state) such that the interaction Hamiltonian due to the qubit reads

$$H_{\text{interaction}} = -\chi m^\dagger m|e\rangle\langle e| - K_g m^{\dagger 2} m^2 |g\rangle\langle g| - K_e m^{\dagger 2} m^2 |e\rangle\langle e| - \chi_{ro} r^\dagger r |e\rangle\langle e| \tag{3.3}$$

We set the signs of our Hamiltonian model such that the dispersive shifts are positive. This leads us to a complete model

$$\begin{aligned} H_{tot} \;=\; & \hbar\omega_a a^\dagger a + \hbar\omega_m m^\dagger m + \hbar\omega_q \tfrac{\sigma_Z}{2} + \hbar\omega_r r^\dagger r \\ & + g(a+a^\dagger)(m+m^\dagger)(p+p^*) \\ & - \chi m^\dagger m|e\rangle\langle e| - K_g m^{\dagger 2} m^2 |g\rangle\langle g| - K_e m^{\dagger 2} m^2 |e\rangle\langle e| - \chi_{ro} r^\dagger r |e\rangle\langle e| \end{aligned} \tag{3.4}$$

The quantum node requires a long lived transmon qubit coupled in the photon selective regime to a high quality factor memory resonator. The latter should be coupled to a transmission bus through a parametric coupling such that when idling it suffers no decay through the bus while still being able to transfer its state rapidly to the bus for coupling to other nodes.

We detail below what experimental constraints drove us during the design of the device. We wish for the transmon qubit to be as ideal as possible, meaning that the experiment should not be limited by the qubit decay, i.e. we wish for total duration of the experiment to be much smaller than the lifetime / coherence time of the qubit $T_{\text{experiment}} \ll T_1, T_2$. Provided that the lifetime of the transmon qubit that our group is currently able to fabricate rarely exceeds $T_1 \approx 10\ \mu$s and we can reach the limit $T_2 = 2T_1$ this actually fixes a limit for the total experiment duration $T_{\text{experiment}} < 1\ \mu$s. As we will see in their dedicated chapters, each experiment have duration mostly lower bounded by the dispersive coupling $\chi$ of the memory to transmon such that $T_{\text{experiment}} \simeq 2\pi/\chi$. We also need to be in the photon number selective regime, i.e. $\chi T_2 \gg 1$ allowing us to do photon number selective $\Pi$ pulses on the qubit that we will need for the remote state preparation experiment ([58]). Hence in the experiment of this thesis we targeted $\chi = 2\pi \times 2$ MHz.

We also need for the memory resonator to be as ideal as possible. This means in our case that it should have a quality factor as high as possible (in our case it is of the order of $10^5$ for 2D resonators and $10^6$ for 3D cavities). It also means that it should be as harmonic as possible, meaning that the self-Kerr term should be as small as possible. Quantitatively we require for the memory self-Kerr rate $K_{g,e}$ to be such that $T_{\text{experiment}} K_{g,e} \bar{n} \ll 2\pi$ with $\bar{n}$ the average number of photon in the memory during the experiment. This constraint imposes that the average dephasing induced by the self-Kerr during the experiment is small. The JRM provides us with a tunable self-Kerr for the memory. But as we will discover later on, the Kerr induced by the transmon in the memory actually largely dominates the Kerr induced by the JRM thus rendering inefficient the Kerr tuning by the JRM.

Finally, our most restrictive constraint is to require for the parametric coupling of the memory to the bus to allow for swap operations to be much faster than the experiment duration. Quantitatively, as we will see when discussing the quantum memory experiment, it implies that a swap operation should be of the order of 10 ns, hence for the coupling rate of the buffer to the bus to be $\kappa_a > 2\pi \times 20$ MHz and the 3-wave coupling rate g to be large enough such that we are able to reach the overcoupling regime, i.e. $\frac{|4gp|}{\kappa_a} > 1$. This feature is crucial for the sequential read-out experiment and is our main technological avantage when compared to similar platform ([3],[59]) as the Quantum Node is more than an order of magnitude faster than them.

We summarize the required features:

- High quality factor harmonic resonator as a memory, $T_m \gg T_{\text{experiment}}$
- Long lived transmon qubit in the photon number selective regime, $T_1, T_2 \gg T_{\text{experiment}}$ and $\chi T_2 \gg 1$
- Ability to do fast swap operation between the memory and the bus, $\gamma_{io} \gg \frac{1}{T_{\text{experiment}}}$
- Auxiliary readout resonator to accurately and rapidly readout the state of the transmon, readout fidelity greater than 95% and $T_{\text{readout}} < \frac{1}{\chi}$

## 3.2 PREVIOUS VERSION OF THE QUANTUM NODE

This work is not the first attempt of our group to build such a quantum node, but rather lean on previous experiments performed in the group. E. Flurin thesis ([5]) studied in detail the JPC (Chapter 2). During this work he built and characterized our first modular quantum memory ([38]) but was missing the transmon qubit and its readout. Later, D. Markovic designed and built a full 3D version of a complete quantum node ([6]) but the slow iteration time imposed by 3D design prevented to converge on a device capable of swapping sufficiently fast the memory into the transmission line while maintaining long memory lifetime. Here we present both works as a starting ground for the development of our device.

### 3.2.1 *Quantum memory experiment*

The quantum node developed by E. Flurin consisted of a 3D high Q resonator used as the memory. This memory is parametrically coupled through the JRM to a low Q strip-line resonator. The latter is coupled to the transmission line (bus). The device is displayed in Fig. 3.3. The device characteristics are the following.

The memory resonator fundamental mode $\hat{m}$ has a frequency $f_m = 7.80$ GHz and a lifetime $T_{1m} = 3.3\ \mu$s. The buffer fundamental mode $f_a = 9.30$ GHz and a coupling rate to the transmission line $\kappa_a = 8 \times 2\pi$ MHz and the maximum coupling of a memory to the transmission line mediated by the parametric conversion through the JPC achieved was $\gamma_{io} = (110\text{ ns})^{-1}$ which is three times smaller than the limit of $\kappa_a/2$.

Indeed as opposed to the case detailed in chapter 2, here the memory is not directly coupled to the JPC. Instead, its coupling is mediated by an antenna mode through a capacitive coupling $\kappa_c$ in series with the parametric coupling $|gp_0|^2$ such that the conversion rate between $m$ and $a$ is given by

$$|gp_0|^2 \leftarrow \frac{1}{\frac{1}{(\kappa_c/2)^2} + \frac{1}{|gp_0|^2}} \tag{3.5}$$

Hence, the effective coupling of the memory to the transmission line becomes

$$\gamma_{io} \leftarrow \frac{\kappa_a}{2}\left(1 - \sqrt{1 - \frac{4}{\kappa_a^2\left(\frac{1}{\kappa_c^2} + \frac{1}{4|gp_0|^2}\right)}}\right) \tag{3.6}$$

In this experiment the antenna's coupling rate $\kappa_c$ was independently measured with a separated strip-line chip directly coupling the antennas to the transmission line. By measuring the direct reflexion coefficient of the memory, they found $\kappa_c = 3$ MHz.

The main metric for a memory is the ratio of the write/read time to the storage time, i.e. the number of write/read operation possible before an error occurs. Here this metric is the product $\gamma_{io}T_{1m} = 30$. At the time this made this memory the state of the art ([60, 61]).

To illustrate the behavior as a quantum memory, Fig. 3.4 details a catch, store and release experiment where a wavepacket is sent on the buffer and caught by a well timed conversion pump. The enveloppe of the incoming wavepacket is exponentially growing and corresponds to the optimal shape for a square pump.

In order to further understand how the shape of the pump controlling the coupling of the memory to the buffer allows to swap the memory content with the state of a given incoming / outgoing wavepacket, let us first consider the simple square release case. The memory mode $m$ initially contains a coherent state $|m(t=0)\rangle = |\alpha\rangle$. At time $t = 0^+$ the pump $p(t)$ is turned on to a constant value $p_0$, thus $p(t) = \Theta(t)p_0$. Owing

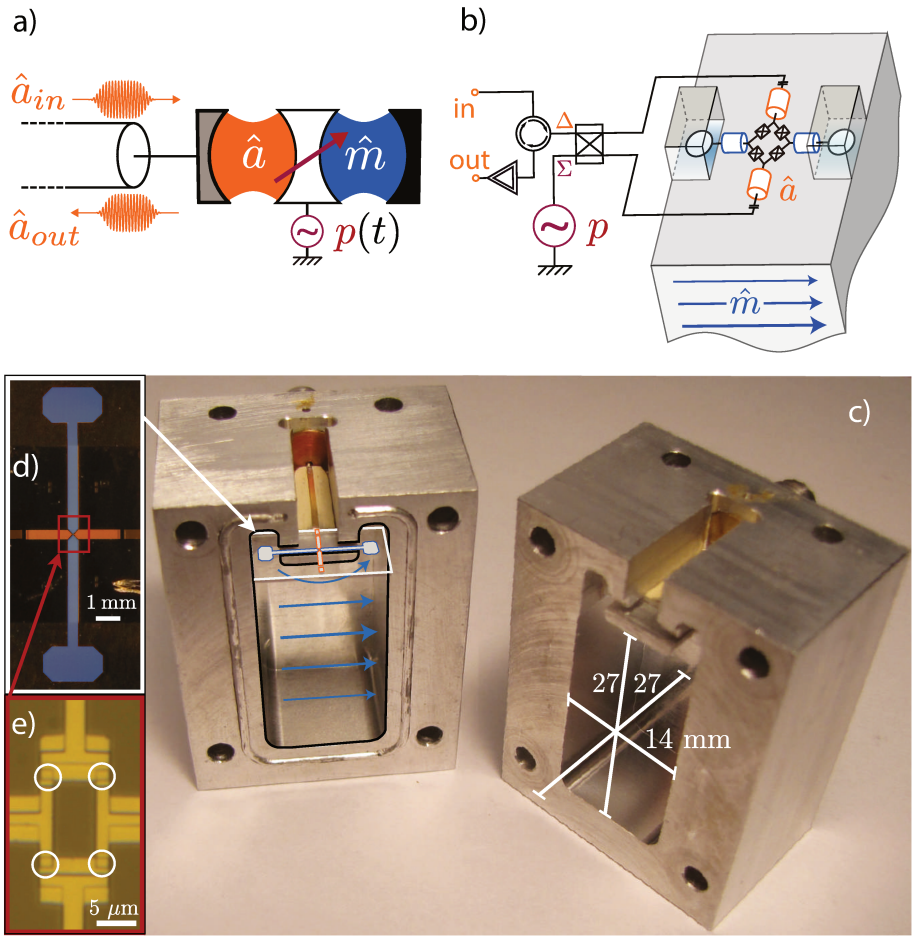


Figure 3.3: Figure reproduced from [38]. a) Scheme of the experiment of E. Flurin *et al.* [38] without a qubit coupled to the memory resonator. The propagating modes of the bus $\hat{a}_{in}$ and $\hat{a}_{out}$ are coupled to a low-Q buffer resonator. A tunable pump $p$ allows to control the parametric coupling of the buffer to the high Q memory resonator. b) Scheme of the device and its wiring. The hybrid coupler combines the pump and the input/output to couples them to the commun / buffer modes. c) Photograph of the device (opened). The blue arrows represent the memory mode's polarisation. The memory couples to the JPC through antennas plunging into chimney. d) False color picture of the stripe-line JPC. In blue the memory antennas and in orange the buffer resonator. e) Optical microscope image of the JRM with the Josephson junctions circled in white.

to the quantum Langevin equation for the field amplitudes in the rotating frame of the coupled system, as seen in chap. 2, the evolution follows

$$\begin{cases} \dot{m} &= -igp^* a \\ \dot{a} &= -igpm - \frac{\kappa_a}{2} a \end{cases} \tag{3.7}$$

Here, we neglect the losses of the memory $\kappa_m$ for simplicity. Assuming that no drive is applied, the input output relation for the buffer mode leads to $\sqrt{\kappa_a} a = a_{out}$. Hence,

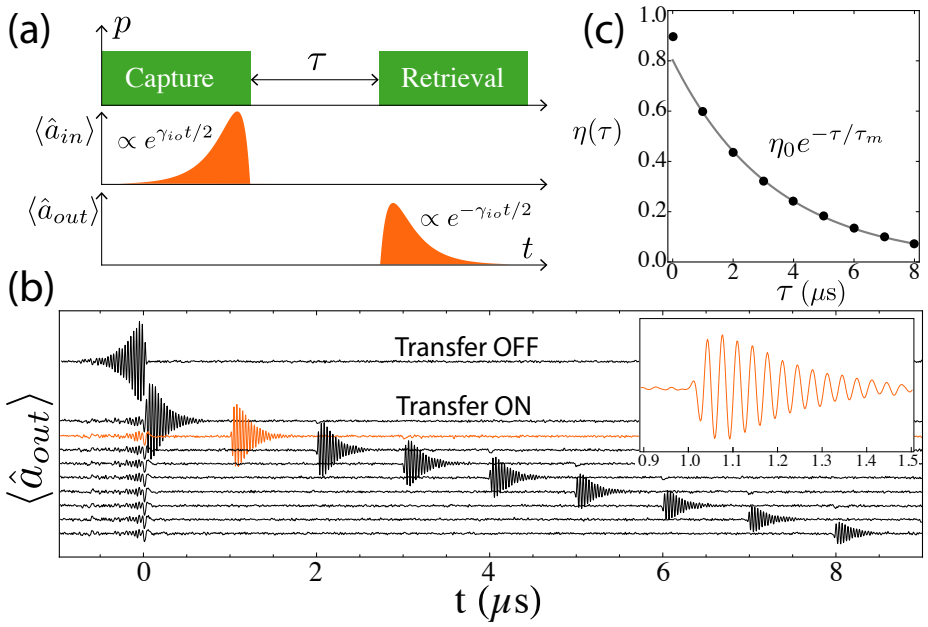


Figure 3.4: Figure reproduced from [38]. a) First row, conversion pump pulse sequence for the catch, store and release experiment, second row incoming wavepacket enveloppe, third row released wavepacket enveloppe. b) Averaged amplitude of the output field after a down conversion to 40 MHz. The first line correspond to no pump applied, hence it is simply the reflected incoming signal. The following ones correspond to various release timing $\tau$ as depicted in a). The inset is a zoom on the case $\tau = 1$ $\mu$s. c) Black dots correspond to the ratio of retrieved energy against sent energy, i.e. the memory efficiency $\eta$. The black line correspond to an exponential fit of characteristic time $\tau_m = T_{1m}$. $\eta_0$ is interpreted as the write & read efficiency.

$$\begin{cases} \ddot{m} + \frac{\kappa_a}{2}\dot{m} + |gp|^2 m &= 0 \\ gp^* \frac{a_{out}}{\sqrt{\kappa_a}} - i\dot{m} &= 0 \end{cases} \tag{3.8}$$

Taking into account our choice for $p(t)$ and assuming the buffer is initially empty leads to

$$\begin{cases} m(t>0) &= \alpha\left(Ae^{-\frac{\gamma_{io}^m}{2}t} - Be^{-\frac{\kappa_a-\gamma_{io}^m}{2}t}\right) \\ a_{out}(t>0) &= i\alpha\frac{\sqrt{\kappa_a}}{gp_0}\left(e^{-\frac{\gamma_{io}^m}{2}t} - e^{-\frac{\kappa_a-\gamma_{io}^m}{2}t}\right) \end{cases} \tag{3.9}$$

with $A = \frac{\kappa_a-\gamma_{io}^m}{\kappa_a-2\gamma_{io}^m}$ and $B = \frac{\gamma_{io}^m}{\kappa_a-2\gamma_{io}^m}$. We recall that $\gamma_{io}^m(p) = \frac{\kappa_a}{2}\left(1-\sqrt{1-\frac{4|gp|^2}{\kappa_a}}\right)$. This expression breaks down in the peculiar case of critical coupling corresponding to $\gamma_{io}^m = \frac{\kappa_a}{2}$. The temporal envelope of $a_{out}$ defines the flying mode into which the memory state was written.

Since there are no loss in an unmonitored channel in this model, one can reverse the time and exchange $a_{out}$ and $a_{in}$ to retrieve the opposite case where we catch an incoming wavepacket and store it in the memory. Both cases were done in this experiment.

In the general case, one can compute the pump shape $p(t)$ to apply in order to catch a given incoming wavepacket or release the memory state into a given temporal mode. Let's treat the simple example of catching an incoming wavepacket $a_{in}(t)$ of known envelope and timing while neglecting the Kerr terms and the memory decay. To compute the required pump shape one simply solve the quantum Langevin equation assuming the desired result: no signal is reflected. Hence, $a_{out} = 0$, i.e. $\sqrt{\kappa_a}a = a_{in}$. Then $p(t)$ is the solution of the implicit system

$$\begin{cases} \dot{m} &= -igp^* a_{in} \\ \dot{a_{in}} &= -i\sqrt{\kappa_a} gpm - \frac{\kappa_a}{2} a_{in} \end{cases} \tag{3.10}$$

For example, setting the input pulse to $a_{in}(t) = \frac{1}{2\sqrt{2}}\text{sech}(\kappa_a t/4)$ leads to an analytic solution for the memory field amplitude $|m(t)| = \frac{\sqrt{e^{\kappa_a t/2}+1/2}}{2}\text{sech}(\kappa_a t/4)$ and for the pump shape $p(t) = \frac{1}{\sqrt{2e^{\kappa_a t/2}+1/2}}\left(1 + \frac{1}{2}\tanh(\kappa_a t/4)\right)$.

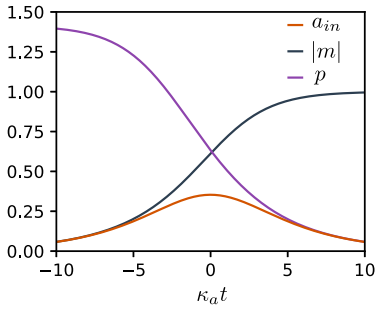


Figure 3.5: Example of the optimal catching pump shape $p(t)$ for input pulse $a_{in}(t) = \frac{1}{2\sqrt{2}}\text{sech}(\kappa_a t/4)$ leading to a full catch into the memory of field amplitude $|m(t)|$. The pump starts at its maximum value, coupling the memory to the transmission line. It is progressively reduced to shut the coupling of the memory to the transmission line as the input pulse enters the memory.

This method can be directly extended, for example to the case where we seek to do a half-swap by setting $a_{out} = \frac{1}{2}a_{in}$ or by taking into account Kerr terms (requiring then a numerical resolution of the implicit system of equations and a time dependent variation of the pump phase).

### 3.2.2 *3D design of the Quantum Node*

Owing to the design of the quantum memory experiment by E. Flurin, our group's next step was naturally to add a transmon qubit and its dedicated read-out resonator to reach a complete Quantum Node while keeping a 3D architecture. This was the work of D. Markovic to which I contributed at the beginning of this work. We briefly present

here the attempt to realize a 3D Quantum Node as it introduced an interesting new design but also had serious flaws (see [6] for more details).

In order to do so, we developed several new designs to benefit from the best features of each part of the device. Namely, we wanted to keep a 3D memory resonator for its high Q but we also wanted to introduce a 3D JPC (3D in an analogous way as for the 3D transmon) as we suspected the participation of the strip-line JPC in the memory mode was introducing internal losses and a possible leakage through the buffer port. Hence we developed a lumped JPC, wirelessly connected to the memory through an antenna and to the transmission line via a waveguide. The latter was designed to have a cutoff frequency $f_{wg}$ such that it prevented the leakage of the memory while allowing for the buffer resonator to be well coupled to the transmission line, i.e. $f_m < f_{wg} < f_a$.

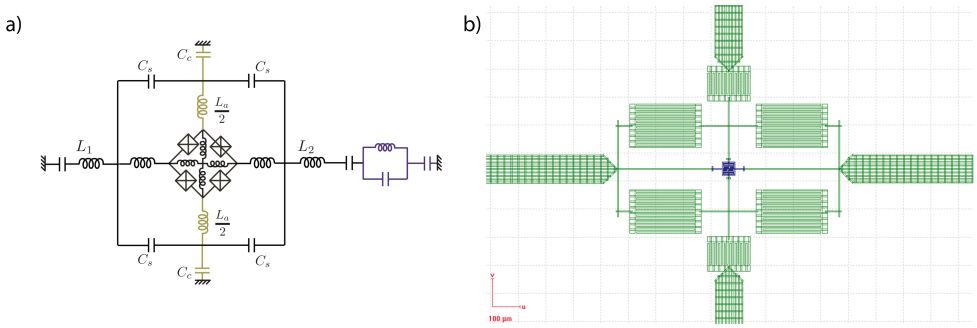


Figure 3.6: a) Equivalent circuit of the lumped wireless JPC. The capacitive part of its frequency is dominated by the four large interdigitated capacitors $C_s$ while the capacitors $C_c$ couples the JRM to antenna and later to the waveguide. In the buffer mode the middle horizontal line is at 0 potential. The inductors $L_1$ and $L_2$ serve as ballast / antenna to couple to the memory resonator (here in purple). b) E-beam lithography design of the wireless JPC displaying the interdigitated capacitors and the gridded antennas.

The 3D architecture of the Quantum Node featured two 3D microwave resonators: the high Q memory and the read-out resonator. The latter is connected to a transmission line through a waveguide for the same reason as the buffer: to prevent the decay of the memory to the transmission line. A 3D transmon lied in a tunnel connecting both as described in the scheme Fig. 3.2. A picture and a scheme of this complex circuit is provided in Fig. 3.7.

With this device we demonstrated the good behavior of the lumped wireless JPC and an overall proof of concept for this device, see [6] for more details. But as can be understood from the Fig.3.7, this device required complex machining of both cavities and the sapphire chips which arguably constituted the main flaw of this design. Indeed, any iteration on the geometric parameters of the device required machining a new one, hence inducing a slow iteration process. Another major flaw of design was that the conversion pump controlling the coupling of the memory to the buffer was filtered out

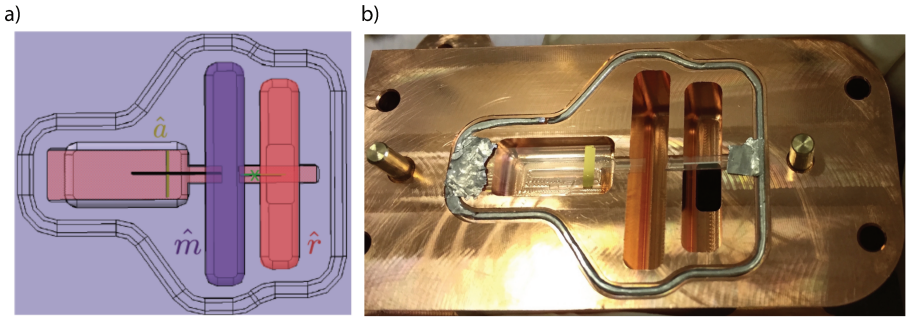


Figure 3.7: a) Catia design of the 3D Quantum Node and b) photograph of its lower half. The middle cavity is the memory. On the left lies the waveguide holding the wireless JPC. On the right is the readout cavity with the transmon qubit. Both the transmon and the JPC have antennas diving into the memory for coupling. The grey ring around all the cavities is an indium seal linked both half of the device.

by the waveguide as we realized too late that $f_a - f_m < f_{wg}$. Moreover the coupling antenna from the JPC to the memory induced a too small participation ratio of the JPC in the memory. Finally our transmon fabrication was plagued with low yield (about 1/10). This low yield also motivated improvement over the traditional Dolan bridge technique for fabricating Josephson junction that we developed during this thesis. As a conclusion we shifted towards 2D coplanar waveguide architecture despite the lower lifetimes of the constituants because this was compensated by larger participation ratio, hence making the whole experiment faster, and more importantly it allowed for fast iteration that allowed us to reach a fully functioning device.

## 3.3 CURENT DESIGN OF THE QUANTUM NODE: A COPLANAR WAVEGUIDE ARCHITECTURE

The Quantum Node is a multicomponent microwave circuit and hence benefits fully from the ease of design of coplanar waveguide circuits. As our group did not master coplanar waveguide architecture and fabrication techniques, an important part of this work was dedicated to setting those up. Nevertheless we converged on a design that realized all the required features. In this section we detail those characteristics and the innovation we brought to the community with this design. The current version is made of niobium on a silicon chip except for the Josephson junction that are made in the standard Al/AlOx/Al.

The eigenmodes of that chip are for most quite explicit on Fig. 3.8. Bare in mind that at the exception of the transmon which is a lumped anharmonic resonator, all the modes are distributed and hence have higher harmonics at frequency $f_{\mathrm{n^{th}\ harmonic}} \approx n f_0$ inducing a dense spectral crowding. It is only approximate because of the different participation ratios of the JRM in each harmonics, for example the first higher harmonic of the memory resonator and the buffer resonator have almost no current going through

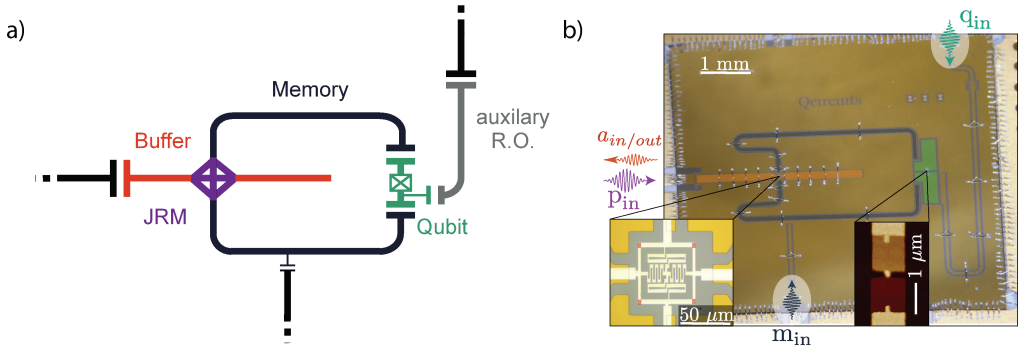


Figure 3.8: a) Scheme of the coplanar waveguide Quantum Node. The $\lambda/2$ buffer resonator in orange is at one end coupled to the transmission line. The JRM (in purple) sits at its middle coupling the buffer to the $\lambda/2$ memory resonator. The latter it curved to be coupled symmetrically to the transmon qubit in green. The auxiliary read-out resonator in grey allows for an independent read-out of the qubit. b) False color optical photograph of an identical chip (but in TiN instead of Nb). The left inset is a zoom on the JRM with the Josephson junctions highlighted in red and in the right inset an AFM tomography of the transmon Josephson junction.

the JRM because of their symmetry and hence only have slightly higher frequency than twice the fundamental frequency.

One mode is less obvious: the so called common mode ([5]). It combines the buffer resonator with the memory resonator while respecting the central symmetry of the Z eigenmode of the JRM (see Chap. 2). This mode is of crucial importance as it is the mode off-resonantly driven by the pump as detailed in chapter 2. This mode frequency can be accurately estimated by $\omega_c = \frac{2\omega_a\omega_m}{\omega_a+\omega_m}$. Moreover the first higher harmonic of the common mode can be used as well when using the JRM as a built phase preserving amplifier and will be referred to by the index *2c*.

Those modes are driven through dedicated ports. The auxiliary read-out and the transmon qubit are addressed through the read-out port on the top right of the chip. The memory mode is driven through a weakly coupled port ($\kappa < 1$ kHz). Hence displacement operations on the memory will refer to pulse applied on that port. The buffer, the common mode and its harmonic are driven through the buffer port on the left side of the chip. This is actually a major innovation in the use of the JRM as compared to other experiments ([45, 62]). A commun misconception is to think that addressing the various eigenmodes of the JPC requires to use a hybrid coupler to excite the device with the symmetry corresponding to the targeted mode. Whereas actually we only require for the mode not to be orthogonal to the drive and this measure of non-orthogonality is already taken into account when considering the coupling of that mode to a given port. In our case the common mode has a coupling $\kappa_c = 1.8$ MHz to the buffer port and hence can be driven through that port. Nevertheless, it can be handy to spatially separate the various emitted / reflected signals by using a hybrid coupler. In our case, as we will detail when discussing the wiring of the experiment in chapter 4, we exploit the frequency separation of the pump and the buffer to filter out the pump.

As we wish for the memory resonator to be as decoupled from the transmission line as possible it is interesting to note that the memory is highly decoupled from the buffer port, first by symmetry as the memory mode is orthogonal to the buffer and the common mode and secondly by filtering through those modes due to their large detuning (of 7 GHz and 2 GHz) that greatly exceeds their coupling rates to the buffer port (20 MHz and 1.8 MHz). Finally the memory decay through the readout port is filtered by both the qubit and the read-out resonator such that the effective coupling to the readout port is negligible. For similar filtering reason, the transmon qubit is not Purcell limited through the readout port.

Another specificity of this device is the low impedance of the buffer mode. Indeed, whereas the memory and the read-out modes are made of an impedance of 50 Ω mostly for simplicity and to ensure minimal dielectric loss by making the coplanar waveguide gap sufficiently large, the impedance of the buffer mode is made to be 21 Ω in order to increase the participation ratio of the JRM in that mode and hence increase the 3-wave mixing term $g$ of the JRM. Indeed the participation ratio of the buffer is

$$\xi_a = \frac{L^a_{JRM}}{Z_a^2 f_a + L^a_{JRM}} \tag{3.11}$$

with $L^a_{JRM}$ the inductance of the JRM in the buffer mode, $Z_a$ the buffer characteristic impedance and $f_a$ its frequency. Hence lowering the impedance of the buffer mode increases the participation ratio of the JRM in the buffer mode. In turns this increases the maximum parametric coupling between the memory and the buffer as we have

$$|gp_{\max}| \propto \sqrt{\xi_a \xi_m \omega_a \omega_m} \tag{3.12}$$

Another interesting design feature is that due to the coupling capacitor of the buffer to the transmission line, the buffer mode is slightly offset towards the port side. Thus to ensure that the JRM sits at the maximum of the current of the buffer mode, the latter is made approximatively 5% longer on the opposite side to compensate. This value was obtained through numerical simulations.

Finally because of the crossing of the buffer and the memory modes in their middle, ground plane currents have to be well routed through wire bonds around the JRM to bypass their tendency to circumvolute the other mode, thus leading to undesired inductance. Moreover wirebonds prevent unwanted strip modes throughout the chip and their impact was studied in this work by realizing dummy chips.

### 3.3.1 *Frequencies and coupling rates*

The spectral crowding, especially when considering our goal to exploit the 3-wave mixing term of the JRM in conversion ($\omega_p = \omega_a - \omega_m$) for the sequential readout experiment, and in amplification ($\omega_p = \omega_a + \omega_m$) for the remote state preparation experiment led us to the following choice for the frequencies: $f_m = 3.7$ GHz, $f_a = 10.2$ GHz, $f_q = 4.4$ GHz, $f_c = 5.4$ GHz, $f_{ro} = 6.45$ GHz. Those choices were made in order to prevent unwanted

terms of the Hamiltonian to be made resonant such that $n_1\omega_1 + n_2\omega_2 + ... = 0$ with $|n_x| \in \mathbb{N}$, $|n_x| < 4$ and $\omega_x$ a mode frequency or a drive frequency.

Figure 3.9 shows the flux dependency of the buffer and memory modes. We qualitatively retrieve the expected flux dependency for the JPC ([5]). The participation ratio can be estimated as the ratio of frequency modulation $\xi = \frac{\Delta\omega}{2\omega}$ and leading to $\xi_a \approx 8\%$ and $\xi_m \approx 1\%$. In this work the operating flux point is chosen to minimize the cross-Kerr term to ensure that the resonators frequencies do not depend on the pump power. This constraint selects a unique flux point for each half pseudo-period of the flux dependency. We choose the one corresponding to the smallest external flux bias. In the small arch regions of the flux dependency, around $\varphi_{\text{ext}} \equiv 4\pi\ \varphi_0 \pmod{8\pi\ \varphi_0}$, the JRM induces several parasitic interaction terms and we did not explore these regions in detail. We note nevertheless that in our device, the flux dependency in the small arch region is abnormal and might be explained by an asymmetry in the areas of the 4 small loops of the JRM (for more detail see [5]).

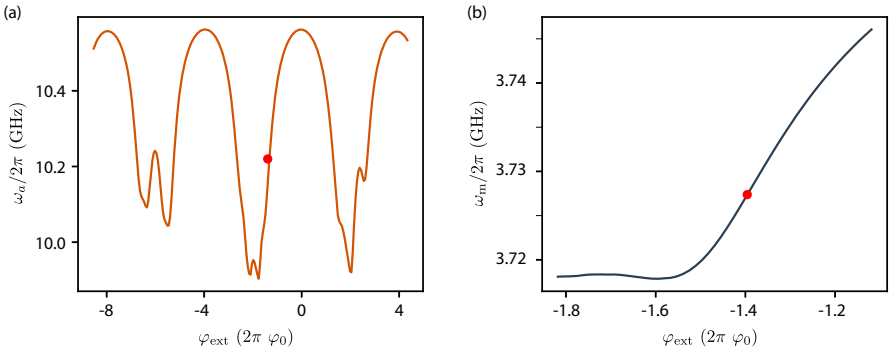


Figure 3.9: a) Frequency of the buffer mode measured through reflectometry on the buffer port with an input power of $-118$ dBm as a function of the flux bias of the JRM. b) Frequency of the memory mode as a function of the JRM flux bias measured through conversion via the buffer. The frequency of the memory mode is found by sweeping the frequency of the conversion pump to find the maximum coupling rate between the buffer and the memory which occurs for $\omega_p = \omega_a - \omega_m$. This measurement method limits the measurement around the maximum of the 3-wave mixing interaction. Both flux dependencies display the qualitative expected behavior except around the small arch regions.

Figure 3.10 shows the measured flux dependency of the coupling terms and of the memory self-Kerr. This measurement is uncalibrated as the power sent on the buffer resonator during this measurement was not calibrated.

Interestingly the qubit is also slightly sensitive to the flux of the JRM. Figure 3.11 displays this small dependency. We can extract $\xi_q \approx 5\ 10^{-5}$ which is non-zero due to the change in cavity pull as the memory frequency shifts with the flux. Actually the coherence time of the qubit at the operating flux point is limited by this flux dependency.

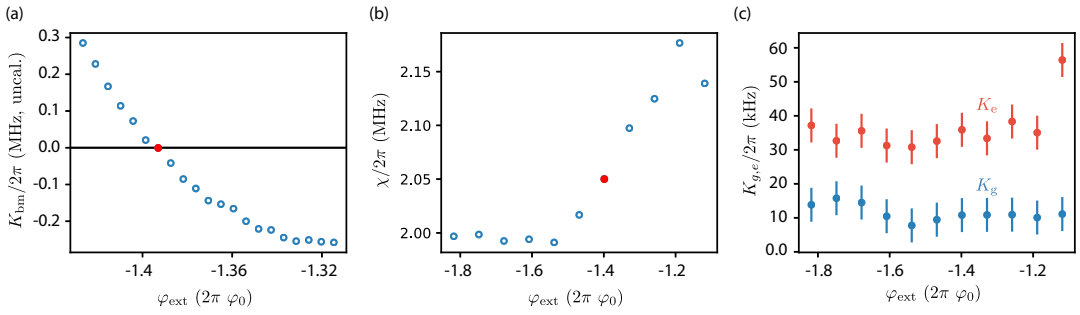


Figure 3.10: a) Uncalibrated measurement of the memory-buffer cross-Kerr rate as a function of the flux bias of the JRM. b) Dispersive shift of the memory-qubit coupling versus the flux. c) Memory self-Kerr rate as a function of the flux and the qubit state.

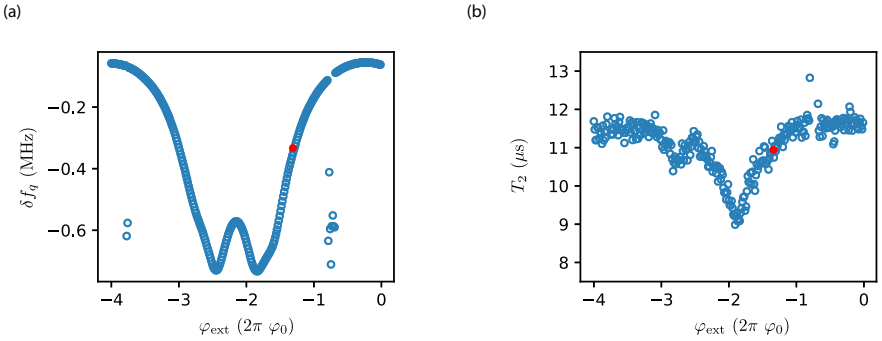


Figure 3.11: a) Detuning of the qubit measured by a Ramsey experiment with a reference frequency at 4.45 GHz as a function of the flux bias of the JRM. b) Coherence time extracted from the same Ramsey experiments.

The table **??** summarizes the device parameters at the operating flux point.

### 3.3.2 *Decoupling the qubit from the common mode*

The choice of symmetrically coupling the memory to the transmon is not mundane. Actually it solves a major flaw of a previous design developed during this thesis: namely the *ionization* ([48–50]) of the transmon when the strong conversion pump is applied. This was due to a non zero coupling of the transmon to the common mode off-resonantly driven by the conversion pump.

The previous design had a common mode to qubit dispersive shift $\chi_{\text{common}} = 2\pi \times 0.8$ MHz . This coupling was not foreseen as an issue for the usage of the Quantum Node. The mistake was to disregard the very large number ( $\simeq 10^3$) of photons in the common mode induced by the stiff conversion despite the detuning between the pump and the common mode. That large number of photons in a resonator coupled to the transmon leads to a rapid excitation of the latter into a highly excited state ([63]), thus

| Main parameters of the Quantum Node in this thesis | | |
|---|---|---|
| Component | Parameter | Value |
| Transmon | $\omega_q/2\pi$ | 4.52 GHz |
| | $\alpha/2\pi$ | 96 MHz |
| | $T_1$ | 6.1 $\mu$s |
| | $T_2$ | 11.2 $\mu$s |
| | $\chi/2\pi$ | 2.05 MHz |
| | $\chi_{ro}/2\pi$ | 0.8 MHz |
| Memory | $\omega_m/2\pi$ | 3.73 GHz |
| | $T_m$ | 4.1 $\mu$s |
| | $K_g/2\pi$ | 10 kHz |
| | $K_e/2\pi$ | 35 kHz |
| | $\xi_m$ | 1% |
| Buffer | $\omega_a/2\pi$ | 10.22 GHz |
| | $\kappa_a/2\pi$ | 20 MHz |
| | $\xi_a$ | 8% |
| Common | $\omega_c/2\pi$ | 5.45 GHz |
| | $\kappa_c/2\pi$ | 1.8 MHz |
| | $\xi_c$ | 4% |
| JRM | $\lvert gp_{\max}\rvert$ | 170 MHz |
| Readout | $\omega_{ro}/2\pi$ | 6.45 GHz |
| | $\kappa_{ro}/2\pi$ | 0.65 MHz |

rendering the transmon unusable during several $T_1$. This waiting time prevented us to do any of the experiments we desired.

To the best of the author's knowledge, the exact threshold for this ionization to occur is still undetermined. Nevertheless reducing the coupling of the transmon to that load of photons should increase this threshold. Bare in mind that the common mode is the only mode that is both coupled to the transmon and driven by the pump.

Our solution was to selectively decouple the common mode from the qubit by symmetrically coupling the common mode to the transmon. This symmetry ensures that driving the common mode induces no potential difference across the transmon Josephson junction as depicted in Fig. 3.12. In our current version, the common mode to qubit dispersive shift is smaller than our measurement accuracy $\chi_{\text{common}} < 2\pi \times 10$ kHz. We effectively reduced the coupling by at least 20 dB and the transmon is no longer excited by the conversion pump.

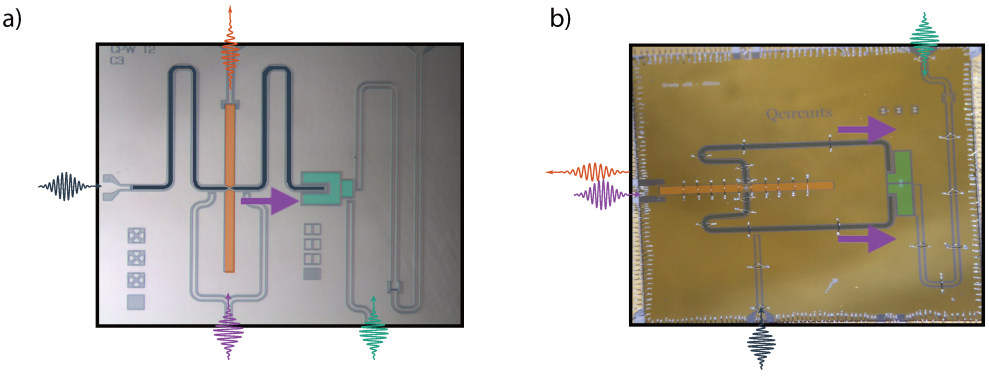


Figure 3.12: a) False color optical image of a previous version of the Quantum Node without symmetrical decoupling of the transmon from the common mode. The pump applied through an on-chip symmetrical coupler drives the qubit on a single side. b) False color optical image of the current design featuring the symmetrical decoupling. The pump applied via the buffer port splits symmetrical along both memory arms and drives the qubit symmetrical thus inducing no potential difference across its junction. On both, colored wave packet indicates the driving port for each mode and the purple arrows illustrate the qubit driving by the pump.

Part II

# PREPRINTS OF THE EXPERIMENTAL RESULTS

# 4

# SEQUENTIAL MEASUREMENT OF A SUPERCONDUCTING QUBIT

> La manière dont on imagine est souvent plus instructive que ce qu'on imagine.
>
> G. Bachelard

We here reproduce the preprint presenting the main experiment done during this work: the sequential measurement of a superconducting qubit. The authors of this work are Théau Peronnin, Danijela Markovic, Quentin Ficheux and Benjamin Huard. This preprint is accepted for publication in Physical Review Letters.

NOMENCLATURE MODIFICATION Contrary to Chap. 3 we denote here the high Q resonator as *readout* instead of *memory* and do not mention the dedicated readout resonator of the transmon. This change was made following the advice of a referee for the purpose of clarity, as in this experiment the qubit's readout is made using the high Q resonator. Labels are also changed accordingly.

ABSTRACT We present a superconducting device that realizes the sequential measurement of a transmon qubit. The device disables common limitations of dispersive readout such as Purcell effect or transients in the cavity mode by turning on and off the coupling to the measurement channel on demand. The qubit measurement begins by loading a readout resonator that is coupled to the qubit. After an optimal interaction time with negligible loss, a microwave pump releases the content of the readout mode by upconversion into a measurement line in a characteristic time as low as 10 ns, which is 400 times shorter than the lifetime of the readout resonator. A direct measurement of the released field quadratures demonstrates a readout fidelity of 97.5 % in a total measurement time of 220 ns. The Wigner tomography of the readout mode allows us to characterize the non-Gaussian nature of the readout mode and its dynamics.

ACKNOWLEDGEMENT We thank Zaki Leghtas, Raphaël Lescanne, Mazyar Mirrahimi, Pierre Rouchon, Alain Sarlette, Hubert Souquet-Basiege, Matthias Droth, Marco Marciani, and Alexander Korotkov for fruitful interactions over the course of this project. The device was fabricated in the cleanrooms of Collège de France, ENS Paris, CEA Saclay, and Observatoire de Paris. The Traveling Wave Amplifier was provided by

the team of Will Oliver at Lincoln labs. The project was partly supported by Agence Nationale de la Recherche under project ANR-14-CE26-0018 and by the European Union's Horizon 2020 research and innovation programme under grant agreement No 820505.

## 4.1 EXPERIMENT DESCRIPTION AND RESULTS

### 4.1.1 *Motivation*

One of the main differences between quantum and classical physics lies in the fact that a measurement inherently disturbs a quantum system. When the measurement does not destroy the system (Quantum Non Demolition measurement or QND), it leads to a backaction that updates its wavefunction. A basic measurement model introduces a probe, which is an ancillary quantum system. The probe is prepared in a given state before interacting with the system under scrutiny for a time $t_{\mathrm{int}}$, which is able to generate an entangled state between probe and system. After this pre-measurement step, the probe is sent to a detector. A random outcome is selected, which leads to the collapse of the system into the state corresponding to that outcome [64].

The inner mechanics of that measurement process can be illustrated in Circuit quantum-electrodynamics (circuit-QED). Owing to the dispersive interaction, a driven stationary microwave mode can act as a probe of the state of a coupled superconducting qubit. The output of the stationary mode is recorded and leads to a continuous measurement record. The record can then be integrated in time to implement an effective single projective measurement [65], or taken into account as a function of time to determine the quantum trajectory followed by the qubit [66–70] or even to realize measurement based feedback [71–75]. However, the three steps of the basic measurement process are simultaneous, as the probe gets refilled and leaks out information during the interaction time.

Here, we present a circuit-QED experiment, where the measurement of a qubit in the $\{|g\rangle, |e\rangle\}$ basis is separated in the three sequential steps of the basic measurement model. The device enables the qubit readout based on tunable cavity couplers that were proposed in the past [11, 76]. For that purpose, we have designed and realized a transmon qubit coupled to a high-Q microwave readout resonator whose state can be flushed on-demand into an output line (see Fig. 4.1a). The release characteristic time can be as short as 10 ns, thus considerably improving a former 3D version of this device [38]. The readout resonator is initialized in a coherent state and evolves unitarily in interaction with the qubit for a time $t_{\mathrm{int}}$. Finally the quantum state of the readout resonator is released into the transmission line and measured, thus revealing information about the qubit state. Interestingly, the scheme alleviates the usual trade-off between QND measurement speed and fidelity by disabling the link between measurement time and qubit relaxation rate [12, 77, 78] and strongly shortening transients in resonator population [78–80], without resorting to the complexity of longitudinal coupling [47, 81, 82]. We obtain performances that are close to state-of-the-art for qubit readout [12]

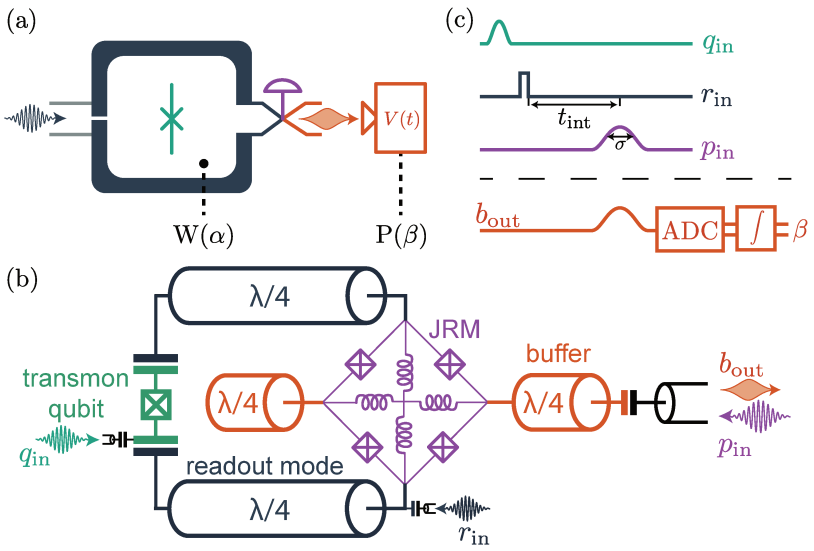


Figure 4.1: (a) The readout resonator (dark gray) is first prepared in a coherent state to probe a transmon qubit. Owing to the dispersive interaction between them, the resonator and the qubit evolve unitarily during a time $t_{\text{int}}$. The readout mode is then upconverted and released into an output line (via purple valve). The complex amplitude $\beta$ of the released mode is encoded in the recorded output voltage $V(t)$. Both the Wigner function $W(\alpha)$ of the readout mode and the probability distribution $P(\beta)$ can be measured. (b) Scheme of the device. The readout mode is a $\lambda/2$ coplanar waveguide resonator (dark gray) that is capacitively coupled to a transmon qubit (green). The readout resonator is coupled to another $\lambda/2$ resonator (buffer in orange) by a Josephson Ring Modulator (JRM in purple). The readout resonator is driven by $r_{\text{in}}$, the transmon (green) by $q_{\text{in}}$, the buffer resonator (orange) outputs in $b_{\text{out}}$, and the JRM is pumped at amplitude $p_{\text{in}}$ by the buffer input. (c) Pulse sequence of the qubit measurement (top) and the released field measurement scheme (bottom).

with a fidelity of 97.5 % in a total time of 220 ns, which shows that our device could be an excellent technical choice once its coupling rates are optimized.

### 4.1.2 *Device description*

The key element of our sequential measurement is a readout mode that couples to a qubit and which is able to store a microwave field and release it on-demand into an output line. In order to realize it, we have used an upgraded version of the Superconducting Quantum Node [38] by coupling it to a transmon qubit. Instead of using 3D architecture as in our previous work, the device (see Fig. 4.1b) is made in coplanar waveguide geometry (CPW) with Niobium on Silicon and Al/AlOx/Al Josephson junctions. The Quantum Node is made of two CPW $\lambda/2$ resonators that are coupled via a Josephson Ring Modulator (JRM) in their center and is cooled down below 30 mK. The readout resonator has a frequency $\omega_r = 2\pi \times 3.73$ GHz and a lifetime $T_r = 4.0$ $\mu$s. The shorter buffer resonator has a frequency $\omega_b = 2\pi \times 10.22$ GHz and is intentionally much more lossy as it is connected to an output transmission line with a rate $\kappa_b = 2\pi \times 21$ MHz.

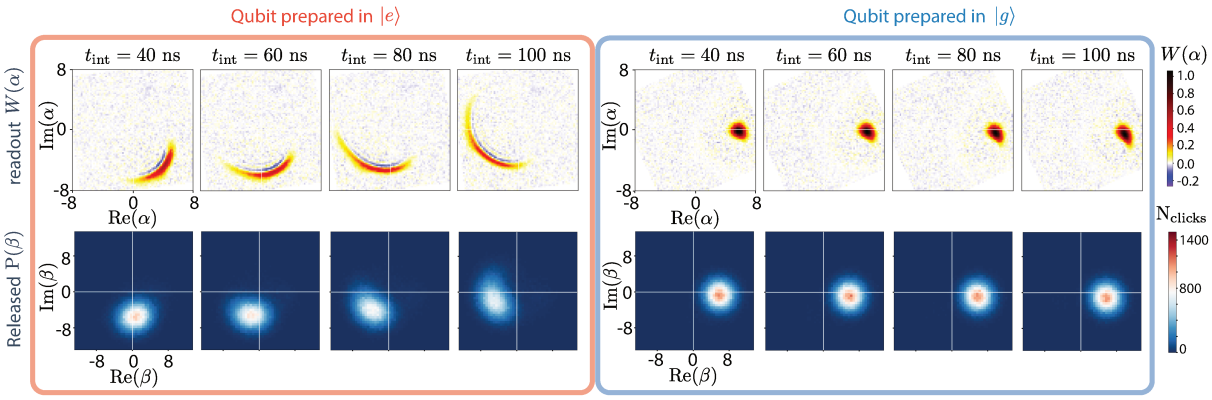


Figure 4.2: Top row: measured Wigner function $W(\alpha)$ of the readout mode after various interaction times $t_{\rm int}$ for a qubit initialized in $|e\rangle$ or $|g\rangle$ and initial coherent state amplitude $\alpha_0 = 5.8$. A global rotation of the quadrature phase space was done numerically (see 4.2 for details). Bottom row: corresponding histograms of the measured complex amplitude $\beta$ of the output field (see text for definition) after it has been released into the transmission line following the interaction time $t_{\rm int}$ for $10^5$ realizations of the experiment.

Close to flux quantum in the Josephson ring, the coupling Hamiltonian is dominated by a three-wave mixing interaction term between the readout mode ($\hat{r}$), the buffer mode ($\hat{b}$) and a common mode of the device that is localized in both arms (see fig. 4.7 of supplementary materials) When the latter is off-resonantly driven by a pump of amplitude $p_{in}$ and frequency $\omega_p = \omega_b - \omega_r$, the effective coupling is described by the beam-splitter Hamiltonian $\hat{H}_{\rm bs} = \hbar(g\hat{b}^\dagger\hat{r} + g^*\hat{b}\hat{r}^\dagger)$, where the conversion rate $g$ is proportional to the pump amplitude $p_{in}$ [83]. With the addition of a frequency conversion between readout and buffer modes, turning on the pump thus results in an effective tunable coupling rate of the readout mode to the output line [25, 38]. In practice, we used a smoothed time dependence of the pump amplitude $p_{\rm in}(t) \propto \left(\cosh\left(\sqrt{\pi/2}t/\sigma\right)\right)^{-1}$ in order to turn on or off the coupling (Fig. 4.1c). While the readout mode can be emptied in a timescale as short as $\sigma_{\rm min} = 10$ ns (see 4.2), we obtained the highest measurement fidelity for a time $\sigma = 28$ ns, and we consider this case only in the rest of the letter.

The system to measure is a transmon qubit with frequency $\omega_q = 2\pi \times 4.45$ GHz, lifetime $T_1 = 6.1$ $\mu$s and coherence time $T_2 = 9.2$ $\mu$s. Crucially, the symmetry of the superconducting circuit is chosen to cancel out its coupling to the common mode while preserving the coupling to the $\lambda/2$ mode of the readout resonator. Therefore the large pump powers have no detrimental effect on the transmon during release. A previous design without this symmetry showed that the pump would otherwise ionize the transmon [48]. The qubit and readout modes are dispersively coupled so that the effective first order interaction term reads $-\hbar\chi\hat{r}^\dagger\hat{r}|e\rangle\langle e|$ where $\chi = 2\pi \times 2.1$ MHz. Once the qubit is prepared in a given state (Fig. 4.1c), the experiment starts by a displacement of the initially empty readout mode (via port $r_{\rm in}$) in 10 ns, which is short enough compared to $1/\chi$ to prepare the readout mode in the coherent state $|\alpha_0\rangle$ irrespective of the qubit state. The measurement probe is thus initialized in a deterministic state and can now interact with the qubit under a unitary evolution for a time $t_{\rm int}$. After this time, the content of the readout mode is released into the transmission line by

upconversion to the buffer frequency using a pump pulse. It is finally amplified and measured to extract its complex amplitude $\beta$ as defined below.

### 4.1.3 *Dynamic of the interaction*

Before discussing how to retrieve the information on the qubit state from the final measurement of the released field, we can benefit from the sequential aspect of the process to experimentally investigate the dynamics of the readout mode during its interaction with the qubit. The dispersive interaction leads to a constant readout amplitude $\langle \hat{r}(t_{\text{int}}) \rangle = \alpha_0$ in the rotating frame at $\omega_r$ when the qubit is in $|g\rangle$, while its phase increases linearly in time $\langle \hat{r}(t_{\text{int}}) \rangle = \alpha_0 e^{i\chi t_{\text{int}}}$ when in $|e\rangle$. This average behavior can be seen as an apparent rotation of the measured Wigner functions $W(\alpha)$ in the quadrature phase space of the readout mode as interaction time increases (Fig. 4.2) only when the qubit is prepared in $|e\rangle$. The Wigner tomography is here realized using the qubit as a photon number parity detector as in previous works [84–87].

In order to read out the state of the qubit as well as possible, it is desirable to maximize the distance between the states of the released microwave mode corresponding to $|g\rangle$ and $|e\rangle$. It was proposed in Ref. [11] that using the superconducting qubit nonlinearity to generate squeezing could help reducing the overlap between the two states. From the measured Wigner functions (Fig. 4.2), it appears that the state of the readout mode is not a coherent state when the qubit is excited, as shown by a non Gaussian shape and by the development of negativities [88]. The ability to realize a direct Wigner tomography of the readout mode, and the measurement of negativities, demonstrates that the measurement probe has not decohered entirely prior to the release into the transmission line. The quantum-classical boundary occurs at a later stage. The dynamics can be understood by expanding the interaction Hamiltonian at least to the next order [89], which gives

$$\hat{H}_{\text{int}}/\hbar = -\chi \hat{r}^\dagger \hat{r} |e\rangle\langle e| - K_g \hat{r}^{\dagger 2} \hat{r}^2 |g\rangle\langle g| - K_e \hat{r}^{\dagger 2} \hat{r}^2 |e\rangle\langle e|. \tag{4.1}$$

The Kerr rates could be independently measured to be $K_g = 2\pi \times 8$ kHz and $K_e = 2\pi \times 37$ kHz (see 4.2 for details). Interestingly, the self-Kerr rate of the readout mode is much larger when the qubit is excited than when it is in the ground state, which explains why the Wigner function shape is little distorted for $|g\rangle$ and strongly distorted for $|e\rangle$. A simple way to qualitatively understand the shape of the Wigner function is to realize that the Kerr term induces an angular velocity in the quadrature phase space that increases with field amplitude. A quantitative study reveals that yet higher order terms need to be taken into account at the large number of photons $|\alpha_0|^2 \approx 34$ that we are using (see 4.2 for details). It is interesting to note that it would be possible to use a single junction for releasing the readout mode [25]. However, the JRM we use allows us to tune the cross-Kerr terms by the magnetic flux in the ring (see 4.2 for details). In this work, we set the flux to cancel out the cross-Kerr effects between the buffer and the readout mode and between the readout mode and the common mode. Hence the strong pump does not shift the resonance frequencies.

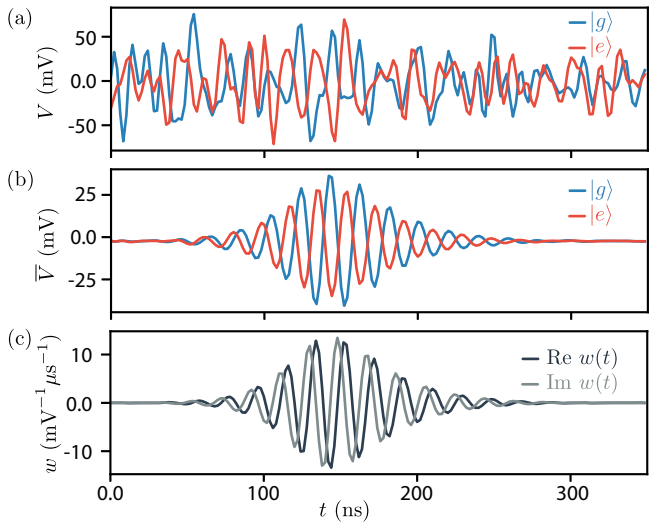


Figure 4.3: (a) Raw traces of the output voltage $V(t)$ for two realizations of the experiment with the qubit prepared either in $|g\rangle$ or in $|e\rangle$ and with an initial displacement $\alpha_0 = 5.8$ and interaction time $t_{\text{int}} = 100$ ns. (b) Average traces over $10^5$ realizations. (c) Real and imaginary part of the weight function $w(t)$ from which the complex amplitude of the released mode is obtained.

### 4.1.4 *Signal analysis*

By releasing the content of the readout mode into the output line by upconversion to $\omega_b$, we can access the information about the qubit that is encoded in the readout resonator. The emitted pulse is amplified by a Traveling Wave Parametric Amplifier [90] followed by cryogenic and room temperature amplifiers (see 4.2). It is finally down-converted to 50 MHz and digitized as a voltage $V(t)$ (Fig. 4.1c). A typical trace $V(t)$ of a single realization is shown in Fig. 4.3a for a qubit prepared in $|g\rangle$ or $|e\rangle$. How to recover the information about the qubit state from the final measurement of the released field? Our solution consists in defining a complex amplitude $\beta$ for the released mode by demodulating the single measurement records $V(t)$ by a single complex weight function $w(t)$ to be determined.

$$\beta = \int V(t)w(t)dt. \tag{4.2}$$

We first average the traces of $10^5$ realizations of the experiment for $t_{\text{int}} = 100$ ns and $\alpha_0 = 5.8$ (Fig. 4.3b). The averages $\overline{V}_{|e,g\rangle}(t)$ reveal the 50 MHz modulation we used and the temporal envelope of the releasing pump $p_{\text{in}}(t)$. We find (see [91] for details) that a way to faithfully map the intraresonator complex field amplitude $\alpha$ to the demodulated amplitude $\beta$, independently of the qubit state, consists in choosing a weight function $w(t)$ whose real part is $\text{Re}[w(t)] = \left(\overline{V}_{|e\rangle}(t) - \overline{V}_{|g\rangle}(t)\right)/2\lambda$ (Fig. 4.3 c). Its imaginary part $\text{Im}[w(t)]$ is then constructed by shifting the phase of the carrier modulation by $\pi/2$. The prefactor $\lambda^{-1}$ is adjusted so that $\beta$ is dimensionless and equal on average to $\alpha_0$ in the case $t_{\text{int}} = 0$. As can be seen in Fig. 4.2, with this choice, the probability densities $P_{g,e}(\beta)$ to measure a complex amplitude $\beta$ for a qubit prepared in $|g\rangle$ and in $|e\rangle$ are indeed smoothed versions of the intraresonator Wigner functions owing to the 11 % efficiency of the detection setup (see 4.2).

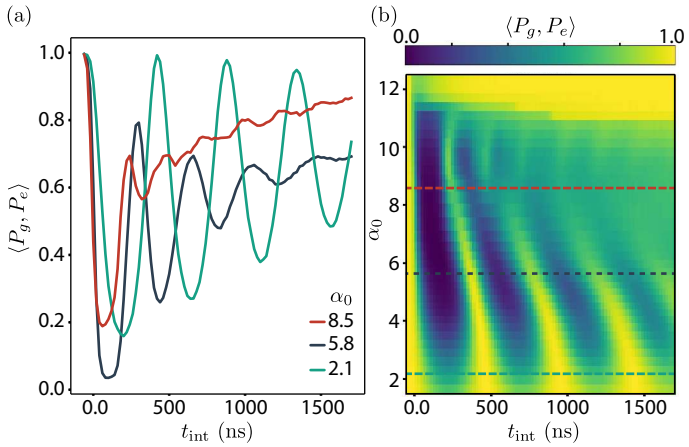


Figure 4.4: (a) Scalar product of the measured distributions $P_{g,e}(\beta)$ of released mode amplitudes when the qubit is prepared in $|g\rangle$ or $|e\rangle$ as a function of interaction time $t_{\text{int}}$, and for various values of initial displacement $\alpha_0$. (b) Same scalar product as a function of $\alpha_0$ and $t_{\text{int}}$. Colored dashed lines indicate cuts corresponding to Fig. (a).

### 4.1.5 *Effective readout*

The qubit measurement then comes down to determining whether a measured amplitude $\beta$ is more likely to occur if the qubit is in the ground or excited state. It is straightforward once we know the distributions of complex amplitudes $P_g(\beta)$ and $P_e(\beta)$. We stress that since the readout and released modes are not in a Gaussian state, there is information in both quadratures, which justifies the use of a phase preserving amplifier. The 2D scalar product between the histograms

$$\langle P_g, P_e \rangle = \frac{\int_{\mathbf{C}} \mathrm{d}\alpha P_g(\alpha) P_e(\alpha)}{\left(\int_{\mathbf{C}} \mathrm{d}\alpha P_g(\alpha)^2\right)^{1/2} \left(\int_{\mathbf{C}} \mathrm{d}\alpha P_e(\alpha)^2\right)^{1/2}} \tag{4.3}$$

quantifies the distinguishability of the measurement outcomes. Fig. 4.4 represents the measured overlap of the two distributions as a function of interaction time $t_{\text{int}}$ and for three values of the initial amplitude $\alpha_0$ of the readout mode.

As mentioned above, the dispersive interaction leads to a global rotation in the quadrature phase space of the readout mode when the qubit is in $|e\rangle$. With dispersive interaction alone, the even and odd integer values of $t_{\text{int}}\chi/\pi$ would thus correspond to maxima and minima of $\langle P_g, P_e \rangle$, which are reached for full turns or half turns of the average complex amplitude of the readout mode. Fig. 4.4 illustrates which phenomena determine the amplitude $\alpha_0$ that maximizes the qubit measurement fidelity. If $\alpha_0$ is too low, the separation between the distribution supports does not overcome the noise. It is what sets the minimum overlap of the green curve at $\alpha_0 = 2.1$, on top of the residual internal losses of the readout mode that dampen the oscillations. If $\alpha_0$ is too large, the higher order terms in the interaction Hamiltonian lead to a uniform distribution in phase, and the time oscillations disappear (red curve at $\alpha_0 = 8.5$). The full dependence of the overlap $\langle P_g, P_e \rangle$ as a function of $\alpha_0$ and $t_{\text{int}}$ (Fig. 4.4b) can be used to determine the optimal measurement conditions. The minimal overlap $\langle P_g, P_e \rangle = 3.4$ % is reached at $\alpha_0 = 5.8$ and $t_{\text{int}} = 100$ ns as in Fig. 4.2 and 4.3. Interestingly, at large amplitudes ($7 < \alpha_0 < 10$) the oscillations become more complicated as a double periodicity appears

and is not understood yet (red curve). At very large values ($\alpha_0 > 10$) the qubit is ionized [48], which sets a stringent bound on the number of photons for quantum non-demolition readout. We note that this platform seems suited to study the dynamics of ionization of the qubit.

In order to characterize the measurement operation for applications, we associate values of $\beta$ where $P_g(\beta) > P_e(\beta)$ to the measurement outcome "g" and "e" otherwise. We can then define the measurement errors $\mathcal{E}_e$ (respect. $\mathcal{E}_g$) as obtaining the result "g" (respect. "e") after having prepared the qubit in $|e\rangle$ (respect. $|g\rangle$). We find $\mathcal{E}_e = 3.4\%$ and $\mathcal{E}_g = 1.6\%$. They can be partially explained by the qubit thermal population of 0.8%, the finite qubit lifetime (1.7% in $\mathcal{E}_e$) and by the 99.5% fidelity of the $\pi$ pulse from ground excited states (see 4.2). The remaining arises from imperfect separation of the histograms. The average fidelity is $\mathcal{F} = 1 - \frac{\mathcal{E}_g + \mathcal{E}_e}{2} = 97.5\ \%$ for a total qubit measurement time is 220 ns. Finally, one may wonder how the release process affects the qubit. We have characterized how QND the measurement is by determining the probability $\mathcal{F}_{\mathrm{QND}} = 95\ \%$ that two successive measurements find the same outcome.

### 4.1.6 *Perspectives*

In conclusion, we have implemented the sequential measurement of a transmon where the probe initialization, interaction with the qubit and detection are all separated in time and space. Our readout scheme is insensitive to the Purcell effect since it is always coupled to a high Q resonator except during release when the buffer resonator acts as a Purcell filter anyway. By releasing the probing field on demand, we also avoid common limitations due to slow reset of the cavity mode in dispersive measurements. Further increasing both $\chi$ and $\kappa_b$ by an order of magnitude should straightforwardly lead to measurement times beyond state-of-the art. The use of a JRM as a switch between the readout mode and the transmission line opens interesting perspectives. Indeed, the JRM can also act as a built-in amplifier [92, 93] (by applying a pump at the frequency $\omega_p = \omega_b + \omega_r$) to amplify the probing field as it is released into the transmission line. Besides, by increasing the participation ratio of the JRM in the readout mode, one could not only adjust but even cancel out the Kerr rates $K_g$ or $K_e$ of the readout mode by tuning the magnetic flux in the JRM. Furthermore it would be interesting to retrieve the information that remains in the autocorrelation of the measured voltage $V(t)$. Indeed, the qubit state dependent Kerr terms in $K_g$ and $K_e$ should allow for extra information to be retrieved in this way [94]. Finally, one could use an ancillary resonator dispersively coupled to the qubit to measure and demonstrate the entanglement between qubit and readout mode along their joint evolution as in Ref. [95].

## 4.2 SUPPLEMENTARY INFORMATIONS

### 4.2.1 *Measurement setup*

#### 4.2.1.1 *Microwave setup*

The sample is cooled down to $T \approx 30$ mK in a BlueFors®dilution refrigerator. The scheme of the microwave input and output lines is provided in Fig. 4.5. The readout, pump and qubit pulses are generated by modulation of continuous microwave tones produced respectively by AnaPico®(APSIN12G), Agilent®(E8752D)and AnaPico®(APSIN12G) sources set at the frequencies $f_r - 100$ MHz, $f_b - f_r + 150$ MHz and $f_q + 128$ MHz. The pump tone is modulated through a single sideband mixer and the readout and qubit tones are modulated through regular mixers. The parasitic sidebands at the output of the mixers are far detuned from any frequency of interest and are neglected. The RF modulation pulses are generated by a 4 channels Tektronix®Abitrary Waveform Generator (AWG5014C) with a sample rate of 1 GS/s. Those pulses are of frequency 100 MHz, 150 MHz and 128 MHz. In order to ensure phase stability during the measurement, the local oscillator used for the demodulation of the output signal is not independent from the other ones. It is generated by mixing the output of the two sources that are close to the readout and pump frequencies, followed by the filtering out of the lower sideband. We thus retrieve a tone at frequency $(f_r - 100\text{ MHz}) + (f_b - f_r + 150\text{ MHz}) = f_b + 50$ MHz which is used to mix the signal down to 50 MHz before digitization.

The signal coming out of the buffer mode is filtered using a wave-guide with a cutoff frequency at 9.8 GHz in order to protect the following amplification stage to be affected by the strong reflected pump tone. The signal is first amplified by a Traveling Wave Parametric Amplifier (provided by W. Oliver group at Lincoln Labs). We tuned the pump frequency ($f_{\text{TWPA}} = 7.773$ GHz) and power in order to reach a gain of 19 dB at 10.220 GHz. The followup amplification is performed by a High Electron Mobility Transistor (HEMT) amplifier (from Caltech) at 4 K and by two room temperature amplifiers.

#### 4.2.1.2 *Sample description*

The sample was fabricated on a substrate of undoped Si (111) of dimension $8.67 \times 8.16 \times 0.28$ mm. The ground planes and resonators are made of 150 nm of sputtered Nb after HF treatment. An optical lithography is performed using a laser writer before dry etching with SF6 the Nb layer. The Josephson junctions of the transmon and the JRM are fabricated using electronic lithography followed by an angle deposition of Al/AlOx/Al in a Plassys MEB550S evaporator. A good contact between Al and Nb is ensured by ion milling the Nb oxide in the Plassys evaporator prior to the evaporation over the overlap pads of $50 \times 50$ $\mu$m$^2$. The Nb sputtering was done in the Quantronics group at CEA Saclay, the wafer dicing at Observatoire de Paris, the Al evaporation in a Plassys®ebeam evaporator and the laser writing at College de France, the electronic lithography at ENS Paris and the HF treatment at Paris Diderot. All measurements were performed at ENS de Lyon.

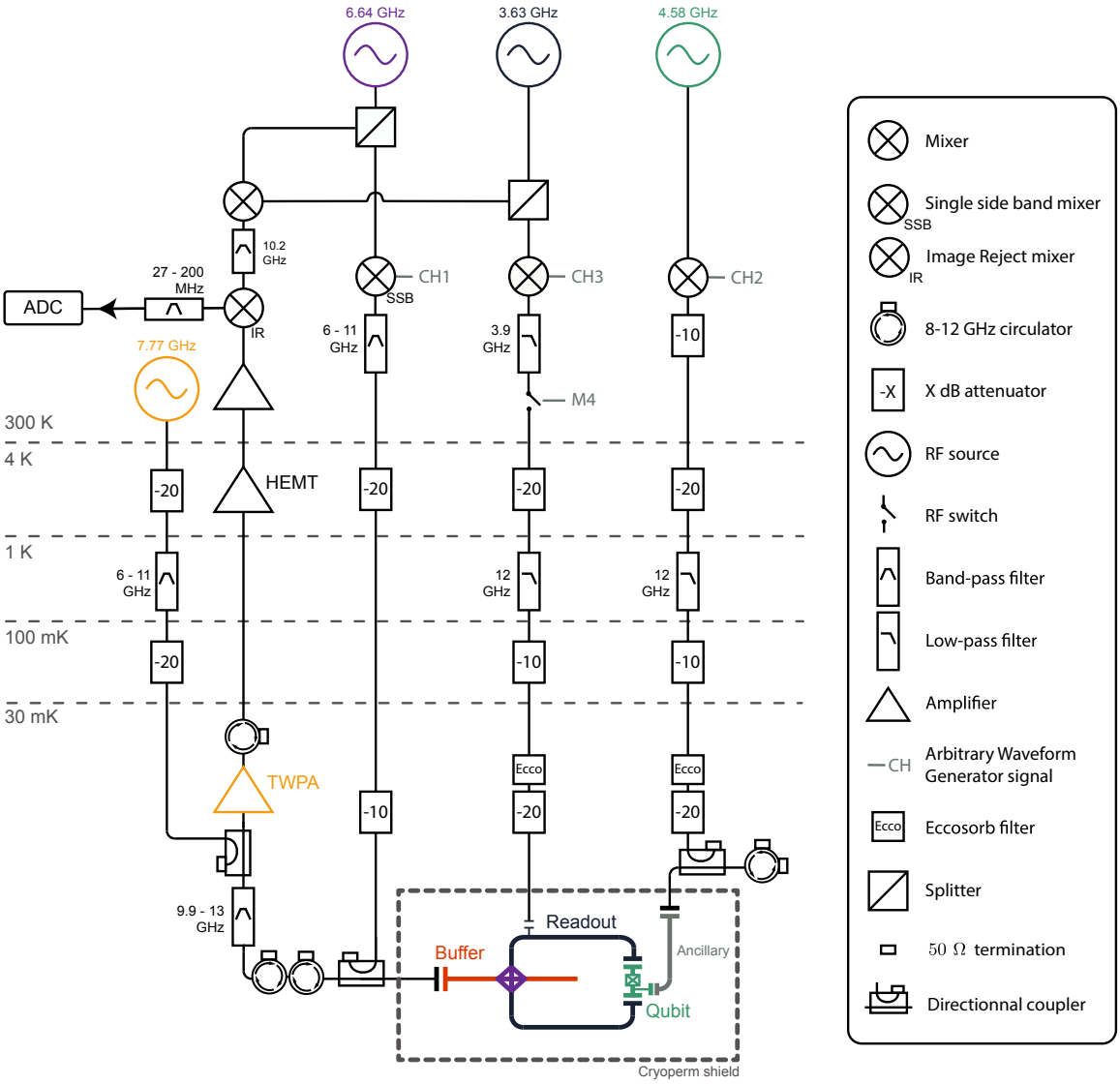


Figure 4.5: Wiring diagram. The RF source colors refer to the frequency of the matching element in the devices up to the modulation frequencies. The unused ancillary 6.3 GHz resonator is coupled to a transmission line at $\kappa_{\mathrm{anc}} = 2 \times 2\pi$ MHz. The $9.9 - 13$ GHz band-pass filter is the combination of a high pass filter (20 cm long WR62 waveguide) and a discrete low pass filter (Minicircuits®).

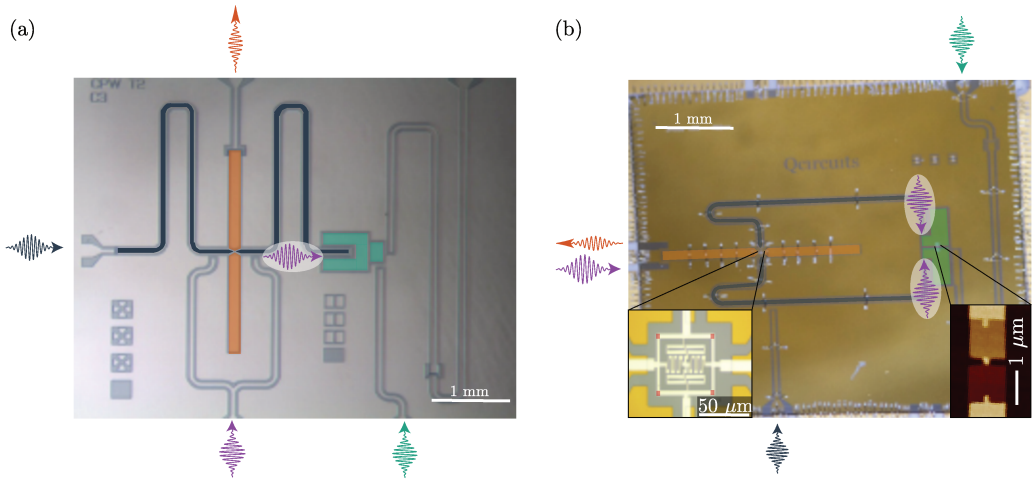


Figure 4.6: False color optical images comparing a previous design where the pump (purple) parasitically directly drives the transmon dipole (left) and the current design where this parasitic driving is avoided by symmetry (right). As in Fig. 1, the buffer is in orange, the readout resonator in dark gray and the transmon in green. Insets show the JRM (left) and single junction of the transmon qubit (right).

The readout and the buffer are $\lambda/2$ resonators in coplanar waveguide architecture. They are coupled in their middle by the JRM. The readout resonator has a gap width of 50 $\mu$m and a central conductor width of 84 $\mu$m whereas the buffer gap width is 10 $\mu$m and its central conductor width is 220 $\mu$m. This design is intended to minimize the buffer characteristic impedance (here 25 $\Omega$) in order to maximize the participation ratio of the JRM in that mode, without compromising too much on the reproducibility of the fabrication. The readout resonator is symmetrically coupled (see Fig. 1c) to the transmon qubit. This is a trick that enables the device to withstand large enough pump powers without affecting the transmon qubit. Indeed, the $\lambda/2$ resonator that acts as the readout mode provides an electric field that couples directly to the transmon dipole. However, the pump populates the common mode between the two resonators (Fig. 4.7c) and which develops the same voltage on each end of the the $\lambda/2$ resonator and develop no voltage difference between the antennas of the transmon qubit. Hence, the pump induces negligible current across the transmon junction. This symmetric design thus reduces the coupling of the qubit to the pump drive by an estimated 20 dB compared to an unpublished previous design (Fig. 4.6). This improvement was determined by measuring the minimal pump power that leads to ionization of the transmon similarly to what we have done in Ref. [96].

#### 4.2.1.3 *Device Hamiltonian*

The full device Hamiltonian reads

$$\hat{\mathcal{H}} = \hat{\mathcal{H}}_0 + \hat{\mathcal{H}}_{\text{JRM}} + \hat{\mathcal{H}}_{\text{int}}, \tag{4.4}$$

where the interaction free Hamiltonian is

$$\hat{\mathcal{H}}_0 = \hbar\omega_{\text{b}}\hat{b}^\dagger\hat{b} + \hbar\omega_{\text{r}}\hat{r}^\dagger\hat{r} + \hbar\frac{\omega_{\text{q}}}{2}\hat{\sigma}_z, \tag{4.5}$$

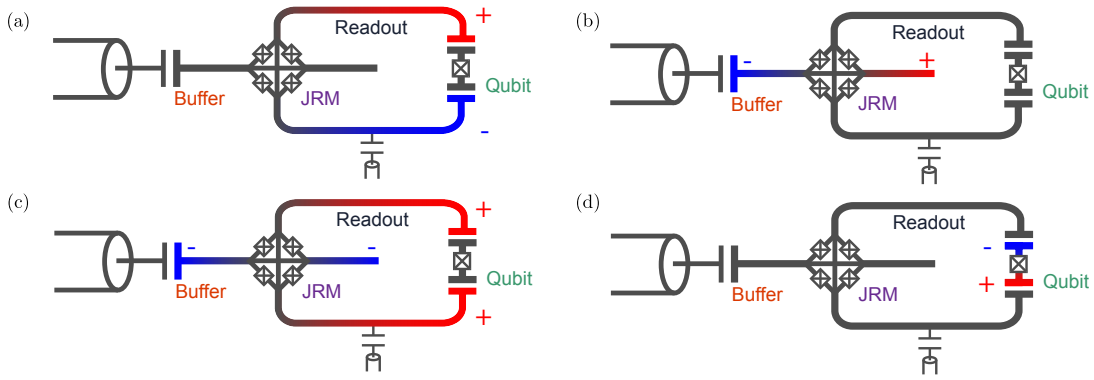


Figure 4.7: Scheme of the resonant modes that are used in the experiment. The color indicates the voltage as a function of position at maximum field amplitude in an oscillation. The readout mode (a) and the buffer mode (b) are $\lambda/2$ resonators. The common mode (c) extends over both CPW lines and does not couple to the transmon mode (d).

the JRM Hamiltonian at the optimal flux point is [5]

$$\hat{\mathcal{H}}_{\mathrm{JRM}} = \hbar g_3 (\hat{r} + \hat{r}^\dagger)(\hat{b} + \hat{b}^\dagger)(\hat{c} + \hat{c}^\dagger), \tag{4.6}$$

The mode $c$ is the common mode of the device (Fig. 4.7c) and is driven by the pump. The dispersive interaction term between the qubit and the readout mode reads (see for instance Ref. [94])

$$\hat{H}_{\mathrm{int}}/\hbar = -\chi \hat{r}^\dagger \hat{r} |e\rangle\langle e| - K_g \hat{r}^{\dagger 2}\hat{r}^2 |g\rangle\langle g| - K_e \hat{r}^{\dagger 2}\hat{r}^2 |e\rangle\langle e|. \tag{4.7}$$

When driven by the pump at $\omega_p = \omega_b - \omega_r$, the off-resonant common mode is occupied by a coherent state such that we can replace $\hat{c}$ by a scalar number $p$ [5]. In the rotating wave approximation, only two terms remain in $\hat{\mathcal{H}}_{\mathrm{JRM}}$, which then reads

$$\hat{\mathcal{H}}_{\mathrm{JRM}} = \hat{H}_{\mathrm{bs}} = \hbar (g \hat{b}^\dagger \hat{r} + g^* \hat{b} \hat{r}^\dagger), \tag{4.8}$$

where $g = p g_3$ is proportional to the pump amplitude $p_{\mathrm{in}}$.

### 4.2.2 *Calibration*

#### 4.2.2.1 *Calibration of the quadratures and photon number of the readout mode*

The calibration of the readout mode quadratures in the Wigner functions and of the photon number in the readout mode were done by monitoring the free temporal evolution of the occupations of the first Fock states. To do so, we apply a readout mode displacement square pulse of 10 ns (or 20 ns for Wigner tomography) with a 2 ns Gaussian edge of a given amplitude to be calibrated in units of inner readout mode quadratures. We then wait for a time $t$ to let the readout mode decay before applying a selective $\pi$ pulse to the qubit at the frequency $\omega_q$ (resp. $\omega_q - \chi$). Hence we only excite the qubit if there is 0 photon (resp. 1 photon) in the readout mode. The selective $\pi$ pulse has a temporal envelope in $1/\cosh(\sqrt{\pi/2}t/\sigma)$ with a spread $\sigma = 200$ ns. We

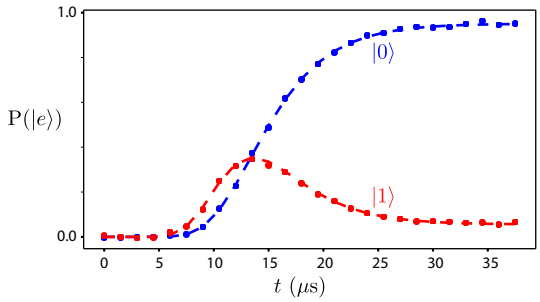


Figure 4.8: Example of photon number calibration by monitoring the readout state during decay. Squares: Measured occupation probabilities of Fock states $|0\rangle$ and $|1\rangle$. Dashed lines: theory prediction with $\kappa_r = 1/T_{\mathrm{r}} = 250 \times 2\pi$ kHz and initial photon number $\bar{n} = 31.8$. Red corresponds to a selective $\pi$ pulse for 1 photon in the readout mode, blue to 0 photon.

assume a constant decay rate and an initial coherent state $|\alpha\rangle = \left|\sqrt{\bar{n}}\right\rangle$. Therefore the probability to excite the qubit follows

$$\begin{cases} P_{|0\rangle}(|e\rangle) &= e^{-\bar{n}e^{-\kappa_r t}} \\ P_{|1\rangle}(|e\rangle) &= \bar{n}e^{-\bar{n}e^{-\kappa_r t}}e^{-\kappa_r t} \end{cases} \tag{4.9}$$

In Fig. 4.8 are shown the measured occupations in the $|0\rangle$ and $|1\rangle$ readout states as a function of time. The data are reproduced by the above equations provided the decay rate of the readout resonator is $\kappa_r = 1/T_{\mathrm{r}} = 250 \times 2\pi$ kHz and the initial average number of photons $\bar{n}$ is 31.8. Note that the theoretical curves (dashed lines) take into account a 0.95 scaling factor for $P_{|1\rangle}(|e\rangle)$ due to a slight imperfection in the selective $\pi$ pulse at $\omega_q - \chi$. We have repeated this procedure for each displacement amplitude and found the same $\kappa_r$ for all of them. This procedure provided a calibration between displacement amplitude and photon number.

#### 4.2.2.2 *Characterization of the cavity pull and of the Kerr nonlinearities*

The measurement of $\chi$, $K_g$ and $K_e$ was done by monitoring the average phase acquired by the readout field as a function of time depending on the state of the qubit and the average photon number.

Having prepared the qubit in either $|g\rangle$ or $|e\rangle$, we load the readout mode with a coherent state of amplitude $\alpha = \sqrt{\bar{n}}$. We wait for a time $t_{\mathrm{int}}$. We then release the state of the readout mode into the transmission line and record the average phase $\phi(t_{\mathrm{int}}) = \arg(\overline{\beta})$ of the released pulse. The detuning $\delta\omega_r$ between the resonant frequency of the readout resonator and a reference resonant frequency (when the readout resonator is in the vacuum state and for a qubit in $|g\rangle$) can be determined as $\delta\omega_r = \dfrac{d\phi}{dt_{\mathrm{int}}}$. In Fig. 4.9 are shown the measured detuning as a function of photon number in the readout resonator and of qubit state.

Our model for the qubit-readout resonator system in the rotating frame of the readout mode when the qubit is in the ground state, reads

$$\hat{H}_{\mathrm{int}}/\hbar = -\chi\hat{r}^\dagger\hat{r}|e\rangle\langle e| - K_g\hat{r}^{\dagger 2}\hat{r}^2|g\rangle\langle g| - K_e\hat{r}^{\dagger 2}\hat{r}^2|e\rangle\langle e|. \tag{4.10}$$

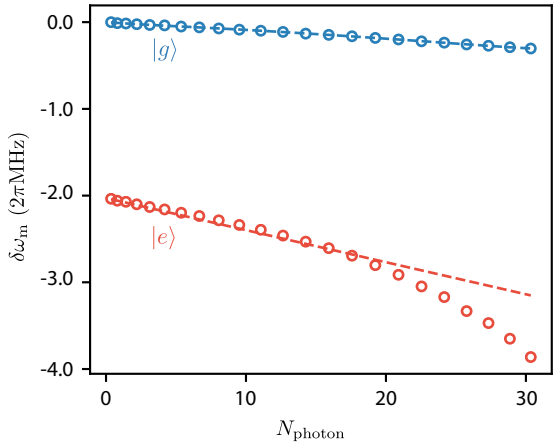


Figure 4.9: Average detuning of the readout resonator as the function of the average photon number and the state of the qubit. Data are cercles and first order fits are dashed lines. As the number of photons increases, the detuning deviates from the linear fit. Hence for the experiment displacement $\alpha = 5.8$ our simple model provides only a qualitative explanation.

| | |
|---|---|
| $\chi/2\pi$ | 2.05 MHz |
| $K_g/2\pi$ | 8.4 kHz |
| $K_e/2\pi$ | 37 kHz |

The cavity pull $\chi = 2.05 \times 2\pi$ MHz can thus be read out as the readout frequency difference between the cases where the qubit is in $|g\rangle$ or $|e\rangle$, when the cavity is in the vacuum. The Kerr terms induce a linear dependence of the readout frequency as a function of average photon number. The Kerr rates $K_g$ and $K_e$ can thus be obtained from the slopes of the curves in Fig. 4.9. At large photon number, a higher order polynomial fit is required to take into account higher order non-rotating terms of the Hamiltonian arising from the expansion of the Josephson cosine potential. As seen in the spiraling shape of the measured Wigner functions (Fig. 2), the readout mode displays much less anharmonicity when the qubit is in the ground state than in the excited state.

#### 4.2.2.3 *Conversion rate and calibration of the coupling rate*

By measuring the reflection coefficient on the buffer port as a function of frequency, one can determine the steady conversion rate $\gamma^r$ between the readout mode and the transmission line directly (see Eq. (216) in Ref. [5]). We have realized this measurement for various pump powers and obtained the measured dependence of $\gamma^r$ on pump amplitude (Fig. 4.10).

This curve can then be used to calibrate how the coupling rate $g$ that enters in the beam-splitter Hamiltonian depends on pump power. The 3-wave mixing Hamiltonian of

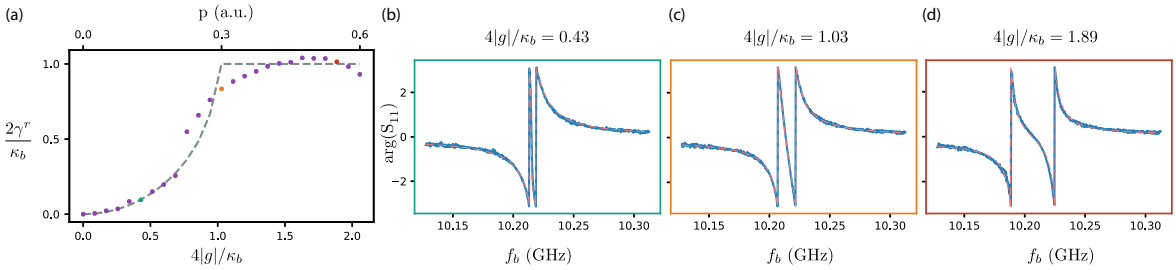


Figure 4.10: (a) Direct coupling measurement (purple square) to the readout mode as a function of the pump amplitude. We obtain the calibration for the coupling g from the fit (dashed gray line). (b) to (d) Blue solid line : phase of the measured reflection coefficient on the buffer port for various pump amplitudes. Red dashed line : corresponding curve obtained by tuning $\gamma^r$, which allows us to plot one dot in (a). The color of each frame corresponds to the color of its corresponding dot in figure (a).

the JRM indeed implies a linear dependence between the coupling rate and the pump amplitude $g(t) \propto p(t)$. In our limit $\kappa_b \gg \kappa_r$, the conversion rate indeed reads [5]

$$\gamma^r = \frac{\kappa_b}{2}\mathrm{Re}\left[1 - \sqrt{1 - 16\frac{|g|^2}{\kappa_b^2}}\right] \tag{4.11}$$

We observe that this model only faithfully reproduces the measurements for small pump powers such that $4|g|/\kappa_\mathrm{b} < 0.7$.

#### 4.2.2.4 *Dynamics of the readout release*

The flushing of the readout mode by the smooth pump pulse is characterized as follows. The readout mode is loaded with a coherent state with amplitude $\alpha = 5.3$. In the following the qubit is assumed to be in its ground state[1]. It is justified by the fact that $\chi \ll \kappa_\mathrm{b}$, for which the release dynamics is similar for the qubit in the ground or in the excited state. A pump pulse with an envelope $p(t) \propto \left(\cosh\left(\sqrt{\pi/2}t/\sigma\right)\right)^{-1}$ is applied for various pump amplitudes and spread (Fig. 4.11). This choice of a smooth pump pulse allows us to limit the spectral broadening of the pump. The Fourier transform of that pulse has the same shape but with a variance $1/\sigma$. In practice, the pump pulse is windowed by a square shaped weight function of duration $8\sigma$. We then measure the remaining average photon number using the technique of cavity state decay as in Fig. 4.8.

The release dynamics is captured by the quantum Langevin equation for the field amplitudes $m$ and $b$ in the rotating frames of the buffer and the readout mode.

$$\begin{cases} \dot{r} &= -ig^\star b - \frac{\kappa_r}{2}r \\ \dot{b} &= -igr - \frac{\kappa_b}{2}b \end{cases} \tag{4.12}$$

Hence,

1 We did not measure the flushing of the readout mode when the qubit is excited

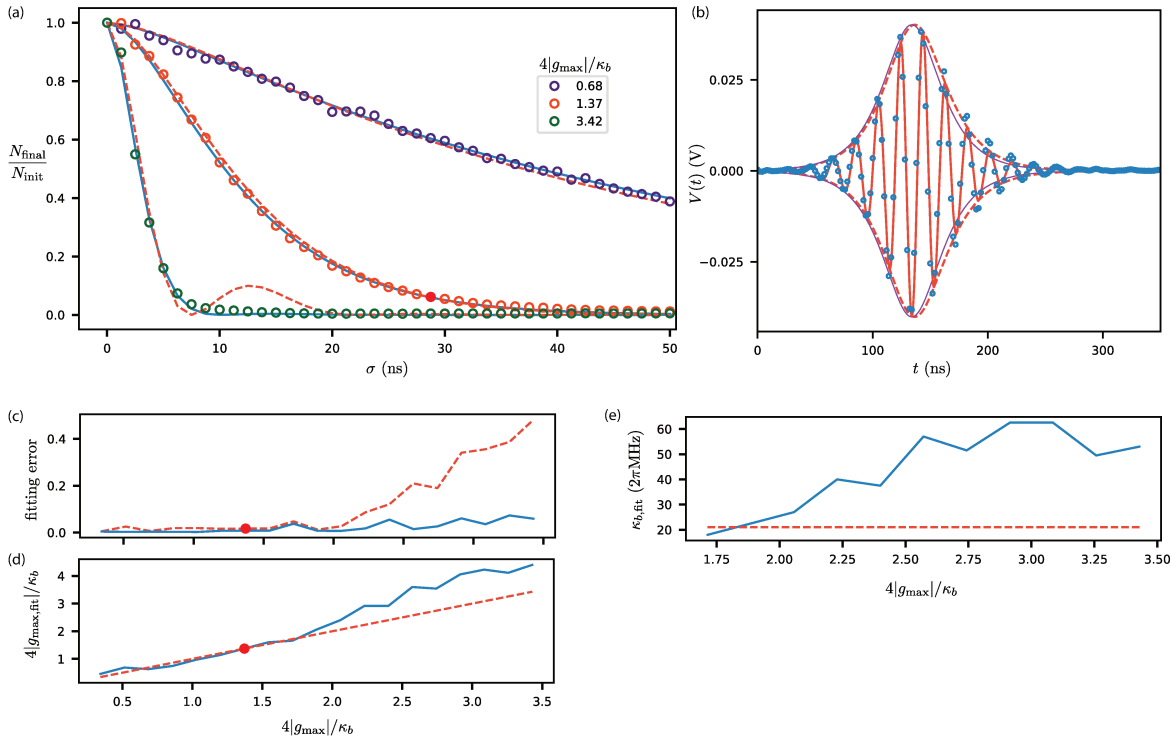


Figure 4.11: (a) Fraction of photons remaining in the readout mode as a function of the spread $\sigma$ of the pump pulse for three pump powers. As in the other panels, the red dot corresponds to the release parameters of the main text. The initial number of photons is $N_{\text{init}} = 28$. Circles: measured photon number fraction through cavity state decay (see Fig. 4.8). Red dashed lines: solutions of (4.13) using the calibrated values of $\kappa_b$ and $g_{\max}$ without fitting parameters. Discrepancies appear for fast flushes between the model and the experiment. We note that an empirical solution can be obtained by effectively increasing $\kappa_b$ and $4|g_{\max}|/\kappa_b$ beyond their calibrated values (blue solid lines). (b) Dots: average recorded signal at the output of the final mixer on the buffer output line when the qubit is in $|g\rangle$, corrected for a DC offset (same as in Fig. 3b). Dashed red line: solution of 4.13 for the buffer amplitude $|b|$. An overall scaling factor is applied as well as an unique offset for the origin of time. Solid red line: same curve with a 51 MHz modulation (50 MHz$+(\chi/2)/2\pi$ because the qubit is in $|g\rangle$) and a fitted initial phase. A pump pulse envelope with the same amplitude is displayed in thin purple line for comparison. (c) Relative fitting error (distance between the curves in (a) and the measured fraction of photon number) as a function of the pump amplitude in units of the independently determined value of $4|g_{\max}|/\kappa_b$. Dashed red line: theory without free parameter. Solid blue line: theory with effective fitted values of $\kappa_b$ and $g_{\max}$. The red dot corresponds to the parameters of the main text. (d) Corresponding effective values of $4|g_{\max}|/\kappa_b$ as a function of the calibrated ones. The dashed line has a slope 1. (e) Corresponding effective values of $\kappa_b$ as a function of the independently calibrated $4|g_{\max}|/\kappa_b$ for pump powers where the theory does not match the experiment. The effective increase of $\kappa_b$ can be interpreted as conversion into extra parasitic modes.

$$\begin{cases} \ddot{r} + \left(\frac{\kappa_b}{2} + \frac{\kappa_r}{2} - \frac{\dot{g}^\star}{g^\star}\right)\dot{r} + \left(|g|^2 + \frac{\kappa_r\kappa_b}{4} - \frac{\kappa_r}{2}\frac{\dot{g}^*}{g^*}\right) r &= 0 \\ g^\star b - i\left(\dot{r} + \frac{\kappa_r}{2} r\right) &= 0 \end{cases} \tag{4.13}$$

with $g(t) = g_{\max}/\cosh\left(\sqrt{\pi/2}t/\sigma\right)$ and $\frac{\dot{g}^\star}{g^\star}(t) = -\frac{\sqrt{\pi/2}\tanh\left(\sqrt{\pi/2}t/\sigma\right)}{\sigma}$.

In Fig. 4.11a are shown the measured readout photon number normalized to the initial number as a function of $\sigma$ and for various pump powers. The numerical solution of the above equation reproduces well these measurements as long as $4|g_{\max}|/\kappa_b$ does not exceed 1.6 (Fig. 4.11c). There, even the average time trace of the buffer output is well captured (Fig. 4.11b).

For the largest pump powers, for which this value is exceeded, the readout mode is flushed more rapidly than theoretically expected. The observed behavior can be captured by allowing to tune the effective values of $\kappa_b$ and $g_{\max}$. The increase of the effective decay rate $\kappa_{\mathrm{b}}$ could be due to the conversion of the readout mode into parasitic unmonitored modes (Fig. 4.11e).

### 4.2.3 *Signal processing*

#### 4.2.3.1 *Demodulation basis construction*

As the readout mode is released into the buffer line, its quantum state is mapped into a propagating microwave mode. How to determine the quadratures of the propagating mode into which the quadratures of the inner readout mode are linearly mapped? Here, the signal is carried by a mode at $\omega_b$ when the qubit is in $|g\rangle$ and $\omega_b - \chi$ when in $|e\rangle$. However, the pulse takes a finite duration corresponding to the temporal extent of the pump pulse. The release operation thus leads to a frequency spread of $\Delta\omega = 1/\sigma$. In our experiment, we have $\Delta\omega = 1/\sigma \approx 2.7\chi$.

Before addressing the general case, let us first disregard this frequency uncertainty due to the qubit state and discuss how to find the quadratures of the propagating mode. One way to determine them would be to measure the average voltage trace at the output of the last mixer in the buffer line detection setup. We denote $\overline{V_{|\alpha\rangle}(t)}$ the average trace when the readout mode is in a coherent state $|\alpha\rangle$. An example of this curve can be found in Fig. 4.11b. The signal coming out of an image reject mixer is oscillating at about 50 MHz so that its amplitude and phase match the ones of the mode close to $\omega_b$ at the input of the image reject mixer. The purpose of this downconversion is to be able to digitize the signal with an acquisition board. We could then construct a demodulation function

$$w_1(t) = \overline{V_{|\alpha=1\rangle}(t)} + i\overline{V_{|\alpha=i\rangle}(t)}. \tag{4.14}$$

We define the complex amplitude $\beta_1 = \int V_\alpha(t) w_1(t) dt$ as in Eq. (2) of the main text. Here $V_\alpha(t)$ is a single voltage trace measured when the readout is in $|\alpha\rangle$. Ideally, we want to have $\overline{\beta_1} = \lambda\alpha$. Scaling $w_1$ using the inverse proportionality factor $\lambda$ would then lead to $\overline{\beta_1} = \alpha$ as required.

In practice, dc measurement offsets and drifts occur and we can simply eliminate them by defining the weight function as

$$w_2(t) = \frac{\overline{V_{|\alpha=1\rangle}(t)} - \overline{V_{|\alpha=-1\rangle}(t)}}{2\lambda} + i\frac{\overline{V_{|\alpha=i\rangle}(t)} - \overline{V_{|\alpha=-i\rangle}(t)}}{2\lambda}. \tag{4.15}$$

It is also possible to avoid two measurements by calculating the imaginary part of $w(t)$ from its real part alone in the case of slowly varying temporal envelope compared to the modulation frequency. Indeed, the imaginary part corresponds to phase shifting the carrier by $\pi/2$ while preserving the signal envelope.

$$\mathrm{Im}[w(t)] = \mathrm{rFT}^{-1}\left[i \times \mathrm{rFT}\left(\mathrm{Re}\left[w(t)\right]\right)\right], \tag{4.16}$$

where rFT and $\mathrm{rFT}^{-1}$ respectively are the real Fourier transform and the inverse real Fourier transform. We can then define the weight function from its real part alone as

$$\mathrm{Re}\left[w_3(t)\right] = \frac{\overline{V_{|\alpha=1\rangle}(t)} - \overline{V_{|\alpha=-1\rangle}(t)}}{2\lambda} \tag{4.17}$$

Now, in the general case, the presence of the qubit leads to two possible frequencies for the propagating mode. We thus need to use a slightly different weight function. The weight functions corresponding to the qubit in $|g\rangle$ or $|e\rangle$ can simply be averaged here. This choice would then lead to

$$\mathrm{Re}\left[w_4(t)\right] = \frac{\overline{V_{|\alpha=1\rangle\otimes|g\rangle}(t)} + \overline{V_{|\alpha=1\rangle\otimes|e\rangle}(t)} - \overline{V_{|\alpha=-1\rangle\otimes|g\rangle}(t)} - \overline{V_{|\alpha=-1\rangle\otimes|e\rangle}(t)}}{4\lambda} \tag{4.18}$$

Since the dc offsets and drifts are assumed to be independent of the qubit state, two of these traces are redundant.

$$\mathrm{Re}\left[w_5(t)\right] = \frac{\overline{V_{|\alpha=1\rangle\otimes|g\rangle}(t)} - \overline{V_{|\alpha=-1\rangle\otimes|e\rangle}(t)}}{2\lambda} \tag{4.19}$$

In the end, we chose to use the measurement of the voltage (Fig. 3b) when $\alpha = 5.8$ initially. In this case, waiting for an interaction time $t_{\mathrm{int}} = 100$ ns leads to $\alpha \approx -5.8$ in the excited state and $\alpha \approx 5.8$ in the ground state. We thus define the final weight function as in the main text as

$$\mathrm{Re}\left[w(t)\right] = \frac{\overline{V_{|\alpha=5.8\rangle\otimes|g\rangle}(t)} - \overline{V_{|\alpha=-5.8\rangle\otimes|e\rangle}(t)}}{2\lambda} \text{ and } \mathrm{Im}[w(t)] = \mathrm{IrFT}\left[i \times \mathrm{rFT}\left(\mathrm{Re}\left[w(t)\right]\right)\right]. \tag{4.20}$$

One can show that the exact value of the field amplitude after the waiting time is unimportant as it simply modifies the complex $\lambda$ scaling factor.

In order to determine $\lambda$, we thus match the scaling of the weight function $w(t)$ so that the measured average complex amplitude $\overline{\beta}$ matches the complex amplitude $\langle\hat{r}\rangle$ in the readout mode when the interaction time is set to $t_{\mathrm{int}} = 0$ and when the qubit is in $|g\rangle$.

#### 4.2.3.2 *Total efficiency*

The total efficiency of the release and detection of the propagating mode can be inferred from the variance of the histogram of measured $\beta$'s for $10^5$ runs of the experiment, when

the readout mode is in a coherent state. We find a total efficiency $\eta = 11$ %. This efficiency can be understood as the product of the efficiency of each step of the signal measurement and analysis. The incomplete release of the readout state induces an efficiency of $\eta_{\text{release}} = 91\%$ (see red dot in Fig 4.11a). The total efficiency is standard [97], and can be understood by the attenuation of the several commercial microwave components between the device and the TWPA, including a 20cm long waveguide acting as a filter (see Fig. 4.5). The TWPA provided 19 dB of gain and its stop-band frequency is 2.4 GHz below the buffer signal frequency.

### 4.2.4 *Choice of parameters*

#### 4.2.4.1 *Optimal release amplitude and temporal envelope*

The goal of this experiment is to demonstrate a sequential single shot read-out with the highest achievable fidelity. We chose the optimal parameters by minimizing the overlap between the distribution $P_{|e\rangle}$ and $P_{|g\rangle}$. The pump temporal shape was chosen to minimize this overlap. There is a trade-off between the speed of the flush and the measurement fidelity. Indeed, a fast flush reduces the efficiency as it dissipates a fraction of the readout energy in unmonitored modes (see Fig. 4.11). On the other hand, a slower flush is not able to release the readout mode when it is at the maximum phase difference. Instead, it continuously releases the content of the readout mode as it interacts with the qubit.

In our experiment, this trade-off yields an optimal pump spread $\sigma = 28$ ns and maximum coupling $|g_{\max}| = 7.2 \times 2\pi$ MHz $> \frac{\kappa_b}{4}$ corresponding to a slight over-critical coupling of the readout resonator and the buffer.

#### 4.2.4.2 *Operating flux bias of the JRM*

The behaviour of the shunted JRM as a function of the external flux was studied in depth in previous works [5]. By measuring the reflection coefficient on the buffer port, we determined the buffer frequency as a function of the external magnetic flux (Fig. 4.12a).

We then characterize the cross-Kerr effect induced by the buffer occupation on the readout resonator. To do so, we displace the readout mode with $\alpha_0 \approx 5$. Then we apply a continuous tone at the buffer frequency on the buffer port for a time $t$ corresponding to an estimated 10 photons in the buffer at the end of the pulse, which is large compare to $1/\kappa_b$. Finally we release the readout mode state into the buffer and measure its average phase $\arg(\overline{\beta})$. The acquired phase as a function of time $t$ provides us the readout mode frequency (as in Fig. 4.9). We subtract to this measured frequency the one measured without driving the buffer and obtain a measurement of the modification of the readout mode frequency by the buffer occupation without any calibration of the buffer photon number at this stage. This cross-Kerr effect cancels out for a given value of the external flux as expected for the JRM. We chose this flux point for the experiment as it ensures that the readout mode is decoupled from the transmission line during the interaction time and as it also cancels out the cross-Kerr effect induced by the pump tone during

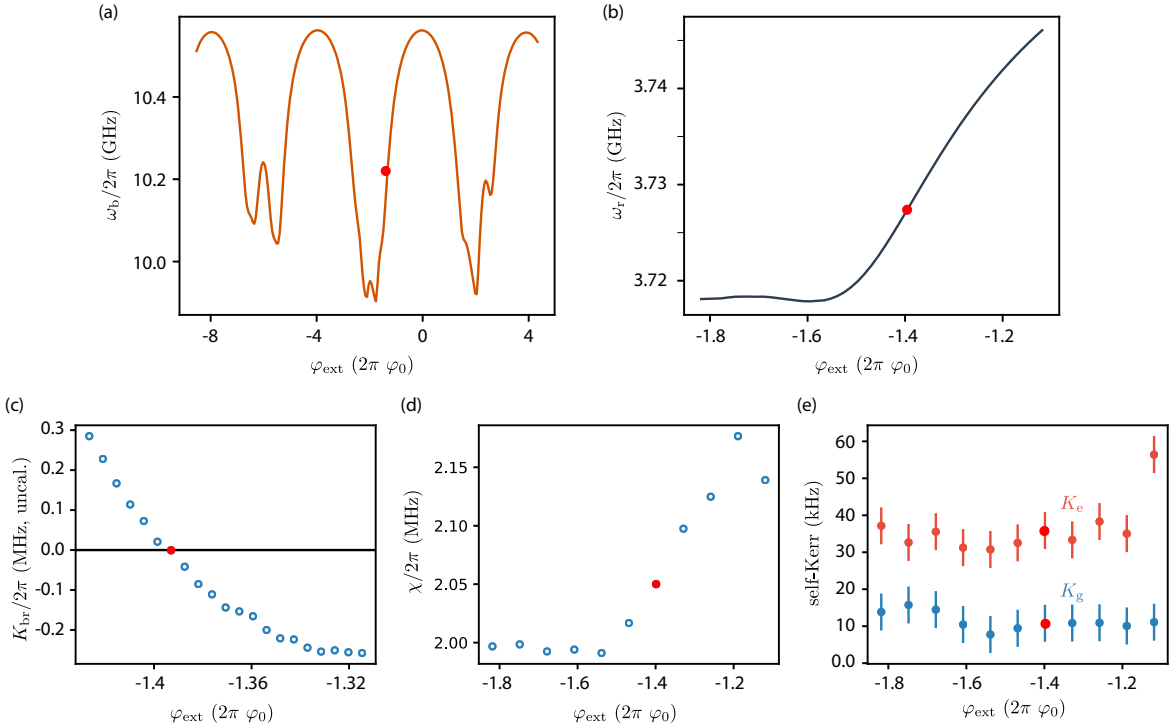


Figure 4.12: Characterisation of the device as the function of external flux. The red dots correspond to the chosen flux point for the experiment in all panels. (a) Measured frequency of the buffer mode displaying a $4\phi_0$ periodicity. The additional non periodic patterns are likely due to an asymmetry between the areas of the four subloops of the ring. (b) Frequency of the readout mode zoomed around the chosen operation point. (c) Frequency shift of the readout mode $K_{br}n_b$ induced by $n_b$ photons in the buffer. Contrary to other plots, this value is uncalibrated as $n_b$ is unknown (estimated $n_b \approx 10$ photons). Canceling out the cross-Kerr rate $K_{br}$ was our criteria for setting the operating flux bias. (d) $\chi$ as the function of the external flux. (e) Kerr rates for the qubit in $|g\rangle$ in blue and for the qubit in $|e\rangle$ in red as a function of the external flux.

the release. We use the same method as in Fig. 4.9 to measure the self-Kerr rate and $\chi$ as a function of the external flux. The self-Kerr rate is dominated by the contribution of the single junction transmon qubit and hence show little to no flux dependency. Increasing the JRM participation ratio should increase this Kerr tunability by the flux and enables a canceling of the average Kerr in the readout mode.

### 4.2.5 *Wigner Tomography*

#### 4.2.5.1 *Measurement*

The measurement protocol for the Wigner tomography matches that of previous work [84–87]. To measure $W(\alpha)$ we start by applying a displacement $D(\alpha)$ on the readout mode with a 20 ns pulse at its frequency. Then we perform two $\pi/2$ unconditional pulses on the qubit[2] separated by a time $\pi/\chi = 236$ ns. We then flush the readout mode (same pulse width $\sigma = 28$ ns) and use our full readout protocol to measure the state of the qubit. The release step avoids the usual cross-Kerr effect between the readout and the readout mode that may distort the estimated Wigner function at large photon number and is mandatory for us as we use the readout resonator to measure the qubits state.

For the Wigner tomography starting with an excited qubit, we simply take the opposite of the result to account for the qubit being initially excited.

Each Wigner tomography is decomposed in 16 square panels spanning the acquired phase space that are each $20 \times 20$ pixels in size. Each pixel is averaged 5000 times. The obtained images are numerically rotated by 24° for $|g\rangle$ (corresponding to setting $\arg(\lambda) = 0$) and 97° for $|e\rangle$. The latter choice accounts for a systematic angular offset between the initial displacement of 10 ns for the qubit readout experiment and the longer Wigner displacement of 20 ns, which is hence more sensitive to the frequency shift $\chi$ of the readout mode.

#### 4.2.5.2 *Numerical simulation of the Wigner function of the readout mode in time*

In order to validate our model for the evolution of the readout mode, we performed simulation of its dynamics using the Python package QuTip [98] with the Hamiltonian (4.10) and the independently measured values for its parameters (see above sections). The fit includes an extra 20 ns delay to account for the duration of the displacement pulse. The results are provided on Fig. 4.13 and display a qualitative agreement with the measurement. It confirms that the dynamics of the readout mode is mainly governed by the $\chi$ and Kerr terms of the Hamiltonian.

### 4.2.6 *Readout characterization*

#### 4.2.6.1 *Measurement fidelity*

To extract a binary answer to whether the qubit is excited or not for a given realization of the experiment, we define two disjoint ensembles of possible outcomes $\beta$. The complex amplitudes corresponding to the answer '$g$' belong to $Z_g = \{\beta \ : \ P_{|g\rangle}(\beta) > P_{|e\rangle}(\beta)\}$, which is defined from the measured probability densities. Obtaining $\beta \notin Z_g$ correspond to the result 'e' (see Fig. 4.14). Given the distributions, the error probability to find an amplitude $\beta$ in $Z_g$ when the qubit was prepared in $|e\rangle$ is $\mathcal{E}_e = 3.4$ % while the reverse error is $\mathcal{E}_g = 1.6$ %. They can be in part explained by the imperfect preparation of the states $|e\rangle$ and $|g\rangle$ because of gate infidelity (0.5 %) and qubit thermal population (0.8 %).

2 In practice, we interleave the pulse sequences to rotate the second pulse by $\pi/2$ or $-\pi/2$ and subtract their average outcome to eliminate parasitic drifts.

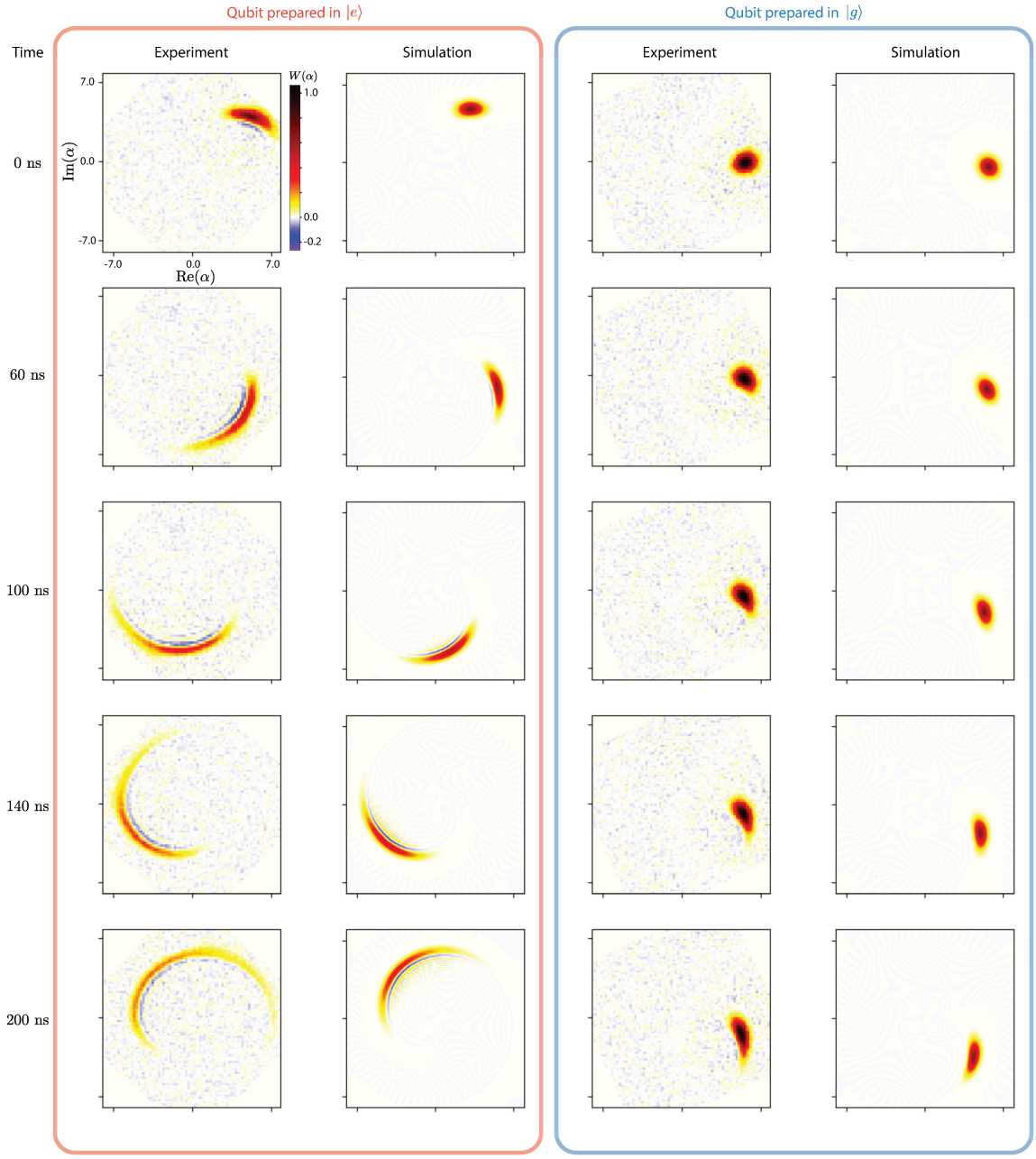


Figure 4.13: Measured Wigner functions for various interaction times when $\alpha_0 = 5.8$ and their simulated counterparts displaying a qualitative agreement. The numerical simulations are done without any free parameters in a Hilbert space that is truncated to the first 150 energy levels (see text).

Those are described below. The qubit decay during the interaction time accounts for 1.7 % of the error in $\mathcal{E}_e$.

#### 4.2.6.2 *Pulse fidelity estimation*

In order to determine the pulse fidelity, we perform an odd number $N$ of $\pi$ pulses in series and measure the probability to find the qubit in the excited state afterwards. The probability decays exponentially with the number of pulses. From the decay, we determine a 99.5 % fidelity whose departure from 100 % mostly comes from the decay

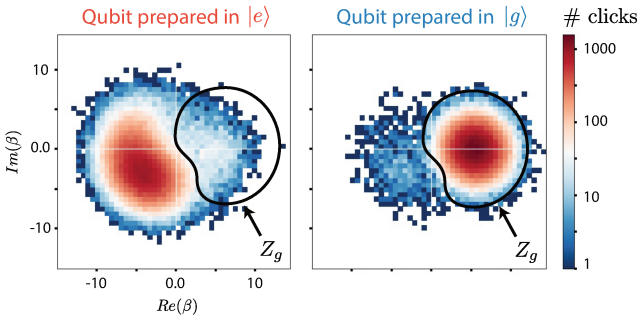


Figure 4.14: Recorded distribution of $\beta$ in logarithmic scale for the number of detection in each bin, when the qubit is prepared in $|e\rangle$ (left panel) or in $|g\rangle$ (right panel). An approximate contour of $Z_g$ is represented in black. $\mathcal{E}_g$ corresponds to clicks outside of $Z_g$ on the right panel and $\mathcal{E}_e$ to clicks inside of $Z_g$ on the left panel.

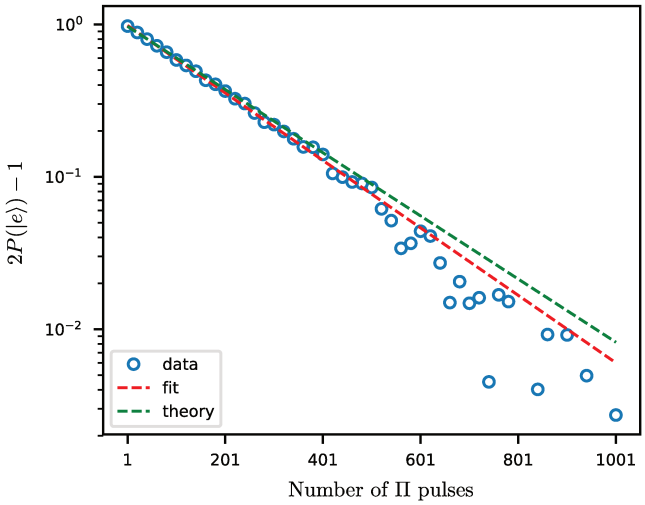


Figure 4.15: Measured population in the excited state of the qubit as a function of the odd number $N$ of $\pi$ pulses in series. Circles: measured probabilities. Red dashed line: exponential fit indicating a decrease by a factor $F = 0.995$ between one pulse and the next. Green dashed line: predicted exponential decay of Rabi oscillations taking the same duration. The decay is $\propto \exp(-N\Delta t_p(T_1^{-1} + T_2^{-1})/2$ [99].

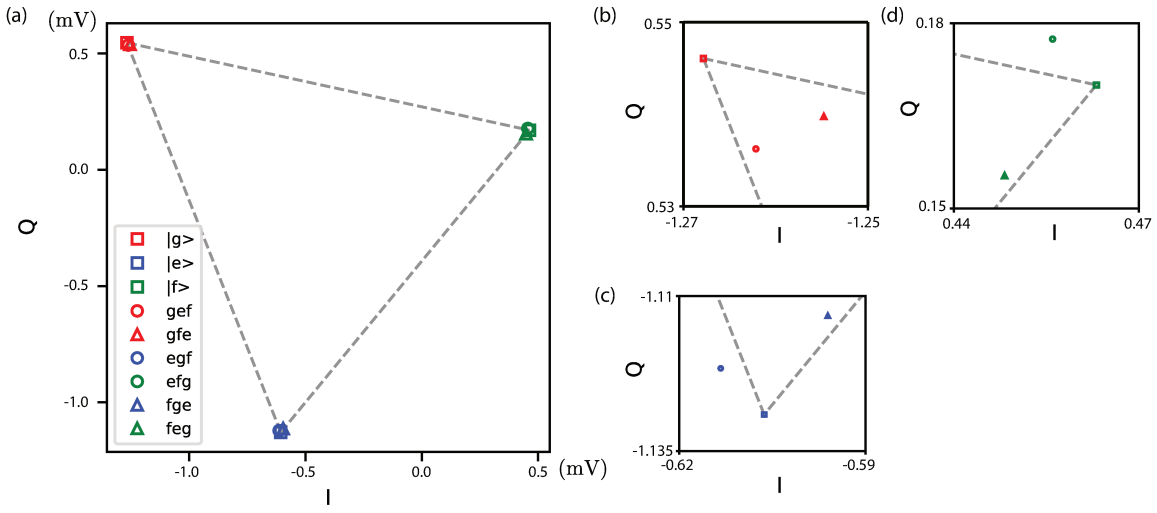


Figure 4.16: Measurement of the transmon temperature. (a) Average response in the IQ plane of the readout mode depending on the population permutations. Squares correspond to the fitted readout response if the transmon were entirely in one of its first three lowest energy states. Other markers correspond to the average measured quadratures after the following pulse sequences (time ordered from left to right) : 'gef' - no pulse; 'gfe' - $\pi_{ef}$; 'egf' - $\pi_{ge}$; 'efg' - $\pi_{ge}\pi_{ef}$; 'fge' - $\pi_{ef}\pi_{ge}$; 'feg' - $\pi_{ge}\pi_{ef}\pi_{ge}$. Solving the associated linear problem yields a temperature of 44 mK corresponding to 0.8 % of the qubit's population not in the ground state. Dashed lines are visual guides connecting the squares. (b),(c) and (d) are zoomed around the apexes. Data points should be inside of the triangle as they are a weighted sum of the apex, with weights given by the populations of each of the three states. The uncertainty on data point is about 0.01 mV.

and decoherence of the qubit during the pulse (Fig. 4.15). Each $\pi$ pulse is 30 ns long and has a sech shape with a spread of 7.5 ns and the $\pi$ pulses are separated by a 5 ns resting time amounting to $\Delta t_p = 35$ ns of period between two pulses.

#### 4.2.6.3 *Qubit thermal population*

The qubit thermal excitation was measured by using the 3rd level of the transmon qubit as a reference. Indeed, by exploring all configurations of population permutation between those 3 levels, one can retrieve the qubit thermal population distribution and its temperature (Fig. 4.16) [99]. The system of linear equations corresponding to the readout response as a function of the population in each state of the transmon is solved through a least square minimization to account for the measurement uncertainty. We find $T_{qubit} = 44$ mK corresponding to 0.8 % of the qubit population out of the ground state.

#### 4.2.6.4 *Quantum Non Demolition nature*

The Quantum Non Demolition characteristic of the measurement (its so-called QND-ness) was determined by doing two readouts, one right after the other (Fig. 4.17). By heralding on the outcome of the first readout for the realizations that give the expected

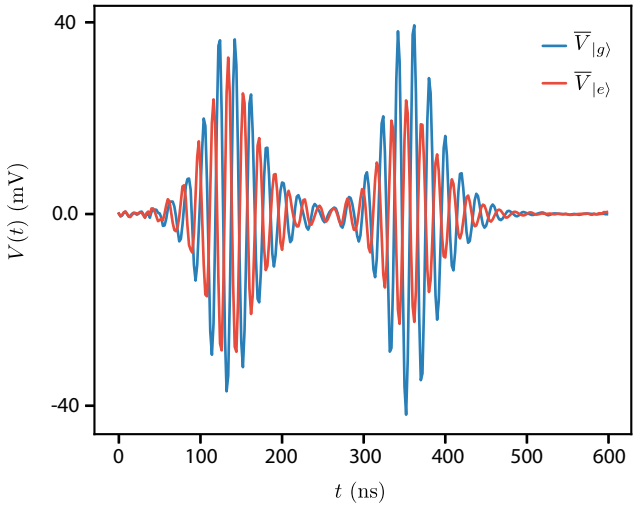


Figure 4.17: Average measured signals for two consecutive readouts for a qubit prepared in $|g\rangle$ (blue) or in $|e\rangle$ (red). The second readout starts 220 ns after the first one.

outcome given the preparation, we measure a probability for the second readout to give the same outcome of 95 % . This slight departure from perfect QNDness is expected as the coupling relies on the dispersive approximation while the field amplitude in the cavity is $\alpha = 5.8$ and thus a photon number of 34, which is above the critical number of photons $n_{\text{crit}} = (\Delta/2g)^2 \approx \alpha/2\chi \approx 24$ [57, 65].

# 5

# MULTIPLEXED PHOTON NUMBER MEASUREMENT

> Nous sommes dans un siècle de l'image. pour le bien comme pour le mal, nous subissons plus que jamais l'action de l'image.
>
> G. Bachelard

We here reproduce the preprint of the Multiplexed photon number measurement experiment. My contribution was to design and fabricate the coplanar waveguide superconducting circuit, and I contributed to the calibration of the first versions of the device until it reached sufficient performances to meet the requirement of the experiment. The authors of this work are Antoine Essig, Quentin Ficheux, Théau Peronnin, Nathanaël Cottet, Raphaël Lescanne, Alain Sarlette, Pierre Rouchon, Zaki Leghtas and Benjamin Huard. This preprint is available on Arxiv.

ABSTRACT The evolution of quantum systems under measurement is a central aspect of quantum mechanics. When a two level system – a qubit – is used as a probe of a larger system, it naturally leads to answering a single yes-no question about the system state followed by its corresponding quantum collapse. Here, we report an experiment where a single superconducting qubit is counter-intuitively able to answer not a single but nine yes-no questions about the number of photons in a microwave resonator at the same time. The key ingredients are twofold. First, we exploit the fact that observing the color of a qubit carries additional information to the conventional readout of its state. The qubit-system interaction is hence designed so that the qubit color encodes the number of photons in the resonator. Secondly, we multiplex the qubit color observation by recording how the qubit reflects a frequency comb. Interestingly the amount of extracted information reaches a maximum at a finite drive amplitude of the comb. We evidence it by direct Wigner tomography of the quantum state of the resonator. Our experiment unleashes the full potential of quantum meters by bringing the measurement process in the frequency domain.

ACKNOWLEDGEMENT This work was made possible through the support of Fondation Del Duca and IDEX Lyon (Contract No. ANR-16-IDEX-0005). We acknowledge IARPA and Lincoln Labs for providing a Josephson Traveling-Wave Parametric Amplifier. The device was fabricated in the cleanrooms of Collège de France, ENS Paris, CEA

Saclay, and Observatoire de Paris. We are grateful to Rémi Azouit, Michel Devoret, and Mazyar Mirrahimi for fruitful discussions.

## 5.1 EXPERIMENT DESCRIPTION AND RESULTS

### 5.1.1 *Introduction*

The most general measurement of a quantum system consists in using a quantum apparatus as a probe. The system interacts with the probe before the latter gets measured projectively. In the simplest case, the probe is a qubit whose readout answers a yes-no question about the system state. Identifying what is the state of a system thus comes down to playing a game of "Guess Who?". A series of binary questions are asked iteratively to refine our knowledge about the state. Unlike the classical game, each answer disturbs the state of the system. To give a concrete example, in order to determine how many photons are stored in a cavity, one may ask a series binary questions such as "are there $n$ photons?" for each integer $n$ (Fig. 6.1A). Such experiments have been implemented with Rydberg atoms or superconducting circuits probing a microwave cavity [100, 101] with the possible refinement of choosing what binary question should be optimally asked conditioned on the previous answers [102]. At most, each answer provides one bit of information about the system state [103] so that determining an arbitrary number of photons in the cavity between 0 and $2^m - 1$ takes at least $m$ consecutive probe measurements. In this work, we experimentally show that one can ask all questions at once using a single qubit as a probe. Daring an analogy with communication protocols, previous measurement schemes with time series of binary questions used time division multiplexing while our experiment demonstrates the analogous of frequency division multiplexing (Fig. 6.1A).

### 5.1.2 *Photocounting a coherent state*

Both approaches can be implemented to count the photon number of a superconducting microwave resonator dubbed the *storage mode*, which resonates at $f_\mathrm{s} = 4.558$ GHz. We couple the latter to two off-resonant transmon qubits (see Fig. 6.1B). The *yes-no qubit* with a frequency $f_\mathrm{yn} = 3.848$ GHz can implement binary questions about the photon number while the *multiplexing qubit* with a frequency $f_\mathrm{mp} = 4.238$ GHz can implement frequency multiplexed photon counting. Both qubits are dispersively coupled to the resonator so that their frequency respectively redshifts by $\chi_\mathrm{s,yn} = 1.4$ MHz and $\chi_\mathrm{s,mp} = 4.9$ MHz per additional photon in the storage mode.

Starting with the standard approach [58, 101], the probability to have $k$ photons is encoded as the probability $\mathbb{P}_\mathrm{e}$ to excite the yes-no qubit by driving it with a $\pi$-pulse at $f_\mathrm{drive} = f_\mathrm{yn} - k\chi_\mathrm{s,yn}$. The state of the yes-no qubit is read out using a dedicated resonator (Fig. 6.1B). To demonstrate this photon counting ability, we initialize the storage mode in a coherent state $|\beta\rangle = e^{-|\beta|^2/2} \sum_{n=0}^{+\infty} \frac{\beta^n}{\sqrt{n!}} |n\rangle$, which is a superposition of all Fock states with mean photon number $\bar{n} = |\beta|^2$ using a microwave tone at $f_\mathrm{s}$.

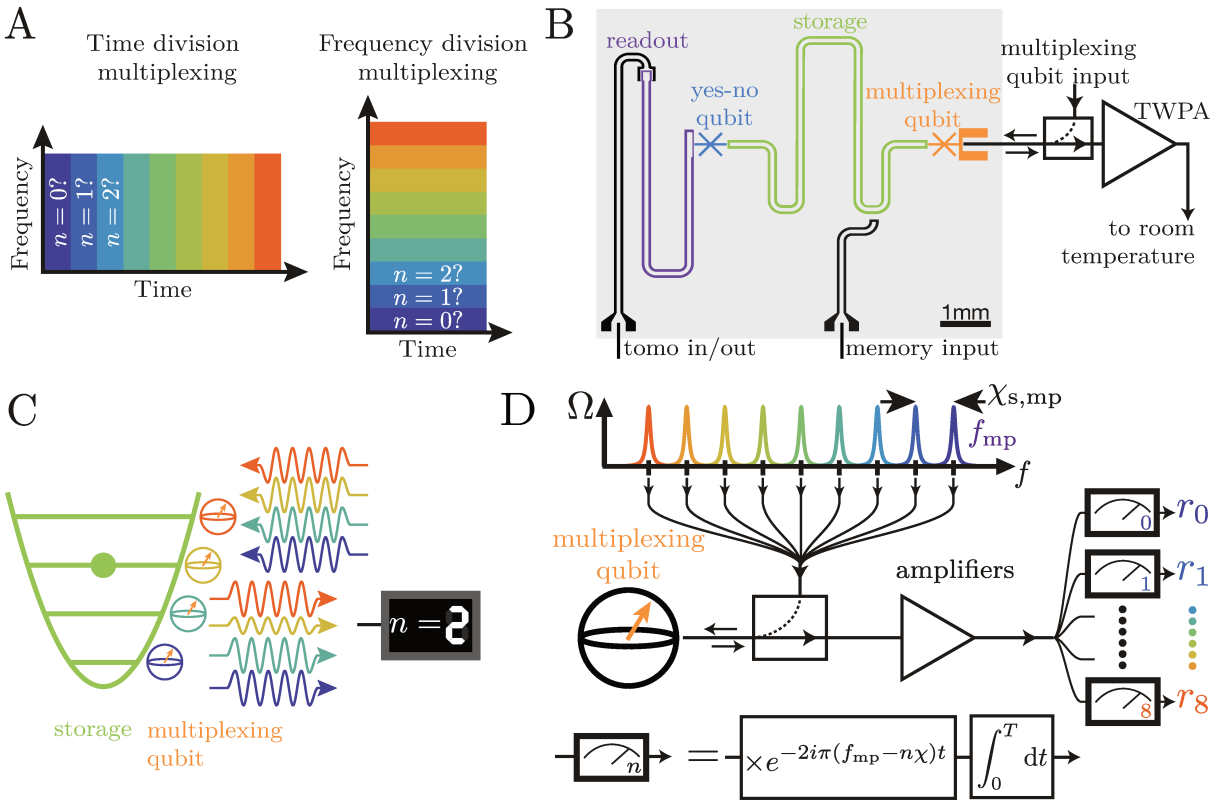


Figure 5.1: **Multiplexing photon counting setup and protocol.** (A) Time domain division multiplexing proceeds one binary question at a time. Frequency division multiplexing simultaneously retrieves multiple binary answers. (B) Scheme of the device in coplanar waveguide architecture. The storage mode (green) is coupled to a transmon multiplexing qubit (orange), which is directly coupled to a transmission line. A directional coupler and broadband Traveling Wave Parametric Amplifier (TWPA) allow us to probe the qubit in reflection. An additional transmon yes-no qubit (blue) and its readout resonator (purple) are used for standard photon counting and Wigner tomography (see section 5.2). (C) The frequency (color) of the multiplexing qubit encodes the storage photon number. The reduction in the reflection amplitude of the qubit at one of the frequencies reveals the number of photons in the storage mode – e.g. here 2 photons. (D) The qubit is illuminated by a frequency comb of amplitude $\Omega$. The reflected pulse is amplified and digitized before numerical demodulation at every frequency $f_{\mathrm{mp}} - k\chi_{\mathrm{s,mp}}$. This multiplexing-demultiplexing process leads to reflection coefficients $r_k$ that each contain the probability that $k$ photons are stored.

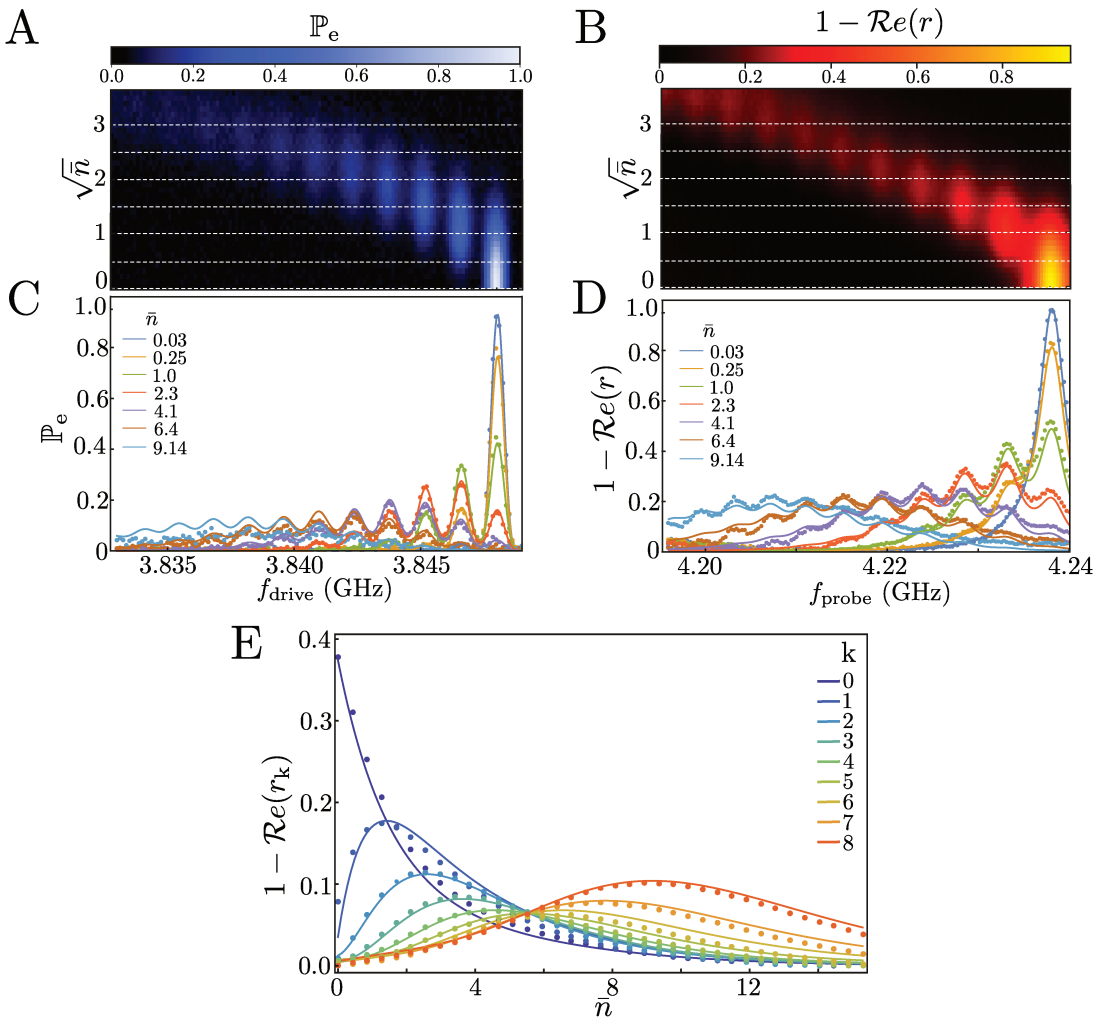


Figure 5.2: **Photocounting a mode in a coherent state.** The storage mode is prepared in a coherent state with $\bar{n}$ photons on average using a microwave pulse at storage frequency and amplitude $V_s$. (A,C) Standard approach to photon counting. A $\pi$-pulse at a tunable frequency $f_{\mathrm{drive}}$ on the yes-no qubit excites the qubit with a measured probability $\mathbb{P}_{\mathrm{e}}$ as a function of $V_s$. Peaks appear at $f_{\mathrm{yn}} - k\chi_{\mathrm{s,yn}}$ and indicate the probability to store $k$ photons. The dots in (C) are cuts along the dashed lines in (A) and match the master equation model (solid lines) using it as a calibration of the storage mode occupation. (B,D) Photon counting using the reflection coefficient $r$ of the multiplexing qubit at a single frequency $f_{\mathrm{probe}}$. The measured emission coefficient $1-\mathcal{R}e(r)$ is shown as a function of $f_{\mathrm{probe}}$ and $V_{\mathrm{s}}$ and exhibits resolved peaks for every photon number. The dots in (D) are cuts along the dashed lines in (B) and are captured by a master equation model (solid lines). (E) Multiplexed photon counting. Dots: simultaneously measured average emission coefficients for each photon number $k$ from 0 to 8 and for various initial state of the storage mode. $r_k$ is here the reflection coefficient at $f_{\mathrm{mp}} - k\chi_{\mathrm{s,mp}}$. Solid lines: prediction based on a master equation without free parameter (see section 5.2).

The probability $\mathbb{P}_e$ is then measured and shows resolved peaks as a function of $f_{\text{drive}}$ for every photon number up to about 7 (Fig. 6.2A,C) and various average photon numbers $\bar{n}$. The linear relation between $\beta$ and the amplitude $V_s$ of the tone at $f_s$ was calibrated using a master-equation based model (see section 5.2) reproducing the measured $\mathbb{P}_e$ (solid lines in Fig. 6.2C).

The intrinsic limitation of the standard approach is that measuring a qubit state can at most reveal one bit of information at a time. We propose to avoid this constraint by observing the qubit frequency (or color) directly without measuring its state. The multiplexing qubit is coupled to the transmission line so that when there are $k$ photons in the storage mode, the qubit emits into the mode of the transmission line that is centered around the qubit frequency $f_{\text{mp}} - k\chi_{\text{s,mp}}$. The qubit thus acts as an encoder of the state of the storage mode into the many modes of the transmission line at frequencies $\{f_{\text{mp}} - k\chi_{\text{s,mp}}\}_k$, which can host much more than one bit of information. This encoding ability can be observed by driving the multiplexing qubit in reflection through the transmission line (Fig. 6.1B) [104–107]. The measured real part $\mathcal{R}e(r)$ of the reflection coefficient of a microwave pulse at frequency $f_{\text{probe}}$ is reduced when the probe resonates with the qubit, hence revealing the photon number $k$ (Fig. 6.1C) [39]. This reduction arises from the coherent emission by the qubit in phase opposition with the reflected drive [108]. Interestingly, the roles of qubit and resonator are here swapped compared to usual qubit readout in circuit-QED [109].

In Fig. 6.2B,D we show the measured qubit *emission coefficient* $1 - \mathcal{R}e(r)$ as a function of a single probe frequency $f_{\text{probe}}$ and of the initial amplitude of the storage mode coherent state $\sqrt{\bar{n}}$. The measurement is performed using a drive strength $\Omega = \chi_{\text{s,mp}}/4$ (expressed as the corresponding Rabi frequency) and pulse duration of 2 $\mu$s, which is smaller than the storage lifetime of 3.8 $\mu$s. Resolved peaks develop for every photon number up to at least 9 which is already a clearer indicator of the photon number than the yes-no probe. Using the former calibration of $\bar{n}$, a master-equation based model enables us to reproduce the measurement results (see section 5.2). In order to get resolved peaks we designed the relaxation rate of the multiplexing qubit $\Gamma_{1,\text{mp}} = (44\text{ ns})^{-1}$ so that the decoherence rate $\Gamma_{2,\text{mp}} = \Gamma_{1,\text{mp}}/2$ is smaller than the dispersive shift $2\pi\chi_{\text{s,mp}}$. Probing the qubit at one of its resonance frequencies opens a communication channel with a maximal bandwidth $\Gamma_{2,\text{mp}}$. Hence we maximized this bandwidth by designing $\Gamma_{1,\text{mp}}$ as large as possible using the direct coupling to the transmission line.

Therefore we have shown that both measurements in Figs. 6.2A,B allow us to ask questions of the kind “are there $k$ photons?". However the yes-no qubit is read out using a pulse that is independent on the storage state. In contrast, each continuous measurement of the frequency mode $f_{\text{mp}} - k\chi_{\text{s,mp}}$ of the transmission line in which the multiplexing qubit emits reveals information about a different photon number $k$. It thus enables the key ingredient of our approach: the multiplexing measurement of reflection at every frequency $f_{\text{mp}} - k\chi_{\text{s,mp}}$.

To do so, we illuminate the multiplexing qubit with a pulse containing a comb with 9 frequencies corresponding to photon numbers from 0 to 8 (see Fig. 6.1D). The efficient measurement of the reflected pulse requires the use of a near-quantum limited amplifier with a dynamical bandwidth of at least a dozen of $\chi_{\mathrm{s,mp}}$ such as a TWPA [90]. This technical challenge is similar to the recently demonstrated high-efficiency multiplexed readout of as many as 6 qubits coupled to a single feed line [110–113]. We then demultiplex the reflected pulse at 9 frequencies $\{f_{\mathrm{mp}} - k\chi_{\mathrm{s,mp}}\}_{0\leq k\leq 8}$ and extract a reflection coefficient $r_k$ for each of them (Fig. 6.1D). The measurement consists in simultaneously measuring the emission coefficients $1-\mathcal{R}e(r_k)$ for each peak in Fig. 6.2B,D, which is of course much faster than measuring them one at a time. They are shown as a function of the average initial photon number in Fig. 6.2E for a drive strength $\Omega = \chi_{\mathrm{s,mp}}/2$ and a measurement duration of 2 $\mu$s. For a given $\bar{n}$, every measurement channel $k$ gives an average signal that is proportional to the probability of having $k$ photons in the storage mode. As $\bar{n}$ is varied, the shape of the average signal of channel $k$ reproduces a Poisson distribution distorted by relaxation processes and channel cross-talk due to large driving strength (see section 5.2). This multiplexed photon counting signal can be reproduced using a master equation approach (solid lines in Fig. 6.2E) without any free parameter. This result thus demonstrates the possibility to multiplex the photon number measurement using a single qubit.

### 5.1.3 *Measurement rate and storage mode dephasing*

How is the measurement affected by the strength $\Omega$ of the driving frequency comb? In the reciprocal case of measuring a qubit using a cavity as a probe, the measurement rate is bounded by the dephasing rate of the qubit, which grows as the square of the cavity driving strength [114, 115]. Thus, characterizing the measurement rate of our multiplexed photon counting can elegantly be done by observing how the storage mode dephases for a given driving strength $\Omega$. Indeed, owing to the inherent quantum backaction of the photon number measurement, the measurement rate is bounded by how fast the conjugated operator, here the mode phase, diffuses. As the probe is a qubit, one expects a different dependence of the measurement rate on $\Omega$ than for standard qubit readout using a probe cavity.

In order to measure this dephasing rate, we perform a direct Wigner tomography of the storage mode at various times $t$ [84, 85, 116]. It provides a representation of the state $\rho$ in the phase space of the mode and can be expressed as $W(\alpha) = \frac{2}{\pi}\mathrm{Tr}(D^\dagger(\alpha)\rho D(\alpha)\mathcal{P})$. Here $D(\alpha) = e^{\alpha a_s^\dagger - \alpha^* a_s}$ is the storage displacement operator, $\mathcal{P} = e^{i\pi a_s^\dagger a_s}$ is the photon number parity operator, and $a_s$ is the canonical annihilation operator of the storage mode. Preparing the storage mode with a coherent state $|\beta = -1.55\rangle$, the Wigner function starts as a Gaussian distribution centered at $\alpha = \beta$. On the left of Fig. 6.4A, one can see how the bare dephasing rate and the self-Kerr effect of the storage mode (0.02 MHz frequency shift per photon) distort the Gaussian distribution towards a torus with no phase when time increases even without any photon counting drives. Using a single drive with $\Omega = \chi_{\mathrm{s,mp}}/2$ to measure whether there is 1 photon, the phase diffuses

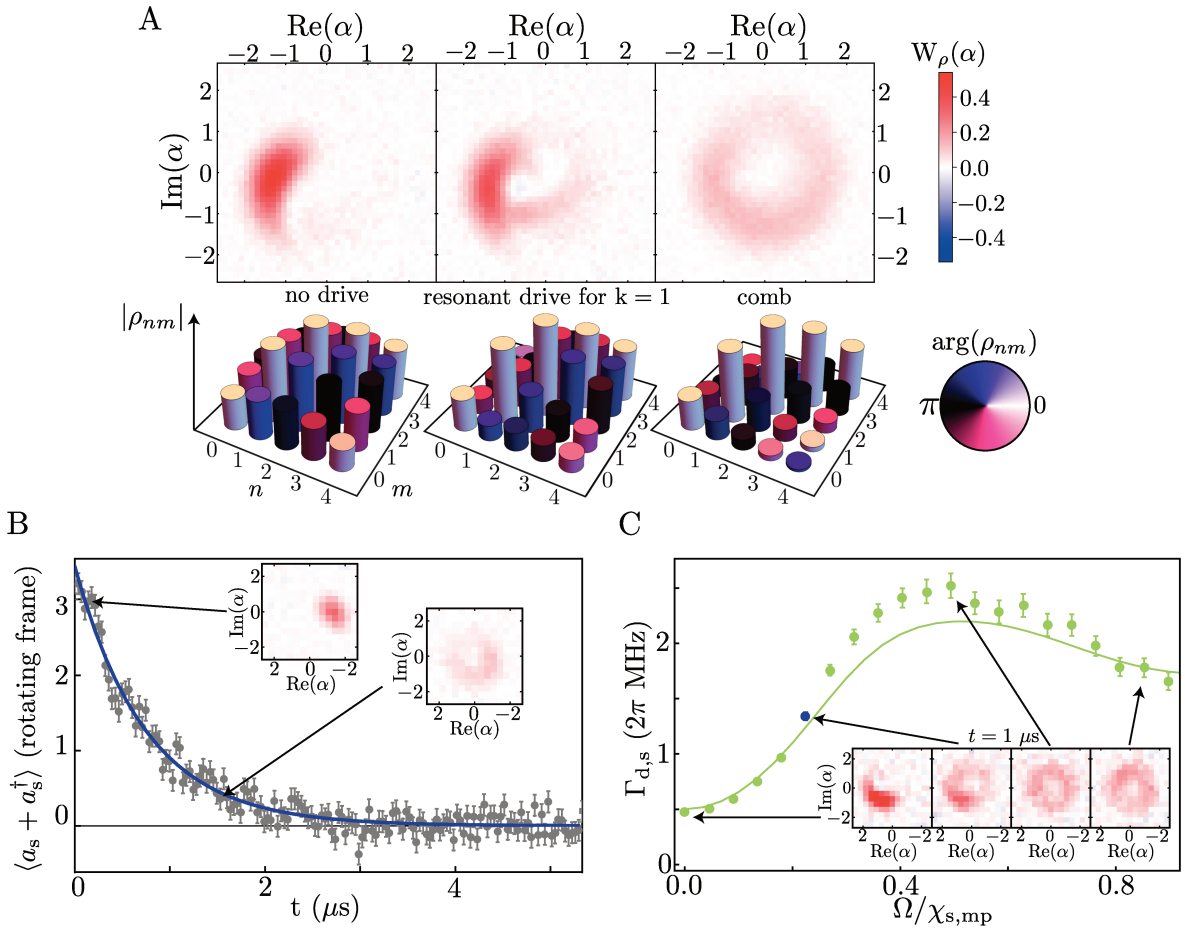


Figure 5.3: **Storage mode dephasing due to multiplexed photon counting.** (A) Direct Wigner tomography of the storage mode at time $t = 0.5$ $\mu$s after initialization in a coherent state with amplitude $\beta = -1.55$. Left: natural evolution without driving. Middle: evolution with a single tone at $f_{\mathrm{mp}} - \chi_{\mathrm{s,mp}}$ that probes whether there is 1 photon in the storage mode. Right: evolution in presence of the frequency comb $\{f_{\mathrm{mp}} - k\chi_{\mathrm{s,mp}}\}_{0\leq k\leq 8}$. Each bottom panel represents the density matrix $\{\rho_{nm}\}_{n,m}$ that is calculated from the Wigner function of its top panel. The cylinder heights represent $|\rho_{nm}|$ and the color encodes $\arg(\rho_{nm})$. (B) Measured exponential decay of the average storage mode quadrature $\langle a_{\mathrm{s}} + a_{\mathrm{s}}^{\dagger}\rangle$ in the case of a driving comb of strength $\Omega = 0.23\chi_{\mathrm{s,mp}}$, and in a frame rotating at the storage mode resonant frequency. Insets show Wigner tomography of the storage mode for two values of $t$. (C) Measured dephasing rate induced on the storage mode as a function of the drive strength $\Omega$ of the frequency comb. Insets show Wigner tomographies of the storage mode at $t = 1$ $\mu$s for four values of $\Omega$.

faster and the Wigner function exhibits negativities in middle of Fig. 6.4A. As seen in the corresponding density matrix, a tone at $f_{\mathrm{probe}} = f_{\mathrm{mp}} - \chi_{\mathrm{s,mp}}$ notably induces dephasing between states $|1\rangle$ and all other states $|m \neq 1\rangle$ (see density matrix as a function of drive frequency in section 5.2). As expected the phase diffusion is more intense when all the tones of the multiplexed readout are turned on than for a single tone with the same drive strength $\Omega$ (right of Fig. 6.4A). Likewise all off-diagonal elements of the density matrix are then reduced.

To be more quantitative, the dephasing rate $\Gamma_{\mathrm{d,s}}$ of the cavity is accessed through the decay of the mean quadrature of the storage mode $\langle a_s + a_s^\dagger \rangle = \int 2xW(x+iy)\mathrm{d}x\mathrm{d}y$ [117]. In Fig. 6.4B, we show $\langle a_s + a_s^\dagger \rangle$ as a function of time under the multiplexed drive with a strength $\Omega = 0.23\chi_{\mathrm{s,mp}}$. Repeating this experiment for various values of the multiplexed driving strength $\Omega$ allows us to determine how the latter affects the dephasing rate $\Gamma_{\mathrm{d,s}}$, and thus the measurement rate. The dephasing rate is non monotonic in the drive strength (Fig. 6.4C). Noticeably, it reaches a maximum when $\Omega = \chi_{\mathrm{s,mp}}/2$ for which information is extracted at a rate approximately 5 times larger than the natural dephasing rate. This maximum is well captured by a measurement model based on a master equation without any free parameter (line in Fig. 6.4C) (see section 5.2).

In conclusion, we have demonstrated that a single qubit can be used to continuously probe a multidimensional system by encoding the information in the frequency domain. The measurement rate depends non-monotonically on the drive strength. Improving further the detection efficiency, the storage lifetime, and lowering the residual qubit thermal excitation should enable single shot photon counting by multiplexing. Our new measurement scheme can readily be applied to stabilize quantum states by feedback control [118], probe quantum trajectories of microwave modes [29], Quantum Zeno dynamics [87], or vary the driving comb tones in real time to engineer desired decoherence channels. Furthermore, exciting the multiplexing qubit and detecting the emitted photon by a series of frequency resolved photodetectors [119–121], one could realize a discrete and projective photocounter. Moving further, one could extend this frequency domain measurement to more complex probes than a single qubit and many possible physical systems beyond superconducting circuits.

## 5.2 SUPPLEMENTARY MATERIALS

### 5.2.1 *Device and Fabrication*

#### 5.2.1.1 *Design*

The circuit is composed of 4 electromagnetic modes whose parameters can be found in Tab. 5.1 and 5.2. A high-Q harmonic oscillator, called storage mode, is composed of a $\lambda/2$ coplanar waveguide (CPW) resonator (green in Fig. 5.4). The storage resonator is capacitively coupled to two transmon qubits. The multiplexing qubit (orange) has a high spontaneous photon emission rate $\Gamma_{1,\mathrm{mp}} = (44\ \mathrm{ns})^{-1}$ into a transmission line compared to other modes. In contrast, the yes-no qubit is capacitively coupled to a low-Q readout resonator and has a long coherence time $T_{2,\mathrm{yn}} = 27\ \mu\mathrm{s}$. As required by Wigner tomography, the yes-no qubit coherence time and the lifetime of storage mode are larger than the time needed for storage photon number parity measurement $1/2\chi_{\mathrm{s,yn}} \ll T_{1,\mathrm{s}}, T_{2,\mathrm{yn}}$. As we use the multiplexing qubit to count the photon number in the storage mode, we need it to be photon number resolved [58] otherwise each record of the multiplexing measurement could not be associated to a single specific photon number. This photon number resolved constraint imposes that the multiplexing qubit decoherence rate must be smaller than the cross-Kerr rate between the multiplexing qubit and the storage mode $\Gamma_{2,\mathrm{mp}} < 2\pi\chi_{\mathrm{s,mp}}$. This resolution constraint is not critical, as in fact a finite amount of photon number information can be extracted as soon as $\chi_{\mathrm{s,mp}}$ is nonzero, but the decoding is much simpler if we can reason in terms of well-separated resonance peaks.

| circuit parameters | Symbol | Hamiltonian term | parameter value |
|---|---|---|---|
| readout resonator frequency | $f_{\mathrm{ro}}$ | $hf_{\mathrm{ro}}\hat{n}_{\mathrm{ro}}$ | 7.138 GHz |
| storage mode frequency | $f_{\mathrm{s}}$ | $hf_{\mathrm{s}}\hat{n}_{\mathrm{s}}$ | 4.558 GHz |
| yes-no qubit frequency | $f_{\mathrm{yn}}$ | $hf_{\mathrm{yn}}\hat{n}_{\mathrm{yn}}$ | 3.848 GHz |
| multiplexing qubit frequency | $f_{\mathrm{mp}}$ | $hf_{\mathrm{mp}}\hat{n}_{\mathrm{mp}}$ | 4.238 GHz |
| readout/yes-no qubit cross-Kerr rate | $\chi_{\mathrm{ro,yn}}$ | $-h\chi_{\mathrm{ro,yn}}\hat{n}_{\mathrm{ro}}\hat{n}_{\mathrm{yn}}$ | 0.4 MHz |
| storage/yes-no qubit cross-Kerr rate | $\chi_{\mathrm{s,yn}}$ | $-h\chi_{\mathrm{s,yn}}\hat{n}_{\mathrm{s}}\hat{n}_{\mathrm{yn}}$ | 1.4 MHz |
| storage/multiplexing qubit cross-Kerr rate | $\chi_{\mathrm{s,mp}}$ | $-h\chi_{\mathrm{s,mp}}\hat{n}_{\mathrm{s}}\hat{n}_{\mathrm{mp}}$ | 4.9 MHz |
| yes-no qubit anharmonicity | $\chi_{\mathrm{yn,yn}}$ | $-h\chi_{\mathrm{yn,yn}}\hat{n}_{\mathrm{yn}}(\hat{n}_{\mathrm{yn}}-1)$ | 160 MHz |
| multiplexing qubit anharmonicity | $\chi_{\mathrm{mp,mp}}$ | $-h\chi_{\mathrm{mp,mp}}\hat{n}_{\mathrm{mp}}(\hat{n}_{\mathrm{mp}}-1)$ | 116 MHz |

Table 5.1: **Table of circuit parameters.** Cross-Kerr rates with the storage mode are measured using qubit spectroscopy for various coherent states. The cross-Kerr rate between yes-no qubit and readout resonator is measured by calibrating the measurement induced dephasing by the readout resonator on the qubit as a function of the drive amplitude and detuning of the readout resonator. Anharmonicities are measured using spectroscopy of the qubit excited state.

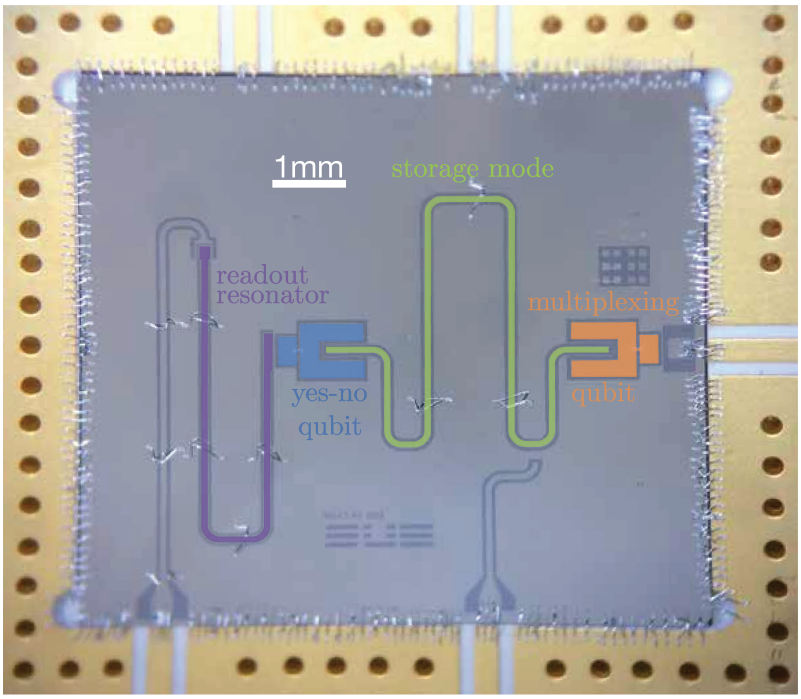


Figure 5.4: **Optical image of the circuit.** The readout resonator is colored in purple, storage mode in green, yes-no qubit in blue and multiplexing qubit in orange. All dark grey areas are silicon, grey areas are niobium on silicon and Josephson junctions are made of Al/AlOx/Al.

#### 5.2.1.2 *Measurement setup*

The readout resonator, the yes-no qubit and the multiplexing qubit are driven by pulses that are generated using a Tektronix® Arbitrary Waveform Generator (AWG) AWG5014C with a sample rate of 1 GS/s. Storage mode pulses are generated using a Zurich Instruments® UHFLI with a sample rate of 1.8 GS/s. The UHFLI allows us to change the pulse amplitude and phase without recompiling the sequence. This feature decreases the time needed for Wigner tomography compared to a standard AWG and makes the pulse sequence simple with the drawback of having to synchronize the two AWGs. AWG pulses are modulated at a frequency 25 MHz for readout, 100 MHz for yes-no qubit, and 75 MHz for storage and multiplexing qubit. They are up-converted using single sideband mixers for readout resonator and multiplexing qubit and regular mixers for the storage resonator and yes-no qubit, with continuous microwave tones produced respectively by AnaPico® APSIN12G, Agilent® E8257D, WindFreak® SynthHD, and AnaPico® APSIN20G sources that are set at the frequencies $f_{\mathrm{ro}}$+25 MHz, $f_{\mathrm{mp}}$+75 MHz, $f_{\mathrm{s}} + 75$ MHz and $f_{\mathrm{yn}} + 100$ MHz.

The two reflected signals from the readout and multiplexing qubit are combined with a diplexer and then amplified with a Travelling Wave Parametric Amplifier (TWPA) provided by Lincoln Labs. We tuned the pump frequency ($f_{\mathrm{TWPA}} = 5.998$ GHz) and power in order to reach a gain of 20 dB at 7.138 GHz and 4.238 GHz. The follow-up amplification is performed by a High Electron Mobility Transistor (HEMT) amplifier

from Low Noise Factory (LNF®) at 4 K and by two room temperature amplifiers. The two signals are down-converted using image reject mixers before digitization by an Alazar® acquisition board and numerical demodulation. The full setup is shown in Fig. 5.5. The Tektronix® AWG is used as the master that triggers the UHFLI and the Alazar® board.

#### 5.2.1.3 *Master equation of the full system*

We give the full Hamiltonian of the circuit up to the second order in photon number, a more complex Hamiltonian is given in section 5.2.3.1. We denote the photon number operator respectively for the readout, storage, yes-no qubit and multiplexing qubit with $\hat{n}_{\mathrm{ro}}$, $\hat{n}_{\mathrm{s}}$, $\hat{n}_{\mathrm{yn}}$, and $\hat{n}_{\mathrm{mp}}$. Note that the annihilation operator $\hat{a}_{\mathrm{s}}$ in the main text is related to these operators by $\hat{n}_{\mathrm{s}} = \hat{a}_{\mathrm{s}}^{\dagger}\hat{a}_{\mathrm{s}}$. With those operators, the undriven Hamiltonian can be written as

$$\begin{aligned}\hat{H} \;=\; & hf_{\mathrm{ro}}\hat{n}_{\mathrm{ro}} + hf_{\mathrm{s}}\hat{n}_{\mathrm{s}} + hf_{\mathrm{yn}}\hat{n}_{\mathrm{yn}} + hf_{\mathrm{mp}}\hat{n}_{\mathrm{mp}} - h\chi_{\mathrm{ro,yn}}\hat{n}_{\mathrm{ro}}\hat{n}_{\mathrm{yn}} - h\chi_{\mathrm{s,yn}}\hat{n}_{\mathrm{s}}\hat{n}_{\mathrm{yn}} \\ & -h\chi_{\mathrm{s,mp}}\hat{n}_{\mathrm{s}}\hat{n}_{\mathrm{mp}} - h\chi_{\mathrm{yn,yn}}\hat{n}_{\mathrm{yn}}(\hat{n}_{\mathrm{yn}}-1) - h\chi_{\mathrm{mp,mp}}\hat{n}_{\mathrm{mp}}(\hat{n}_{\mathrm{mp}}-1)\end{aligned}, \tag{5.1}$$

with $\chi_{a,b}$ the cross-Kerr rate between mode $a$ and $b$ and $\chi_{a,a}$ the anharmonicity of the mode $a$. The values of all parameters are given in Table 5.1.

To this Hamiltonian, we need to add seven dephasing and relaxation channels in order to get the Lindblad equation describing the circuit dynamics.

$$\begin{aligned}\dot{\rho} \;=\; & -\frac{i}{\hbar}[\hat{H},\rho] + \Gamma_{\mathrm{ro}}\mathcal{L}(\hat{a}_{\mathrm{ro}})\rho + 2\Gamma_{\phi,\mathrm{s}}\mathcal{L}(\hat{n}_{\mathrm{s}})\rho + \Gamma_{1,\mathrm{s}}\mathcal{L}(\hat{a}_{\mathrm{s}})\rho \\ & +2\Gamma_{\phi,\mathrm{yn}}\mathcal{L}(\hat{n}_{\mathrm{yn}})\rho + \Gamma_{1,\mathrm{yn}}\mathcal{L}(\hat{a}_{\mathrm{yn}})\rho + 2\Gamma_{\phi,\mathrm{mp}}\mathcal{L}(\hat{n}_{\mathrm{mp}})\rho + \Gamma_{1,\mathrm{mp}}\mathcal{L}(\hat{a}_{\mathrm{mp}})\rho,\end{aligned} \tag{5.2}$$

where $\mathcal{L}$ is the Lindblad superoperator defined as $\mathcal{L}(\hat{L})\rho = \hat{L}\rho\hat{L}^{\dagger} - \left\{\hat{L}^{\dagger}\hat{L},\rho\right\}/2$ , $\hat{a}_b$ is the annihilation operator of mode $b$. For a qubit mode $b$, the dephasing rate $\Gamma_{\phi,\mathrm{b}}$ is linked to the decoherence rate by $\Gamma_{2,\mathrm{b}} = \Gamma_{1,\mathrm{b}}/2 + \Gamma_{\phi,\mathrm{b}}$. Table 5.2 gives the values of all relaxation and decoherence rates.

#### 5.2.1.4 *Electromagnetic simulation*

The circuit was simulated using Sonnet® software. The length of the readout resonator and storage mode was designed to obtain the resonant frequencies $f_{\mathrm{ro}} \sim 7$ GHz and $f_{\mathrm{s}} \sim 4.5$ GHz. In the simulation, the qubit Josephson junctions were replaced by linear inductances. The value of the inductances and of the capacitive couplings between modes were adjusted to match the resolved number resolved condition (see section 5.2.1.1) between the qubits and the storage mode. Couplings were extracted from the electromagnetic simulation by varying the Josephson junction inductances and by predicting the avoided crossing between the qubits and the storage and readout resonators.

#### 5.2.1.5 *Device fabrication*

The circuit consists of a sputtered 120 nm-thick Niobium film deposited on a 280 $\mu$m-thick undoped silicon wafer. The resonators and feed lines are dry etched after optical

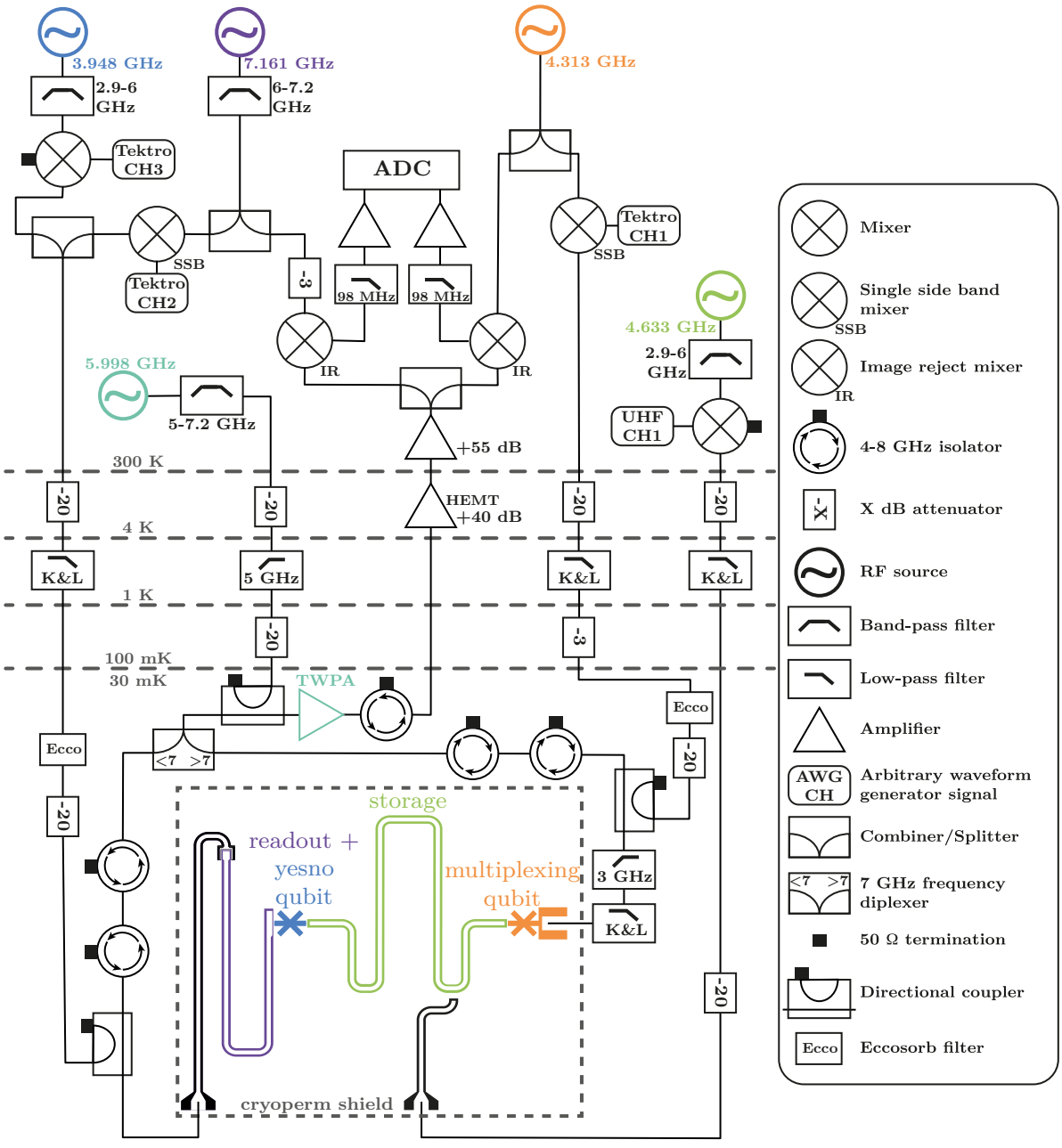


Figure 5.5: **Schematic of the setup.** Each electromagnetic mode of the experiment is driven by a RF generator detuned by the modulation frequency and whose color matches the color of the corresponding mode in Fig. 5.4. Room temperature isolators are not represented for the sake of clarity.

| parameters | symbol | value |
|---|---|---|
| readout decay rate | $\Gamma_{\mathrm{ro}}$ | $(40\ \mathrm{ns})^{-1}$ |
| storage decay rate | $\Gamma_{1,\mathrm{s}}$ | $(3.8\ \mu s)^{-1}$ |
| storage decoherence rate | $\Gamma_{2,\mathrm{s}}$ | $(2\ \mu s)^{-1}$ |
| yes-no decay rate | $\Gamma_{1,\mathrm{yn}}$ | $(20\ \mu s)^{-1}$ |
| yes-no decoherence rate | $\Gamma_{2,\mathrm{yn}}$ | $(27\ \mu s)^{-1}$ |
| multiplexing decay rate | $\Gamma_{1,\mathrm{mp}}$ | $(44\ ns)^{-1}$ |
| multiplexing decoherence rate | $\Gamma_{2,\mathrm{mp}}$ | $(88\ ns)^{-1}$ |

Table 5.2: **Table of all relaxation and decoherence rates.** The readout decay rate is obtained from the measurement induced dephasing rate of the yes-no qubit by readout photons. The yes-no qubit decay rate is measured using the time evolution of probability to find the qubit excited after a $\pi$ pulse. The yes-no qubit decoherence rate is measured using Ramsey interferometry. The storage decay rate is measured using the time evolution of the probability to have zero photon after populating the storage mode. Storage decoherence rate is measured using what we define as a Ramsey interferometry experiment for an harmonic oscillator (see section 5.2.2.3). The multiplexing decay and decoherence rates are measured by fitting the qubit resonance for various probe amplitudes.

lithography. The Josephson junctions are made out of e-beam evaporated Al/AlOx/Al through a PMMA/MAA resist mask patterned in a distinct e-beam lithography step. For each transmon qubit a single Dolan bridge is used to make the junctions.

The first cooldown of the device revealed that the multiplexing qubit frequency and storage frequency were too close to be modeled by a dispersive Hamiltonian. They were detuned by about 100 MHz and the storage mode was significantly hybridized with the multiplexing qubit, entailing a large photon loss rate. We estimated that a 10% increase of the junction resistance should decrease the frequency of the multiplexing qubit by 200 MHz. We warmed up the circuit at room temperature and placed it on a hot plate during 60 min at 100°C. We monitored the resistance of 9 test junctions located on the chip every 10 minutes until we reached a 10% increase. During the second cool down we measured a detuning between the multiplexing qubit and the storage mode of about 320 MHz, as targeted.

### 5.2.2 *Calibration*

#### 5.2.2.1 *Calibration of the storage mode displacement amplitude*

The storage mode can be displaced by driving it on resonance with a voltage $V_{\mathrm{s}}(t)\cos(2\pi f_{\mathrm{s}}t + \phi_{\mathrm{s}})$, where $V_{\mathrm{s}}(t)$ is the pulse envelope. The driving Hamiltonian of the storage mode reads $\hbar(\epsilon_{\mathrm{s}}(t)\hat{a}_{\mathrm{s}}^{\dagger} + \epsilon_{\mathrm{s}}^{*}(t)\hat{a}_{\mathrm{s}})$ where $\epsilon_{\mathrm{s}}(t) = \mu V_{\mathrm{s}}(t)e^{i\phi_{\mathrm{s}}}$. The scaling factor $\mu = 1.45\ (\mathrm{mV}.\mu\mathrm{s})^{-1}$ is calibrated by fitting the photocounting measurement results obtained using the yes-no qubit with the master equation simulation (see section 5.2.3.1).

Fig. 5.6a shows the evolution of $\epsilon_s$ with $V_\mathrm{s}$. For every experiment, the storage mode displacements are realized using a Gaussian pulse shape $\epsilon_\mathrm{s}(t) = \lambda(t)\epsilon_\mathrm{max}$ with a maximum amplitude $\epsilon_\mathrm{max}$, a width 25 ns and a duration 100 ns. We simulated the dynamics of the storage mode under this Gaussian displacement taking into account the couplings, relaxation and decoherence rates (see section 5.2.3.2) for various amplitudes $\epsilon_\mathrm{max}$. We then computed the expectation value of the number of photon operator $\langle \hat{n}_\mathrm{s} \rangle$ at the end of the pulse. Fig. 5.6b shows the square root of $\langle \hat{n}_\mathrm{s} \rangle$ as a function of $\epsilon_\mathrm{max}$. Fitting with a linear function, we find that $\sqrt{\langle \hat{n}_\mathrm{s} \rangle} = 59.1\epsilon_\mathrm{max}$. As $\epsilon_s$ increases linearly with $V_\mathrm{s}$, $\epsilon_\mathrm{max}$ increases linearly with the maximum voltage amplitude $V_\mathrm{max,s}$ of the Gaussian pulse $V_\mathrm{s}(t) = \lambda(t)V_\mathrm{max,s}$. Using the two linear regressions, we can express the photon number of the storage mode as $\sqrt{\langle n_\mathrm{s} \rangle} = (85.9\ \mathrm{V}^{-1})\, V_\mathrm{max,s}$.

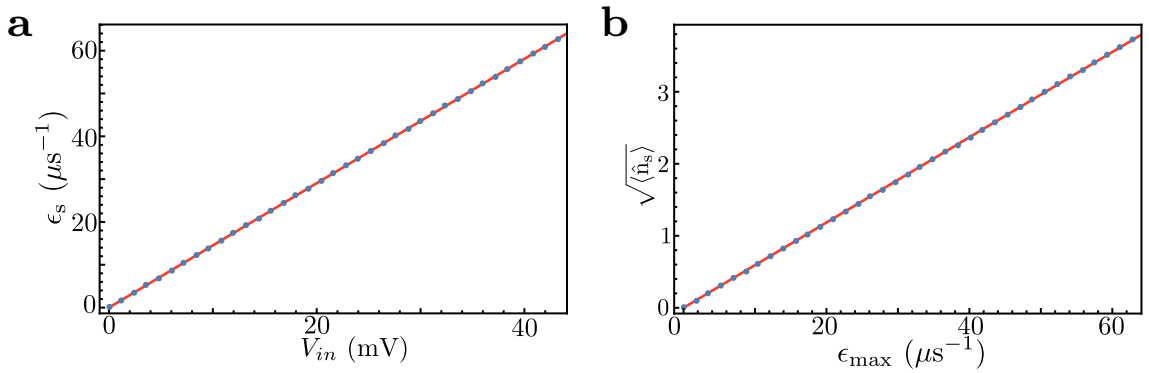


Figure 5.6: **Calibration of the average number of photons $\langle n_\mathrm{s} \rangle$ in the storage mode as a function of the displacement amplitude. a.** Evolution of the displacement amplitude $\epsilon_s$ with the pulse envelope $V_s$. The calibration is obtained by comparing the results of a photon counting experiment using the yes-no qubit with a master equation simulation (see section 5.2.3.1). **b.** Square root of the average photon number $\langle n_\mathrm{s} \rangle$ in the storage mode as a function of the drive amplitude. The storage is displaced by 100 ns long Gaussian pulse with a width of 25 ns. The same pulse shape is used in the simulation. From the two linear fits we extract the evolution of the mean number of photons with the amplitude of the pulse $\sqrt{\langle n_\mathrm{s} \rangle} = (85.9\ \mathrm{V}^{-1})\ V_\mathrm{max,s}$.

### 5.2.2.2 *Wigner tomography calibration*

The Wigner function of a harmonic oscillator with density matrix $\rho$ is defined as $W(\alpha) = 2\,\mathrm{Tr}(D^\dagger(\alpha)\rho D(\alpha)\mathcal{P})/\pi$ where $\mathrm{D}(\alpha) = e^{\alpha \hat{a}_\mathrm{s}^\dagger - \alpha^* \hat{a}_\mathrm{s}}$ is the displacement operator of the storage mode by a coherent field $\alpha$ and $\mathcal{P} = e^{i\pi \hat{a}_\mathrm{s}^\dagger \hat{a}_\mathrm{s}}$ is the photon number parity operator. A Wigner function is the expectation value of the parity after a displacement by an amplitude $\alpha$. The Wigner tomography sequence is represented on Fig. 5.7a . It starts by realizing a displacement on the storage mode with a 100 ns long Gaussian pulse at frequency $f_\mathrm{s}$ (or detuned for Ramsey interferometry of the storage mode, see section 5.2.2.3) with a width of 25 ns. Then two successive $\pi/2$ Gaussian pulses of 18 ns with a width of 4.5 ns are sent to the yes-no qubit at $f_\mathrm{yn}$ and are separated by a waiting time $\Delta\tau = 337$ ns $\approx 1/2\chi_\mathrm{s,yn}$. It implements a parity measurement and maps the parity of the storage mode onto the $z$-axis on the yes-no qubit [84, 85, 116]. The sequence terminates by a 2 $\mu$s long square pulse on the readout resonator to read out

the state of the yes-no qubit. For high amplitude $\alpha$, higher order Kerr terms distort the Wigner function. To mitigate this effect, we interleaves two sequences with a final pulse of phase either $+\pi/2$ or $-\pi/2$.(see Fig. 5.7a). The difference between the two signals gives us the Wigner function without the distortion due to the storage mode anharmonicity and enables us to remove low frequency noise. The $z$ axis of Fig. 5.7b is calibrated using the yes-no qubit Rabi oscillation amplitude to express the signal using Pauli operators. Multiplying the result by $2/\pi$ yields the Wigner function $\mathrm{W}(\alpha)$ in Fig. 5.7c.

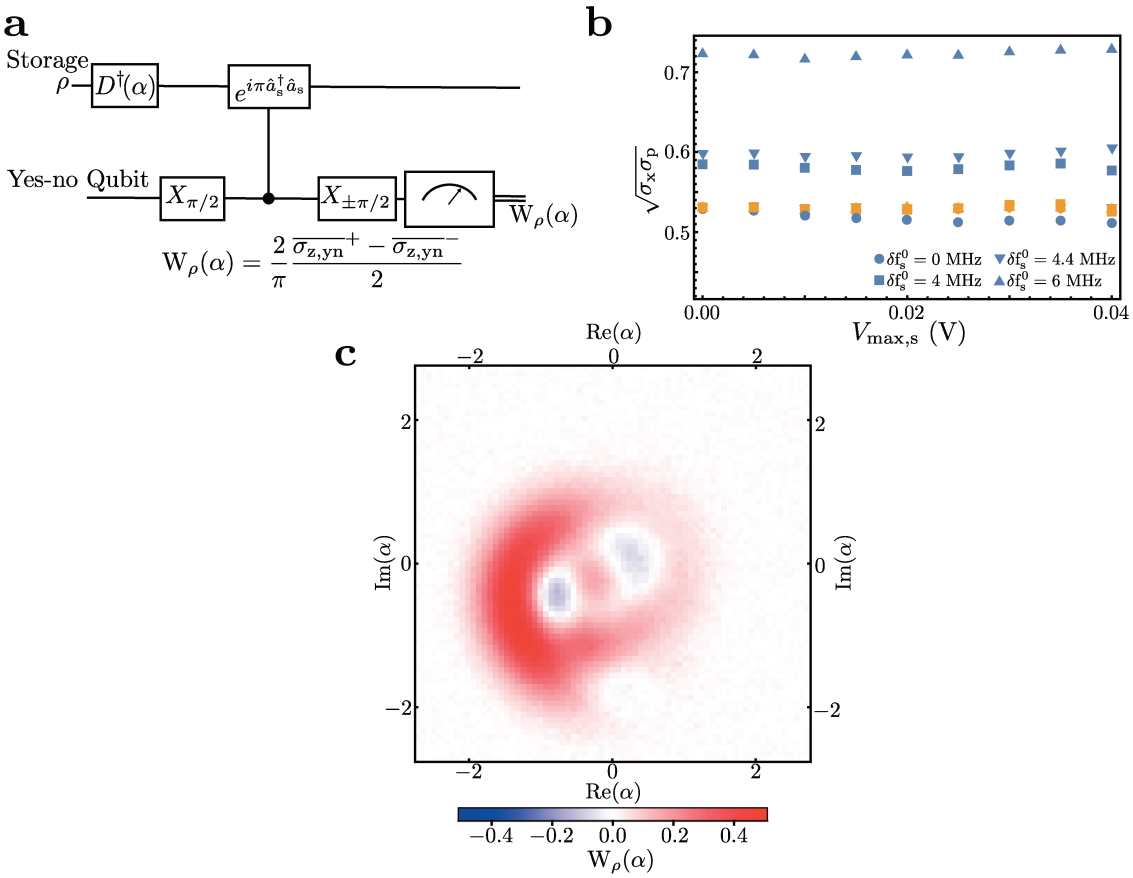


Figure 5.7: **Direct Wigner tomography of the storage mode a.** Circuit diagram of a Wigner tomography using a parity measurement based on dispersive interaction. After a 100 ns displacement pulse on the storage mode, an unconditional $\pi/2$ pulse is applied to the yes-no qubit. The qubit evolves freely during a time $\Delta\tau = 337$ ns $\approx 1/2\chi_{\mathrm{s,yn}}$ before a new $\pm\pi/2$ pulse is sent and the state of the yes-no qubit is measured using the readout resonator. **b.** Calibration of the quadrature axes for Wigner tomography. Blue dots represent the standard deviation of the quadratures of the displaced thermal equilibrium state of the storage mode as a function of drive amplitude for various detuning using the photon number calibration alone (see section 5.2.2.1). In contrast, yellow dots show the same standard deviation with the noise based quadrature calibration. **c,** Wigner tomography of the storage mode. Here, the mode was prepared in two steps. First, the storage mode is displaced by a pulse with an amplitude 1.7 and then the multiplexing qubit is driven at a single tone at $f_{\mathrm{mp}} - 1.4\chi_{\mathrm{s,mp}}$ during 750 ns with an amplitude $\Omega = \chi_{\mathrm{s,mp}}/2$. The appearance of negative values in the Wigner function demonstrate that one can prepare non classical states in the storage mode using the multiplexing qubit backaction alone.

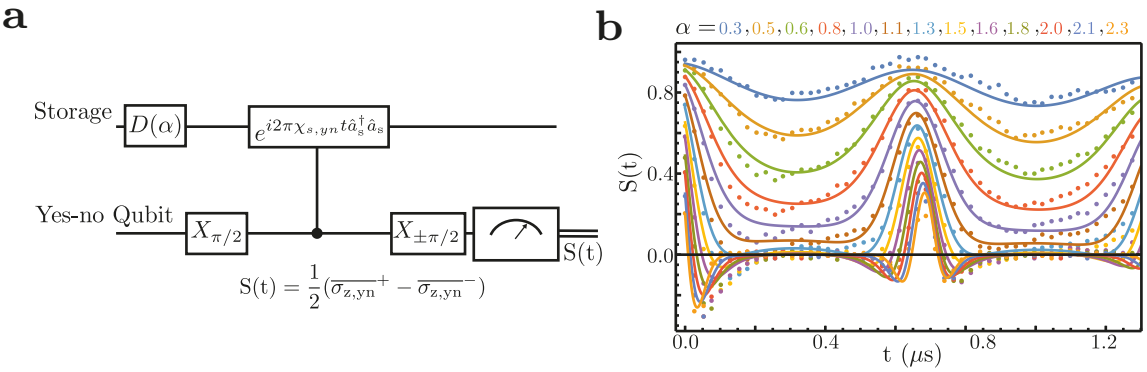


Figure 5.8: **Revival of the Ramsey interferometry on the yes-no qubit a.** Circuit diagram for Ramsey interferometry in the presence of storage photons. After a 100 ns displacement pulse at the storage frequency, an unconditional $\pi/2$ pulse is applied to the yes-no qubit. We then let the qubit evolve freely during a time $t$ before doing a new $\pm\pi/2$ pulse and measure the state of the yes-no qubit. The signal S(t) is half the difference between the average outcomes of the two sequences. **b.** Measured (dots) and predicted (lines) signal S as a function of waiting time $t$. Predicted signal is computed from Eq. (5.4). yes-no qubit revivals occur every $1/\chi_{s,yn} \approx 0.7\mu$s.

The axes of the phase space $x, p$ are calibrated using the same pulse sequence. The photon number calibration realized before (see section 5.2.2.1) cannot be used here for two reasons. First Ramsey oscillations of the storage mode impose to play the Wigner sequence with displacement pulses detuned from the storage mode frequency, while the photon number calibration is only valid for resonant pulses. Second high order Kerr interaction affects the calibration when the storage mode hosts a large number of photons. We decided to use the width of the Wigner function when the storage mode is in the thermal equilibrium state to calibrate the phase space axes. For a thermal state with a thermal photon number $n_{\text{th}}$ the Wigner function is a 2D Gaussian function with a width $\sqrt{n_{\text{th}} + 1/2}$ [29]

$$W_{\rho(n_{\text{th}})}(\alpha = x + ip) = \frac{2}{\pi}\frac{1}{2n_{\text{th}} + 1}e^{-2|\alpha|^2/(2n_{\text{th}}+1)}. \tag{5.3}$$

For a thermal state displaced by an amplitude $\beta$ the Wigner function is still a 2D Gaussian function with a width $\sqrt{n_{\text{th}} + 1/2}$ but centered on $\beta$. In thermal equilibrium, the storage mode has an average photon number $n_{\text{th}} = 0.03$, which is measured using the photon counting experiment. We calibrated the quadrature axes in order to get the expected geometrical mean $\sqrt{\sigma_x\sigma_p} = 0.53$ of the spread along the quadratures $x$ and $p$ when the storage mode is at thermal equilibrium. To take into account high order Kerr effects, we displace the storage mode equilibrium state and measure its Wigner function. We adjust the calibration to still find a spread of $\sqrt{\sigma_x\sigma_p} = 0.53$. The function used for the calibration is a third order polynomial function which gives $|\alpha|$ as a function of the pulse amplitude $V_{\text{max,s}}$. We repeat this protocol for 3 detuning values $\delta f_{\text{s}}$ between the displacement pulse and storage mode frequencies. Fig. 5.7b shows the mean quadrature spread of the displaced storage mode thermal state Wigner function as a function of drive amplitude $V_{\text{max,s}}$ for the photon number calibration and the Wigner phase space calibration. For example, the polynomial function for a detuning

of 4 MHz reads $\alpha = x + ip = e^{i\phi_s}(77.3V_{\mathrm{max,s}} + 86.7V_{\mathrm{max,s}}^2 - 1343V_{\mathrm{max,s}}^3)$ where $V_{\mathrm{max,s}}$ is expressed in Volt and $\phi_s$ is the phase of the pulse. For a typical value $V_{\mathrm{max,s}} = 20$ mV, the second order term is a correction of about 2% and the third one is a correction of about 0.07%.

The duration $\Delta\tau$ is calibrated using qubit state revival during Ramsey interferometry (see supplementary material of Ref. [87]). We used a Ramsey interferometry sequence (Fig. 5.8a) for the yes-no qubit at its resonance frequency for various coherent states in the storage mode. Revivals happen every $1/\chi_{\mathrm{s,yn}}$ which allows us to set $\Delta\tau$ as half the revival time in Fig. 5.8b. The signal difference between the final $-\pi/2$ and $+\pi/2$ pulses can be expressed as

$$S(t) = \frac{\overline{\sigma_{\mathrm{z,yn}}}^{+} - \overline{\sigma_{\mathrm{z,yn}}}^{-}}{2} = e^{|\alpha|^2(\cos(2\pi\chi_{\mathrm{s,yn}}t)-1)}\cos(|\alpha|^2\sin(2\pi\chi_{\mathrm{s,yn}}t))e^{-t\Gamma_{2,\mathrm{yn}}-\gamma|\alpha|^2 t} \quad (5.4)$$

This expression is derived in the supplementary material of Ref. [87]. The last exponential decay factor was added to take into account the intrinsic decoherence of the yes-no qubit and the measurement induced dephasing rate of the storage mode on the yes-no qubit during the waiting time. We also take into account a second order Kerr correction that shifts the revival time with the amplitude of the coherent state [87]. At first order this shift is given by

$$t_{\mathrm{revival}} = 2\Delta\tau\left(1 + 2|\alpha|^2\chi_{\mathrm{s,s,yn}}\Delta\tau\right). \quad (5.5)$$

Finding the above parameters that allow the model to match the measured signal shown in Fig. 5.8b, we find $\Delta\tau = 337$ ns, $\gamma = 0.23\ \mu\mathrm{s}^{-1}$ and $\chi_{\mathrm{s,s,yn}} = 14$ kHz. However, this simple expression does not take into account the finite lifetime of the storage mode and we prefer not to take these values as accurate enough compared to what we can obtain with the other methods presented in this work.

#### 5.2.2.3 *Ramsey oscillations of the storage mode*

For a qubit, Ramsey oscillations correspond to the evolution of the real part of the coherence between the $|g\rangle$ and $|e\rangle$ states. A typical sequence starts by a $\pi/2$ pulse detuned from resonance by $\delta f$ to create a coherent superposition of $|g\rangle$ and $|e\rangle$ states. Then the qubit is let to evolve freely before its state tomography is performed. Both $\sigma_x$ and $\sigma_y$ oscillate at $\delta f$ while decaying at the decoherence rate $\Gamma_2$.

We decided to realize an analogous sequence based on the same idea for a harmonic oscillator (a similar sequence was recently performed in Ref. [117]). The first $\pi/2$ pulse is replaced by a detuned displacement pulse $D(\beta)$ on the storage mode. The field then evolves freely during a time $t$ before a Wigner tomography is realized. The expectation value of $\hat{X} = (\hat{a}_s + \hat{a}_s^\dagger)/2$ and $\hat{P} = (\hat{a}_s - \hat{a}_s^\dagger)/2i$ quadratures are computed from the Wigner tomography.

Indeed for any operator $\hat{O}$, we can apply the Wigner transform to obtain the operator Wigner map $W_{\hat{O}}$ [29] as

$$W_{\hat{O}}(\alpha = x+ip) = W_{\hat{O}}(x,p) = \frac{1}{\pi}\int \mathrm{d}y\, e^{-2ipy}\langle x+y/2|\hat{O}|x-y/2\rangle = \frac{2}{\pi}\,\mathrm{Tr}(D^\dagger(\alpha)\hat{O}D(\alpha)\mathcal{P}) \tag{5.6}$$

where $\{|x\rangle\}$ is the eigenbasis of the quadrature operator $\hat{X}$. With this tool, the Wigner function of a state $|\Psi\rangle$ (respectively a density matrix $\rho$) is simply given by $W_{|\Psi\rangle\langle\Psi|}(\alpha)$ (respectively $W_\rho(\alpha)$). The mean value of an operator $\hat{O}$ can be derived from the integral over the phase-space of the product of the two Wigner distributions times $\pi$,

$$\begin{aligned}
&\pi\int \mathrm{d}x\int \mathrm{d}p\, W_\rho(x,p)W_{\hat{O}}(x,p)\\
&= \tfrac{1}{\pi}\int \mathrm{d}x\int \mathrm{d}p\int \mathrm{d}y\int \mathrm{d}y\prime\, e^{-2ip(y+y\prime)}\langle x+y/2|\rho|x-y/2\rangle\langle x+y\prime/2|\hat{O}|x-y\prime/2\rangle\\
&= \int \mathrm{d}x\int \mathrm{d}y\int \mathrm{d}y\prime\,\delta(y+y\prime)\langle x+y/2|\rho|x-y/2\rangle\langle x+y\prime/2|\hat{O}|x-y\prime/2\rangle\\
&= \int \mathrm{d}x\int \mathrm{d}y\,\langle x+y/2|\rho|x-y/2\rangle\langle x-y/2|\hat{O}|x+y/2\rangle = \int \mathrm{d}u\int \mathrm{d}v\,\langle u|\rho|v\rangle\langle v|\hat{O}|u\rangle\\
&= \mathrm{Tr}(\rho\hat{O}) = \langle\hat{O}\rangle_\rho
\end{aligned} \tag{5.7}$$

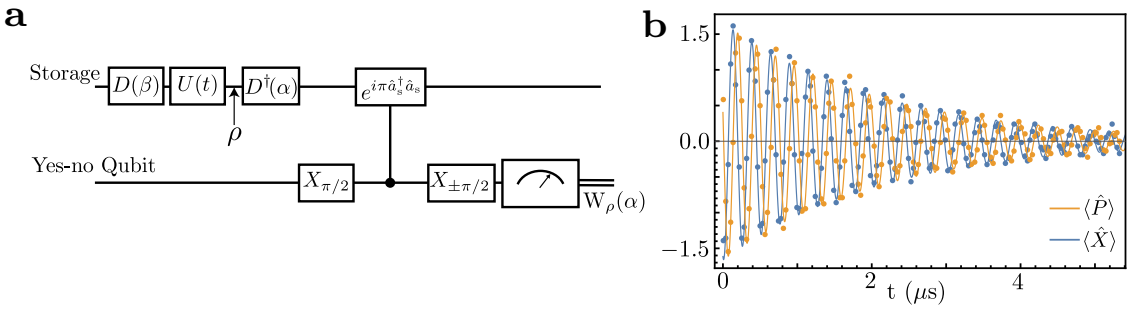


Figure 5.9: **Ramsey oscillations of the storage mode a.** Circuit diagram for Ramsey oscillations of an harmonic oscillator. All storage displacement pulses are performed in 100 ns with a Gaussian envelope of 25 ns width. For this experiment $\beta$ is the amplitude of the prepared coherent state and is set to -1.55. The detuning between displacement pulse and bare storage frequencies is $\delta f_s^0 = 3.96$ MHz. **b.** Measured (dots) and expected (lines) signals for $\langle\hat{X}\rangle$ (blue) and $\langle\hat{P}\rangle$ (orange). The expected signals are matched to the experiment using Eq. (5.11), when we set a frequency detuning of $\delta f_s = 3.96$ MHz and a decay rate $\Gamma_{2,s} = (2\ \mu s)^{-1}$.

In the case of $\hat{X}$ and $\hat{P}$ operators, Wigner maps take a simple expression

$$\begin{aligned}
W_{\hat{X}}(\alpha = x+ip) &= x/\pi\\
W_{\hat{P}}(\alpha = x+ip) &= p/\pi
\end{aligned} \tag{5.8}$$

For any density matrix $\rho$, one can extract $\langle\hat{X}\rangle = \mathrm{Tr}(\hat{X}\rho)$ and $\langle\hat{P}\rangle = \mathrm{Tr}(\hat{P}\rho)$ from the Wigner function $W \equiv W_\rho$ as

$$\begin{aligned}
\langle\hat{X}\rangle &= \int \mathrm{d}x\int \mathrm{d}p\, W(x,p)x\\
\langle\hat{P}\rangle &= \int \mathrm{d}x\int \mathrm{d}p\, W(x,p)p
\end{aligned} \tag{5.9}$$

The time trace of $\langle\hat{X}\rangle$ and $\langle\hat{P}\rangle$ is what we call the Ramsey oscillations for the storage mode. As in the qubit case, the frequency of the oscillations is set by the detuning $\delta f_s$

between the drive and the resonant frequency of the mode, which allows us to extract the frequency of the storage mode. At this point, a distinction has to be made between the detuning $\delta f_{\mathrm{s}}^{0} = f_{\mathrm{drive}} - f_s$ between the drive and the bare storage mode frequency (the resonant frequency when the multiplexed qubit and the storage are undriven) and the detuning $\delta f_{\mathrm{s}}$ between the drive and the resonant frequency of the storage mode, which depends on the multiplexed measurement strength in perfect analogy with the AC-Stark effect for a qubit readout. Note that the Wigner tomography sequence uses the same detuned frequency $\delta f_{\mathrm{s}}$ for its displacement pulse $D(\alpha)$ in order to keep the same phase reference. The measurement of Ramsey oscillations of a harmonic oscillator takes longer than the ones of a qubit because we fully determine the quantum state of an oscillator at each time instead of a simple Bloch vector. From Eq. (5.2), one can compute the time derivative of $\langle a \rangle$ and find

$$\langle \dot{\hat{a}}_{\mathrm{s}} \rangle = (2i\pi\delta f_{\mathrm{s}} - \Gamma_{2,\mathrm{s}})\langle \hat{a}_{\mathrm{s}} \rangle. \tag{5.10}$$

This differential equation can be easily solved and taking the real and imaginary parts, one finds that $\langle \hat{X} \rangle$ and $\langle \hat{P} \rangle$ evolve as

$$\begin{aligned} \langle \hat{X} \rangle &= |\beta| \cos(2\pi\delta f_{\mathrm{s}} t + \phi) e^{-t\Gamma_{2,\mathrm{s}}} \\ \langle \hat{P} \rangle &= |\beta| \sin(2\pi\delta f_{\mathrm{s}} t + \phi) e^{-t\Gamma_{2,\mathrm{s}}} \end{aligned} \tag{5.11}$$

where $\beta = |\beta| e^{i\phi} = \langle \hat{a}_s \rangle (t = 0)$. For each time $t$, we computed $\langle \hat{X} \rangle$ and $\langle \hat{P} \rangle$ and define the storage mode decoherence rate as $\Gamma_{2,\mathrm{s}}$. Fig. 5.9 shows an example of measured Ramsey oscillations.

In the main text, Fig. 3B does not exhibit oscillations because it is the mean value $\langle \hat{a}_{\mathrm{s}} + \hat{a}_{\mathrm{s}}^{\dagger} \rangle$ in the frame rotating at the resonant frequency of the storage mode. In practice, we measured them with a detuning shown in Fig. 5.10c and numerically computed the non-oscillating quantity $2\mathcal{R}e((\langle \hat{X} \rangle + i\langle \hat{P} \rangle)\exp(-2i\pi\delta f_{\mathrm{s}} t))$.

#### 5.2.2.4 *Storage mode frequency shift and induced dephasing rate by driving a comb on the multiplexing qubit*

By analogy with the AC Stark effect that shifts a qubit frequency when its readout cavity is driven, we will call AC Stark shift the detuning of the storage mode when the multiplexing qubit is driven. In order to measure this frequency shift and to measure the dephasing rate that is induced by the multiplexing qubit on the storage mode, we realize the reciprocal protocol for a qubit measured by a cavity. We decided to use a Ramsey interferometry sequence for the storage mode while the multiplexing qubit is continuously driven by a frequency comb during the time of free evolution $t$ (see Fig. 5.10a). The frequency comb is a Gaussian envelope of duration $t$ and width $t/4$ multiplied by the sum of nine sine functions at the frequencies $[f_{\mathrm{mp}}, f_{\mathrm{mp}} - \chi_{\mathrm{s,mp}}, ..., f_{\mathrm{mp}} - 8\chi_{\mathrm{s,mp}}]$.

For small measurement strength ($\Omega/\chi_{\mathrm{s,mp}} < 0.9$) we generated the Ramsey sequence with a displacement pulse detuned from the bare storage mode frequency by $\delta f_{\mathrm{s}}^{0} = 3.96$

MHz, and an amplitude $\beta = -1.55$. We fit the time evolution of $\langle \hat{X} \rangle$ and $\langle \hat{P} \rangle$ using the damped sine function

$$\begin{aligned} \langle \hat{X} \rangle &= A\cos(2\pi\delta f_s t + \phi)e^{-t\Gamma_{d,s}} \\ \langle \hat{P} \rangle &= A\sin(2\pi\delta f_s t + \phi)e^{-t\Gamma_{d,s}} \end{aligned} . \tag{5.12}$$

The parameters $A$, $\delta f_s$, $\phi$, and $\Gamma_{d,s}$ are determined altogether by fitting the model to the measured oscillations. $\Gamma_{d,s}$ is interpreted as the sum of the intrinsic storage dephasing rate $\Gamma_{2,s}$ and of the measurement induced dephasing rate. $\delta f_s$ is the sum of the detuning from the bare storage mode frequency $\delta f_s^0$ and of the AC stark shift of the storage mode. Both parameters are shown in Fig. 5.10c,d (blue dots) as a function of $\Omega/\chi_{s,mp}$.

For larger measurement strength ($\Omega/\chi_{s,mp} > 0.9$) we generated the Ramsey sequence with a displacement pulse detuning of $\delta f_s^0 = 5.96$ MHz, an amplitude of $\beta = -1.27$, and we model the time evolution of $\langle \hat{X} \rangle$ and $\langle \hat{P} \rangle$ by the sum of two sine functions with an exponential decay

$$\begin{aligned} \langle \hat{X} \rangle &= A(\cos(2\pi\delta f_s t + \phi) + \zeta\cos(2\pi\nu t + \psi_X))e^{-t\Gamma_{d,s}} \\ \langle \hat{P} \rangle &= A(\sin(2\pi\delta f_s t + \phi) + \zeta\sin(2\pi\nu t + \psi_P))e^{-t\Gamma_{d,s}} \end{aligned} . \tag{5.13}$$

This empirical model originates from three ideas. The first term is identical to the simple model in Eq. (5.12). Second, the measured Ramsey oscillations seem to show a small modulation in amplitude, which we try to capture with a second sine function. Third we try to keep the model as simple as possible.

Fig. 5.10b shows an example of Ramsey oscillations of the storage mode with a large amplitude of measurement. The two signals are used altogether to extract the parameters A, $\delta f_s$, $\nu$, $\phi$, $\psi_X$, $\psi_P$, and $\Gamma_{d,s}$. The frequency $\nu$ varies from 2.15 MHz to 2.5 MHz. The parameter $\zeta$ is roughly constant, it varies between 0.2 to 0.27. We decompose $\Gamma_{d,s}$ as the intrinsic storage dephasing rate $\Gamma_{2,s}$ plus the measurement induced dephasing rate and $\delta f_s$ as the detuning from the storage frequency $\delta f_s^0$ plus the measurement induced frequency shift of the storage mode. Fig. 5.10c shows measurement induced detuning as a function of measurement drive amplitude.

#### 5.2.2.5 *Calibration of Rabi frequency* $\Omega$

In order to realize the calibration of the Rabi frequency $\Omega$ for the multiplexing qubit we recorded Rabi oscillations and measured their frequency for various drive amplitudes. We played a square pulse of 1 $\mu$s on the multiplexing qubit at its bare frequency $f_{mp}$ with an amplitude $V_{mp}$. We demodulated the reflected pulse by time steps of 10 ns at $f_{mp}$. The reflection coefficient shows damped Rabi oscillations at a frequency that depends on $V_{mp}$. We matched to the measurement the Rabi oscillations for seven different amplitudes $V_{mp}$ using the model [70]

$$\mathcal{R}e\left(r(t)\right) - \mathcal{R}e\left(r_{ss}\right) = A\cos\left[\sqrt{(2\pi\xi V_{mp})^2 - \left(\frac{\Gamma_{1,mp} - 2\Gamma_{2,mp}}{16}\right)^2}(t - t0) + \phi\right] e^{-(t-t0)/T}, \tag{5.14}$$

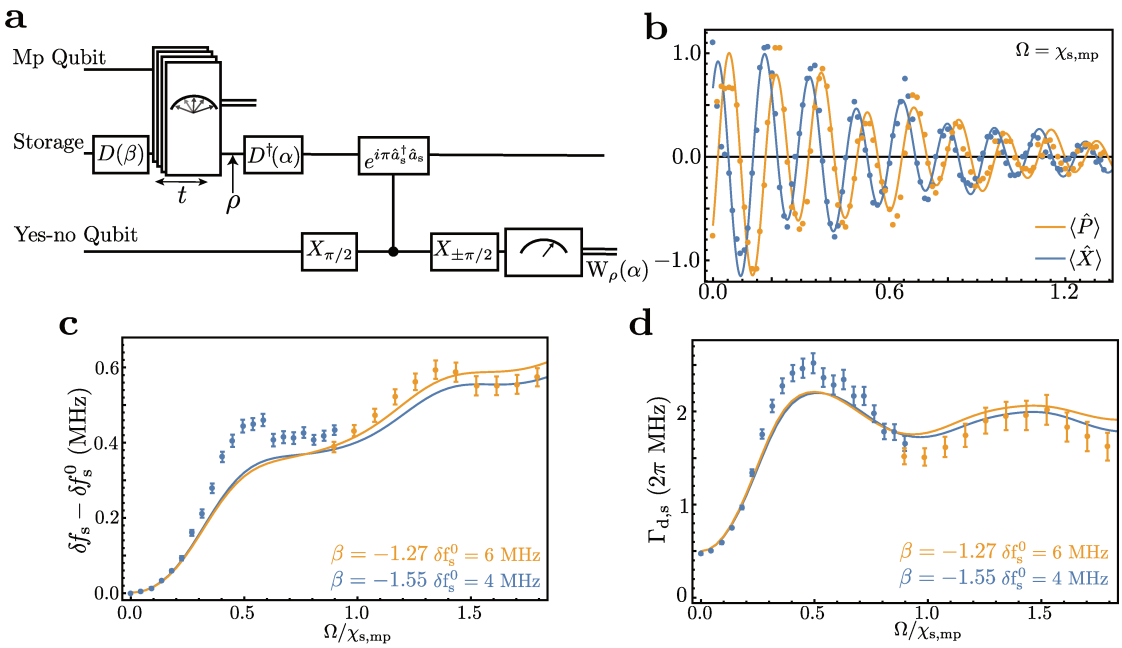


Figure 5.10: **Frequency shift and dephasing rate of the storage mode induced by the multiplexed photocounting measurement. a.** Circuit diagram of the protocol that determines the dephasing rate and frequency shift of the storage mode induced by the multiplexed photocounting measurement. The amplitude $\beta$ of the initial displacement is set at -1.55 for small measurement amplitude $\Omega/\chi_{s,mp} < 0.9$ and -1.27 for large measurement amplitude $\Omega/\chi_{s,mp} > 0.9$. The blocks linking the multiplexing qubit and the storage mode represent the continuous multiplexed measurement during a time $t$ made by the qubit on the storage mode. This measurement is realized by driving the qubit with a frequency comb $[f_{mp}, f_{mp} - \chi_{s,mp}, ..., f_{mp} - 8\chi_{s,mp}]$ within a Gaussian envelope. **b.** Ramsey oscillations of the storage mode for "large" measurement amplitude $\Omega/\chi_{s,mp} = 1$. One can see that the dynamics $\langle\hat{X}\rangle$ and $\langle\hat{P}\rangle$ are not governed by a simple decaying sine function. The theory does not reproduce quantitatively the measurement when using the simple version of the model Eq. (5.12). We use a simple model in order to capture this modulation, the model is described by Eq. (5.13). **c and d.** AC Stark shift and measurement induced dephasing rate measured (dots) and simulated (line) as a function of multiplexing qubit drive amplitude $\Omega$ normalised by $\chi_{s,mp}$. The evolution of the detuning and dephasing rate are strongly non linear with drive amplitude.

where $r_{ss}$ is the value of the reflection coefficient in the steady state. We obtain $\xi = 0.543$ GHz.V$^{-1}$ so that the Rabi frequency is thus calibrated as $\Omega = \xi V_{mp} = 0.543$ GHz.V$^{-1}$ $V_{mp}$ (see Fig. 5.11).

### 5.2.3 *Qutip simulations*

In this section, we briefly describe the master equation simulations used to understand our experimental results. We simulated the main photon counting experiments with both qubits as well as the photon number calibration of the storage mode, and the dephasing rate induced by the multiplexed measurement of the storage mode.

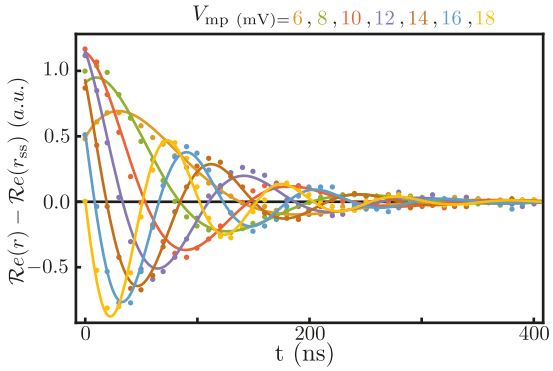


Figure 5.11: **Multiplexing qubit Rabi oscillations for various driving amplitude.** The measured Rabi oscillations observed in the reflection coefficient (dots) is reproduced by theory (solid line from Eq. (5.14). The vertical axis represents the deviation of the real part of the reflection coefficient to its steady state value. This calibration allows us to extract the scaling parameter $\xi$ such that $\Omega = \xi V_{\mathrm{mp}} = (0.543\ \mathrm{GHz.V}^{-1}\ )V_{\mathrm{mp}}$.

All simulations were performed using Python package *QuTiP* [98]. We simulated the complete system composed of the storage mode, the yes-no qubit and the multiplexing qubit with all couplings, except in the case of the measurement induced dephasing rate for which we only took into account the storage mode and the multiplexing qubit. The storage mode was modeled as an harmonic oscillator while the qubits were replaced by two level systems. The Hilbert space of the storage mode was truncated at a photon number ranging from 10 to 25 photons depending on the simulation. In this section we will use Pauli matrices to describe operators acting on qubits.

#### 5.2.3.1 *Photocounting simulations*

**Photocounting with the yes-no qubit**

Both photon counting approaches are simulated in a very similar manner. The first simulation (yes-no simulation) describes the use of conditional operations on the yes-no qubit. This experiment serves as a calibration of the number of photons in the storage mode and of all relevant parameters. This experiment starts with a displacement of the storage mode followed by a conditional $\pi$ pulse on the yes-no qubit at frequency $f_{\mathrm{yn}} - \delta f_{\mathrm{yn}}$ before detecting the Pauli operator $\sigma_{\mathrm{z,yn}}$.

We write the Hamiltonian of the system in a frame rotating at $f_{\mathrm{s}} - \chi_{\mathrm{s,mp}}/2 - \chi_{\mathrm{s,yn}}/2$ for storage mode, $f_{\mathrm{yn}} - \delta f_{\mathrm{yn}}$ for yes-no qubit mode and $f_{\mathrm{mp}}$ for multiplexing qubit mode as follows

$$\begin{aligned}\hat{H}_1/h \;=\; & \delta f_{\mathrm{yn}}\frac{\hat{\sigma}_{\mathrm{z,yn}}}{2} - \chi_{\mathrm{s,yn}}\hat{n}_{\mathrm{s}}\frac{\hat{\sigma}_{\mathrm{z,yn}}}{2} - \chi_{\mathrm{s,mp}}\hat{n}_{\mathrm{s}}\frac{\hat{\sigma}_{\mathrm{z,mp}}}{2} - \chi_{\mathrm{s,s}}\hat{n}_{\mathrm{s}}(\hat{n}_{\mathrm{s}}-1) \\ & -\chi_{\mathrm{s,s,yn}}\hat{n}_{\mathrm{s}}(\hat{n}_{\mathrm{s}}-1)\frac{\hat{\sigma}_{\mathrm{z,yn}}}{2} - \chi_{\mathrm{s,s,mp}}\hat{n}_{\mathrm{s}}(\hat{n}_{\mathrm{s}}-1)\frac{\hat{\sigma}_{\mathrm{z,mp}}}{2} + \frac{\epsilon_{\mathrm{yn}}(t)}{h}\hat{\sigma}_{\mathrm{x,yn}}\ , \\ & +\frac{\lambda(t)}{2\pi}(\epsilon_{\max}e^{i\pi(\chi_{\mathrm{s,mp}}+\chi_{\mathrm{s,yn}})t}\hat{a}_{\mathbf{s}} + \epsilon^{*}_{\max}e^{-i\pi(\chi_{\mathrm{s,mp}}+\chi_{\mathrm{s,yn}})t}\hat{a}^{\dagger}_{\mathbf{s}})\end{aligned} \tag{5.15}$$

where $\lambda(t)$ is a Gaussian function with duration 100 ns, width 25 ns and a maximum of 1 so that the storage mode displacement pulse reads $\epsilon_{\mathrm{s}}(t) = \lambda(t)\epsilon_{\max}$ and $\epsilon_{\mathrm{yn}}(t)$ is the time

envelope of a Gaussian pulse with duration 1.9 $\mu$s and width 475 ns. The amplitude of the pulse is chosen to obtain a $\pi$ rotation on the yes-no qubit. The term $-\delta f_{\mathrm{yn}}\frac{\hat{\sigma}_{\mathrm{z,yn}}}{2}$ takes into account the detuning between the $\pi$ pulse and the yes-no qubit frequency. $\epsilon_{\mathrm{yn}}(t)$ is delayed with respect to $\lambda(t)$ to match the experimental pulse sequence. In comparison with Hamiltonian (5.1), this simulation adds cross-Kerr interactions between each qubit and the storage mode, a self-Kerr term on the storage mode but it does not take into account the readout resonator.

In addition to the Hamiltonian (5.15), we supply the solver with eight collapse operators to simulate the dynamics of the following master equation

$$\begin{aligned}\dot{\rho} &= -\frac{i}{\hbar}[\hat{H}_1,\rho] + 2\Gamma_{\phi,\mathrm{s}}\mathcal{L}(\hat{n}_{\mathrm{s}})\rho + (1+n_{\mathrm{th,s}})\Gamma_{1,\mathrm{s}}\mathcal{L}(\hat{a}_{\mathrm{s}})\rho + n_{\mathrm{th,s}}\Gamma_{1,\mathrm{s}}\mathcal{L}(\hat{a}_{\mathrm{s}}^{\dagger})\rho \\ &\quad + \frac{1}{2}\Gamma_{\phi,\mathrm{yn}}\mathcal{L}(\hat{\sigma}_{\mathrm{z,yn}})\rho + \Gamma_{1,\mathrm{yn}}\mathcal{L}(\hat{\sigma}_{\mathrm{yn}}^{-})\rho + \frac{1}{2}\Gamma_{\phi,\mathrm{mp}}\mathcal{L}(\hat{\sigma}_{\mathrm{z,mp}})\rho + \Gamma_{1,\mathrm{mp}}\mathcal{L}(\hat{\sigma}_{\mathrm{mp}}^{-})\rho\end{aligned}, \tag{5.16}$$

with $n_{\mathrm{th,s}}$ the expectation values of $\hat{n}_{\mathrm{s}}$ when the system is at rest due to thermal occupation. All decoherence and relaxation rates are measured using previously explained calibration.

The master equation is solved using the function "mesolve" of QuTiP starting from a thermal state with $n_{\mathrm{th,s}}$ photon in storage mode, the yes-no qubit in the ground state $|g\rangle$ and the multiplexing qubit also in the ground state $|g\rangle$. The solver iteratively computes the density matrix with a 10 ns time step during the displacement pulse and the $\pi$ pulse. We compute the expectation value $\langle\hat{\sigma}_{\mathrm{z,yn}}\rangle$ at the end of the sequence and convert it into a probability $\mathbb{P}_e$ of finding the yes-no qubit in the $|e\rangle$ state.

This simulation can be used to reproduce the experiment in Fig. 2A,C of the main text by adjusting the following parameters $\{\mu = \epsilon_{\mathrm{max}}/V_{\mathrm{max,s}}, \chi_{\mathrm{s,yn}}, \chi_{\mathrm{s,s}}, \chi_{\mathrm{s,s,yn}}, n_{\mathrm{th,s}}\}$. Note that we need to run the simulation for every couple of parameters ($V_{\mathrm{max,s}}$,$\delta f_{\mathrm{yn}}$). The table Tab. 5.3 compiles the values of fitted parameters.

**Photocounting with the multiplexing qubit**

A second simulation (fluorescence simulation) was carried out to compare the photon counting experiment in Fig. 2B,D using a single drive on the multiplexing qubit with theory. This experiment also starts with a storage mode displacement but it is followed by a 2 $\mu$s Gaussian pulse on the multiplexing qubit at the frequency $f_{\mathrm{mp}} - \delta f_{\mathrm{mp}}$ with an amplitude expressed as a Rabi frequency $\Omega = \chi_{\mathrm{s,mp}}/4$. The measured reflection coefficient of the multiplexing qubit $r(\delta f_{\mathrm{mp}})$ can be expressed using input-output theory as [122]

$$r(\delta f_{\mathrm{mp}}) = \frac{\langle a_{\mathrm{out}}\rangle}{\langle a_{\mathrm{in}}\rangle} = \frac{\langle a_{\mathrm{in}}\rangle - \sqrt{\Gamma_{1,\mathrm{mp}}}\langle\sigma_{-,\mathrm{mp}}\rangle}{\langle a_{\mathrm{in}}\rangle} = 1 - \frac{\sqrt{\Gamma_{1,\mathrm{mp}}}}{\langle a_{\mathrm{in}}\rangle}\langle\hat{\sigma}_{-,\mathrm{mp}}\rangle.$$

And since the Rabi frequency is given by $\Omega = \sqrt{\Gamma_{1,\mathrm{mp}}}|\langle a_{\mathrm{in}}\rangle|/\pi$ we get an emission coefficient

$$1 - \mathcal{R}e\left(r(\delta f_{\mathrm{mp}})\right) = \frac{\Gamma_{1,\mathrm{mp}}}{\pi\Omega}\mathcal{R}e\left(e^{-i\arg(\langle a_{\mathrm{in}}\rangle)}\langle\hat{\sigma}_{-,\mathrm{mp}}\rangle\right)$$

in the frame rotating at $f_{\mathrm{mp}} - \delta f_{\mathrm{mp}}$ for the multiplexing qubit. If we set the phase of the drive so that $i\langle a_{\mathrm{in}}\rangle \geq 0$, meaning we drive the qubit along $\sigma_{\mathrm{x,mp}}$, the emission coefficient becomes

$$1 - \mathcal{R}e\left(r(\delta f_{\mathrm{mp}})\right) = \frac{\Gamma_{1,\mathrm{mp}}}{2\pi\Omega}\langle\hat{\sigma}_{\mathrm{y,mp}}\rangle.$$

The Hamiltonian of the problem in the frame rotating at $f_{\mathrm{s}} - \chi_{\mathrm{s,mp}}/2 - \chi_{\mathrm{s,yn}}/2$ for storage mode, $f_{\mathrm{yn}}$ for yes-no qubit and $f_{\mathrm{mp}} - \delta f_{\mathrm{mp}}$ for multiplexing qubit reads

$$\begin{aligned}\hat{H}_2/h \;=\; & \delta f_{\mathrm{mp}}\frac{\hat{\sigma}_{\mathrm{z,mp}}}{2} - \chi_{\mathrm{s,yn}}\hat{n}_{\mathrm{s}}\frac{\hat{\sigma}_{\mathrm{z,yn}}}{2} - \chi_{\mathrm{s,mp}}\hat{n}_{\mathrm{s}}\frac{\hat{\sigma}_{\mathrm{z,mp}}}{2} - \chi_{\mathrm{s,s}}\hat{n}_{\mathrm{s}}(\hat{n}_{\mathrm{s}}-1) \\ & -\chi_{\mathrm{s,s,yn}}\hat{n}_{\mathrm{s}}(\hat{n}_{\mathrm{s}}-1)\frac{\hat{\sigma}_{\mathrm{z,yn}}}{2} - \chi_{\mathrm{s,s,mp}}\hat{n}_{\mathrm{s}}(\hat{n}_{\mathrm{s}}-1)\frac{\hat{\sigma}_{\mathrm{z,mp}}}{2} + \frac{\Omega}{2}\epsilon_{\mathrm{mp}}(t)\hat{\sigma}_{\mathrm{x,mp}} \\ & +\frac{\lambda(t)}{2\pi}(\epsilon_{\max}e^{i\pi(\chi_{\mathrm{s,mp}}+\chi_{\mathrm{s,yn}})t}\hat{a}_{\mathbf{s}} + \epsilon^*_{\max}e^{-i\pi(\chi_{\mathrm{s,mp}}+\chi_{\mathrm{s,yn}})t}\hat{a}^\dagger_{\mathbf{s}}),\end{aligned} \tag{5.17}$$

where $\epsilon_{\mathrm{mp}}(t) \geq 0$ is a Gaussian function of duration 2 $\mu$s, width 250 ns and with an amplitude 1. $\epsilon_{\mathrm{mp}}(t)$ is delayed compare to $\lambda(t)$ to reproduce the experimental pulse sequence. We add to this Hamiltonian the same relaxation and decoherence channels as for the yes-no simulation (see Eq. (5.16)) for which the decoherence and relaxation rates were measured independently. The resulting master equation only differs from the yes-no simulation by the Rabi drive that addresses the multiplexing qubit instead of the yes-no qubit. The master equation is solved using the "mesolve" function of QuTiP with a time step of 5.25 ns starting from a thermal state with $n_{\mathrm{th,s}}$ photons for storage and the yes-no qubit and the multiplexing qubit in the ground state $|g\rangle$. Finally, the expectation value $\langle\hat{\sigma}_{\mathrm{y,mp}}\rangle$ is computed and integrated during the 2 $\mu$s of the pulse.

We compare the measured emission coefficient in Fig. 2B,D to the simulated signal $A\langle\hat{\sigma}_{\mathrm{y,mp}}\rangle$ where $A$ is left as a free parameter due to a small parasitic reflection in the measurement setup and thermal population. The parameters $\{\mu, \chi_{\mathrm{s,t}}, \chi_{\mathrm{s,s}}, \chi_{\mathrm{s,s,t}}, n_{\mathrm{th,s}}\}$ is already set by the calibration above using the simulation of the yes-no qubit. From the fluorescence simulation, we thus extract the parameters $\{\chi_{\mathrm{s,mp}}, \chi_{\mathrm{s,s,mp}}, A\}$ by comparing the experimental observation in Fig. 2B,D with the simulation for various $V_{\mathrm{max,s}}$ and $\delta f_{\mathrm{mp}}$. Fitted values are given in Tab. 5.3. Finally, we ran the yes-no simulation again taking into account the updated multiplexing qubit parameters. As expected only small changes in the results of the yes-no qubit simulation are observed.

#### 5.2.3.2 *Evolution of the average photon number in the storage mode*

We simulated the filling of the storage mode by a displacement pulse on the cavity. We simulated the same master equation used for the photocounting simulations with parameters obtained from the photocounting simulations (see Tab. 5.3) but without applying any drive on the qubits. Only the displacement pulse on the storage mode is modeled i.e. $\epsilon_{\mathrm{mp}}(t) = 0$, $\delta f_{\mathrm{mp}} = 0$, $\epsilon_{\mathrm{yn}}(t) = 0$, and $\delta f_{\mathrm{yn}} = 0$.

| parameter | fitted values |
|---|---|
| $\mu$ | 1.45 $(\text{mV}.\mu\text{s})^{-1}$ |
| $\chi_{\text{s,yn}}$ | 1.42 MHz |
| $\chi_{\text{s,mp}}$ | 4.9 MHz |
| $\chi_{\text{s,s}}$ | -0.02 MHz |
| $\chi_{\text{s,s,yn}}$ | -0.003 MHz |
| $\chi_{\text{s,s,mp}}$ | -0.08 MHz |
| $n_{\text{th,s}}$ | 0.03 |

Table 5.3: **Parameters extracted from the photocounting simulations using the multiplexing or yes-no qubit.** All parameters except those related to the multiplexing qubit are determined using a fit of the yes-no qubit simulation to the Fig. 2A,C. Parameters related to multiplexing qubit are obtained using a fit of the simulation to the Fig. 2B,D.

The "mesolve" function of QuTiP computes the density matrix with a time step of 10 ns and returns the mean number of photons in the storage mode at the end of the displacement pulse for various drive amplitudes. Fig. 5.6 shows the square root of the expected mean photon number as a function of the amplitude $\epsilon_{\text{max}}$. We obtain a scaling factor $\sqrt{\langle n_{\text{s}}\rangle} = 85.9\ \text{V}^{-1}V_{\text{max,s}}$ used in the photon number calibration of the storage mode.

#### 5.2.3.3 *Simulation of multiplexed readout*

In this subsection, we simulate how a frequency comb reflects off the multiplexing qubit. We write the Hamiltonian in the frame rotating at $f_{\text{s}} - \chi_{\text{s,mp}}/2 - \chi_{\text{s,yn}}/2$ for the storage mode and at the qubit frequencies for the qubits as

$$\begin{aligned}\hat{H}_3/h \;=\; & -\chi_{\text{s,yn}}\hat{n}_{\text{s}}\frac{\hat{\sigma}_{\text{z,yn}}}{2} - \chi_{\text{s,mp}}\hat{n}_{\text{s}}\frac{\hat{\sigma}_{\text{z,mp}}}{2} - \chi_{\text{s,s}}\hat{n}_{\text{s}}(\hat{n}_{\text{s}}-1) - \chi_{\text{s,s,yn}}\hat{n}_{\text{s}}(\hat{n}_{\text{s}}-1)\frac{\hat{\sigma}_{\text{z,yn}}}{2} \\ & -\chi_{\text{s,s,mp}}\hat{n}_{\text{s}}(\hat{n}_{\text{s}}-1)\frac{\hat{\sigma}_{\text{z,mp}}}{2} + \frac{\Omega}{2}(\epsilon_{\text{comb}}(t)\hat{\sigma}^{+}_{\text{mp}} + \epsilon^{*}_{\text{comb}}(t)\hat{\sigma}^{-}_{\text{mp}}) \\ & +\tfrac{\lambda(t)}{2\pi}(\epsilon_{\text{max}}e^{i\pi(\chi_{\text{s,mp}}+\chi_{\text{s,yn}})t}\hat{a}_{\mathbf{s}} + \epsilon^{*}_{\text{max}}e^{-i\pi(\chi_{\text{s,mp}}+\chi_{\text{s,yn}})t}\hat{a}^{\dagger}_{\mathbf{s}})\end{aligned} \quad , \tag{5.18}$$

where $\Omega = \chi_{\text{s,mp}}/2$ and $\epsilon_{\text{comb}}(t)$ is the product of a Gaussian function with the sum of nine complex exponential $\sum_{k=0}^{8}\exp(2i\pi\chi_{\text{s,mp}}kt)$. The Gaussian envelope of $\epsilon_{\text{comb}}(t)$ has a duration of 2 $\mu s$, a width of 250 ns, and a maximum amplitude of 1 and the delay between $\epsilon_{\text{comb}}(t)$ and $\lambda(t)$ reproduces the experimental sequence. The master equation (5.16) is used with a time step of 1 ns for various amplitude $\epsilon_{\text{max}}$. We obtain the time evolution of $\langle\sigma_{y,mp}\rangle$ enabling us to compare the experimental measurements of Fig. 2E to the model. To do so, we integrate the simulated function $\langle\sigma_{y,mp}\rangle \times \cos(2\pi\chi_{\text{s,mp}}kt)$ for each integer $k$, similarly to the demultiplexing processing we perform on the multiplexed experimental signal. Note that, in the case $k = 0$, we need to divide the integral by 2 in order to perform a proper demultiplexing (it is easy to understand it when demultiplexing a signal of the form $\cos(\omega t)$ when $\omega = 0$ or not). By combining this simulation with the photon number calibration, we get the expected values of the 9

multiplexing readout signals as a function of the mean number of photon in the storage mode used in Fig. 2E.

#### 5.2.3.4 *Simulation of measurement induced dephasing on the storage mode*

In this part, we only simulate the multiplexing qubit and the storage mode to decrease the computational cost of the simulation. The Hamiltonian of the simulation in the frame rotating at the multiplexing qubit resonant frequency and at $f_\mathrm{s} + \delta f_\mathrm{s}^0$ for the storage mode is

$$\begin{aligned} \hat{H}_4/h &= -\chi_{\mathrm{s,mp}}\frac{\hat{\sigma}_{\mathrm{z,mp}}+1}{2}\hat{n}_\mathrm{s} - \delta f_\mathrm{s}^0\hat{n}_\mathrm{s} - \chi_{\mathrm{s,s,mp}}\hat{n}_\mathrm{s}(\hat{n}_\mathrm{s}-1)\frac{\hat{\sigma}_{\mathrm{z,mp}}+1}{2} \\ &\quad + \frac{\Omega}{2}(\epsilon_\mathrm{comb}(t)\hat{\sigma}_\mathrm{mp}^{+} + \epsilon_\mathrm{comb}^*(t)\hat{\sigma}_\mathrm{mp}^{-\prime}) \end{aligned}, \tag{5.19}$$

where $\epsilon_\mathrm{comb}(t)$ is the product of a Gaussian function with the sum of nine complex exponential $\sum_{k=0}^{8}\exp(2i\pi\chi_{\mathrm{s,mp}}k\tau)$. The width of the Gaussian function is equal to one quarter of the duration $t$ of the pulse. We add four dephasing and relaxation channels to this Hamiltonian to obtain the master equation

$$\dot{\rho} = -\frac{i}{\hbar}[\hat{H}_4,\rho] + 2\Gamma_{\phi,\mathrm{s}}\mathcal{L}(\hat{n}_\mathrm{s})\rho + \Gamma_{1,\mathrm{s}}\mathcal{L}(\hat{a}_\mathrm{s})\rho + \frac{1}{2}\Gamma_{\phi,\mathrm{mp}}\mathcal{L}(\hat{\sigma}_{\mathrm{z,mp}})\rho + \Gamma_{1,\mathrm{mp}}\mathcal{L}(\hat{\sigma}_\mathrm{mp}^{-})\rho. \tag{5.20}$$

The storage is initialized in a coherent state of amplitude $\beta = 1.55$ and the multiplexing qubit is initialized in state $|g\rangle$. We simulate the dynamics of the system for a pulse duration $t$ going from 100 ns to 5 $\mu$s and for $\Omega$ ranging from 0 to $2\chi_{\mathrm{s,mp}}$. We compute the expectation value of $\hat{X} = (\hat{a}_\mathrm{s}+\hat{a}_\mathrm{s}^\dagger)/2$ at the end of each simulation. For a given $\Omega$, we extract the time evolution of $\langle\hat{X}\rangle$ under the influence of the multiplexed measurement as shown on Fig. 5.12a. This decaying sinusoid is fitted using Eq. (5.12) to obtain the oscillation frequency $\delta f_\mathrm{s}$ and the decay rate $\Gamma_{\mathrm{d,s}}$. Fig. 5.10c and d show the measurement induced dephasing and AC Stark shift as a function of amplitude of the comb $\Omega$ for two sets of coherent state amplitudes $\beta$ and detuning $\delta f_\mathrm{s}^0$.

We identify three interesting features. The first one is the evolution of the shape of the curves $\delta f_\mathrm{s}(\Omega)$ and $\Gamma_{\mathrm{d,s}}(\Omega)$ with $\chi_{\mathrm{s,mp}}$. We repeat the simulation using a square pulse envelope instead of Gaussian pulse for $\epsilon_\mathrm{comb}$ to make the simulation faster for several values of $\chi_{\mathrm{s,mp}}$ from 1.5 to 13.2 MHz by steps of 1.4 MHz. We observe that $\delta f_\mathrm{s}(\Omega)$ and $\Gamma_{\mathrm{d,s}}(\Omega)$ increase as $\chi_{\mathrm{s,mp}}$ becomes larger but that the maxima and minima of the curve are always found for the same $\Omega/\chi_{\mathrm{s,mp}}$ ratio (Fig. 5.12b).

The second observation is that $\delta f_\mathrm{s}(\Omega)$ and $\Gamma_{\mathrm{d,s}}(\Omega)$ vary with the initial coherent state amplitude $\beta$ (Fig. 5.12c).

The third observation is that in the regime $\chi_{\mathrm{s,mp}} \gg \Gamma_{1,\mathrm{mp}}/2\pi$, the dephasing rate and AC Stark shift are a function of the ratio $2\pi\Omega/\Gamma_{1,\mathrm{mp}}$ as shown on Fig. 5.12d. The dephasing rate increases as $\Omega^2$ until a plateau is reached for $2\pi\Omega/\Gamma_{1,\mathrm{mp}} = 0.7$. In contrast, the Stark shift is constant for $2\pi\Omega/\Gamma_{1,\mathrm{mp}} < 0.3$ and splits into two frequencies (two oscillations on top of each other in Ramsey interferometry) with a splitting proportional to $2\pi\Omega/\Gamma_{1,\mathrm{mp}}$. Since there are two frequencies, we use Eq. (5.13) to fit the

simulated Ramsey oscillations for $\chi_{\mathrm{s,mp}} \gg \Gamma_{1,\mathrm{mp}}/2\pi$. In practice Eq. (5.13) is a good fit function because a Fourier analysis shows that the signal is composed of two frequencies with the same amplitude. Fig. 5.12e shows an example of simulated Ramsey oscillations for $\chi_{\mathrm{s,mp}} \gg \Gamma_{1,\mathrm{mp}}/2\pi$.

### 5.2.4 *Density Matrix Elements*

In this part, we explain how one can calculate the density matrix of the storage mode from the measured Wigner function. It is the recipe we used to produce the bottom part of Fig. 3A in the main text. We further present original results on the decay of density matrix elements when the multiplexing qubit is driven by a single tone or by the comb of frequencies. We characterize the quantum non-demolition nature of our photocounter. Finally, we present an experiment in which we show revivals of density matrix elements as a function of time and show simulations that reproduce them qualitatively. We discuss a new quantity called the mean coherence and show its measured evolution in various measurement configurations.

#### 5.2.4.1 *Density matrix reconstruction*

The Wigner tomography contains all the information about the state of the storage mode. We explain below how we reconstruct the density matrix from the measured Wigner function. We compute the Wigner map for every operator $|n\rangle\langle m|$ with $|n\rangle$ and $|m\rangle$ two fock states with $n$ and $m$ photons. The mean value of those operators is equal to the $(n, m)$ element $\rho_{\mathrm{nm}}$ of the density matrix. Using the mathematical expression of $\langle x|n\rangle$

$$\langle x|n\rangle = \psi_n(x) = \left(\frac{2}{\pi}\right)^{1/4} \frac{1}{\sqrt{2^n n!}} \mathcal{H}_n(\sqrt{2}x) e^{-x^2} \tag{5.21}$$

with $\mathcal{H}_n(x) = (-1)^n e^{x^2} \frac{d^n}{dx^n} e^{-x^2}$ the Hermite polynomial function of order $n$ and $|x\rangle$ the eigenvector of the quadrature $(\hat{a}_{\mathrm{s}} + \hat{a}_{\mathrm{s}}^\dagger)/2$ associated to the eigenvalue $x$. The Wigner map of the operator $|n\rangle$ and $|m\rangle$ becomes

$$W_{|n\rangle\langle m|}(x, p) = \frac{1}{\pi} \int \mathrm{d}y e^{-2ipy} \psi_n(x + y/2) \overline{\psi_m}(x - y/2) \tag{5.22}$$

and the matrix element $\rho_{\mathrm{nm}}$ of the storage mode is given by Eq. (5.7)

$$\rho_{\mathrm{nm}} = \pi \iint \mathrm{d}x\mathrm{d}p W_{|n\rangle\langle m|}(x, p) W_\rho(x, p). \tag{5.23}$$

In order to characterize the decoherence due to the multiplexed measurement, we use a renormalization of the density matrix elements in order to remove most of the effects of the storage mode relaxation. Let us now show that the quantity $|\rho_{\mathrm{nm}}|/\sqrt{\rho_{\mathrm{nn}}\rho_{\mathrm{mm}}}$ evolves only because of dephasing and that its dynamics is not affected by relaxation. We consider the storage mode alone under the influence of its relaxation and dephasing channels in a frame rotating at $f_{\mathrm{s}}$

$$\dot{\rho} = \Gamma_{1,s} \mathcal{L}(\hat{a}_{\mathrm{s}})\rho + 2\Gamma_{\phi,s} \mathcal{L}(\hat{a}_{\mathrm{s}}^\dagger \hat{a}_{\mathrm{s}})\rho. \tag{5.24}$$

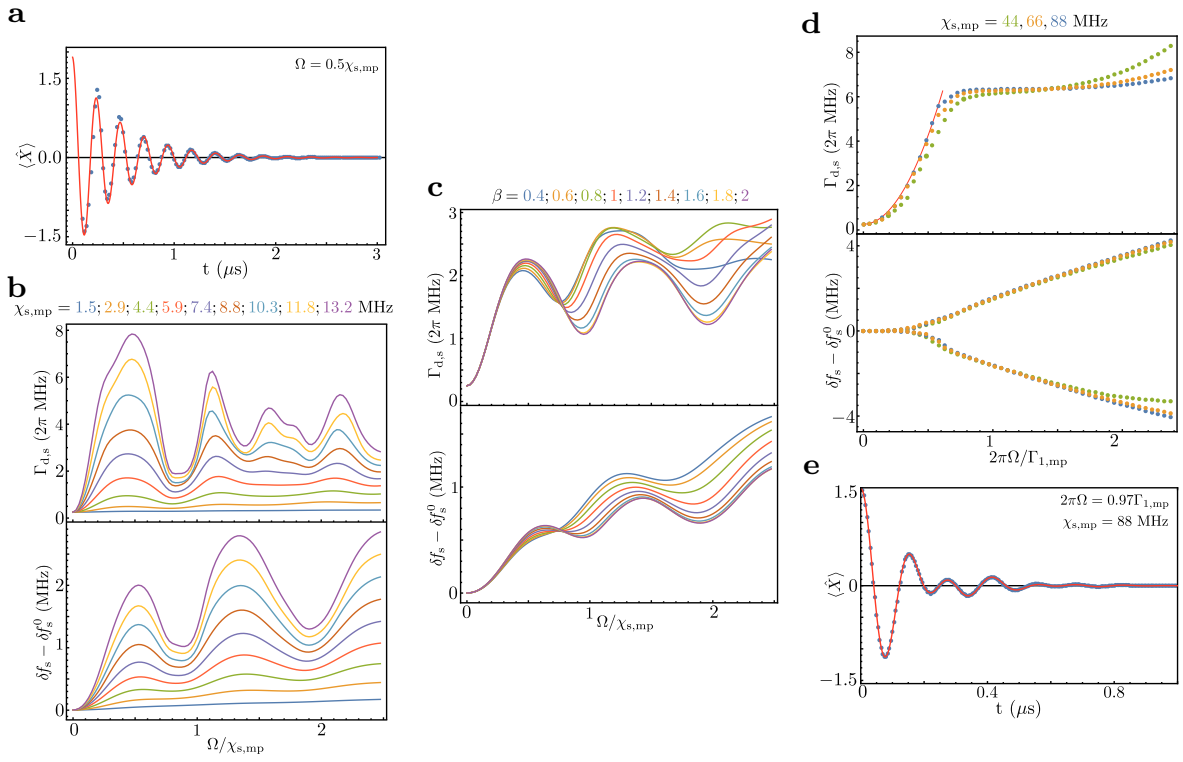


Figure 5.12: **Simulations of the measurement induced dephasing rate and of the AC Stark shift induced by a frequency comb. a.** Ramsey-like oscillations of the storage mode for $\Omega = \chi_{s,mp}/2$ and an initial coherent field amplitude $\beta = -1.55$. Blue dots are the simulated expectation values of $\hat{X}$ and red line is the theory given by the Eq. (5.12). **b.** Simulated measurement induced dephasing rate $\Gamma_{\mathrm{d,s}}$ and AC Stark shift as a function of $\Omega/\chi_{s,mp}$ for various values of $\chi_{\mathrm{s,mp}}$. Simulations show the same pattern with maxima and minima for some specific values of $\Omega/\chi_{s,mp}$ as in the experiment in Fig. 3C. **c.** Simulated measurement induced dephasing rate and AC Stark shift as a function of $\Omega/\chi_{s,mp}$ for various initial coherent state amplitudes $\beta$ in the storage mode. For $\Omega/\chi_{s,mp} > 1$, we see a difference of about 20 % between $\beta = 1.6$ and $\beta = 1.2$. **d.** Simulations for $\chi_{\mathrm{s,mp}} \gg \Gamma_{1,\mathrm{mp}}$. The evolution of the measurement induced dephasing and AC Stark shift with $\Omega$ is different compared to the case of **b**. The evolution of the measurement induced dephasing rate and the AC Stark shift seems to be given by the ratio $2\pi\Omega/\Gamma_{1,\mathrm{mp}}$. The red line is a guide for eyes representing a square function. It shows that the measurement induced dephasing rate increases linearly with $\Omega^2$ for small drive amplitudes. For the AC Stark shift, on the contrary with **b**, the detuning is constant at the small drive amplitudes, then two frequencies appear with comparable contributions to the Ramsey oscillations. The two frequencies evolve linearly with $\Omega$. **e.** Example of simulated Ramsey oscillations exhibiting two frequencies.

From this equation we can compute the time derivative of the density matrix element

$$\dot{\rho}_{\mathrm{nm}} = \Gamma_{1,\mathrm{s}} \left( \rho_{\mathrm{n+1m+1}} \sqrt{(n+1)(m+1)} - \frac{n+m}{2} \rho_{\mathrm{nm}} \right) - \Gamma_{\phi,\mathrm{s}} \rho_{\mathrm{nm}} (n-m)^2. \tag{5.25}$$

If the storage mode is initialized in a coherent state $|\alpha_o\rangle$, the solution of the equation is

$$\rho_{\mathrm{nm}}(t) = e^{-|\alpha_o|^2 e^{-\Gamma_{1,\mathrm{s}} t}} \frac{\alpha_o^m e^{-m\Gamma_{1,\mathrm{s}} t/2} (\alpha_o^*)^n e^{-n\Gamma_{1,\mathrm{s}} t/2}}{\sqrt{n!m!}} e^{-\Gamma_{\phi,\mathrm{s}}(n-m)^2 t}, \tag{5.26}$$

and we get

$$\frac{|\rho_{\mathrm{nm}}|}{\sqrt{\rho_{\mathrm{nn}}\rho_{\mathrm{mm}}}}(t) = e^{-\Gamma_{\phi,\mathrm{s}}(n-m)^2 t}. \tag{5.27}$$

Thus indeed, the renormalization removes the effect of the relaxation rate $\Gamma_{1,s}$ and only characterizes the dephasing rate. Under the action of measurement, we expect that the dephasing rate $\Gamma_{\phi,\mathrm{s}}$ is increased by the measurement induced dephasing rate. In the following sections, we will see that, indeed, the measurement process to distinguish photon numbers $n$ and $m$ can well be captured by $|\rho_{\mathrm{nm}}|/\sqrt{\rho_{\mathrm{nn}}\rho_{\mathrm{mm}}} = e^{-\Gamma_{\mathrm{d,s}}^{nm} t}$, where $\Gamma_{\mathrm{d,s}}^{nm}$ is the sum of $\Gamma_{\phi,\mathrm{s}}(n-m)^2$ and of a well-characterized measurement-induced dephasing rate.

#### 5.2.4.2 *Decoherence of the storage mode induced by a single measurement drive*

By essence of quantum mechanics, measuring with a single drive whether there are $n$ photons induces a dephasing between Fock state $|n\rangle$ and Fock state $|m \neq n\rangle$. This dephasing can be probed by observing the dynamics of $\rho_{\mathrm{nm}}$.

We prepare the storage mode state in a coherent state with an amplitude $\beta = -1.7$, and probe the multiplexing qubit during a time $t$ with a drive at the frequency $f_{\mathrm{mp}} - \Delta_{\mathrm{mp}}$ before doing a Wigner tomography. For various times $t$ and detunings $\Delta_{\mathrm{mp}}$, we compute the density matrix of the storage mode using Eq. (5.23). One can fit the time evolution of $|\rho_{\mathrm{nm}}|/\sqrt{\rho_{\mathrm{nn}}\rho_{\mathrm{mm}}}$ with a decreasing exponential function. The extracted decoherence rate $\Gamma_{\mathrm{d,s}}^{nm}(\Delta_{\mathrm{mp}})$ is then compared to the theoretical value.

In Ref. [123], we show that an exact, infinite-order adiabatic elimination of the multiplexing qubit probed with a single frequency drive is possible under the assumption that there is no photon loss in the storage mode. They show that the decoherence rate between the Fock state $|n\rangle$ and $|m\rangle$ due to the measurement is given by the highest eigenvalue of the following matrix

$$\begin{pmatrix} -\Gamma_{1,\mathrm{mp}}/2 & -2\pi\Delta + \tilde{\chi} & 0 & 0 \\ 2\pi\Delta - \tilde{\chi} & -\Gamma_{1,\mathrm{mp}}/2 & -2\pi\Omega & 0 \\ 0 & 2\pi\Omega & -\Gamma_{1,\mathrm{mp}} & -\Gamma_{1,\mathrm{mp}} - i\tilde{\chi} \\ 0 & 0 & -i\tilde{\chi} & 0 \end{pmatrix} \tag{5.28}$$

with $\tilde{\chi} = \frac{n+m}{2} 2\pi\chi_{\mathrm{s,mp}}$. Fig. 5.13 shows the measured density matrix decoherence rates $\Gamma_{\mathrm{d,s}}^{nm}$ and the above theory for $n$ and $m$ going from 0 to 4 (with an offset corresponding to the natural dephasing rate in Eq. (5.27)). As expected in a regime with resolved

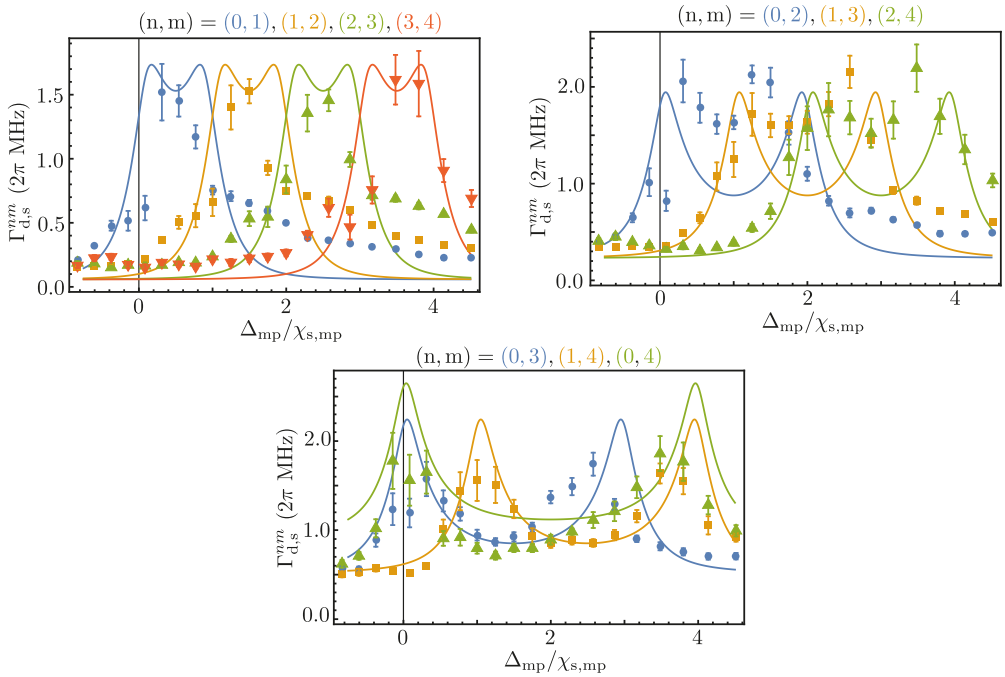


Figure 5.13: **Decoherence rate of superpositions between Fock states induced by a single drive on the multiplexing qubit.** In each panel, dots are obtained using Eq. (5.23) on the measured Wigner function of the storage mode when driven by a single drive at $f_{\mathrm{mp}} - \Delta_{\mathrm{mp}}$ with an amplitude $\Omega = \chi_{\mathrm{s,mp}}/2$. Lines represent the highest eigenvalue of (5.28) without any free parameters. An offset equals to $\Gamma_{\phi,\mathrm{s}}(n-m)^2$, which is the intrinsic dephasing of the storage mode, is added to the simple model.

resonance peaks ($2\pi\chi_{\mathrm{s,mp}}|m-n| > \Gamma_{2,\mathrm{mp}}$), the decoherence rate $\Gamma^{nm}_{\mathrm{d,s}}$ between Fock states $|n\rangle$ and $|m\rangle$ is larger when the single drive probes whether there are $n$ photons or $m$ photons with a moderate drive amplitude $\Omega$ (dependence on $\Omega$ not shown here). For much larger drive amplitude $\Omega$, one can increase the decoherence rate $\Gamma^{nm}_{\mathrm{d,s}}$ by driving with a detuning $\Delta_{\mathrm{mp}} = (n+m)\chi_{\mathrm{s,mp}}/2$, similarly to dispersive qubit readout which is optimal for information extraction at large drive power and for a drive frequency detuned by $\chi_{\mathrm{s,mp}}/2$. In fact this regime would become particularly attractive for poorly resolved resonances as a function of photon number ($2\pi\chi_{\mathrm{s,mp}}|m-n| < \Gamma_{2,\mathrm{mp}}$). Premises of this effect are visible on Fig. 5.13, as the maximal decoherence rate occurs at a detuning slightly closer to $(n+m)\chi_{\mathrm{s,mp}}/2$, with a stronger effect for small $|m-n|$, both in theory and in the experimental data. The small discrepancy between theory and experiment, in particular the asymmetry as a function of $n$ and $m$, may be explained by the photon loss rate of the storage mode, which is not captured in the simplified theoretical model.

#### 5.2.4.3 *Multiplexed measurement vs single tone measurement*

In Fig. 3A of the main text, one sees that the dephasing of the storage mode induced by the measurement is stronger for multiplexed measurement than for single tone measurement. This figure is based on the Wigner tomography of the storage mode in three distinct cases. The storage mode is initialized in a coherent state of amplitude

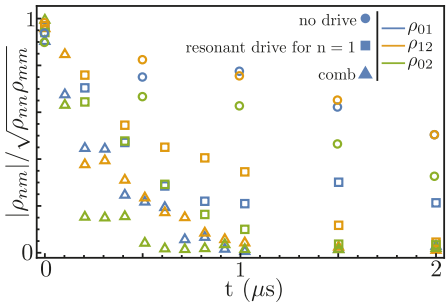


Figure 5.14: **Dynamics of the storage mode coherences under various measurement schemes.** Normalized off-diagonal elements of the density matrix extracted from the measured Wigner function of the storage mode as a function of time. The figure focuses on three elements $\rho_{01}$ (blue), $\rho_{12}$ (orange) and $\rho_{02}$ (green). Circles: case (i) without driving the multiplexing qubit. Squares: case (ii) where a single tone at $f_{\mathrm{mp}} - \chi_{\mathrm{s,mp}}$ drives the multiplexing qubit with a strength $\Omega = \chi_{\mathrm{s,mp}}/2$. Triangles: case (iii) where the multiplexing qubit is driven by a comb of 9 peaks with the same strength $\Omega$ each.

$\beta = -1.55$, then, before performing the tomography of the storage mode, we either (i) wait for a time $t$, (ii) probe the multiplexing qubit for a time $t$ at a single frequency $f_{\mathrm{mp}} - \chi_{\mathrm{s,mp}}$ corresponding to 1 photon or (iii) with a frequency comb.

From the measured Wigner functions, we compute the density matrix of the storage mode $\rho(t)$ for various times $t$ for the three cases and compare the evolution of the normalized elements $\rho_{\mathrm{nm}}(t)$ (see Fig. 5.14). Without any drive on the multiplexing qubit (circles and case (i)), the density matrix elements decay due to natural dephasing only. Clearly, the drive on the multiplexing qubit induces a decay of the coherences, with a stronger effect when the comb is turned on than when a singe drive is turned on. We conclude that a multiplexing measurement extracts more information than a single measurement.

The effect on $\rho_{02}$ when probing with a resonant drive for $n = 1$, is consistent with the significant measurement-induced detuning that can be read off the top right plot of Fig. 5.13 (blue, value 1 on the horizontal axis). Apparently, when driving with a comb, such an effect combines with the ones on $n = 0$ and $n = 2$ resonances, and other components, to induce a stronger overall measurement rate. We will investigate this comb effect more precisely in the section 5.2.4.5.

#### 5.2.4.4 *Quantum Non Demolition nature of the multiplexed measurement*

The goal of this subsection is to quantify the *Quantum Non Demolition* (QND) nature of our multiplexed measurement. A measurement is said to be QND if

- the measurement time is very short compared to the timescale of evolution of the system under study,
- the interaction with the probe does not disturb the quantum state of the system if it belongs to the measurement basis.

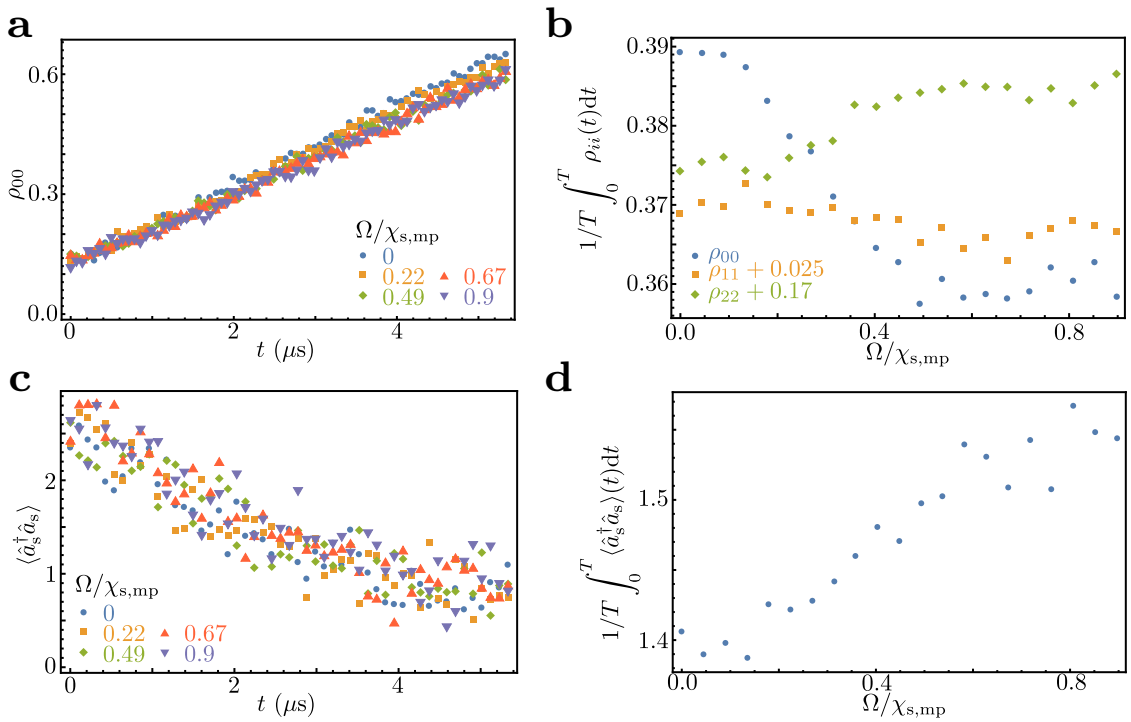


Figure 5.15: **Impact of multiplexed measurement on the occupation of the Fock states. a.** Measured probability to find the storage mode in Fock state $|0\rangle$ as a function of time $t$ for various comb drive amplitudes $\Omega/\chi_{\mathrm{s,mp}}$. **b.** Measured diagonal elements of the density matrix integrated during 5 $\mu$s as a function of drive amplitude $\Omega/\chi_{\mathrm{s,mp}}$. **c.** Decay of the average photon number in time for various drive amplitudes. **d.** Average photon number evolution as a function of $\Omega/\chi_{\mathrm{s,mp}}$.

If a photocounter is QND, the diagonal elements of the density matrix of the resonator are unchanged (on average on all measurements) by the measurement process. In our experiment, we observe that the diagonal elements of the density matrix in the energy basis predominantly evolve owing to the decay of the storage mode. The probability of having 0 photon in the storage increases in time (Fig. 5.15a) while the average photon number decreases with time (Fig. 5.15c). Interestingly, we notice that for large probe amplitude (red and purple points in Fig. 5.15a), the probability of finding the storage mode with 0 photon is slightly lower. This dependence on the amplitude of the drive $\Omega$ is best characterized by extracting the populations (Fig. 5.15b) and photon number (Fig. 5.15d) integrated during $T = 5$ $\mu$s as a function of $\Omega/\chi_{\mathrm{s,mp}}$. For small drive amplitude $\Omega/\chi_{\mathrm{s,mp}} < 0.1$, the probability to find the a given number of photon does not change with $\Omega/\chi_{\mathrm{s,mp}}$ but for larger drive amplitude the cavity gets populated probably because of deviations from the dispersive approximation.

In practice, for small drive amplitude and a measurement time of 5 $\mu$s, the relaxation dynamics of the system during the measurement process increases the probability of having 0 photon at the end of the measurement by approximately 10 %. We find that the mean photon number is decreased by the same percentage.

#### 5.2.4.5 *Off-diagonal density matrix elements and revivals of the coherence*

In the main text we determined that the storage mode dephases faster in the presence of measurement by measuring how much faster the Ramsey oscillations decay. Ramsey oscillations give access to the decay of $a_\mathrm{s} + a_\mathrm{s}^\dagger$, which is sensitive to the decay of coherences of the form $\rho_{n,n+1}$. In fact it is also possible to visualize the dynamics of individual off-diagonal elements of the storage density matrix to gain insight into the physics of the dephasing process. For that, we use Eq. (5.23) on the directly measured Wigner function of the storage mode.

First, we study the decay of off-diagonal elements $\rho_{12}$ and $\rho_{13}$ (Fig. 5.16a and b). For small drive amplitude $\Omega < 0.5\chi_{\mathrm{s,mp}}$, off-diagonal elements decay faster when $\Omega$ is increased since more and more information is extracted per unit time by the drive. As larger drive amplitudes are reached, off-diagonal elements start oscillating. The contrast of these coherence revivals become more pronounced as the drive amplitude becomes larger and they exhibit a quasi periodicity. The time between the first and second revivals is 10 % shorter than the time between the second and the third.

This behavior is qualitatively reproduced by our simulations (Fig. 5.16c). We found that the amplitude of the revivals is strongly enhanced when the coupling rate between the multiplexing qubit $\Gamma_{1,\mathrm{mp}}$ and the transmission line is lowered. The revivals are periodic with a frequency equal to $\Delta f$, the frequency difference between two successive tones of the comb. The presence of revivals in the coherences is a strong indication that the dephasing process on the storage mode cannot be described as an open quantum system coupled to a Markovian bath. This memory effect originates from the finite lifetime of the multiplexing qubit. Pushing even further the measurement amplitude $\Omega > 0.9\chi_{\mathrm{s,mp}}$ in the experiment, we observe that revivals remain but their time structure is no longer periodic (see Fig. 5.17).

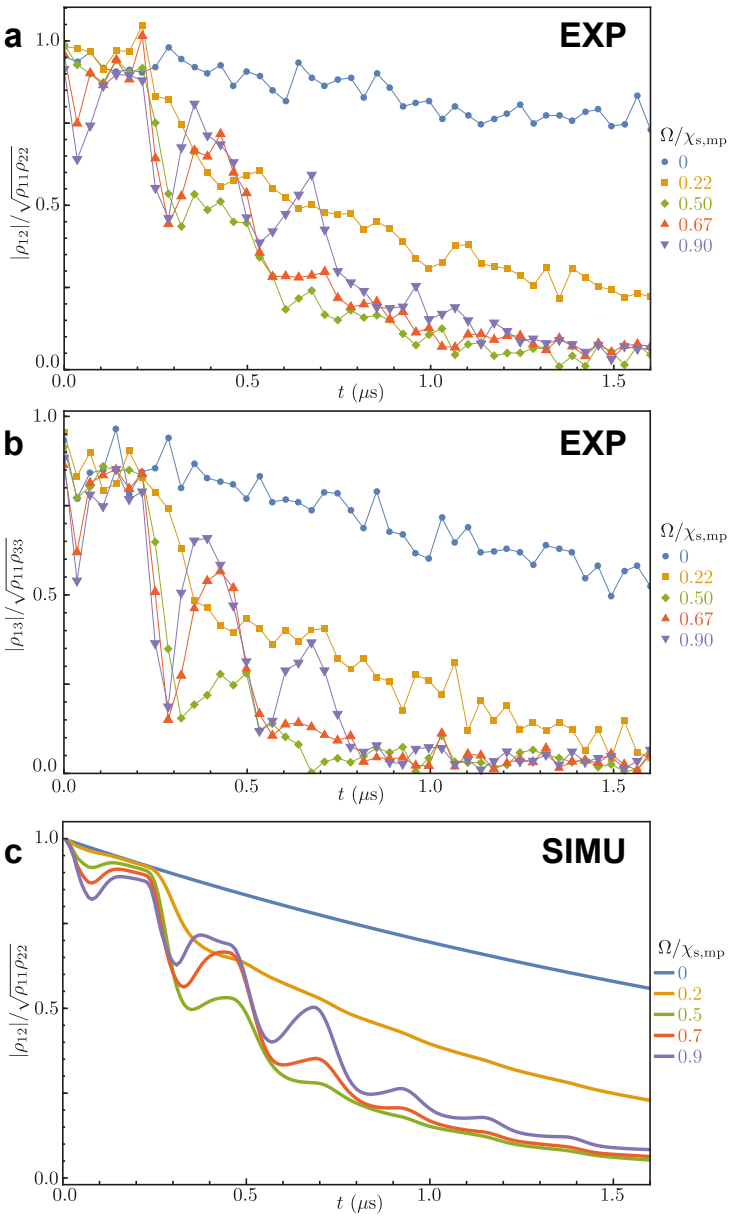


Figure 5.16: **Normalized off-diagonal elements of the storage matrix density. a.** Measured normalised coherence $|\rho_{12}|$ between Fock states $|1\rangle$ and $|2\rangle$ of the storage mode as a function of time and for various amplitudes $\Omega$ of the driving frequency comb. **b.** Similar plot for $|\rho_{13}|$. **c.** Results of the simulation (5.20) for the normalized $|\rho_{12}|$.

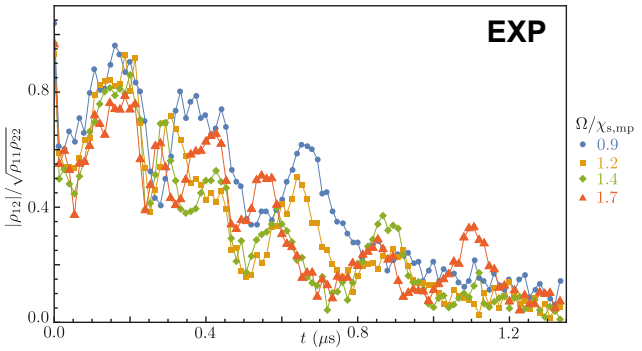


Figure 5.17: **Normalized off-diagonal elements of the storage matrix density for the largest measurement amplitudes.** Measured normalized coherence $|\rho_{12}|$ between Fock states $|1\rangle$ and $|2\rangle$ of the storage mode as a function of time and for various amplitudes $\Omega > 0.9\chi_{\mathrm{s,mp}}$ of the driving frequency comb.

#### 5.2.4.6 *Mean coherence between Fock states*

Since the driving frequency comb holds the promise to probe how many photons are in the storage mode, it should affect all coherences $\rho_{nm}$. In this section, we introduce two ways of characterizing the impact of the multiplexed photocounting on the global coherence of the storage mode.

The first one, shown in the main text in Fig. 3B, is the quadrature of the storage mode in the frame rotating at the frequency of this mode when the qubit is probed by a comb. It can be expressed as $\mathrm{Re}[(\langle\hat{X}\rangle+i\langle\hat{P}\rangle)e^{-2i\pi\delta f_{\mathrm{s}}t}]$ with $\langle\hat{X}\rangle$ and $\langle\hat{P}\rangle$ the expectation values of the quadratures in the frame rotating at the frequency of the storage drive. This quantity is related to the first off-diagonal of the density matrix.

We introduce a second quantity: the mean coherence $C_\rho$ between Fock states 0 to 4. It is defined as

$$C_\rho = \underset{4\geq i>j\geq 0}{\mathrm{Mean}}\left[\frac{|\rho_{ij}|}{\sqrt{\rho_{ii}\rho_{jj}}}\right]. \tag{5.29}$$

$C_{\rho(t)}$ contains the information about the dephasing between every different Fock states. The left part of Fig. 5.18 shows oscillations of the storage mode quadratures in the frame of the drive on the storage mode for various drive amplitudes. On the right part of Fig. 5.18 we display the mean quadrature $\langle\hat{a}_{\mathrm{s}}+\hat{a}_{\mathrm{s}}^\dagger\rangle$ in the frame rotating at the storage mode frequency and the mean coherence $C_\rho$. Those two quantities show the same dynamics, leading to the same dephasing rate and both quantities can be used to characterize it. The revivals that can be seen on each of the density matrix off-diagonal elements (see Fig. 5.16) also appear in the evolution of the quadrature and of the mean coherence betwee Fock states.

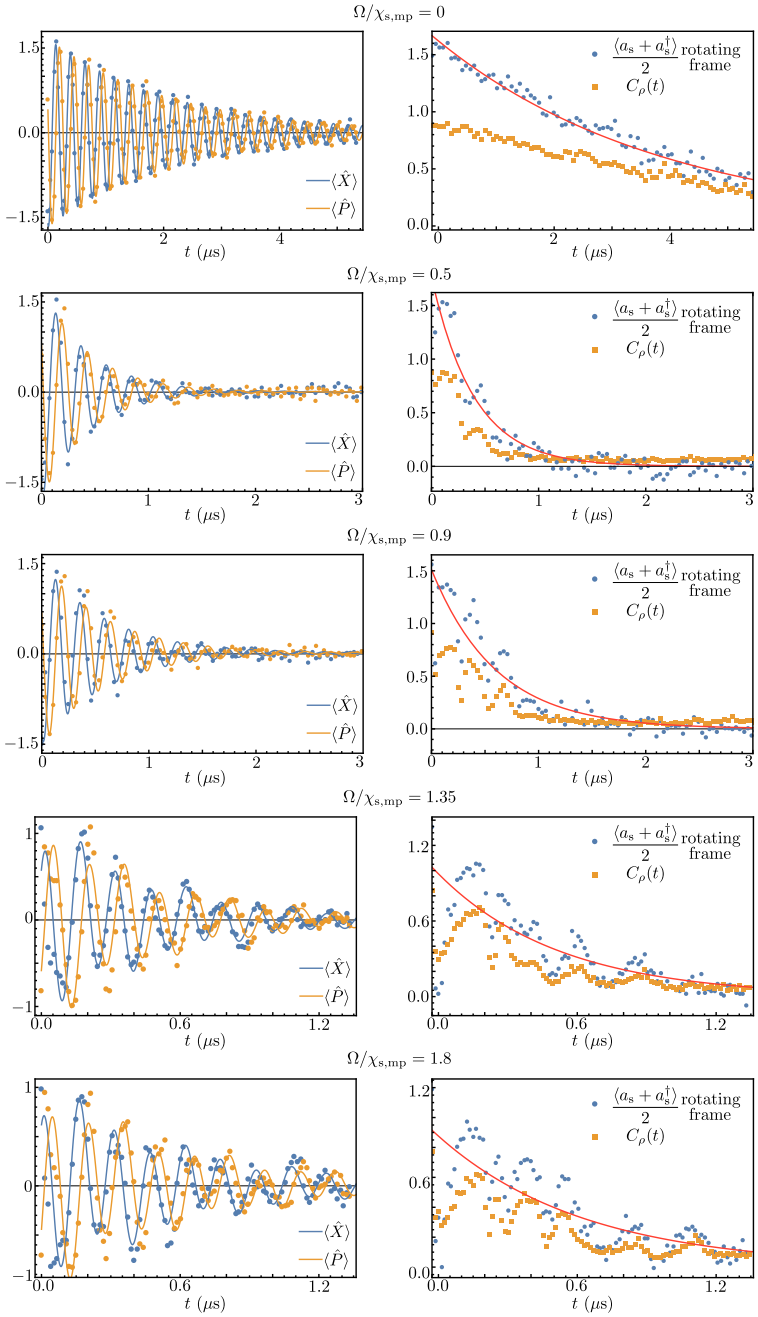


Figure 5.18: **Impact of the multiplexed drive on storage mode quadrature and mean coherence between Fock states.** Left column: Ramsey oscillations measured (dots) and fits (line) using Eq. 5.12 and 5.13 for five multiplexing drive amplitudes. Right column: quadrature of storage mode in the frame rotating at its resonance frequency (blue dots) and mean coherence between Fock states $C_\rho(t)$ (orange squares) defined in Eq. (5.2.4.6) for the five same drive amplitudes. Incertiture are about 0.07 for the quadrature and 0.015 for the mean coherence. The red solid lines are exponential fits of the quadrature decay.

# 6

# EXPONENTIAL SUPPRESSION OF BIT-FLIPS IN A QUBIT ENCODED IN A SCHRÖDINGER CAT STATE

> Il faut la mémoire de beaucoup d'instants pour faire un souvenir complet.
>
> G. Bachelard

We here reproduce the preprint of the Exponential suppression of bit-flips in a qubit encoded in a Schrödinger cat state of a microwave resonator. I contributed by this work through the development of coplanar waveguide design and fabrication technics. I also advised the design of the ATS element: the non-linear element at the core of this experiment. The authors of this work are Raphaël Lescanne, Marius Villiers, Théau Peronnin, Alain Sarlette, Matthieu Delbecq, Benjamin Huard, Takis Kontos, Mazyar Mirrahimi and Zaki Leghtas. This paper is now published in Nature Physics (2020).

AUTHORS CONTRIBUTION RL designed, fabricated and measured the device, and analyzed the data. RL and ZL conceived the ATS element with help from BH and TP. RL and ZL wrote the paper with input from all authors. MV fabricated the parametric amplifier. TK and MD provided experimental support. AS and MM provided theory support. ZL managed the project. All authors contributed to extensive discussions of the results.

ABSTRACT A quantum system interacts with its environment, if ever so slightly, no matter how much care is put into isolating it. As a consequence, quantum bits (qubits) undergo errors, putting dauntingly difficult constraints on the hardware suitable for quantum computation. New strategies are emerging to circumvent this problem by encoding a qubit non-locally across the phase space of a physical system. Since most sources of decoherence are due to local fluctuations, the foundational promise is to exponentially suppress errors by increasing a measure of this non-locality. Prominent examples are topological qubits which delocalize quantum information over real space and where spatial extent measures non-locality. In this work, we encode a qubit in the field quadrature space of a superconducting resonator endowed with a special mechanism that dissipates photons in pairs. This process pins down two computational states to separate locations in phase space. As we increase this separation, we measure an exponential decrease of the bit-flip rate while only linearly increasing the phase-flip rate.

Since bit-flips are continuously and autonomously corrected at the single qubit level, only phase-flips are left to be corrected via a one-dimensional quantum error correction code. This exponential scaling demonstrates that resonators with non-linear dissipation are promising building blocks for universal fault-tolerant quantum computation with drastically reduced hardware overhead.

ACKNOWLEDGEMENT The authors acknowledge fruitful discussions with Pierre Rouchon and Clarke Smith. ZL acknowledges support from ANR project ENDURANCE, and EMERGENCES grant ENDURANCE of Ville de Paris. AS acknowledges support from ANR project HAMROQS. The devices were fabricated within the consortium Salle Blanche Paris Centre. This work has been supported by the Paris Île-de-France Region in the framework of DIM SIRTEQ.

## 6.1 EXPERIMENT DESCRIPTION AND RESULTS

### 6.1.1 *Introduction*

Protecting quantum states against decoherence is a fundamental problem in physics, and is pivotal for the future of quantum computing. The theory of quantum error correction (QEC) and its fault-tolerant implementation [124, 125] provides a solution. In QEC, groups of noisy physical qubits are arranged together to encode qubits with reduced noise, and fault-tolerance establishes that noisy quantum computers can operate reliably if the noise is below a threshold. A strong focus in quantum architecture design has been to increase this threshold to a value within experimental reach, but the required hardware overhead remains daunting [19]. Therefore, there is a pressing need for new ideas to encode and protect quantum information.

Let us start by understanding why classical information is so stable. Consider a light switch, which has two stable states labeled 0 and 1. Their stability is provided by two properties. First, in order to change states one needs to apply a force to overcome an energy barrier, usually provided by the deformation of a spring. Second, friction between mechanical parts is essential for stability: when a perturbation randomly deviates the switch from its stable state, the gained entropy must be dissipated into a reservoir in order to recover the initial state. Can these two properties be transposed to protect quantum information?

The $|0\rangle$ and $|1\rangle$ states of a qubit, such as electronic orbitals of an ion or energy levels of a non-linear resonator, often have overlapping supports in phase space. First, one needs to isolate the two states so that they no longer overlap [126] and separate them by an energy barrier [127–132]. The second property, friction (or dissipation) leaks information about the system and therefore seems incompatible with the requirement for a qubit to adopt quantum superpositions of states. Remarkably, there exists a dissipative mechanism, known as two-photon dissipation, which stabilizes the $|0\rangle$ and $|1\rangle$ states of a qubit without affecting quantum superpositions of the two [133].

Recent superconducting circuit experiments [20, 46] have demonstrated that a resonator endowed with two-photon dissipation develops a manifold of steady states

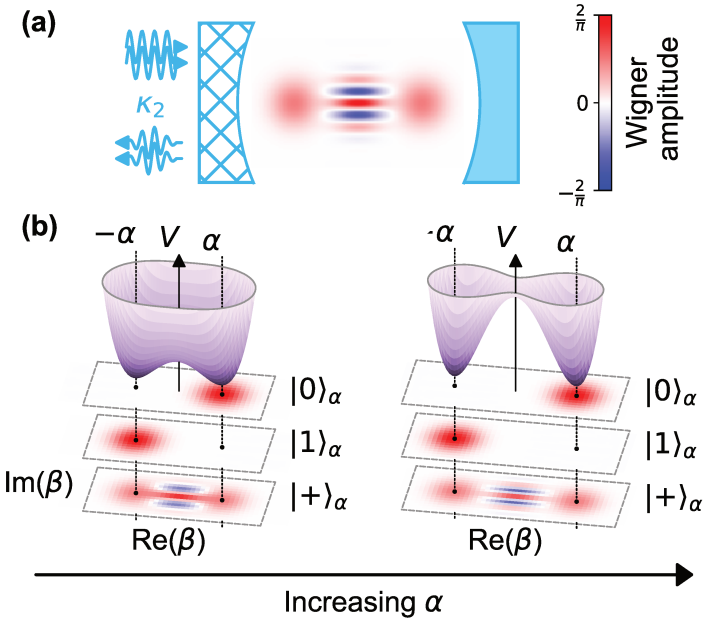


Figure 6.1: **The cat-qubit** (**a**) Quantum information is encoded in a resonator (blue mirrors) coupled to its environment through a special apparatus (hatched mirror) where pairs of photons are exchanged at rate $\kappa_2$ (double arrows). (**b**) This dynamics is illustrated by a pseudo-potential $V$ (purple) defined over the resonator quadrature phase space ($\beta$ plane). The cat-qubit states $|0\rangle_\alpha$ and $|1\rangle_\alpha$ lie in the minima of $V$ and are separated in phase space as shown by their Wigner representations (stacked color plots). Bit-flip errors, which randomly swap $|0\rangle_\alpha$ and $|1\rangle_\alpha$, are exponentially suppressed by increasing this separation. Crucially, this pseudo-potential does not alter quantum superpositions of $|0\rangle_\alpha$ and $|1\rangle_\alpha$ such as the Schrödinger cat state $|+\rangle_\alpha$.

spanned by two states $|0\rangle_\alpha$ and $|1\rangle_\alpha$, lying in two distinct locations of the resonator two-dimensional (2D) phase space. The combination of dissipation and non-locality should prevent random swaps between $|0\rangle_\alpha$ and $|1\rangle_\alpha$ (bit-flips). However, the circuit architectures mediating the two-photon dissipation impinged errors on the resonator. These experiments fell short of crossing the demanding threshold where the correction is faster than the occurrence of all errors, including those induced by the correcting mechanism itself.

In this work, we measure an exponential decrease of the bit-flip rate as we increase the separation between states $|0\rangle_\alpha$ and $|1\rangle_\alpha$, while only linearly increasing the phase-flip rate (errors that scramble the phase of a superposition of $|0\rangle_\alpha$ and $|1\rangle_\alpha$). The bit-flip time reaches 1 ms, a 300-fold improvement over the energy decay time of the resonator. This was made possible by inventing a circuit which mediates a pristine non-linear coupling between the resonator and its environment, thus circumventing the problems of previous implementations [20, 46]. Our qubit combines two unique features: only phase-flips remain to be actively corrected [134], and its 2D phase space can be accessed to perform gates [134–137], making it an ideal building block for scalable fault-tolerant quantum computation with a significant reduction in hardware overhead [134].

We follow the paradigm of cat-qubits [135, 138] where information is encoded in quantum superpositions of resonator states (see Fig. 6.1):

$$\begin{aligned} |0\rangle_\alpha &= \frac{1}{\sqrt{2}}\left(|+\rangle_\alpha + |-\rangle_\alpha\right) = |+\alpha\rangle + \mathcal{O}(e^{-2|\alpha|^2}) \\ |1\rangle_\alpha &= \frac{1}{\sqrt{2}}\left(|+\rangle_\alpha - |-\rangle_\alpha\right) = |-\alpha\rangle + \mathcal{O}(e^{-2|\alpha|^2}) \end{aligned}$$

where $|\pm\rangle_\alpha = \mathcal{N}_\pm\left(|\alpha\rangle \pm |-\alpha\rangle\right)$, $|\alpha\rangle$ is a coherent state with complex amplitude $\alpha$, and $\mathcal{N}_\pm = 1/\sqrt{2(1 \pm e^{-2|\alpha|^2})}$. All these states contain an average number of photons $\approx |\alpha|^2$ for $|\alpha| > 1$. A significant source of errors in a resonator is energy decay which collapses all states ($|0\rangle_\alpha$ and $|1\rangle_\alpha$ included) towards the vacuum, thus erasing any encoded information. This decay is balanced by a mechanism where the resonator exchanges only pairs of photons with its environment (Fig. 6.1a) [133], known as two photon dissipation. This dynamics is modeled by the following loss operator

$$\boldsymbol{L}_2 = \sqrt{\kappa_2}\left(\boldsymbol{a}^2 - \alpha^2\right) , \tag{6.1}$$

where $\boldsymbol{a}$ is the annihilation operator of the resonator, $\kappa_2$ is the rate at which pairs of photons are exchanged with the environment and the term in $\alpha^2$ results from a drive which inserts pairs of photons (see section 6.2). The cat-qubit states $|0\rangle_\alpha$, $|1\rangle_\alpha$ and all their superpositions are steady states of this dynamics. A convenient tool to visualize the semi-classical dynamics of (6.1) is the pseudo-potential $V$ defined over the complex plane as $-\nabla V(\beta) = \frac{d\beta}{dt}$, where $\beta$ is the expectation value of $\boldsymbol{a}$ at time $t$ in a semi-classical approximation (see section 6.2). Stable steady states are local minima of $V$ (see Fig. 6.1b) and correspond to $\beta = \pm\alpha$. An error process can disrupt the stability of these states and induce transitions between them. By analogy with a particle in a double well potential, tunneling (or bit-flips) from one well to another is exponentially suppressed in the separation between the two wells (here defined as $|\alpha|^2$), as long as the error process fulfills two criteria: it has to be local and sufficiently weak. An error process is local if it transforms a state into neighboring states in phase space [139]. As an example, dominant errors such as photon loss, gain and dephasing are local. Moreover, the effective error rate $\kappa_{\text{err}}$ must be weaker than the confining rate $\kappa_{\text{conf}} = 2|\alpha|^2\kappa_2$ (see section 6.2) inherited from the confining potential $V$, in order for the cat-qubit states to remain localized near the potential minima. The outstanding challenge to observe an exponential increase in the bit-flip time is therefore to engineer $\kappa_{\text{conf}} > \kappa_{\text{err}}$ for all dominant local error processes.

Two-photon exchange between a resonator and its environment does not occur spontaneously. Instead, it is synthesized by engineering an interaction that exchanges pairs of photons of the cat-qubit resonator with one photon of an intentionally lossy mode referred to as the buffer [20]. The interaction Hamiltonian takes the form

$$\boldsymbol{H}_i/\hbar = g_2\boldsymbol{a}^{\dagger 2}\boldsymbol{b} + g_2^*\boldsymbol{a}^2\boldsymbol{b}^\dagger , \tag{6.2}$$

where $\boldsymbol{b}$ is the annihilation operator of the buffer and $g_2$ is the interaction strength. Adding a resonant drive on the buffer, we recover (6.1) with $\kappa_2 \approx 4|g_2|^2/\kappa_b$ and $\alpha^2 = -\epsilon_d/g_2^*$, where $\epsilon_d$ is the drive amplitude and $\kappa_b$ is the buffer energy decay rate, engineered to be larger than $g_2$ [20, 140]. Conveniently, the separation $|\alpha|^2$ between the

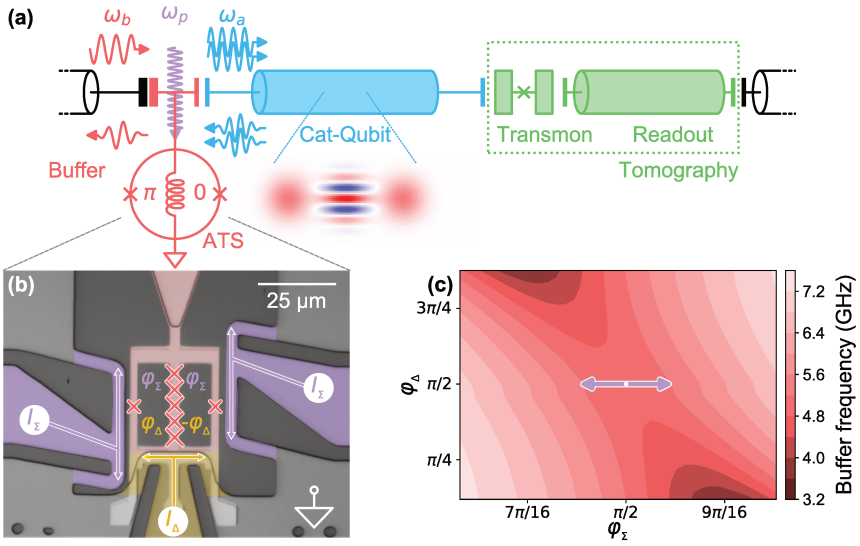


Figure 6.2: **Circuit diagram and implementation** (**a**) The cat-qubit resonator (blue) is coupled on one end to a transmon qubit and a readout resonator (green) to measure its Wigner function, and on the other end to the buffer (red), a lumped element resonator connected to ground through a non-linear element coined the Asymmetrically Threaded SQUID (ATS). The ATS consists of a SQUID shunted by an inductance, forming two loops. Pumping the ATS at frequency $\omega_p = 2\omega_a - \omega_b$ (purple arrow), where $\omega_{a,b}$ are the cat-qubit and buffer frequencies, mediates the exchange of two photons of the cat-qubit (blue arrows) with one photon of the buffer (red arrows) (**b**) False color optical image of the ATS. The shunt inductance is made of an array of 5 Josephson junctions (marked by large red crosses). The left and right flux lines (purple) are connected to the same input through an on-chip hybrid (not represented). They carry the radio-frequency pump and the DC current $I_\Sigma$, which thread both loops with flux $\varphi_\Sigma$. The bottom flux line (yellow) carries current $I_\Delta$ and threads each loop with flux $\pm\varphi_\Delta$. Combining these two controls, we bias the ATS at the $\pi/0$ asymmetric DC working point. (**c**) Measured buffer frequency (color) as a function of $\varphi_\Sigma$ (x-axis) and $\varphi_\Delta$ (y-axis), around the working point $\varphi_\Sigma, \varphi_\Delta = \pi/2, \pi/2$ (white dot). As expected, for $\varphi_\Sigma = \pi/2$ (open SQUID), the buffer frequency does not depend on $\varphi_\Delta$. We operate the ATS by modulating the flux along the orthogonal direction $\varphi_\Sigma$ (purple arrow). From this measurement, we extract all the ATS parameters (see section 6.2).

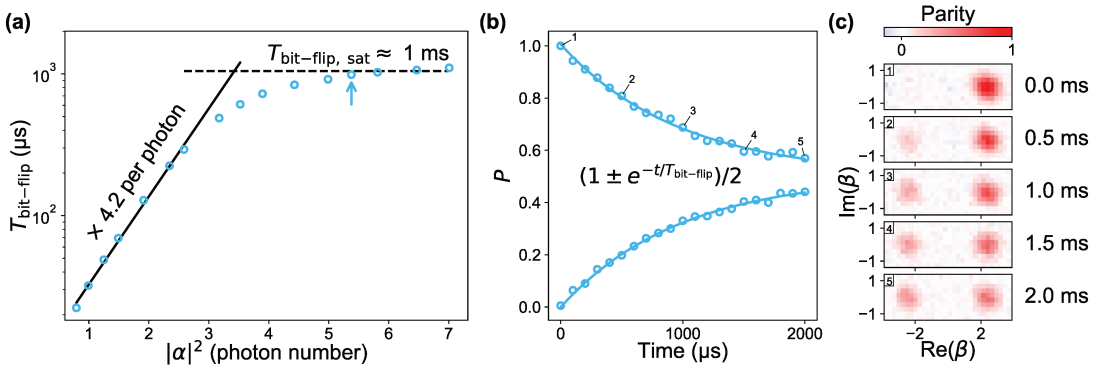


Figure 6.3: **Exponential increase of the bit-flip time with the cat size.** (**a**) The bit-flip time (y-axis) is measured (open circles) as a function of the cat size defined as $|\alpha|^2$ (x-axis). Up to $|\alpha|^2 \approx 3.5$, $T_{\text{bit-flip}}$ undergoes an exponential increase to $\approx 0.8$ ms, rising by a factor of 4.2 per added photon (solid line). The bit-flip time then saturates (dashed line is a guide for the eye) for $|\alpha|^2 \geq 5$ at 1 ms, a factor of 300 larger than the cat-qubit resonator lifetime $T_1$ in the absence of the pump and drive. Each circle is obtained from measurements such as in (b) for the circle indicated by the blue arrow. (**b**) The cat-qubit is initialized in $|0\rangle_\alpha$, for a cat size $|\alpha|^2 = 5.4$. After applying the pump and drive for a variable duration (x-axis), the population $P$ (y-axis) of $|0\rangle_\alpha$ (top curve) and $|1\rangle_\alpha$ (bottom curve) is measured. The data (open circles) are fitted to decaying exponential functions (solid lines) from which we extract the bit-flip time. (**c**) Each panel displays the measured Wigner function of the cat-qubit after a pump and drive duration indicated on the right of each plot. Labels 1-5 mark the correspondence with (b). The cat-qubit is initialized in $|0\rangle_\alpha$ (top panel) and over a millisecond timescale, the population escapes towards $|1\rangle_\alpha$ (lower panels). The two-photon dissipation ensures that the cat-qubit resonator state remains entirely in the steady state manifold spanned by $|0\rangle_\alpha$ and $|1\rangle_\alpha$.

cat-qubit states is readily tunable *in situ* since it is proportional to the buffer drive amplitude.

We implement our cat-qubit in a circuit quantum electrodynamics architecture described in Fig 6.2a operated at 10 mK. It consists of a sputtered niobium film on a silicon substrate patterned into coplanar waveguide resonators. The cat-qubit mode resonates at $\omega_a/2\pi = 8.0381$ GHz, has a single photon lifetime $T_1 = 3.0$ $\mu$s and is probed through a transmon qubit coupled to a readout resonator followed by a parametric amplifier. At the flux operating point, the buffer mode resonates at $\omega_b/2\pi = 4.8336$ GHz and has an energy decay rate $\kappa_b/2\pi = 13$ MHz.

It is a technical challenge to engineer the interaction (6.2) without inducing spurious effects which are detrimental for the protection of quantum information. Examples of such effects are induced relaxation [50, 141], escape to unconfined states [96] and quasiparticle generation [142]. To mitigate these effects, the interaction (6.2) is induced by a novel non-linear dipole: the Asymmetrically Threaded SQUID (ATS, Fig 6.2b). The ATS consists of a symmetric SQUID (Superconducting Quantum Interference Device) shunted in its center by a large inductance, thus forming two loops. Here the inductance is built from an array of 5 Josephson junctions. The ATS mediates an interaction of the form $U = -2E_J \cos(\varphi_\Sigma)\cos(\boldsymbol{\varphi} + \varphi_\Delta)$, where $E_J$ is the Josephson energy of the SQUID junctions, $\boldsymbol{\varphi}$ is the phase across the dipole, and $2\varphi_{\Sigma,\Delta}$ are the sum and differences of

flux threading the two loops (see section 6.2). We bias the ATS at $\varphi_\Sigma = \varphi_\Delta = \pi/2$, or equivalently, we thread the left and right loops with flux $\pi$ and 0, respectively. In addition, we drive the sum port with a radio-frequency flux pump $\epsilon(t)$. At this bias point $U = -2E_J \sin(\epsilon(t)) \sin(\boldsymbol{\varphi})$. The ATS is coupled to the buffer and cat-qubit, so that $\boldsymbol{\varphi}$ is a linear combination of $\boldsymbol{a}, \boldsymbol{a}^\dagger, \boldsymbol{b}, \boldsymbol{b}^\dagger$, and $\sin(\boldsymbol{\varphi})$ contains only odd powers of these operators. The desired interaction (6.2) is present in the expansion of $\sin(\boldsymbol{\varphi})$, and is resonantly selected by a flux pump frequency $\omega_p = 2\omega_a - \omega_b$ [143]. In contrast with previous strategies [20, 46], the ATS mediates a pristine two-photon coupling, since (6.2) is the only leading order non-rotating term, the presence of the inductive shunt prevents instabilities [63], and the device operates at a first order flux insensitive point (Fig 6.2c). These features are key in order not to introduce inherent error processes that cannot be corrected by two-photon dissipation.

The root advantage of the cat-qubit is that its computational states $|0\rangle_\alpha$ and $|1\rangle_\alpha$ can be made arbitrarily long-lived simply by increasing the cat size $|\alpha|^2$, provided that $\kappa_{\text{conf}} > \kappa_{\text{err}}$. In this experiment, the dominant error is due to energy decay so that $\kappa_{\text{err}}/2\pi = (2\pi T_1)^{-1} = 53$ kHz (see section 6.2), and $\kappa_{\text{conf}} = 2|\alpha|^2\kappa_2$ with a measured $\kappa_2/2\pi = 40$ kHz (from which we infer $g_2/2\pi = 360$ kHz). Hence, we enter the regime $\kappa_{\text{conf}} > \kappa_{\text{err}}$ as soon as $|\alpha|^2 > 0.6$. We have measured that for each added photon in the cat-qubit state, the bit-flip time is multiplied by 4.2. This exponential scaling persists up to $|\alpha|^2 \approx 3.5$, and the bit-flip time saturates for $|\alpha|^2 \geq 5$ at 1 ms, a 300-fold improvement over the resonator intrinsic lifetime (see Fig. 6.3). We expect a saturation when the corrected bit flip rate reaches the rate of residual errors which are not correctable, such as non-local errors. In the present experiment, we attribute this saturation to the coupling with the transmon employed for the resonator tomography (see section 6.2), which has a thermal occupation of 1%, a lifetime $T_{1,q} = 5$ $\mu$s and is dispersively coupled to the cat-qubit resonator with a rate $\chi/2\pi = 720$ kHz. Over a timescale in the millisecond range, the transmon acquires a thermal excitation that shifts the cat-qubit resonator frequency by $\chi$. This triggers a rotation of the resonator states which overcomes the confining potential since in this experiment $\chi \gg \kappa_{\text{conf}}/2$ (see section 6.2) (note that tomography protocols compatible with smaller values of $\chi$ have been recently demonstrated [46]). During an average time $T_{1,q}$, the resonator states acquire an angle of order $\chi T_{1,q} \gg 2\pi$. When the transmon excitation decays, the rotation stops and the two-photon dissipation brings the resonator state back into the cat-qubit computational basis. By virtue of the dissipative nature of the protection mechanism, this process may result in a bit-flip but does not cause any leakage.

Schrödinger cat states like $|\pm\rangle_\alpha$ living in a resonator with a lifetime $T_1$, lose their coherence at a rate $2|\alpha|^2/T_1$ [29]. In the cat-qubit paradigm, this translates into a phase-flip rate which increases linearly with the cat size $|\alpha|^2$. In addition, our cat-qubit undergoes a flux pump, a drive and non-linear interactions, which could further increase the phase-flip rate. We measure the phase-flip rate for increasing $|\alpha|^2$ and confirm a linear scaling (Fig. 6.4a). Moving towards three dimensional cavities and engineering ever-improving non-linear interactions should decrease the phase-flip rate below a threshold where a line repetition code can actively correct remaining errors [134].

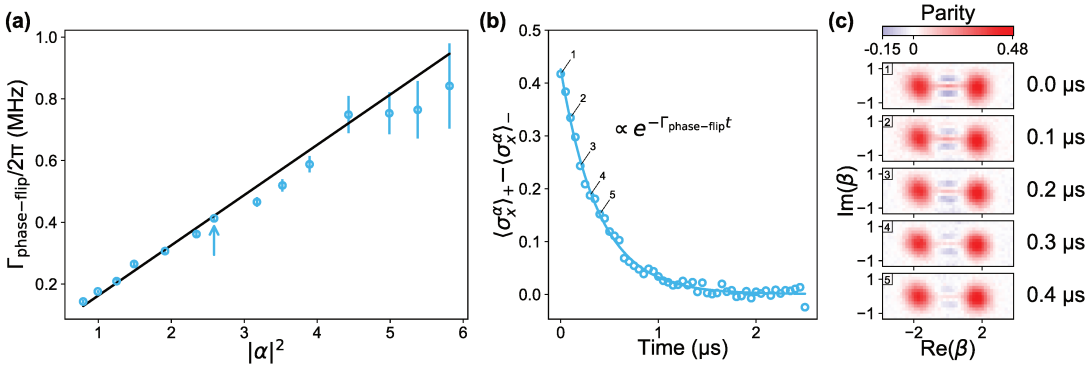


Figure 6.4: **Linear increase of the phase-flip rate with the cat size**. (**a**) The phase-flip rate (y-axis) is measured as a function of the cat size $|\alpha|^2$. The data (open circles) follow a linear trend (solid line) as expected for the decay rate of a Schrödinger cat coherence $\Gamma_{\text{phase-flip}} = 2|\alpha|^2/T_{1,\text{eff}}$. We measure $T_{1,\text{eff}} = 2.0$ $\mu$s, comparable to the intrinsic resonator lifetime of 3.0 $\mu$s. Each circle is obtained from measurements such as in (b) for the circle indicated by the blue arrow. (**b**) The cat-qubit is prepared in the initial states $|\pm\rangle_\alpha$, for a cat size $|\alpha|^2 = 2.6$. After applying the pump and drive for a variable duration (x-axis), $\langle\sigma_x^\alpha\rangle_\pm$ is measured for each initial state and the difference is represented on the y-axis. The $X$ Pauli operator of the cat-qubit $\sigma_x^\alpha$ corresponds to the photon number parity. The data (open circles) are fitted to a decaying exponential (solid line) from which we extract the phase-flip rate. (**c**) Each panel displays the measured Wigner function of the cat-qubit after a pump and drive duration indicated on the right of each plot. Labels 1-5 mark the correspondence with (b). The cat-qubit is initialized in the $|+\rangle_\alpha$ state and the positive and negative fringes demonstrate the quantum nature of this initial state (top panel). The fringe contrast is reduced by single photon loss which mixes $|+\rangle_\alpha$ with $|-\rangle_\alpha$.

In conclusion, we have observed the exponential decrease of the bit-flip rate between our cat-qubit states $|0\rangle_\alpha$ and $|1\rangle_\alpha$, as a function of their separation in phase space, while only linearly increasing their phase-flip rate. Such an exponential scaling is necessary to bridge the gap between the modest performance of quantum hardware and the exquisite performance needed for quantum computation [19]. This was made possible by inventing a Josephson circuit which mediates a pristine non-linear coupling between our cat-qubit mode and its environment. Further improving the lifetime of the cavity to the state of the art of a millisecond [144] and a cat size of $|\alpha|^2 \approx 5$ (resp. 10) should lead to a bit-flip time of $\approx 1$ second (resp. 0.5 hour), and a phase-flip time of $\approx 100$ $\mu$s (resp. 50 $\mu$s). With such a long bit-flip time, the entire effort of active QEC will be focused on correcting the only significant error: phase-flips. In addition, conditional rotations in the 2D phase space of our cat-qubit form a universal set of gates, thus bypassing the need for magic states. These features suggest a significant reduction in hardware overhead for QEC [134].

## 6.2 SUPPLEMENTARY MATERIALS

### 6.2.1 *Full device and wiring*

The circuit consists of a sputtered niobium film with a thickness of 120 nm deposited on a 280 $\mu$m-thick wafer of intrinsic silicon. The main circuit is etched after an optical lithography step. The Josephson junctions are made of evaporated aluminum through a PMMA/MAA resist mask patterned in a distinct e-beam lithography step. A single Dolan bridge is used to make the small junctions of the ATS and of the transmon, and a series of 3 Dolan bridges delimit the 5-junction array which serves as the ATS inductor. The full device layout and the experiment wiring are displayed in Figs. 6.5, 6.6.

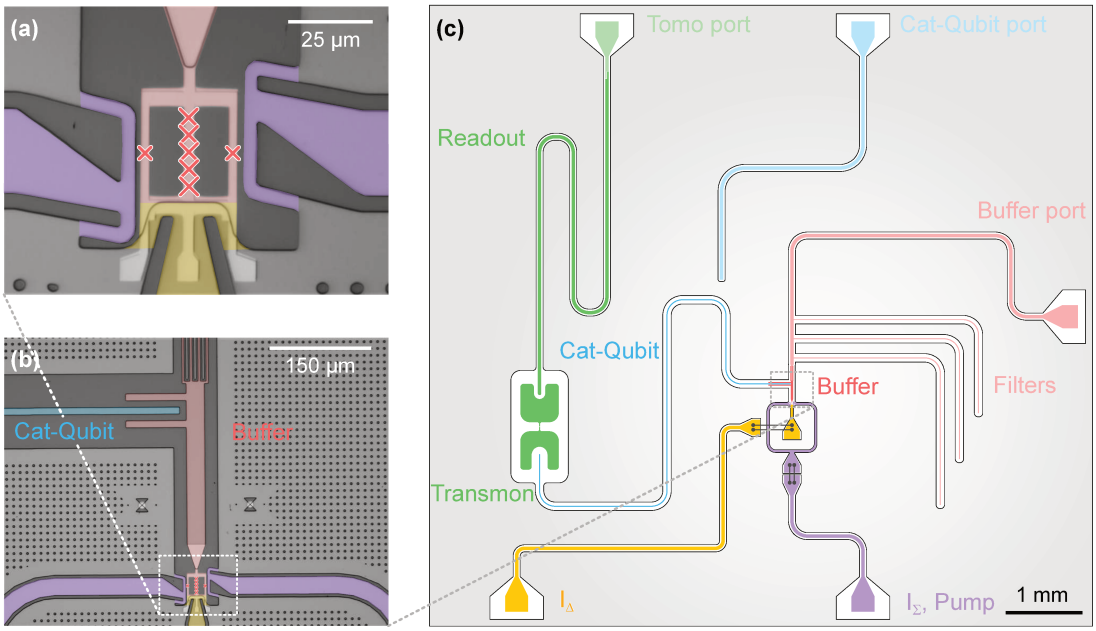


Figure 6.5: **Full device layout.** (**a**) False color optical image of the ATS. Note that the 5 junction symbols are separated for clarity, the actual junctions are much closer and centered in the middle of the arm. (**b**) False color optical image of the buffer. The buffer (red) is strongly coupled to its transmission line via an interdigitated capacitor (top). It is also capacitively coupled to the cat-qubit resonator (blue). This is actually a picture of a twin sample where this coupling was smaller. In panel (c), the real size of the coupling capacitor is shown. (**c**) Full device layout. The cat-qubit resonator is coupled on its other side to a transmon qubit, itself coupled to a readout resonator which together enable to perform the cat-qubit tomography. After the interdigitated capacitor, the buffer input is filtered via three $\lambda/4$-stub filters. These stop-band filters are centered at the cat-qubit resonance frequency to mitigate its direct coupling to the input line of the buffer [77] (b). The on-chip hybrid along the pump path (purple), equally splits the pump tone to RF-flux bias the ATS with the right symmetry. The black lines linking two dots are a schematic representation of the crucial wirebonds of the device. The wirebonds linking the pump input to the on-chip hybrid where implemented to reduce the area of the loop delimited by the center conductor and the ground plane, leading to a reduced sensitivity to flux noise.

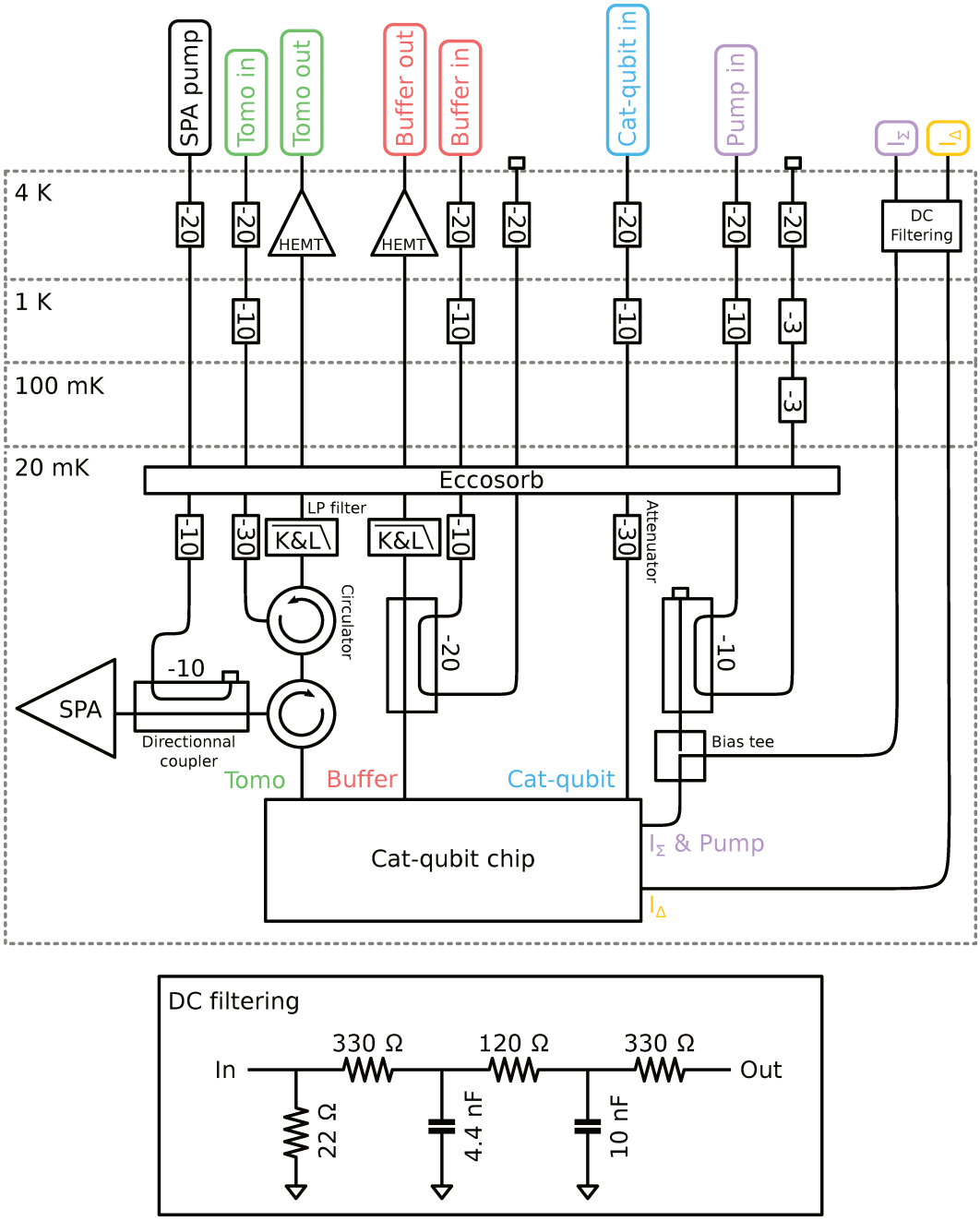


Figure 6.6: **RF and DC wiring of the dilution refrigerator.** Note that the pump and drive tones are attenuated at the base plate via directional couplers so that the attenuated power is dissipated at higher fridge stages, far from the sample. The $I_\Sigma$ DC current and the RF pump signal are combined at 20 mK with a bias-tee. We have used a homemade "Snail Parametric Amplifier" (SPA) [145].

### 6.2.2 *Hamiltonian derivation*

In this section, we derive the potential energy of the ATS dipole alone, and then calculate the full system Hamiltonian when the ATS mediates a non-linear coupling between the buffer and cat-qubit modes.

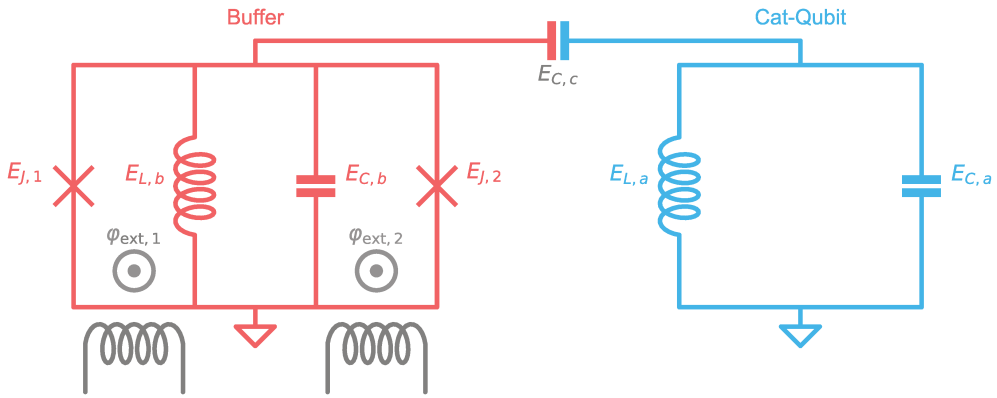


Figure 6.7: Equivalent circuit diagram. The cat-qubit (blue), a linear resonator, is capacitively coupled to the buffer (red). One recovers the circuit of Fig. 6.2 by replacing the buffer inductance with a 5-junction array and by setting $\varphi_\Sigma = (\varphi_{\text{ext},1} + \varphi_{\text{ext},2})/2$ and $\varphi_\Delta = (\varphi_{\text{ext},1} - \varphi_{\text{ext},2})/2$. Not shown here: the buffer is capacitively coupled to a transmission line, the cat-qubit resonator is coupled to a transmon qubit

#### 6.2.2.1 *The potential energy of the ATS dipole element*

Let us first derive the potential energy of the ATS element alone. Its equivalent circuit is represented in red in Fig. 6.7 and the phase across its inductor $\varphi$ is the only degree of freedom (here we assume that the coupling capacitor to the cat-qubit mode is replaced by an open circuit). The potential energy of the ATS reads

$$U(\varphi) = \frac{1}{2}E_{L,b}\varphi^2 - E_{J,1}\cos(\varphi + \varphi_{\text{ext},1}) - E_{J,2}\cos(\varphi - \varphi_{\text{ext},2})\ . \tag{6.3}$$

Due to fabrication imperfections, the ATS junctions are not symmetric. We introduce $E_J$ and $\Delta E_J$ such that $E_{J,1} = E_J + \Delta E_J$ and $E_{J,2} = E_J - \Delta E_J$. We obtain

$$U(\varphi) = \frac{1}{2}E_{L,b}\varphi^2 - 2E_J\cos(\varphi_\Sigma)\cos(\varphi + \varphi_\Delta) + 2\Delta E_J\sin(\varphi_\Sigma)\sin(\varphi + \varphi_\Delta)\ , \tag{6.4}$$

where $\varphi_\Sigma = (\varphi_{\text{ext},1} + \varphi_{\text{ext},2})/2$ and $\varphi_\Delta = (\varphi_{\text{ext},1} - \varphi_{\text{ext},2})/2$. We DC bias the ATS at the asymmetric flux bias point $\varphi_\Sigma = \varphi_\Delta = \pi/2$ (this is a saddle point of the buffer frequency map). In addition, an RF flux bias on $\varphi_\Sigma$ is applied, so that

$$\varphi_\Sigma = \pi/2 + \epsilon(t)\ ,\ \text{with}\ \epsilon(t) = \epsilon_0\cos(\omega_p t) \tag{6.5}$$

$$\varphi_\Delta = \pi/2\ . \tag{6.6}$$

The time-dependent potential at first order in $\epsilon(t)$ then reads

$$U(\varphi) = \frac{1}{2}E_{L,b}\varphi^2 - 2E_J\epsilon(t)\sin(\varphi) + 2\Delta E_J\cos(\varphi)\ . \tag{6.7}$$

This potential is an unbounded function of $\varphi$, which prevents the system from escaping towards higher energy states in the presence of the pump [63, 96]. In practice, with the 5-junction array replacing the inductance, the confining part of the potential is replaced by $5E_{J,L}\cos(\varphi/5)$ where $E_{J,L} = 5E_{L,b}$ is the Josephson energy of each individual junction of the array. This potential is no longer unbounded, however the bound is high enough ($5E_{J,L} \gg 2E_J\epsilon_0$) for our pump power regime.

In the ideal case ($\Delta E_J = 0$), this potential only produces odd powers of $\varphi$ from the sine non-linearity. A small asymmetry of the junctions produces small even powers of $\varphi$, leading to parasitic Kerr non-linearities. Typically $|\Delta E_J/E_J| \approx 10\%$. In the following we assume $\Delta E_J = 0$ for simplicity.

#### 6.2.2.2 *The coupled buffer and cat-qubit resonators*

We now consider the buffer and cat-qubit modes, and their coupling through the ATS dipole element. The full Hamiltonian reads

$$\begin{aligned} \boldsymbol{H} &= \hbar\omega_{a,0}\boldsymbol{a}^\dagger\boldsymbol{a} + \hbar\omega_{b,0}\boldsymbol{b}^\dagger\boldsymbol{b} - 2E_J\epsilon(t)\sin\left(\boldsymbol{\varphi}_b + \boldsymbol{\varphi}_a\right) && (6.8)\\ \text{with } \boldsymbol{\varphi}_a &= \varphi_a(\boldsymbol{a} + \boldsymbol{a}^\dagger)\,,\ \boldsymbol{\varphi}_b = \varphi_b(\boldsymbol{b} + \boldsymbol{b}^\dagger) && (6.9)\end{aligned}$$

where $\boldsymbol{a}/\boldsymbol{b}$ are the annihilation operators of the cat-qubit and buffer modes, $\omega_{a/b,0}$ their resonant frequencies, and $\varphi_{a/b}$ their zero point phase fluctuations across the ATS dipole. Due to the circuit geometry, we expect $\varphi_b \gg \varphi_a$. When expanding the sine up to third order in $\boldsymbol{\varphi} = \boldsymbol{\varphi_b} + \boldsymbol{\varphi_a}$ we get

$$\begin{aligned}\boldsymbol{H} = \hbar\omega_{a,0}\boldsymbol{a}^\dagger\boldsymbol{a} + \hbar\omega_{b,0}\boldsymbol{b}^\dagger\boldsymbol{b} - 2E_J\epsilon(t)\varphi_b(\boldsymbol{b} + \boldsymbol{b}^\dagger) - 2E_J\epsilon(t)\varphi_a(\boldsymbol{a} + \boldsymbol{a}^\dagger)\\ + \frac{1}{3}E_J\epsilon(t)\left(\boldsymbol{\varphi}_b + \boldsymbol{\varphi}_a\right)^3\end{aligned} \tag{6.10}$$

The first two terms of the expansion are drives at frequency $\omega_p$ on the buffer and cat-qubit respectively. They can be absorbed in the frame displaced by $\xi_a(t) = \xi_a e^{-i\omega_p t}$ and $\xi_b(t) = \xi_b e^{-i\omega_p t}$ for $\boldsymbol{a}$ and $\boldsymbol{b}$ respectively, where

$$\xi_{a/b} \xrightarrow[t\gg 1/\kappa_{a/b}]{} \frac{i(E_J/\hbar)\epsilon_0\varphi_{a/b}}{\kappa_{a/b}/2 + i(\omega_{a/b,0} - \omega_p)} \tag{6.11}$$

In this displaced frame, the Hamiltonian reads

$$\begin{aligned}\boldsymbol{H}_{\text{disp}} &= \hbar\omega_{a,0}\boldsymbol{a}^\dagger\boldsymbol{a} + \hbar\omega_{b,0}\boldsymbol{b}^\dagger\boldsymbol{b}\\ &+ \frac{1}{3}E_J\epsilon(t)\Big(\varphi_b(\boldsymbol{b} + \boldsymbol{b}^\dagger + \xi_b e^{-i\omega_p t} + \xi_b^* e^{i\omega_p t}) + \varphi_a(\boldsymbol{a} + \boldsymbol{a}^\dagger + \xi_a e^{-i\omega_p t} + \xi_a^* e^{i\omega_p t})\Big)^3\end{aligned} \tag{6.12}$$

In practice, the buffer mode is driven with an additional microwave drive at frequency $\omega_d$, not included here for simplicity. We place ourselves in the frame rotating at $(\omega_p + \omega_d)/2$ and $\omega_d$ for $\boldsymbol{a}$ and $\boldsymbol{b}$ respectively. In this rotated frame, the Hamiltonian reads

$$\begin{aligned}\boldsymbol{H}_{\text{rot}} &= \hbar\left(\omega_{a,0} - \frac{\omega_p + \omega_d}{2}\right)\boldsymbol{a}^\dagger\boldsymbol{a} + \hbar\left(\omega_{b,0} - \omega_d\right)\boldsymbol{b}^\dagger\boldsymbol{b}\\ &+ \frac{1}{3}E_J\epsilon(t)\Big(\varphi_b(\boldsymbol{b}e^{-i\omega_d t} + \boldsymbol{b}^\dagger e^{i\omega_d t} + \xi_b e^{-i\omega_p t} + \xi_b^* e^{i\omega_p t}) + \varphi_a(\boldsymbol{a}e^{-i\frac{\omega_p+\omega_d}{2}t} + \boldsymbol{a}^\dagger e^{i\frac{\omega_p+\omega_d}{2}t} + \xi_a e^{-i\omega_p t} +\end{aligned}$$

Performing the rotating wave approximation (RWA), we get

$$\boldsymbol{H}_{\text{RWA}}/\hbar = \left(\omega_a - \frac{\omega_p + \omega_d}{2}\right)\boldsymbol{a}^\dagger\boldsymbol{a} + \left(\omega_b - \omega_d\right)\boldsymbol{b}^\dagger\boldsymbol{b} + g_2^*\boldsymbol{a}^2\boldsymbol{b}^\dagger + g_2\boldsymbol{a}^{\dagger 2}\boldsymbol{b}\,, \tag{6.13}$$

where the modes frequencies are AC-Stark shifted to $\omega_{a/b} = \omega_{a/b,0} - \Delta_{a/b}$ and

$$\hbar\Delta_{a/b} = \frac{1}{3}E_J\varphi_{a/b}^2\left(\text{Re}(\xi_b)\varphi_b + \text{Re}(\xi_a)\varphi_a\right) \tag{6.14}$$

with $\hbar g_2 = E_J\epsilon_0\varphi_a^2\varphi_b/2$. When we verify the frequency matching condition

$$\omega_d = \omega_b, \qquad \omega_p = 2\omega_a - \omega_b\,,$$

we recover Eq. (6.2), which we recall here

$$\boldsymbol{H_i}/\hbar = g_2^*\boldsymbol{a}^2\boldsymbol{b}^\dagger + g_2\boldsymbol{a}^{\dagger 2}\boldsymbol{b}\,.$$

### 6.2.3 *Circuit parameters*

Most of the circuit parameters can be readily deduced from standard circuit-QED measurements and are gathered in Table 6.1. Here we explain the methodology we used to deduce the 6 dipole parameters of Fig. 6.7 (see Table 6.2) and the mapping of $(I_\Sigma, I_\Delta)$ to $(\varphi_\Sigma, \varphi_\Delta)$. Independently of this mapping, the ATS saddle point is unambiguously found. At this flux point, $E_J \cos(\varphi_\Sigma) = 0$, and we directly measure $\omega_{a_0}$ and $\omega_{b,0}$. The energies $E_J$ and $E_{L,b}$ are computed from the Ambegaokar-Baratoff and the room temperature measurements of neighbouring test junction resistances. The general linear transformation mapping $(I_\Sigma, I_\Delta)$ to $(\varphi_\Sigma, \varphi_\Delta)$ is found by fitting the measured buffer frequency as a function of $(I_\Sigma, I_\Delta)$ (see Fig. 6.8c,d). The impedance $Z_a$ of the cat-qubit resonator is estimated from the aspect ratio of the coplanar waveguide geometry. The energy $E_{C,c}$ is adjusted to match the measured anti-crossing of the buffer and cat-qubit mode when $I_\Sigma$ is varied (see Fig. 6.8b).

| Cat-qubit mode | |
|---|---|
| $\omega_a/2\pi$ | 8.03805 GHz |
| $\omega_{a,0}/2\pi$ | 8.0389 GHz |
| $T_1$ | 3 $\mu$s |
| $\kappa_a/2\pi$ | 53 kHz |
| $\chi_{aa}/2\pi$ | $-7$ kHz |

| Buffer | |
|---|---|
| $\omega_b/2\pi$ | 4.8336 GHz |
| $\omega_{b,0}/2\pi$ | 4.886 GHz |
| $\kappa_b/2\pi$ | 13 MHz |
| $\chi_{bb}/2\pi$ | $-32$ MHz |
| $\chi_{ba}/2\pi$ | 0.79 MHz |

| Pump | |
|---|---|
| $\omega_p/2\pi$ | 11.2425 GHz |

| Transmon | |
|---|---|
| $\omega_q/2\pi$ | 4.4156 GHz |
| $T_{1,q}$ | 5 $\mu$s |
| $T_{2,q}$ | 8 $\mu$s |
| $\chi_{qq}/2\pi$ | 180 MHz |
| $\chi_{qa}/2\pi$ | 720 kHz |
| $\pi/\chi_{qa}$ | 0.69 $\mu$s |

Table 6.1: Measured system parameters at the ATS working point. The pump shifts the cat-qubit resonator and buffer frequencies. The frequencies in the absence of the pump are noted $\omega_{a/b,0}$ and those in its presence are denoted $\omega_{a/b}$. The Kerr couplings $\chi_{mn}$ enter the full Hamiltonian in the form $-\chi_{mn} m^\dagger m n^\dagger n$ when $m \neq n$ and $-\frac{\chi_{mm}}{2} {m^\dagger}^2 m^2$, where $m, n$ denote the mode indices.

| Circuit parameters | |
|---|---|
| $\omega_{a,0}/2\pi$ | 8.0389 GHz |
| $Z_a$ | 90 $\Omega$ |
| $\omega_{b,0}/2\pi$ | 4.886 GHz |
| $E_{C,c}/h$ | 720 MHz |
| $E_{L,b}/h$ | 45 GHz |
| $E_J/h$ | 90 GHz |

| Dipole parameters | |
|---|---|
| $E_{L,a}/h$ | 96.6 GHz |
| $E_{C,a}/h$ | 92.7 MHz |
| $E_{C,b}/h$ | 73.5 MHz |
| $E_{C,c}/h$ | 720 MHz |
| $E_{L,b}/h$ | 45 GHz |
| $E_J/h$ | 90 GHz |

Table 6.2: Measured and estimated circuit parameters (left), and their corresponding dipole energies (right).

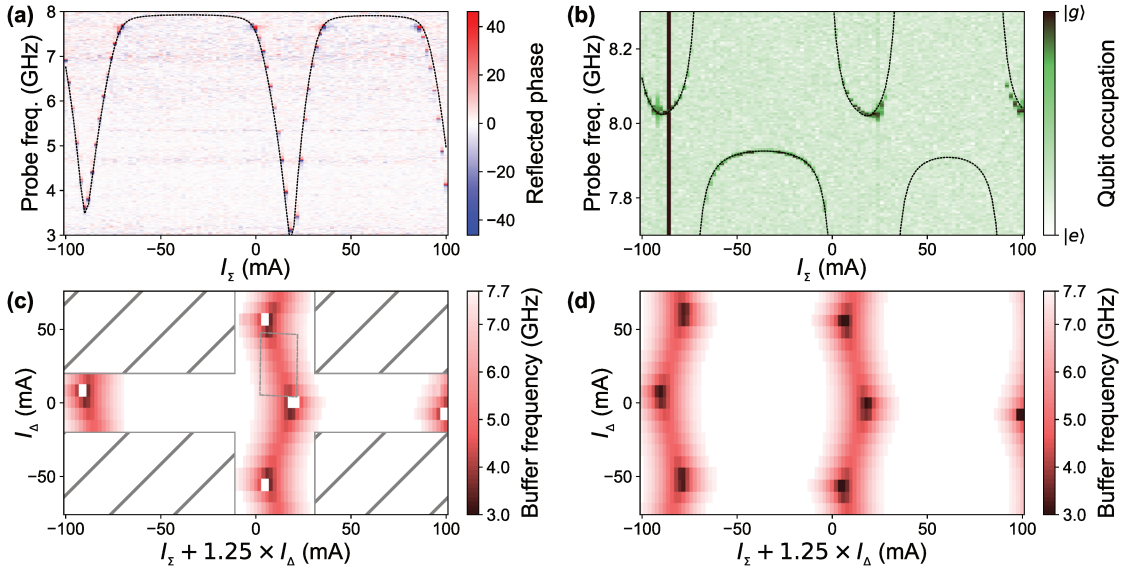


Figure 6.8: **Flux dependence.** (**a**) Buffer spectroscopy. Phase of the reflected probe signal (colormap) on the buffer port as a function of $I_\Sigma$ (x-axis) and probe frequency (y-axis). The buffer frequency follows an arch-like pattern typical of SQUID-based devices. The probing frequency range is limited to 3-8 GHz due to the 4-8 GHz circulator on the output line. The black dashed line represents the expected buffer/cat-qubit frequency for the best fitting parameter set. The slight aperiodicity may be explained by small asymmetries in the loop areas of the ATS. (**b**) Cat-qubit resonator two-tone spectroscopy. A continuous probe is applied on the cat-qubit resonator at various frequencies (y-axis) and a second tone attempts to $\pi$-pulse the qubit on resonance. When the probe populates the cat-qubit, the qubit shifts in frequency due to the cross-Kerr coupling, and is insensitive to the $\pi$-pulse. The resulting qubit state is plotted in color and we repeat the experiment for various values of $I_\Sigma$ (x-axis). The black dashed line represents the expected buffer/cat-qubit frequency for the best fitting parameter set. The black vertical line corresponds to a flux bias were the buffer is at the qubit frequency resulting in a strong decrease in the qubit lifetime. (**c**) For each value of $I_\Sigma$ (x-axis) and $I_\Delta$ (y-axis), we extract the buffer frequency from a spectroscopy measurement (panel a) and report it in color (white is when the resonance frequency is beyond the measurement range). Contrary to what they were designed for, the two flux lines do not perfectly apply symmetric ($I_\Sigma$) and antisymmetric ($I_\Delta$) bias on the ATS. We compensate for this imbalance while taking the data by shifting the $I_\Sigma$ span for each value of $I_\Delta$ as indicated on the x-axis label. Data were only taken on the area outside the hatched regions to prevent the heating of the dilution refrigerator beyond a tolerable temperature. The grey dashed-rectangle corresponds to the flux range presented in Fig. 6.2 of the main text. (**d**) Simulated flux dependence of the buffer mode for the best fitting parameter set.

### 6.2.4 *Semi-classical analysis*

In this section, we compute the semi-classical dynamics of the cat-qubit resonator in the presence of various imperfections (single photon loss and detuning). We gain insight into these dynamics by introducing a pseudo-potential function. For a more complete approach, we refer the reader to Refs. [146].

#### 6.2.4.1 *Two-photon dynamics*

Under two-photon dissipation, the cat-qubit resonator state $\rho$ undergoes the following dynamics

$$\frac{d}{dt}\rho = \kappa_2 D[\boldsymbol{a}^2 - \alpha^2]\rho \,, \tag{6.15}$$

where the Lindblad operator $D$ is defined for any operator $\boldsymbol{O}$ as $D[\boldsymbol{O}]\rho = \boldsymbol{O}\rho\boldsymbol{O}^\dagger - \frac{1}{2}\rho\boldsymbol{O}^\dagger\boldsymbol{O} - \frac{1}{2}\boldsymbol{O}^\dagger\boldsymbol{O}\rho$. Any combination of the states $|0,1\rangle_\alpha$ is a steady state of this dynamics. Moreover, these steady states are global attractors. To gain insight, we restrict this dynamics to the set of coherent states $\rho(t) = |\beta(t)\rangle\langle\beta(t)|$, and introduce the pseudo-potential $V$ defined over the resonator phase space as $-\nabla V(\beta) = \frac{d\beta}{dt}$. This pseudo-potential depicts in which direction of the phase space a coherent state $|\beta\rangle$ evolves, and coherent steady states of the dynamics are the minima of $V$. Following ref. [20], we have

$$\frac{d\beta}{dt} = -\kappa_2\beta^*(\beta^2 - \alpha^2) \,. \tag{6.16}$$

In the following we introduce $x = \mathrm{Re}(\beta)$ and $y = \mathrm{Im}(\beta)$ and we consider $\alpha$ real. Separating the real and imaginary part of equation (6.16), we get

$$\begin{aligned} \frac{dx}{dt} &= -\kappa_2\left(x^3 + xy^2 - x\alpha^2\right) \\ \frac{dy}{dt} &= -\kappa_2\left(y^3 + yx^2 + y\alpha^2\right) \,. \end{aligned}$$

The velocity of a coherent state $|\beta\rangle$ in phase space is $(\frac{dx}{dt}, \frac{dy}{dt})$ (see Fig. 6.9a,6.10a). By integrating this velocity over space, we get the pseudo-potential

$$V(x,y) = \kappa_2\left(\frac{1}{4}(x^4 + y^4) + \frac{1}{2}x^2y^2 - \alpha^2(x^2 - y^2)\right) \tag{6.17}$$

depicted in Fig. 6.1b of the main text. It has two minima in $-\alpha$ and $\alpha$. Analyzing the evolution of small deviations $\delta x$ and $\delta y$ around these minima, we find

$$\begin{aligned} \frac{d}{dt}\delta x &= -\kappa_{\mathrm{conf}}\delta x \\ \frac{d}{dt}\delta y &= -\kappa_{\mathrm{conf}}\delta y \,, \end{aligned}$$

where the confinement rate $\kappa_{\mathrm{conf}}$ is defined as

$$\kappa_{\mathrm{conf}} = 2\kappa_2\alpha^2 \,. \tag{6.18}$$

This confinement pins down a computational state at each potential minimum, and protects the cat-qubit against errors. Next, we analyze the effect of errors on the cat-qubit resonator.

#### 6.2.4.2 *Single photon loss*

When added, most Hamiltonian or dissipative mechanisms (such as detuning, single photon loss or gain, and dephasing) will perturb the system so that the two-dimensional cat-qubit space is no longer a steady-manifold of the overall dynamics. Instead, only one mixed state is a steady-state. However, this steady-state is exponentially (in $|\alpha|^2$)

long to reach from the cat-qubit computational states $|0\rangle_\alpha$ and $|1\rangle_\alpha$ [146]. We refer to these states as metastable states. We will now use the pseudo-potential representation to visulalize the main effects of single photon loss and detuning.

Let us calculate $V$ in the presence of single photon loss at rate $\kappa_a$. The loss operator is $\boldsymbol{L}_1 = \sqrt{\kappa_a}\boldsymbol{a}$ and the overall dynamics reads

$$\frac{d}{dt}\rho = \kappa_2 D[\boldsymbol{a}^2 - \alpha^2]\rho + \kappa_a D[\boldsymbol{a}]\rho\,. \tag{6.19}$$

Following the same computation as previously, we have

$$\frac{d\beta}{dt} = -\kappa_2\beta^*(\beta^2 - \alpha^2) - \frac{1}{2}\kappa_a\beta$$

so that

$$\begin{aligned}\frac{dx}{dt} &= -\kappa_2\left(x^3 + xy^2 - x\alpha^2\right) - \frac{1}{2}\kappa_a x \\ \frac{dy}{dt} &= -\kappa_2\left(y^3 + yx^2 + y\alpha^2\right) - \frac{1}{2}\kappa_a y\,.\end{aligned} \tag{6.20}$$

This velocity field is represented in Fig. 6.9a for $\kappa_a = \kappa_2$ and $\alpha = 2$. By integrating it over space we get

$$V(x,y) = \kappa_2\left(\frac{1}{4}(x^4+y^4) + \frac{1}{2}x^2y^2 - \alpha^2(x^2-y^2)\right) + \frac{1}{4}\kappa_a\left(x^2+y^2\right)\,. \tag{6.21}$$

Cuts that pass through the two minima are plotted in Fig. 6.9b for various values of $\kappa_a$ and $\alpha$.

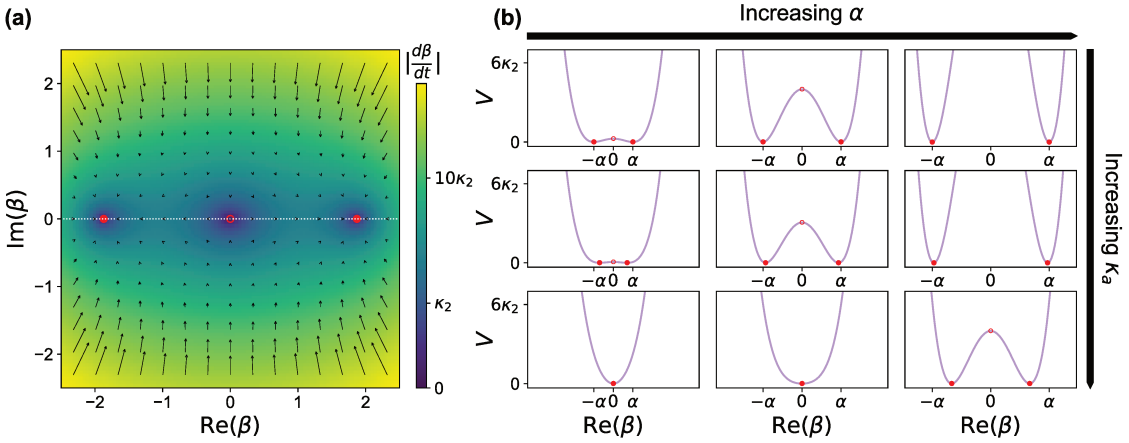


Figure 6.9: **Dynamics under single photon loss. (a)** This colormap represents the magnitude of the velocity field (6.20) over phase space ($\beta$ plane) for $\kappa_a = \kappa_2$ and $\alpha = 2$. The black arrows represent the velocity at various locations. The two stable/ one unstable steady-states are indicated with full/open red circles (the stability is infered from the direction of the arrows). The white dotted line represents the cut along which we plot the potential. **(b)** Cuts ($\mathrm{Re}(\beta) = 0$) of the potential (6.21) with $\alpha = (1,2,3)$ (left to right) and $\kappa_a = (0, \kappa_2, 10\kappa_2)$ (top to bottom). The top row represents the unperturbed potential and the steady states are $-\alpha$ and $\alpha$ (red circles). As we increase $\kappa_a$, the amplitude $\alpha_\infty$ of the metastable states (red circles) decreases until reaching 0. However for a given value of $\kappa_a$, we can always find a value of $\alpha$ to recover two metastable states (bottom row).

The minima of $V$ are located in $\pm\alpha_\infty$ with

$$\alpha_\infty = \begin{cases} \sqrt{\alpha^2 - \kappa_a/(2\kappa_2)} & \text{if } \alpha^2 \geq \kappa_a/(2\kappa_2) \\ 0 & \text{otherwise} \end{cases} \tag{6.22}$$

In this semi-classical analysis, we find that two metastable states form when the error rate $\kappa_a$ is below the threshold

$$\kappa_a < \kappa_{\text{conf}} = 2|\alpha|^2\kappa_2 \,.$$

#### 6.2.4.3 *Detuning*

In the main text, we discussed the causes of the bit-flip time saturation and blamed the random frequency shifts of the cat-qubit resonator induced by the transmon thermal excitations. Let us see how a detuning $\Delta$ of the cat-qubit frequency affects the two-photon stabilization. In this case, we have

$$\frac{d\beta}{dt} = -\kappa_2\beta^*(\beta^2 - \alpha^2) - i\Delta\beta \tag{6.23}$$

so that

$$\begin{aligned} \frac{dx}{dt} &= -\kappa_2\left(x^3 + xy^2 - x\alpha^2\right) + \Delta y \\ \frac{dy}{dt} &= -\kappa_2\left(y^3 + yx^2 + y\alpha^2\right) - \Delta x \,. \end{aligned} \tag{6.24}$$

Note that $\text{rot}(\frac{dx}{dt}, \frac{dy}{dt}) = -2\Delta \neq 0$ so we cannot perform the spatial integration to find $V(x, y)$. We can obtain the steady states directly by analyzing the velocity field (Fig. 6.10a) but there exists a direction in phase-space parametrized by a real parameter $\lambda$ such that $y = \lambda x$ and $\frac{dy}{dt} = \lambda\frac{dx}{dt}$ along which the integration is meaningful. Plugging in this relation into (6.24) we get the following condition on $\lambda$

$$\begin{aligned} \lambda^2\Delta + 2\lambda\kappa_2\alpha^2 + \Delta = 0 \\ \lambda = -\frac{\kappa_{\text{conf}}}{2\Delta} + \sqrt{(\frac{\kappa_{\text{conf}}}{2\Delta})^2 - 1} \end{aligned} \tag{6.25}$$

with $\kappa_{\text{conf}} = 2\kappa_2\alpha^2$. We have chosen the solution $\lambda$ which approaches 0 when $\Delta \to 0$ and for which the chosen direction crosses the steady states. Along this cut indexed by $\beta'$, we have

$$\frac{d\beta'}{dt} = \left(\sqrt{\left(\frac{\kappa_{\text{conf}}}{2}\right)^2 - \Delta^2}\right)\beta' - \kappa_2\beta'^3 \tag{6.26}$$

leading to

$$V(\beta') = -\frac{1}{2}\left(\sqrt{\left(\frac{\kappa_{\text{conf}}}{2}\right)^2 - \Delta^2}\right)\beta'^2 + \frac{1}{4}\kappa_2\beta'^4 \tag{6.27}$$

that is plotted in Fig. 6.10b. There are two minima located along the direction $\beta'$ in

$$|\alpha_\infty| = \begin{cases} \left(\alpha^4 - \left(\frac{\Delta}{\kappa_2}\right)^2\right)^{\frac{1}{4}} & \text{if } \Delta < \frac{\kappa_{\text{conf}}}{2} \\ 0 & \text{otherwise} \end{cases} \tag{6.28}$$

In this semi-classical analysis, we find that two metastable states form provided $\Delta$ is below the threshold

$$\Delta < \kappa_{\text{conf}}/2 = |\alpha|^2\kappa_2 \ .$$

In our experiment, the detuning induced by a thermal photon entering the transmon is $\Delta/2\pi = \chi/2\pi = 720\,\text{kHz}$ which is larger than $\kappa_{\text{conf}}/2/2\pi = 7\kappa_2/2\pi \approx 280\,\text{kHz}$ for the largest $|\alpha|^2 = 7$.

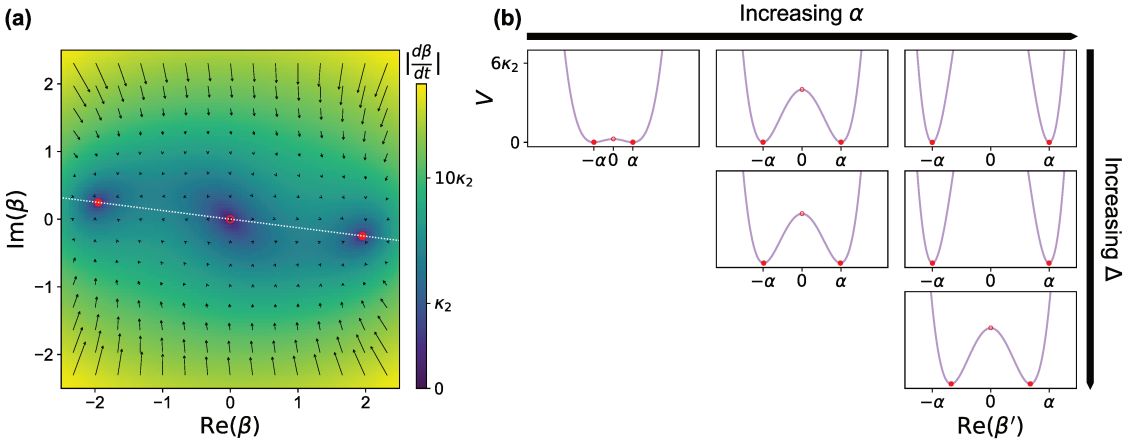


Figure 6.10: **Dynamics under detuning. (a)** This colormap represents the magnitude of the velocity field (6.24) over the phase space ($\beta$ plane) for $\Delta = \kappa_2$ and $\alpha = 2$. The black arrows represent the velocity at various locations. The two stable/ one unstable steady-states are indicated with full/open red circles (the stability is infered from the knowledge of the direction of the arrows). The white dotted line represents the cut along which we represent the potential. **(b)** Cuts ($\text{Im}(\beta) = \lambda\text{Re}(\beta)$) of the potential (6.27) with $\alpha = (1, 2, 3)$ (left to right) and $\Delta = (0, \kappa_2, 8\kappa_2)$ (top to bottom). The top row represents the unperturbed potential and the steady states are $-\alpha$ and $\alpha$ (red circles). As we increase $\Delta$, the amplitude $|\alpha_\infty|$ of the metastable states (red circles) decreases until reaching 0. However for a given value of $\Delta$, we can always find a value of $\alpha$ to recover two metastable states (bottom row).

### 6.2.5 *Bit-flip time simulation*

In the previous part, we gained insight on how single photon loss and detuning affect the cat-qubit protection. In the following, we perform a full master equation simulation of the system with the measured system parameters. The system consists of three relevant modes: the buffer and cat-qubit resonator, and the transmon qubit. We can write the Hamiltonian and loss operators (in the rotating frame for each mode)

$$\begin{aligned} \boldsymbol{H_3}/\hbar &= \left(g_2^*(\boldsymbol{a}^2 - \alpha^2)\boldsymbol{b}^\dagger + \text{h.c}\right) - \frac{\chi_{aa}}{2}\boldsymbol{a}^{\dagger 2}\boldsymbol{a}^2 - \chi_{qa}\boldsymbol{a}^\dagger\boldsymbol{a}\boldsymbol{q}^\dagger\boldsymbol{q} \qquad (6.29) \\ \boldsymbol{L}_a = \sqrt{\kappa_a}\boldsymbol{a},\ \boldsymbol{L}_b &= \sqrt{\kappa_b}\boldsymbol{b},\ \boldsymbol{L}_q = \sqrt{\kappa_q(1+n_{\text{th}})}\boldsymbol{q},\ \boldsymbol{L}_{q^\dagger} = \sqrt{\kappa_q n_{\text{th}}}\boldsymbol{q}^\dagger \end{aligned}$$

where we have (from left to right) in the Hamiltonian, the two-to-one photon exchange factored with a drive on the buffer with strength $\epsilon_d = -g_2^*\alpha^2$, the Kerr of the cat-qubit, the cross-Kerr between the cat-qubit and the transmon. The two last loss operators model the decay rate of the transmon (rate $\kappa_q$), and its thermal occupation measured

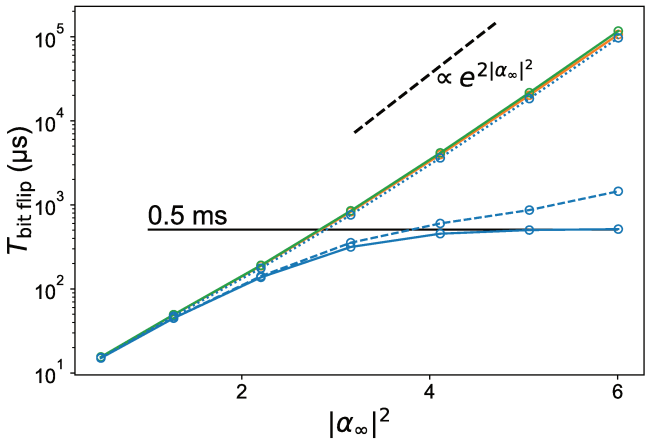


Figure 6.11: Simulated bit-flip time as a function of the cat-qubit size $|\alpha_\infty|^2$. We simulate the experiment displayed in Fig. 6.3 of the main text given the measured system parameters (Tables 6.1 and 6.2) with a master equation solver (QuTiP) for various values of $\alpha^2$. The cat-qubit size is given by $|\alpha_\infty|^2 = |\langle \boldsymbol{a}^2 \rangle|$ after a time $t \gg \kappa_2^{-1}$. We simulate three models of increasing complexity: a one, two and three modes model. The green curve corresponds to the simulation of the equivalent dynamics of the cat-qubit resonator alone (6.31). We get an exponential increase of the bit-flip time with a dependence on the cat size close to the theoretical prediction $\exp(2|\alpha_\infty|^2)$ [146] (dashed black line is a guide for the eye). The orange curve corresponds to the simulation of the dynamics of the buffer and cat-qubit together (6.30). The good agreement between these two curves indicates that the adiabatic elimination of the buffer is valid (indeed $g_2 \ll \kappa_b$). Finally the blue solid curve is the simulation including the transmon with its thermal occupation (6.29). In this case, the bit-flip time saturates at around 0.5 ms which is compatible to the experimentally measured value (1 ms). This saturation follows a prior exponential increase where the bit-flip time is multiplied by 3.7 for each added photon (experimentally 4.2). We also simulate for $\chi_{qa} = \chi_{qa,\text{exp}}/3$ (dashed blue line) and $\chi_{qa,\text{exp}}/10 = 72$ kHz (dotted blue line) and as expected, the curve approaches the exponential scaling when $\chi_{qa}$ is low enough.

to be $n_{th} \sim 1\%$ in the presence of the pump and drive. In order to determine the effect of the transmon on the cat-qubit, it is useful to remove the transmon from the simulation. We simulate the dynamics generated by

$$\begin{aligned} \boldsymbol{H_2}/\hbar &= \left(g_2^*(\boldsymbol{a}^2 - \alpha^2)\boldsymbol{b}^\dagger + \text{h.c}\right) - \frac{\chi_{aa}}{2}\boldsymbol{a}^{\dagger 2}\boldsymbol{a}^2 \\ \boldsymbol{L}_a &= \sqrt{\kappa_a}\boldsymbol{a},\ \boldsymbol{L}_b = \sqrt{\kappa_b}\boldsymbol{b} \end{aligned} \tag{6.30}$$

Finally by adiabatically eliminating the buffer [20] we reduce to the following equivalent Hamiltonian and loss operator (provided $g_2 \ll \kappa_b$)

$$\begin{aligned} \boldsymbol{H_1}/\hbar &= -\frac{\chi_{aa}}{2}\boldsymbol{a}^{\dagger 2}\boldsymbol{a}^2 \\ \boldsymbol{L}_a &= \sqrt{\kappa_a}\boldsymbol{a},\ \boldsymbol{L}_2 = \sqrt{\kappa_2}(\boldsymbol{a}^2 - \alpha^2) \end{aligned} \tag{6.31}$$

with $\kappa_2 = 4|g_2|^2/\kappa_b$.

For each of these models, we numerically solve the master equation for the cat-qubit resonator prepared in state $|+\alpha\rangle$ for various $\alpha$. By fitting the decay of $\langle \boldsymbol{a} \rangle$ to an exponential decay, we extract $T_{\text{bit-flip}}$ that we reported in Fig. 6.11 (full lines). For

the last two models, we recover the exponential increase of the bit-flip time which scales as $\sim \exp(2\alpha^2)$. The three modes model reproduces the saturation we have in the experiment and associates it with the thermal excitation of the transmon. Indeed one transmon excitation detunes the cat-qubit by $\chi$ which exceeds $\kappa_{\text{conf}}/2$ when $\alpha^2 < 29$, well above cat sizes we could achieve experimentally. In future experiment, we plan on reducing $\chi$. By dividing $\chi$ by 10, we expect to fully circumvent this saturation (dotted lines in Fig. 6.11).

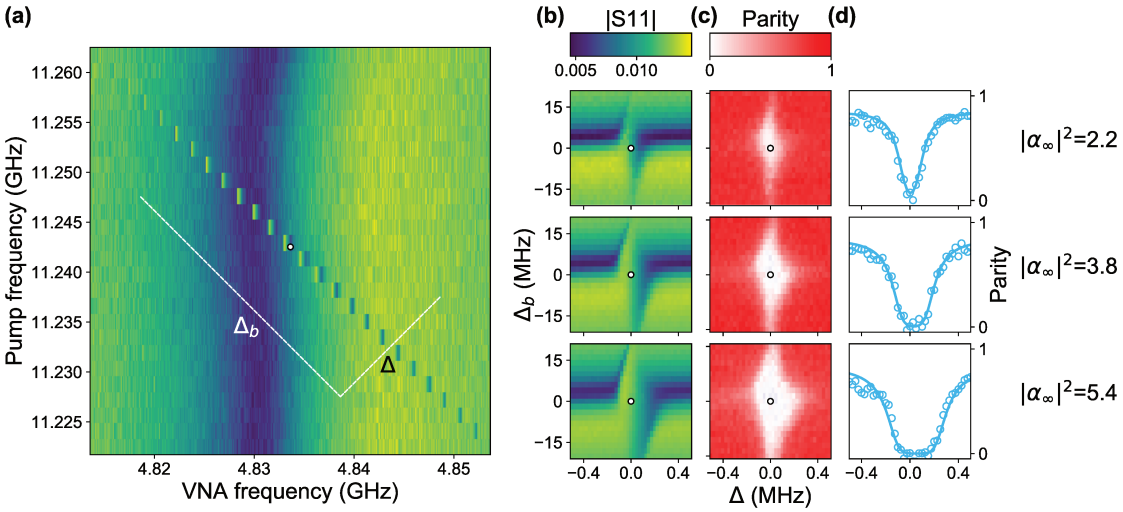


Figure 6.12: **Tuning the pump and drive frequencies**. (**a**) Reflected relative drive amplitude (VNA measurement) as a function of drive frequency (x-axis) and pump frequency (y-axis). When $\omega_p = 2\omega_a - \omega_d$, a sharp feature indicates that the two-to-one photon exchange is resonant and as expected, it has a slope $-1$. To observe this feature, we switch to the basis $\Delta = (\Delta_{\text{pump}} + \Delta_{\text{drive}})/2$, $\Delta_b = (\Delta_{\text{pump}} - \Delta_{\text{drive}})/2$. (**b,c**) Reflected relative drive amplitude (color) and parity of the cat-qubit resonator (red) as a function of $\Delta$ (x-axis) and $\Delta_b$ (y-axis) for increasing drive amplitude (top to bottom). The drive amplitude is expressed in units of the cat-size $|\alpha_\infty|^2$ which is calibrated using the data of Fig 6.13. (**c**) When the two-to-one photon exchange is resonant, the cat-qubit resonator is displaced and the parity drops to 0 if we measure after a time greater than $\kappa_a^{-1}$. We also perform the cat-qubit resonator tomography and verify that the resonator is in a balanced mixture of $|0\rangle_\alpha$ and $|1\rangle_\alpha$. In all these plots, the white circles correspond to the chosen pump and drive frequencies. We verify that for all used drive amplitudes, this point remains centered in the resonant range. Therefore, we do not need to adapt the drive and pump frequencies when increasing the cat size. (**d**) Cut of the color plot (c) at $\Delta_b = 0$ representing the parity (open circle) of the cat-qubit steady state as a function of $\Delta$. The relation (6.28) shows that the frequency window over which a non-trivial state is stabilized in the cavity scales as $2\kappa_2|\alpha|^2$. This enables us to determine $\kappa_2$ assuming photon loss is the main loss mechanism. We fit (solid line) the measured parity with the expected steady-state parity (QuTiP) where the two fitting parameters are the parity contrast and $\kappa_2$. We find $\kappa_2/2\pi = 40$ kHz.

### 6.2.6 *Tuning the cat-qubit*

As explained in the main text, the flux point at which the ATS should operate is a saddle point of the buffer frequency map. It is very simple to find experimentally as we do not need to know the full mapping between ($I_\Sigma$, $I_\Delta$) and ($\varphi_\Sigma$, $\varphi_\Delta$) to recognize a saddle point. There are actually two types of saddle points as one can see on Fig. 6.8, the ones that are tilted to the left and the ones tilted to the right. If the two junctions forming the SQUID of the ATS were perfectly symmetric, these points would be equivalent. Otherwise, the buffer acquires a Kerr non-linearity and the two-points differ by the sign of this Kerr.

Once we find the buffer and cat-qubit frequencies we perform two-tone spectroscopy on the buffer (Fig. 6.12). A weak tone, referred to as the drive, probes the buffer resonance and the pump is swept in the relevant frequency range (around $2\omega_a - \omega_b$). When the two-to-one exchange occurs between the buffer and the cat-qubit, we observe a sharp feature within the buffer resonance (Fig. 6.12a,b). The width of this feature depends on the weak tone strength and more importantly on the pump power. The pump power is pushed until before this feature becomes ill defined, when other non-linear dynamics start to play a significant role. On the cat-qubit side, within this feature the drive combined with the pump should populate the cat-qubit resonator. We check so by measuring the parity of the cat-qubit resonator and verify that it is indeed displaced. We tune the pump and buffer frequency in the middle of the displacement area (Fig. 6.12c). The width along $\Delta$ of this region enables us to determine $\kappa_2$.

We perform the cat-qubit resonator full tomography after a long (20 $\mu$s $\gg \kappa_a^{-1}$) pump and drive pulse (Fig. 6.13a) and we set the drive amplitude to produce the desired cat size (Fig. 6.13b). The experiment is now tuned and the cat-qubit characteristics ($T_{\text{bit-flip}}, \Gamma_{\text{phase-flip}}$, time evolution of the Wigner function) can be measured.

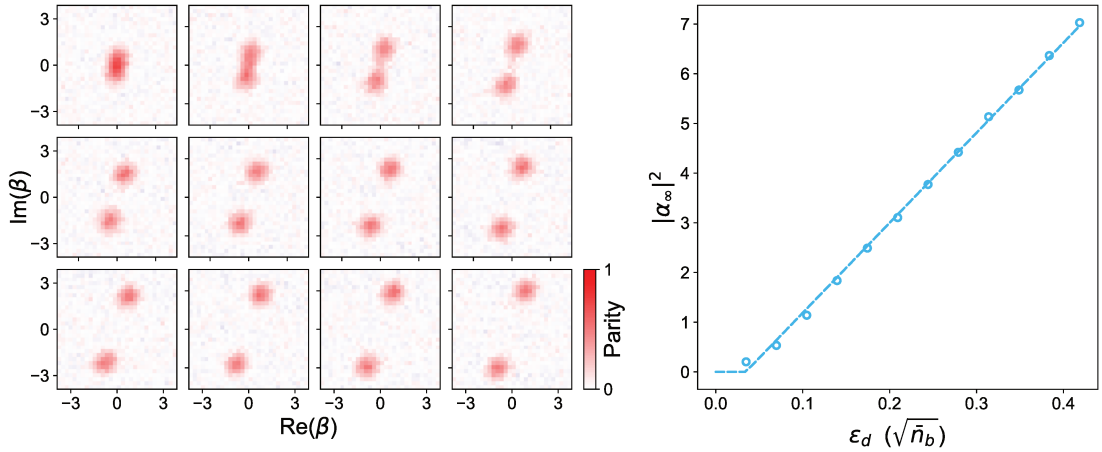


Figure 6.13: **Increasing the cat-qubit size.** (**a**) Measured Wigner distribution of the cat-qubit state as a function of drive amplitude (left to right, top to bottom) after a pump and drive pulse duration of 20 $\mu$s. (**b**) Fitted cat size $|\alpha_\infty|^2$ (open circles) as a function of the drive amplitude $\epsilon_d$. The drive amplitude is expressed in terms of the square root of the photon number the buffer would contain without the conversion process. For each Wigner distribution of panel (a), we fit a sum of two 2D-Gaussian functions (coherent states) diametrically opposed which are separated by a distance $2|\alpha_\infty|$. Note that for simplicity, in the main text, we use $|\alpha|^2$ instead of $|\alpha_\infty|^2$. In the presence of single photon loss at rate $\kappa_a$, we expect $|\alpha_\infty|^2$ to follow the relation (6.22) (dashed line): a linear dependence on $\epsilon_d$ shifted by $\kappa_a/(2\kappa_2)$. By fitting this relation to the data, we calibrate the x-axis scaling.

# 7

# CONCLUSION AND PERSPECTIVES

> Devant une flamme, dès qu'on rêve,
> ce que l'on perçoit n'est rien au
> regard de ce qu'on imagine.
>
> G. Bachelard

In conclusion, I succeeded in developing a fully functional version of the quantum node. I used it to realize the first implementation of a 6 years old theoretical proposal [11] (see chapter 4). The group is currently performing a variety of experiments using this device. More importantly, the techniques of fabrication and design for coplanar waveguide superconducting quantum circuits developed during this PhD work significantly contributed to 2 other important results: the multiplexed photon number measurement (see chapter 5) and the exponential suppression of bit-flip in qubits encoded using Schrödinger Cat states of a microwave mode (see chapter 6).

Beyond these contributions, I believe this work illustrates of the technological and conceptual leap forward initiated by the Black Box Quantization [147–151] approach to circuit modeling. Indeed, its main take away is that superconducting circuit design is now mature enough to engineer a broad spectrum of Hamiltonians and controlled dissipation channels. This ability to shape Hamiltonians at will allows for the exploration of exotic physics as well as for the development of quantum machines.

It seems to me that the most interesting scientific directions that I would encourage after this work would be the study of the quantum noise time-correlators in itinerant wave packet and its link to quantum state tomography. Indeed, the investigation of the signal acquired from the measurement of the released itinerant wave packet in the sequential readout experiment, led me to remark that a measurement of the squeezing of a the state could be made by looking at the signal self-correlator as proposed in Ref. [94]. Then one could ask whether it is possible to retrieve higher moments of the quantum state distribution in the various time-correlators of the signal. This investigation would bridge to the multiplexed photo-counting experiment (see chapter 5). There, a pulsed multiplexed measurement would lead to a single frequency channel containing photons. Hence the power of a given frequency channel should be anti-correlated with the other frequency channels.

But I currently choose to follow another path opened by the insights of this PhD work: the quest for a universal fault-tolerant quantum computer. Indeed, I was brought to this field by an article about quantum computers in the IEEE Spectrum journal back

in 2014. I used have two passions, electronics and physics. But I rapidly understood that I was 40 years late for electronics and that nowadays no major revolution was possible in electronics. The perspective of recreating the quest of the 40s and 50s for industrial computing machines, this time with the fascinating rules of quantum mechanics, echoed strongly with my passions. During this work, I grew to think that not only the technology is getting closer to reaching the required performances, but also that we had in France a unique know-how, a unique approach to quantum computing: a realistic way towards fault-tolerant universal quantum computers using autonomous error correction, implemented for example with Schrödinger cat qubits. Indeed the recent work of J. Guillaud ([134]) provides a clear roadmap to build such a machine.

The purpose of the start-up company Alice&Bob that R. Lescanne and I are launching is to provide the required resources to amplify the strong historical excellence in superconducting quantum circuits in France, experimentally demonstrated by CEA Saclay, Néel Institute, Ecole Normale Supérieure, Ecole Normale Supérieure de Lyon and University Paris Saclay, and leverage the promising results of the Quantic team. We aim at supporting the academic research groups to establish a flagship consortium around this unique technology.

The scientific roadmap of Alice&Bob is to first improve our current cat qubit to reach the point where the exponential suppression is so strong that a bit-flip becomes a very unlikely event during the duration of a computation. Then we will correct for the remaining phase-flip errors through a linear repetition code. To do so we will need to develop CNOT gates between cat qubits, which is our next milestone. Then J. Guillaud's work demonstrates that with a Toffoli gate, we will be able to perform universal fault-tolerant computation. The realistic part of this roadmap comes from the fact that the CNOT and the Toffoli gates can be done using only 3-wave and 4-wave mixing Hamiltonian with reasonable coupling, thus being within the scope of current state-of-the-art.

Part III

# APPENDIX

# a

# TOOLBOX OF MICROWAVE QUANTUM OPTICS

L'imagination trouve plus de réalité à
ce qui se cache qu'à ce qui se montre

G. Bachelard

The goal of this appendix is to provide the reader with some of the necessary tools to understand the experiment done in this thesis. In particular, we present the description of the quantum state of a harmonic oscillator and several useful quantum states and how to obtain and manipulate them. We define and detail various technics of tomography for bosonic quantum state.

## A.1 QUANTUM STATES OF A HARMONIC OSCILLATOR

The depiction of the quantum state of a harmonic oscillator requires more parameters than its classical counterpart. Indeed in the classical formalism, a harmonic oscillator is fully described by only two real numbers : its position and impulsion for a mechanical oscillator, and the current and charge in an electrical oscillator. We remind the reader here of the canonical description a harmonic oscillator in the quantum world.

### A.1.1 *Description of a bosonic state*

We saw in chapter 2 that the diagonal Hamiltonian of an isolated resonator mode $a$ is

$$H = \hbar\omega(a^\dagger a + \frac{1}{2}). \tag{a.1}$$

We defined the photon number operator $N = a^\dagger a$ whose eigenvalues are integers corresponding to equally spaced energy levels. The basis constructed by the eigenvectors of the operator $N$ is called the Fock basis (see [29] for more details). This illustrates that the description of the quantum state of an oscillator, in the general case, requires an infinite (but countable) number of complex parameters. Indeed, owing to this basis, any pure state $|\varphi\rangle$ can be written

$$|\varphi\rangle = \sum_{i\in\mathbb{N}} c_i|i\rangle. \tag{a.2}$$

Pure states can only describe the cases where we have a complete knowledge of our system. To encompass the general case of incomplete knowledge, either due to noise,

decoherence or loss of a subsystem entangled with the oscillator, one must use the density matrix formalism. The density matrix $\rho$ of a pure state $|\varphi\rangle$ is

$$\rho = |\varphi\rangle\langle\varphi|. \tag{a.3}$$

And the formalism of the density matrix allows to consider states made out of the statistical mixture of a collection of pure states $|\varphi_i\rangle$

$$\rho = \sum_i p_i |\varphi_i\rangle\langle\varphi_i|. \tag{a.4}$$

Thus, in the most general case, even when truncating the Hilbert space of the oscillator to a maximum photon number $m$, describing its state requires $m^2$ complex parameters. This large number can become rapidly intractable as we consider larger $m$ and experimentally challenging to access. This is why we introduce tomography methods latter on as a way to retrieve efficiently the state of the oscillator.

Nevertheless, several states can be easily defined and are of practical use. In particular, coherent states $|\alpha\rangle$, defined as displaced vacuum

$$|\alpha\rangle = D(\alpha)|0\rangle = e^{i(\alpha a^\dagger - \alpha^* a)}|0\rangle \tag{a.5}$$

are of practical use as they can be described by a single complex number $\alpha$. They are eigenstate of the annihilation operator $a|\alpha\rangle = \alpha|\alpha\rangle$ and thus are steady states of a lossy oscillator driven by a classical source. Also the propagating state emitted by a microwave source can be modeled by a coherent state. Coherent states have many useful properties that can all be retrieved from its expression in the Fock basis

$$|\alpha\rangle = e^{\frac{-|\alpha|^2}{2}} \sum_i \frac{\alpha^i}{i!^{1/2}} |i\rangle. \tag{a.6}$$

One can also construct an over complete basis out of the continuous set of coherent states as for the Glauber-Sudarshan P-representation (see below and [152], [153]).

We also define the thermal states as the statistical mixture of Fock state respecting the Boltzmann distribution of energy

$$\rho_{\text{th}} = \left(1 - e^{-\frac{\hbar\omega}{kT}}\right) \sum_n e^{-n\frac{\hbar\omega}{kT}} |n\rangle\langle n| \tag{a.7}$$

where the average number of photon $n_{\text{th}}$ is linked to the effective temperature of the mode by

$$1 + \frac{1}{n_{\text{th}}} = e^{\frac{\hbar\omega}{kT}} \tag{a.8}$$

This means that the density matrix of a thermal state is solely composed of diagonal terms describing the energy distribution and has no off-diagonal terms, thus no coherence whatsoever.

Finally, we introduce dimensionless observables equivalent to the classical position and impulsion as in chapter 2,

$$\begin{cases} I &= \frac{a+a^\dagger}{2} \\ Q &= \frac{a-a^\dagger}{2i} \\ [I,Q] &= \frac{i}{2} \end{cases} \tag{a.9}$$

In the following these will be referred to as the quadrature operators. Those quadrature operators are fundamental for the tomography we will consider. It is interesting to remark that for a coherent state $|\alpha\rangle$, we have

$$\begin{cases} \langle I \rangle &= \mathrm{Re}(\alpha) \\ \langle Q \rangle &= \mathrm{Im}(\alpha) \\ \langle a^\dagger a \rangle &= \langle (I^2 + Q^2) \rangle - \frac{1}{2} = |\alpha|^2 \end{cases} \tag{a.10}$$

Thus a coherent maximize the uncertainty principal and is a gaussian in $I$ and $Q$ of standard deviation $\sigma = \frac{1}{2}$ centered in $\alpha$. Similarly, one can show that a thermal state is described also a gaussian centered in 0 and of standard deviation $\sigma = \frac{1}{2} + \frac{1}{e^{\frac{\hbar\omega}{kT}} - 1}$.

Here we take a moment to emphasize fundamental origin of this minimal standard deviation of 1/2. It is crucial to bare in mind that it sole origin, as for the vacuum energy offset, is the non-commutation of the operators $I$ and $Q$. This indetermination manifest itself during the measurement process (see phase-space representations below) when using continuous variables. For example, a mode $a$ in the vacuum is in a pure state but its phase-space representation is a gaussian of finite width. This distribution's minimal width does not imply any missing information about the quantum state but rather an improper choice of measurement basis. In our example one could obtain a deterministic answer by photo-counting and thus projecting over the Fock basis. In particular, when reconstructing quantum trajectories (see [154]) this *quantum noise* is actually directly interpreted as innovation and contains the information needed to compute the back-action of the measurement. Finally, we remark that this minimal spread is called the *zero point fluctuations* and that the parameters appearing in the BBQ method are named in consequence.

$I$ and $Q$ operators are related to one-another by the Fourrier transform. Their eigenstates are equivalent to plane waves in wave optics : they trade a perfect definition of one quadrature at the cost of being fully undetermined over the other. Furthermore, by analogy with wave optics, one can tell that the coherent state basis is linked to the two quadrature basis in the same manner as the gaussian wavelets are related to plane waves.

We remark that the quadrature description of a state differs fundamentally from its description in the Fock basis by the fact the first is a description in continuous basis whereas the latter is a discrete one. It is crucial to adapt the choice of the basis to the characteristics of the system under study and the measurement apparatus. In this work we will which from one to the other. In particular we will prefer the Fock state basis to describe the interaction of an oscillator with a qubit due to the presence of the photon number operator in the dispersive coupling. And we will prefer the quadrature depiction when describing amplification and continuous variable measurements.

### A.1.2 *Squeezed light*

Coherent states and thermal states are not the only quantum state of a harmonic oscillator described a gaussian distribution in the phase-space (see below for detail on

phase-space representations). We also need to consider squeezed states which are 2D gaussian distribution with two distinct standard deviations (and for simplicity in the following we will consider the two main axis of this 2D gaussian to be along I and Q). A squeezed state can be obtained by applying a squeezing operator $S$ on a mode $a$ in the vacuum, with $S$ being defined by

$$S = e^{ra^2 - r^* a^{\dagger 2}}, \tag{a.11}$$

where $r$ is the complex squeezing parameter, whose phase dictates the direction of squeezing and whose amplitude sets the ratio of the two main standard deviations of the squeezed distribution $\cosh|r| = \sqrt{\frac{\sigma_{\max}}{\sigma_{\min}}}$. As for the displacement, this squeezing operator can be obtained by applying a squeezing Hamiltonian $H_S$ for a given duration,

$$H_S = ga^2 + g^* a^\dagger 2. \tag{a.12}$$

From a historical experimental point of view, this squeezing Hamiltonian can be obtained directly from the non-linearity provided by a Josephson junction as in a Josephson Parametric Amplifier (JPA) ([155], [156], [157]). Indeed, applying the BBQ method seen in chapter 2 to a harmonic mode $a$ weakly coupled to a Josephson junction and driven by a stiff pump $p_0$ at its resonant frequency leads to a $4^{\text{th}}$-order term

$$H_S = E_J \frac{\varphi_{\text{zpf}}^4}{24} (p_0^2 a^2 + p_0^{*2} a^{\dagger 2}). \tag{a.13}$$

A more modern approach consist in engineering a 3-wave mixing term as provided by the SNAIL element ([158], [145]) to suppress at the first order the limiting Kerr terms.

The squeezing operation can always be seen as just a rescaling of the axis. In particular, Liouville's theorem implies that the squeezing is just a rescaling of the axes $I$ and $Q$. Due to this rescaling, the squeezing operator and the displacement operator do not commute. Finally, it is interesting to note that a plane wave, defined as an eigenvector of either quadrature, can be seen as the limit of an infinitely squeezed state.

In this work we also make use of two-squeezed states as it is direct application of the JPC (see [5] for details). We remind the reader here of a handful of key results. The two-mode squeezing is also a simple application of Liouville's theorem but on the 4 dimensional phase space made by the $2 \times 2$ quadratures of the two modes. If we consider 2 modes $a$ and $b$, the 2 modes squeezing operator reads

$$S_r = e^{rab - r^* a^\dagger b^\dagger}, \tag{a.14}$$

with similar notation to the single mode case. It can be directly obtained by driving a JPC at the frequency $\omega_a + \omega_b$ during a given duration. Indeed in the rotating wave approximation, the 3-wave mixing Hamiltonian of the driven JPC boils down to

$$H_S = gp_0 ab + g^* p_0^* a^\dagger b^\dagger. \tag{a.15}$$

It is a two mode squeezed state because when starting from the vacuum, the joint quadrature show correlation of the two mode squeezed state reads

$$\begin{aligned} \langle X_a \pm X_b \rangle &= \tfrac{1}{2} e^{\pm 2r} \\ \langle P_a \mp P_b \rangle &= \tfrac{1}{2} e^{\pm 2r} \end{aligned} \tag{a.16}$$

One can explicit the two mode squeezing even more by looking at the covariance matrix $V$ in the basis $(X_a, P_a, X_b, P_b)$

$$V = \begin{pmatrix} \cosh(2r) & 0 & \sinh(2r) & 0 \\ 0 & \cosh(2r) & 0 & -\sinh(2r) \\ \sinh(2r) & 0 & \cosh(2r) & 0 \\ 0 & -\sinh(2r) & 0 & \cosh(2r) \end{pmatrix} \tag{a.17}$$

where Liouville's theorem directly appears from the hyperbolic trigonometry relations. This state obtained by preparing both modes in the vacuum and applying the two-mode squeezing operator is called an EPR (Einstein-Podolsky-Rosen) state. It is the maximally entangled state, which in the Fock basis reads

$$|\mathrm{EPR}\rangle = S_r |0\rangle_a |0\rangle_b = \cosh(|r|)^{-1} \sum_{n=0}^{\infty} e^{in\mathrm{Arg}(r)} \tanh(|r|)^n |n\rangle_a |n\rangle_b. \tag{a.18}$$

It is indeed a maximally entangled state as when tracing over either mode, the other one becomes a thermal state, i.e. maximally entropic,

$$\rho_a = \mathrm{Tr}_b(|\mathrm{EPR}\rangle\langle\mathrm{EPR}|) = \cosh(|r|)^{-2} \sum_{n=0}^{\infty} \tanh(|r|)^{2n} |n\rangle_a \langle n|_a. \tag{a.19}$$

which shows that all the information encoded in the EPR state is stored in joint quadratures.

### A.1.3 *Manipulation a bosonic state*

We have seen the main gaussian Hamiltonian operations, meaning operation that preserve the gaussian nature of a distribution in the phase space, namely displacement and squeezing. Those were already available on the previous version of the quantum node. The goal of this thesis was to broaden the capabilities of our quantum node by providing it with arbitrary Hamiltonian generation using an ancillary qubit.

Indeed, as shown by R. W. Heeres *et al.* ([159]) any Hamiltonian operation on a harmonic oscillator can be constructed by repeating Selective Number-dependent Arbitrary Phase (SNAP) gates and displacement operation.

The SNAP operator $S_n(\theta)$ is nothing but a photon number dependent Berry phase ([160]) applied on each of the amplitudes of the Fock basis description of the oscillator state. The gate sequence is the following. To do so experimentally, one requires the ancilla qubit to be in the photon number selective regime, meaning $\chi \gg 1/T_2$ such that it is possible to apply $\Pi$ pulses on the qubit conditioned on the number of photon in the oscillator. The SNAP operator is then simply made in two steps : first the ancillary

qubit is unconditionally excited by a Π pulse along a given meridian and then it is de-excited by a selective Π pulse along a different meridian for each photon number in the oscillator, such that we select the geometrical phase $\theta(n)$ acquired between the excitation and de-excitation for each coefficient of the Fock basis decomposition of the oscillator quantum state.

Even though this method allows for arbitrary state preparation and Hamiltonian gate (see [161] for proof of universal control) it often requires several steps alternating displacements and SNAP gates which parameters are analytically not easily computable. Thus it requires sufficient coherence time for the oscillator to be performed and the gate sequence must be numerically computed (e.g. using the python package QuTip).

## A.2 PHASE SPACE REPRESENTATIONS

In classical mechanics, the state of a harmonic oscillator can be describe by the trajectory of a point in a phase-space representation (i.e. position and momentum space or in our case $I$ and $Q$ ). In the right rotating frame the phase space-representation is often reduced to a single stationary point. The measurement of the phase-space trajectory leads to an unambiguous knowledge of the system.

It is not that simple in quantum mechanics. Indeed, the wave-like behavior of a quantum system induces the Heisenberg uncertainty principal (which should be called the indetermination principal). In turn, this indetermination means that the system's representation in the phase-space must be a distribution where the product of the variance must be greater than 1/4, i.e.

$$\Delta I \Delta Q \geq \frac{1}{4}. \tag{a.20}$$

Nevertheless, phase-space representations are uniquely defined for each quantum state. Hence, provided a phase-space tomography of a quantum state, one can uniquely deduce the corresponding density matrix. This equivalence is crucial as we will see that phase-space representation of harmonic oscillators can be experimentally accessed in cQED and are thus an unparalleled tool to investigate quantum dynamics. Interestingly, several phase-space representations can be defined such that they uniquely describe a quantum state.

We provide here a definition of the two main phase-space representations used in this thesis and some examples to provide the reader with intuition on how to read those tomographies. We will see that the Wigner function is a practical way to access intra-cavity state using an ancillary qubit and the Husimi Q function is directly measured for flying bosonic state with an heterodyne measurement apparatus. Finally we will generalize those representations and detail how to commute from one to another. But first we define the characteristic function, not used in this thesis, as a basis for defining the following representation and because it is becoming a useful experimental tool as it only requires a weakly coupled qubit to measure it.

### A.2.1 *Characteristic function*

The characteristic function, denoted $C_s(\tilde{\alpha})$, is defined for a pure state $|\varphi\rangle$ as the overlap between that state and its copy displaced by $\tilde{\alpha}$,

$$C_s(\tilde{\alpha}) = \langle\varphi|D(\tilde{\alpha})|\varphi\rangle \tag{a.21}$$

Hence it can be understood as a tomography of the expectation values of displacements $D(\tilde{\alpha})$. Provided this point of view, the characteristic function can be defined for any state described by a density matrix $\rho$

$$C_s(\tilde{\alpha}) = \langle D(\tilde{\alpha})\rangle = \mathrm{Tr}(D(\tilde{\alpha})\rho). \tag{a.22}$$

Note that the subscript s of the characteristic function represent the symmetric ordering of $D(\tilde{\alpha})$ (see [29] for details on operator ordering). Also, $C_s(\tilde{\alpha})$ is a complex number with a symmetry inherited from the displacement operator

$$C_s(-\tilde{\alpha}) = \langle D(-\tilde{\alpha})\rangle = \langle D^\dagger(\tilde{\alpha})\rangle = C_s(\tilde{\alpha})^*. \tag{a.23}$$

Thus if $\rho$ is composed of symmetric wavefunctions in $I$ and $Q$, then $C_s$ is real.

Intuiting the form of a characteristic function is not obvious. But it is fairly simple for the vacuum,

$$C_s^{|0\rangle}(\tilde{\alpha}) = \langle 0|D(\tilde{\alpha})|0\rangle = \langle 0|\tilde{\alpha}\rangle = e^{-\frac{|\tilde{\alpha}|^2}{2}}. \tag{a.24}$$

Hence it is a gaussian centered in 0 with a standard deviation $\sigma = 1$.

This tomography was not used in this thesis, but we provide the measurement protocol here as it might come handy for our futur experiments. Indeed, it only requires for the ancillary qubit to be weakly coupled ($\chi \ll 1$ MHz) to the oscillator and it can be measured (almost) arbitrary fast. This is particularly useful for experiments that are very sensitive to dephasing arising from thermal excitation of the ancillary and hence need the ancilla to be as weakly coupled as possible, and experiments where the decay of the oscillator is the limiting factor and hence require fast tomography methods.

To measure the characteristic function of an oscillator mode $a$ dispersively coupled to an ancillary qubit, one need to induce a longitudinal coupling between the oscillator and the qubit by driving the qubit at the oscillator's frequency with a pump $p$ for a duration $t$ and compensating the induced displacement of the oscillator by a direct displacement of $a$ (as described in chapter 2, and demonstrated in ([46], [47])). This leads to the following interaction Hamiltonian

$$H_{\text{longi}} = g_{\text{longi}} a\sigma_z + \text{h.c.} \tag{a.25}$$

where $g_{\text{longi}}$ is complex, and its phase and amplitude are controlled by the pump complex amplitude $p$, it can thus be made sufficiently large by driving strongly (limited by the ionization of the ancilla). This interaction integrated over the duration $t$ leads to a conditional displacement of the oscillator

$$\begin{aligned} D(\tilde{\alpha}) &= e^{(\tilde{\alpha}a^\dagger - \tilde{\alpha}^* a)\sigma_z} \\ &= \tfrac{1}{2}((D(\tilde{\alpha}) + D(-\tilde{\alpha})\mathbb{I} + (D(\tilde{\alpha}) + D(-\tilde{\alpha})\sigma_z \end{aligned} \tag{a.26}$$

where $\tilde{\alpha} = g_{\text{longi}} t$.

To encode the characteristic function onto the qubit state, we initialize the qubit in the $|+\rangle$ state and then apply our conditional displacement. One can show that tracing over the oscillator the obtained state produces

$$\text{Tr}_a \left( D\left(\frac{\tilde{\alpha}}{2}\sigma_z\right) \rho_a \otimes |+\rangle\langle+| D\left(-\frac{\tilde{\alpha}}{2}\sigma_z\right)\right) = \frac{1}{2}\left(\mathbb{1} + \text{Re}(C_s(\tilde{\alpha}))\sigma_x + \text{Im}(C_s(\tilde{\alpha}))\sigma_y\right), \tag{a.27}$$

thus measuring the ancilla along $\sigma_x$ and $\sigma_y$ gives the desired characteristic function. Experimentally, the displacement $\tilde{\alpha}$ can be calibrated from the characteristic function of the vacuum. This tomography is still challenging to implement in experiments as it requires to master the longitudinal coupling engineering which is not trivial. Nevertheless, this method was used to investigate GKP state in a recent groundbreaking experiment ([117]).

### A.2.2 *Wigner function*

The most widely used tomography method for intracavity field analysis in cQED is the Wigner function since its experimental introduction in 2002 by Bertet *et al.* ([85]). It is a convenient tool as it bare some features reminiscent from the classical phase-space and it is relatively easy to read.

One way to define the Wigner function is as the 2D Fourier transform of the characteristic function,

$$W(\alpha) = \frac{1}{\pi^2}\int d^2\tilde{\alpha}\; C_s(\tilde{\alpha}) e^{\alpha\tilde{\alpha}^* - \alpha^*\tilde{\alpha}}. \tag{a.28}$$

Provided this definition, it inherits the symmetry of the characteristic function, namely $C_s(-\tilde{\alpha}) = C_s(\tilde{\alpha})^*$ which leads to $W$ to be real. Furthermore, the Wigner function is normalized

$$\int d^2\tilde{\alpha}\; W(\alpha) = C_s(0) = 1. \tag{a.29}$$

In order to better interpret the Wigner function, we decompose $\alpha = I + iQ$ and from the appendix of ([29]) we obtain

$$W(I,Q) = \frac{1}{\pi}\int du\; e^{-2iQu}\langle I + \frac{u}{2}|\rho|I - \frac{u}{2}\rangle \tag{a.30}$$

This expression allows us to retrieve any coefficient of $\rho$ from the following inverted equation. In particular, it shows that the Wigner function contains all the information required to characterize the oscillator's state, and since all the phase-space representation we present here are related by bijective processes, it proves that any of those tomography are sufficient to characterize the quantum state of the oscillator.

$$\langle I + \frac{u}{2}|\rho|I - \frac{u}{2}\rangle = \int dQ\; e^{-2iQu} W(I,Q) \tag{a.31}$$

An interesting remark to analyze Wigner function is to note that by taking $u = 0$ in eq. a.31 we retrieve the probability for the oscillator to have a given position $I$ from

the marginal of the Wigner function. Indeed those marginals are normalized to 1 and positive thanks to the normalization of the Wigner function, and

$$\langle I|\rho|I\rangle = \int dQ\ W(I,Q). \tag{a.32}$$

From the symmetry between $I$ and $Q$ one can guess that this is also true for $Q$ and more generally for rotation of the basis,

$$\langle Q|\rho|Q\rangle = \int dI\ W(I,Q). \tag{a.33}$$

We showed that the Wigner function is real, but can take positive and negative values. Since its marginals along any direction are probabilities, the areas where it takes negative values (called *negativities*) must be encircled by areas of positive values sufficiently large to compensate. The negativities of Wigner function are purely quantum features with no classical analogue. Furthermore, if $\rho$ is made of the statistical mixture of several pure states, its Wigner tomography is also the statistical average of each Wigner corresponding to those pure states. And due to the constraints listed previously on the negativities, the latter tend to vanish as $\rho$ becomes more and more impure. Thus the negativities are often read as a sign of coherence and purity of the state of the oscillator.

We describe here how Wigner function are measured using an ancilla qubit coupled with the usual dispersive Hamiltonian interaction ([162], [84], [85])

$$H_{\text{int}} = \chi a^\dagger a \frac{\sigma_z}{2}. \tag{a.34}$$

To understand the measurement method, lets rewrite eq. a.30,

$$e^{-iQu}|I - \frac{u}{2}\rangle = e^{-iIQ} D(I+iQ)|-\frac{u}{2}\rangle \tag{a.35}$$

$$\langle I - \frac{u}{2}|e^{-iQu} = \langle \frac{u}{2}|D(-I-iQ)e^{iIQ}, \tag{a.36}$$

hence,

$$\begin{aligned} W(\alpha) &= \tfrac{1}{\pi}\textstyle\int du\ \langle \frac{u}{2}|D(-\alpha)\rho D(\alpha)|-\frac{u}{2}\rangle \\ &= \tfrac{1}{\pi}\textstyle\int du\ \langle \frac{u}{2}|D(-\alpha)\rho D(\alpha)\mathbb{P}|\frac{u}{2}\rangle \\ &= \tfrac{2}{\pi}\langle D(\alpha)\mathbb{P}D(-\alpha)\rangle \end{aligned} \tag{a.37}$$

where $\mathbb{P} = e^{i\pi a^\dagger a}$ is the parity operator that correspond to a central symmetry of the phase-space. Thus the Wigner function can be understood as the expectation value of the displaced parity operator up to a normalization factor.

In order to measure this expectation value, we remark that letting the ancilla qubit interact with the oscillator for a duration $t_{\text{parity}} = \pi/\chi$ leads to the effective interaction $e^{i\pi a^\dagger a \sigma_z/2}$, that is a rotation by an angle $\pi$ of the qubit around the z-axis of the ancilla conditioned of the number of photon in the oscillator.

The measurement protocol of the Wigner function is thus similar to the measurement of the characteristic function: we initialize the qubit in the $|+\rangle$ state, displace the oscillator by $-\alpha$ and let it interact with the qubit for $t_{\text{parity}}$ and measure the qubit

along $\sigma_x$. We detail below the proof that this implements a measurement of the Wigner function (up to a normalization factor).

We begin by writing the displaced state of the oscillator in the Fock basis,

$$D(\alpha)\rho_a D(-\alpha) = \sum_{k,l} c_{k,l}|k\rangle\langle l|. \tag{a.38}$$

Thus after the interaction with the qubit, the system reads

$$\begin{aligned} e^{-i\pi a^\dagger a\sigma_z/2}\left(D(\alpha)\rho_a D(-\alpha)\right)|+\rangle\langle+|e^{i\pi a^\dagger a\sigma_z/2} & \\ &= \sum_{k,l} c_{k,l} e^{-i\pi a^\dagger a\sigma_z/2}|k\rangle\langle l||+\rangle\langle+|e^{i\pi a^\dagger a\sigma_z/2} \\ &= \sum_{k,l} \left(c_{2k,2l}|2k\rangle\langle 2l||+\rangle\langle+| + c_{2k+1,2l+1}|2k+1\rangle\langle 2l+1||-\rangle\langle-|\right) \\ &\quad + \text{off-diagonal oscillator terms.} \end{aligned} \tag{a.39}$$

We do not detail the off-diagonal terms of the oscillator as we will trace over the oscillator as for the characteristic function. We denote the probability to measure even/odd terms off this density matrix by

$$\begin{aligned} P_e &= \textstyle\sum_{k,l} c_{2k,2l} \\ P_o &= \textstyle\sum_{k,l} c_{2k+1,2l+1} \end{aligned} \tag{a.40}$$

Thus, discarding the oscillator after the interaction leads to

$$\begin{aligned} \mathrm{Tr}_a(e^{-i\pi a^\dagger a\sigma_z/2}D(\alpha)\rho_a D(-\alpha)|+\rangle\langle+|e^{i\pi a^\dagger a\sigma_z/2}) & \\ &= P_e|+\rangle\langle+| + P_o|-\rangle\langle-| \\ &= \frac{(P_e+P_o)\mathbb{I} + (P_e-P_o)\sigma_x}{2} \\ &= \frac{\mathbb{I} + \langle D(\alpha)\mathbb{P}D(-\alpha)\rangle\sigma_x}{2}, \end{aligned} \tag{a.41}$$

*quod erat demonstrandum*. We indeed encoded the displaced parity expectation value on the $\sigma_x$ operator of the qubit.

# BIBLIOGRAPHY


[1] D. M. Pozar, *Microwave Engineering* (John Wiley {&} Sons, 1998) (Cited on pages 1, 8, 9, 27).

[2] E. Grumbling and M. Horowitz, eds., *Quantum Computing* (National Academies Press, Washington, D.C., 2019) (Cited on page 1).

[3] W. Pfaff et al., "Controlled release of multiphoton quantum states from a microwave cavity memory," Nature Physics (2017) 10.1038/nphys4143 (Cited on pages 1, 35).

[4] E Flurin et al., "Generating Entangled Microwave Radiation Over Two Transmission Lines," Physical Review Letters **109**, 183901 (2012) (Cited on pages 1, 2).

[5] E. Flurin, "The Josephson Mixer, a Swiss army knife for microwave quantum optics," Theses (Ecole Normale Supérieure, Paris, 2014) (Cited on pages 1, 2, 14, 16–18, 24, 27, 32, 33, 35, 42, 44, 62, 64, 65, 69, 144).

[6] D. Marković, "Applications of the Josephson mixer : ultrastrong coupling , quantum node and injection locking in Danijela Marković To cite this version : HAL Id : tel-01774258 Applications of the Josephson mixer," (2018) (Cited on pages 1, 14, 35, 40).

[7] J. M. Martinis and A. Megrant, "UCSB final report for the CSQ program: Review of decoherence and materials physics for superconducting qubits," (2014) (Cited on page 1).

[8] A. Nersisyan et al., "Manufacturing low dissipation superconducting quantum processors," (2019) (Cited on page 1).

[9] C. Wang et al., "Surface participation and dielectric loss in superconducting qubits," Applied Physics Letters **107**, 162601 (2015) (Cited on page 1).

[10] J. M. Kreikebaum, K. P. O'Brien, and I. Siddiqi, "Improving wafer-scale Josephson junction resistance variation in superconducting quantum coherent circuits," (2019) (Cited on page 1).

[11] E. A. Sete et al., "Catch-Disperse-Release Readout for Superconducting Qubits," (2013) 10.1103/PhysRevLett.110.210501 (Cited on pages 2, 32, 52, 55, 137).

[12] T. Walter et al., "Rapid High-Fidelity Single-Shot Dispersive Readout of Superconducting Qubits," Physical Review Applied (2017) 10.1103/PhysRevApplied.7.054020 (Cited on pages 3, 22, 52).

[13] R. Dassonneville et al., "Fast High-Fidelity Quantum Nondemolition Qubit Readout via a Nonperturbative Cross-Kerr Coupling," Physical Review X **10**, 011045 (2020) (Cited on page 3).

[14] A. Roy and M. Devoret, "Introduction to parametric amplification of quantum signals with Josephson circuits," Comptes Rendus Physique **17**, 740–755 (2016) (Cited on page 3).

[15] F. Mallet et al., "Single-shot qubit readout in circuit quantum electrodynamics," Nature Physics **5**, 791–795 (2009) (Cited on page 3).

[16] A. Eddins et al., "High-Efficiency Measurement of an Artificial Atom Embedded in a Parametric Amplifier," Physical Review X **9**, 011004 (2019) (Cited on page 3).

[17] A. Kronwald, F. Marquardt, and A. A. Clerk, "Arbitrarily large steady-state bosonic squeezing via dissipation," Physical Review A **88**, 063833 (2013) (Cited on page 3).

[18] A. R. Calderbank and P. W. Shor, "Good quantum error-correcting codes exist," Physical Review A **54**, 1098–1105 (1996) (Cited on page 4).

[19] A. G. Fowler et al., "Surface codes: Towards practical large-scale quantum computation," Physical Review A **86**, 32324 (2012) (Cited on pages 4, 114, 121).

[20] Z Leghtas et al., "Confining the state of light to a quantum manifold by engineered two-photon loss," Science **347**, 853–857 (2015) (Cited on pages 4, 114–116, 119, 128, 132).

[21] D. J. Wineland, "Superposition, Entanglement, and Raising Schrödinger's Cat (Nobel Lecture)," Angewandte Chemie International Edition **52**, 10179–10189 (2013) (Cited on page 7).

[22] S. Haroche, "Nobel Lecture: Controlling photons in a box and exploring the quantum to classical boundary," Reviews of Modern Physics **85**, 1083–1102 (2013) (Cited on page 7).

[23] Y. Nakamura, Y. A. Pashkin, and J. S. Tsai, "Coherent control of macroscopic quantum states in a single-Cooper-pair box," (1999) 10.1038/19718 (Cited on pages 7, 8).

[24] L. B. Nguyen et al., "The high-coherence fluxonium qubit," (2018) (Cited on page 8).

[25] W. Pfaff et al., "Controlled release of multiphoton quantum states from a microwave cavity memory," Nature Physics **13**, 882–887 (2017) (Cited on pages 8, 54, 55).

[26] S. Haroche, "Controlling photons in a box and exploring the quantum to classical boundary," Annalen der Physik **525**, 753–776 (2013) (Cited on page 9).

[27] J. M. Martinis and A. Megrant, "UCSB final report for the CSQ program: Review of decoherence and materials physics for superconducting qubits," (2014) (Cited on page 9).

[28] M. Devoret et al., eds., *Quantum Machines: Measurement and Control of Engineered Quantum Systems* (Oxford University Press, 2014) (Cited on page 10).

[29] S. Haroche and J.-M. Raimond, "Exploring the Quantum," Oxford Graduated Text, 616 (2006) (Cited on pages 11, 26, 84, 92, 94, 119, 141, 147, 148).

[30] V. Ambegaokar and A. Baratoff, "Tunneling Between Superconductors," Physical Review Letters **10**, 486–489 (1963) (Cited on page 12).

[31] N. E. Frattini et al., "3-Wave Mixing Josephson Dipole Element," (2017) 10.1063/1.4984142 (Cited on page 12).

[32] P. Campagne-Ibarcq, "Measurement back action and feedback in superconducting circuits," Theses (Ecole Normale Supérieure (ENS), 2015) (Cited on pages 13, 21).

[33] A. Wallraff et al., "Strong coupling of a single photon to a superconducting qubit using circuit quantum electrodynamics," Nature **431**, 162–167 (2004) (Cited on page 13).

[34] N. Bergeal et al., "Phase-preserving amplification near the quantum limit with a Josephson ring modulator," Nature **465**, 64–68 (2010) (Cited on page 14).

[35] B. Abdo et al., "Josephson amplifier for qubit readout," Applied Physics Letters **99**, 162506 (2011) (Cited on page 14).

[36] B. Abdo, A. Kamal, and M. Devoret, "Nondegenerate three-wave mixing with the Josephson ring modulator," Physical Review B **87**, 14508 (2013) (Cited on page 14).

[37] T. Roy et al., "Implementation of Pairwise Longitudinal Coupling in a Three-Qubit Superconducting Circuit," Physical Review Applied **7**, 054025 (2017) (Cited on page 14).

[38] E Flurin et al., "Superconducting quantum node for entanglement and storage of microwave radiation," Phys. Rev. Lett. **114**, 90503 (2014) (Cited on pages 14, 24, 33, 35, 37, 38, 52–54).

[39] M. F. Gely and G. A. Steele, "QuCAT: Quantum Circuit Analyzer Tool in Python," (2019) arXiv:1908.10342 (Cited on pages 18, 81).

[40] S Nigg et al., "Black-Box Superconducting Circuit Quantization," Physical Review Letters **108**, 240502 (2012) (Cited on page 19).

[41] F. Solgun, D. W. Abraham, and D. P. DiVincenzo, "Blackbox quantization of superconducting circuits using exact impedance synthesis," Physical Review B **90**, 134504 (2014) (Cited on pages 19, 22).

[42] M. Malekakhlagh and H. E. Tureci, "Origin and Implications of $A^2$-like Contribution in the Quantization of Circuit-QED Systems," (2015) 10.1103/PhysRevA.93.012120 (Cited on page 19).

[43] R. J. Schoelkopf et al., "Qubits as Spectrometers of Quantum Noise," in *Quantum noise in mesoscopic physics* (Springer Netherlands, Dordrecht, 2003), pp. 175–203 (Cited on page 22).

[44] P. Krantz et al., "A Quantum Engineer's Guide to Superconducting Qubits," (2019) (Cited on page 22).

[45] B. Abdo et al., "Time-multiplexed amplification in a hybrid-less and coil-less Josephson parametric converter," (2016) 10.1063/1.4976962 (Cited on pages 24, 42).

[46] S. Touzard et al., "Gated conditional displacement readout of superconducting qubits," (2018) 10.1103/PhysRevLett.122.080502 (Cited on pages 25, 114, 115, 119, 147).

[47] J. Ikonen et al., "Qubit Measurement by Multichannel Driving," (2018) 10.1103/PhysRevLett.122.080503 (Cited on pages 25, 52, 147).

[48] R. Lescanne et al., "Observing the escape of a driven quantum Josephson circuit into unconfined states," (2018) 10.1103/PhysRevApplied.11.014030 (Cited on pages 26, 45, 54, 58).

[49] M. D. Reed et al., "High-Fidelity Readout in Circuit Quantum Electrodynamics Using the Jaynes-Cummings Nonlinearity," (2010) 10.1103/PhysRevLett.105.173601 (Cited on pages 26, 45).

[50] D. Sank et al., "Measurement-induced state transitions in a superconducting qubit: Beyond the rotating wave approximation," (2016) 10.1103/PhysRevLett.117.190503 (Cited on pages 26, 45, 118).

[51] M. Reagor et al., "Reaching 10 ms single photon lifetimes for superconducting aluminum cavities," Applied Physics Letters **102**, 192604 (2013) (Cited on page 27).

[52] S. Ohya et al., "Sputtered TiN films for superconducting coplanar waveguide resonators," (2013) (Cited on page 27).

[53] B Misra and E. C. G. Sudarshan, "The Zeno paradox in quantum theory," Journal of Mathematical Physics **18**, 756 (1977) (Cited on page 29).

[54] P Facchi et al., "Quantum Zeno dynamics," Physics Letters A **275**, 12–19 (2000) (Cited on page 29).

[55] G. Salerno and I. Carusotto, "Dynamical decoupling and dynamical isolation in temporally modulated coupled pendulums," EPL (Europhysics Letters) **106**, 24002 (2014) (Cited on page 29).

[56] P. Campagne-ibarcq, "Measurement back action and feedback in superconducting circuits," Theses (Ecole Normale Sup{é}rieure, 2015), p. 223 (Cited on page 32).

[57] J. Koch et al., "Charge-insensitive qubit design derived from the Cooper pair box," Physical Review A **76**, 42319 (2007) (Cited on pages 33, 75).

[58] D. I. Schuster et al., "Resolving photon number states in a superconducting circuit," Nature **445**, 515–518 (2007) (Cited on pages 34, 78, 85).

[59] P Kurpiers et al., "Deterministic quantum state transfer and remote entanglement using microwave photons," Nature **558**, 264–267 (2018) (Cited on page 35).

[60] J Wenner et al., "Catching Shaped Microwave Photons with 99.4{%} Absorption Efficiency," arXiv:1311.1180 (2013) (Cited on page 36).

[61] C Simon et al., "Quantum memories," The European Physical Journal D **58**, 1–22 (2010) (Cited on page 36).

[62] K. M. Sliwa et al., "The reconfigurable Josephson circulator/directional amplifier," (2015) 10.1103/PhysRevX.5.041020 (Cited on page 42).

[63] L. Verney et al., "Structural Instability of Driven Josephson Circuits Prevented by an Inductive Shunt," Physical Review Applied **11**, 024003 (2019) (Cited on pages 45, 119, 124).

[64] Zurek, "Decoherence, einselection, and the quantum origins of the classical," Reviews of Modern Physics **75**, 715–775 (2003) (Cited on page 52).

[65] A Blais et al., "Quantum-information processing with circuit quantum electrodynamics," Physical Review A **75**, 32329 (2007) (Cited on pages 52, 75).

[66] J. Gambetta et al., "Quantum trajectory approach to circuit QED: Quantum jumps and the Zeno effect," Physical Review A **77**, 12112 (2008) (Cited on page 52).

[67] K. W. Murch et al., "Observing single quantum trajectories of a superconducting quantum bit.," Nature **502**, 211–214 (2013) (Cited on page 52).

[68] D Tan et al., "Prediction and retrodiction for a continuously monitored superconducting qubit," 6 (2014) (Cited on page 52).

[69] S. J. Weber et al., "Quantum trajectories of superconducting qubits," Comptes Rendus Physique **17**, 766–777 (2016) (Cited on page 52).

[70] Q. Ficheux et al., "Dynamics of a qubit while simultaneously monitoring its relaxation and dephasing," Nature Communications **9**, 1926 (2018) (Cited on pages 52, 96).

[71] R Vijay et al., "Stabilizing Rabi oscillations in a superconducting qubit using quantum feedback.," Nature **490**, 77–80 (2012) (Cited on page 52).

[72] D Ristè et al., "Feedback Control of a Solid-State Qubit Using High-Fidelity Projective Measurement," Physical Review Letters **109**, 240502 (2012) (Cited on page 52).

[73] P Campagne-Ibarcq et al., "Persistent Control of a Superconducting Qubit by Stroboscopic Measurement Feedback," Physical Review X **3**, 21008 (2013) (Cited on page 52).

[74] D Ristè et al., "Deterministic entanglement of superconducting qubits by parity measurement and feedback.," Nature **502**, 350–354 (2013) (Cited on page 52).

[75] G de Lange et al., "Reversing Quantum Trajectories with Analog Feedback," Physical Review Letters **112**, 80501 (2014) (Cited on page 52).

[76] B. T. Gard et al., "Fast, High-Fidelity, Quantum Non-demolition Readout of a Superconducting Qubit Using a Transverse Coupling," (2018) (Cited on page 52).

[77] M. D. Reed et al., "Fast reset and suppressing spontaneous emission of a superconducting qubit," Applied Physics Letters **96**, 203110 (2010) (Cited on pages 52, 122).

[78] E. Jeffrey et al., "Fast Accurate State Measurement with Superconducting Qubits," Physical Review Letters **112**, 190504 (2014) (Cited on page 52).

[79] D. T. McClure et al., "Rapid Driven Reset of a Qubit Readout Resonator," arxiv:1503.01456 (2015) (Cited on page 52).

[80] C. C. Bultink et al., "Active Resonator Reset in the Nonlinear Dispersive Regime of Circuit QED," Physical Review Applied **6**, 034008 (2016) (Cited on page 52).

[81] N. Didier, J. Bourassa, and A. Blais, "Fast quantum non-demolition readout from longitudinal qubit-oscillator interaction," Phys. Rev. Lett. **115**, 203601 (2015) (Cited on page 52).

[82] S Touzard et al., "Coherent Oscillations inside a Quantum Manifold Stabilized by Dissipation," Physical Review X **8**, 21005 (2018) (Cited on page 52).

[83] B. Abdo et al., "Full Coherent Frequency Conversion between Two Propagating Microwave Modes," Physical Review Letters **110**, 173902 (2013) (Cited on page 54).

[84] L. G. Lutterbach and L Davidovich, "Method for Direct Measurement of the Wigner Function in Cavity QED and Ion Traps," Physical Review Letters **78**, 2547–2550 (1997) (Cited on pages 55, 71, 82, 90, 149).

[85] P Bertet et al., "Direct Measurement of the Wigner Function of a One-Photon Fock State in a Cavity," Physical Review Letters **89**, 200402 (2002) (Cited on pages 55, 71, 82, 90, 148, 149).

[86] B. Vlastakis et al., "Deterministically Encoding Quantum Information Using 100-Photon Schrodinger Cat States," Science **342**, 607–610 (2013) (Cited on pages 55, 71).

[87] L Bretheau et al., "Quantum dynamics of an electromagnetic mode that cannot have N photons," Science **348**, 776 (2015) (Cited on pages 55, 71, 84, 93).

[88] M. Khezri et al., "Measuring a transmon qubit in circuit QED: Dressed squeezed states," Physical Review A **94**, 012347 (2016) (Cited on page 55).

[89] G. Kirchmair et al., "Observation of quantum state collapse and revival due to the single-photon Kerr effect," Nature **495**, 205–209 (2013) (Cited on page 55).

[90] C Macklin et al., "A near-quantum-limited Josephson traveling-wave parametric amplifier," Science **350**, 307–310 (2015) (Cited on pages 56, 82).

[91] "No Title," Supplementary Material (Cited on page 56).

[92] N Bergeal et al., "Phase-preserving amplification near the quantum limit with a Josephson ring modulator," Nature **465**, 64 (2010) (Cited on page 58).

[93] N Roch et al., "Widely Tunable, Nondegenerate Three-Wave Mixing Microwave Device Operating near the Quantum Limit," Physical Review Letters **108**, 147701 (2012) (Cited on page 58).

[94] J. Atalaya et al., "Correlators Exceeding One in Continuous Measurements of Superconducting Qubits," Physical Review Letters **122**, 223603 (2019) (Cited on pages 58, 62, 137).

[95] B. Vlastakis et al., "Characterizing entanglement of an artificial atom and a cavity cat state with Bell's inequality," Nature Communications **6**, 8970 (2015) (Cited on page 58).

[96] R. Lescanne et al., "Dynamics of an off-resonantly pumped superconducting qubit in a cavity," arXiv:1805.05198 (2018) (Cited on pages 61, 118, 124).

[97] C. C. Bultink et al., "General method for extracting the quantum efficiency of dispersive qubit readout in circuit QED," Applied Physics Letters **112**, 092601 (2018) (Cited on page 69).

[98] J. R. Johansson, P. D. Nation, and F. Nori, "QuTiP 2: A Python framework for the dynamics of open quantum systems," Computer Physics Communications **184**, 1234–1240 (2013) (Cited on pages 71, 98).

[99] Q. Ficheux, "Quantum Trajectories with Incompatible Decoherence Channels," (2018) (Cited on pages 73, 74).

[100] C. Guerlin et al., "Progressive field-state collapse and quantum non-demolition photon counting.," Nature **448**, 889–893 (2007) (Cited on page 78).

[101] B. R. Johnson et al., "Quantum non-demolition detection of single microwave photons in a circuit," Nat Phys **6**, 663–667 (2010) (Cited on page 78).

[102] B Peaudecerf et al., "Adaptive Quantum Nondemolition Measurement of a Photon Number," Physical Review Letters **112**, 80401 (2014) (Cited on page 78).

[103] S. Haroche, M. Brune, and J. M. Raimond, "Measuring photon numbers in a cavity by atomic interferometry: optimizing the convergence procedure," Journal de Physique II **2**, 659–670 (1992) (Cited on page 78).

[104] A. A. Houck et al., "Generating single microwave photons in a circuit," Nature **449**, 328–331 (2007) (Cited on page 81).

[105] O Astafiev et al., "Resonance Fluorescence of a Single Artificial Atom," Science **327**, 840–843 (2010) (Cited on page 81).

[106] A. A. Abdumalikov et al., "Dynamics of Coherent and Incoherent Emission from an Artificial Atom in a 1D Space," Physical Review Letters **107**, 43604 (2011) (Cited on page 81).

[107] P Campagne-Ibarcq et al., "Observing Interferences between Past and Future Quantum States in Resonance Fluorescence," Phys. Rev. Lett. **112**, 180402 (2014) (Cited on page 81).

[108] C. Cohen-Tannoudji, J. Dupont-Roc, and G. Grynberg, *Atom-Photon Interactions* (Wiley-VCH Verlag GmbH, Weinheim, Germany, 1998) (Cited on page 81).

[109] A Wallraff et al., "Strong coupling of a single photon to a superconducting qubit using circuit quantum electrodynamics," Nature **431**, 162–167 (2004) (Cited on page 81).

[110] V. Schmitt et al., "Multiplexed readout of transmon qubits with Josephson bifurcation amplifiers," Physical Review A **90**, 062333 (2014) (Cited on page 82).

[111] J. Heinsoo et al., "Rapid High-fidelity Multiplexed Readout of Superconducting Qubits," Physical Review Applied **10**, 034040 (2018) (Cited on page 82).

[112] S. Kundu et al., "Multiplexed readout of four qubits in 3D circuit QED architecture using a broadband Josephson parametric amplifier," Applied Physics Letters **114**, 172601 (2019) (Cited on page 82).

[113] F. Arute et al., "Quantum supremacy using a programmable superconducting processor," Nature **574**, 505–510 (2019) (Cited on page 82).

[114] A. A. Clerk et al., "Introduction to quantum noise, measurement, and amplification," Reviews of Modern Physics **82**, 1155–1208 (2010) (Cited on page 82).

[115] Boissonneault, Gambetta, and Blais, "Dispersive regime of circuit QED: Photon-dependent qubit dephasing and relaxation rates," Physical Review A **79**, 13819 (2009) (Cited on page 82).

[116] B. Vlastakis et al., "Deterministically encoding quantum information using 100-photon Schr{ö}dinger cat states.," Science (New York, N.Y.) **342**, 607–610 (2013) (Cited on pages 82, 90).

[117] P. Campagne-Ibarcq et al., "A stabilized logical quantum bit encoded in grid states of a superconducting cavity," (2019) (Cited on pages 84, 93, 148).

[118] H. M. Wiseman and G. J. Milburn, *Quantum Measurement and Control* (Cambridge University Press, 2009) (Cited on page 84).

[119] S Kono et al., "Quantum non-demolition detection of an itinerant microwave photon," Nature Physics **14**, 546–549 (2018) (Cited on page 84).

[120] J.-C. Besse et al., "Single-Shot Quantum Nondemolition Detection of Individual Itinerant Microwave Photons," Physical Review X **8**, 21003 (2018) (Cited on page 84).

[121] R. Lescanne et al., "Exponential suppression of bit-flips in a qubit encoded in an oscillator," (2019) (Cited on page 84).

[122] N. Cottet and B. Huard, "Maxwell's demon in superconducting circuits," arXiv:1805.01224 (2018) (Cited on page 99).

[123] A. Sarlette et al., "Quantum adiabatic elimination at arbitrary order for photon number measurement," (2020) (Cited on page 105).

[124] P. W. Shor, "Scheme for reducing decoherence in quantum computer memory," Physical Review A **52**, R2493–R2496 (1995) (Cited on page 114).

[125] A Steane, "Multiple-Particle Interference and Quantum Error Correction," Proceedings of the Royal Society A: Mathematical, Physical and Engineering Sciences **452**, 2551–2577 (1996) (Cited on page 114).

[126] C. Flühmann et al., "Encoding a qubit in a trapped-ion mechanical oscillator," Nature **566**, 513–517 (2019) (Cited on page 114).

[127] P. Brooks, A. Kitaev, and J. Preskill, "Protected gates for superconducting qubits," Physical Review A **87**, 052306 (2013) (Cited on page 114).

[128] S. M. Albrecht et al., "Exponential protection of zero modes in Majorana islands," Nature **531**, 206–209 (2016) (Cited on page 114).

[129] Y.-H. Lin et al., "Demonstration of Protection of a Superconducting Qubit from Energy Decay," Physical Review Letters **120**, 150503 (2018) (Cited on page 114).

[130] N. Earnest et al., "Realization of a <math display="inline"> <mi mathvariant="normal">Λ</mi> </math> System with Metastable States of a Capacitively Shunted Fluxonium," Physical Review Letters **120**, 150504 (2018) (Cited on page 114).

[131] W. C. Smith et al., "Superconducting circuit protected by two-Cooper-pair tunneling," npj Quantum Information **6**, 8 (2020) (Cited on page 114).

[132] S. Puri, S. Boutin, and A. Blais, "Engineering the quantum states of light in a Kerr-nonlinear resonator by two-photon driving," npj Quantum Information **3**, 18 (2017) (Cited on page 114).

[133] M. Wolinsky and H. J. Carmichael, "Quantum noise in the parametric oscillator: From squeezed states to coherent-state superpositions," Physical Review Letters **60**, 1836–1839 (1988) (Cited on pages 114, 116).

[134] J. Guillaud and M. Mirrahimi, "Repetition Cat Qubits for Fault-Tolerant Quantum Computation," Physical Review X **9**, 041053 (2019) (Cited on pages 115, 119, 121, 138).

[135] M. Mirrahimi et al., "Dynamically protected cat-qubits: a new paradigm for universal quantum computation," New Journal of Physics **16**, 45014 (2014) (Cited on pages 115, 116).

[136] A. Grimm et al., "The Kerr-Cat Qubit: Stabilization, Readout, and Gates," (2019) (Cited on page 115).

[137] S. Puri et al., "Bias-preserving gates with stabilized cat qubits," (2019) (Cited on page 115).

[138] Z. Leghtas et al., "Hardware-Efficient Autonomous Quantum Memory Protection," Physical Review Letters **111**, 120501 (2013) (Cited on page 116).

[139] D. Gottesman, A. Kitaev, and J. Preskill, "Encoding a qubit in an oscillator," Physical Review A **64**, 012310 (2001) (Cited on page 116).

[140] H. J. Carmichael, *Statistical Methods in Quantum Optics 2*, Theoretical and Mathematical Physics (Springer Berlin Heidelberg, Berlin, Heidelberg, 2008) (Cited on page 116).

[141] Y. Y. Gao et al., "Programmable Interference between Two Microwave Quantum Memories," Physical Review X **8**, 021073 (2018) (Cited on page 118).

[142] C. Wang et al., "Measurement and control of quasiparticle dynamics in a superconducting qubit," Nature Communications **5**, 5836 (2014) (Cited on page 118).

[143] A. Vrajitoarea et al., "Quantum control of an oscillator using a stimulated Josephson nonlinearity," Nature Physics **16**, 211–217 (2020) (Cited on page 119).

[144] M. Reagor et al., "A quantum memory with near-millisecond coherence in circuit QED," arxiv:1508.0588 (2015) (Cited on page 121).

[145] N. E. Frattini et al., "Optimizing the nonlinearity and dissipation of a SNAIL Parametric Amplifier for dynamic range," (2018) 10.1103/PhysRevApplied.10.054020 (Cited on pages 123, 144).

[146] Joachim Cohen, "Autonomous quantum error correction with superconducting qubits," Thesis (2017) (Cited on pages 127, 129, 132).

[147] S. E. Nigg et al., "Black-box superconducting circuit quantization," Physical Review Letters **108** (2012) 10.1103/PhysRevLett.108.240502 (Cited on page 137).

[148] F. Solgun, D. W. Abraham, and D. P. DiVincenzo, "Blackbox Quantization of Superconducting Circuits using exact Impedance Synthesis," arxiv:1403.7341 (2014) (Cited on page 137).

[149] M. Malekakhlagh, A. Petrescu, and H. E. Türeci, "Cutoff-Free Circuit Quantum Electrodynamics," Physical Review Letters **119**, 073601 (2017) (Cited on page 137).

[150] M. F. Gely and G. A. Steele, "QuCAT: quantum circuit analyzer tool in Python," New Journal of Physics **22**, 013025 (2020) (Cited on page 137).

[151] Z. Minev, "pyEPR," (Cited on page 137).

[152] E. C. G. Sudarshan, "Equivalence of Semiclassical and Quantum Mechanical Descriptions of Statistical Light Beams," Physical Review Letters **10**, 277–279 (1963) (Cited on page 142).

[153] R. J. Glauber, "Coherent and Incoherent States of the Radiation Field," Physical Review **131**, 2766–2788 (1963) (Cited on page 142).

[154] Q Ficheux et al., "Dynamics of a qubit while simultaneously monitoring its relaxation and dephasing," Nature Communications **9**, 1926 (2018) (Cited on page 143).

[155] B Yurke et al., "A low-noise series-array Josephson junction parametric amplifier," Applied Physics Letters **69**, 3078 (1996) (Cited on page 144).

[156] M. A. Castellanos-Beltran et al., "Bandwidth and dynamic range of a widely tunable Josephson parametric amplifier," arXiv **cond-mat.m** (2009) (Cited on page 144).

[157] F Mallet et al., "Quantum State Tomography of an Itinerant Squeezed Microwave Field," Physical Review Letters **106**, 220502 (2011) (Cited on page 144).

[158] N. E. Frattini et al., "3-Wave Mixing Josephson Dipole Element," (2017) 10.1063/1.4984142 (Cited on page 144).

[159] R. W. Heeres et al., "Cavity State Manipulation Using Photon-Number Selective Phase Gates," (2015) 10.1103/PhysRevLett.115.137002 (Cited on page 145).

[160] M. V. Berry, "Quantal Phase Factors Accompanying Adiabatic Changes," Proceedings of the Royal Society A: Mathematical, Physical and Engineering Sciences **392**, 45–57 (1984) (Cited on page 145).

[161] S. Krastanov et al., "Universal control of an oscillator with dispersive coupling to a qubit," Phys. Rev. A **92**, 40303 (2015) (Cited on page 146).

[162] L Sun et al., "Tracking photon jumps with repeated quantum non-demolition parity measurements," Nature **511**, 444–448 (2014) (Cited on page 149).